High spectral resolution gamma ray astronomy in the energy region 50keV to l0MeV

Richard Michael Myers

HIGH SPECTRAL RESOLUTION GAMMA RAY ASTRONOMY IN THE ENERGY REGION 50 keV TO 10 MeV

by

RICHARD MICHAEL MYERS B.Sc.

A Thesis
Submitted to the University of Durham
for the Degree of
Doctor of Philosophy

To my mother,
and in memory of my father.

Abstract.

Observations of the Crab nebula region and of the unusual active galaxy NGC1275 made during a balloon flight of the Durham high spectral resolution gamma ray telescope are described. From the Crab, spectral line fluxes were detected at 79 keV (transient), 405 keV, and at 1050 keV. The first two are possible confirmation of previous results. From NGC1275, evidence of two-photon electron-positron annihilation radiation with the expected redshifted energy of 502 keV was observed. Possible interpretations are suggested.

Contents.

List of symbols.

Unless otherwise stated the following symbols have the indicated meaning throughout the text.

h	Planck's constant
c	velocity of light in vacuo
k	Boltzmann constant
E_γ	gamma ray energy
T	temperature
ν	frequency
m_0	electron rest mass
v	velocity
γ	Lorentz factor
ϵ_0	permittivity of free space
r_0	classical electron radius
Z	atomic number
G	gravitational constant
α	fine structure constant
$\mathrm{M}_\odot$	solar mass ($1.99 \times 10^{30}\,\mathrm{kg}$)

NOTE ON UNITS

Unfortunately the adoption of a consistent system of units is not practical at present in a thesis which has to cover engineering, observational and theoretical areas. Mks (SI) units are common for engineering description and are convenient for flux measurement, whilst cgs units are generally used for theoretical astrophysics. The use of other units such as the electron volt ($1\,\mathrm{eV} = 1.602 \times 10^{-19}\,\mathrm{Joules} = 1.602 \times 10^{-12}\,\mathrm{ergs}$) and the parsec ($1\,\mathrm{pc} = 3.0856 \times 10^{16}\,\mathrm{m}$) is inevitable and often justifiably convenient. The imposition of a common system throughout would probably do more harm than good even though it would eliminate some unfortuate inconsistency.

Chapter 1.

Introduction.

The experimental study of astronomical gamma ray lines at nuclear transition energies developed rapidly in the late 1970s through the use of high spectral resolution spectrometers. It could potentially provide unique information in fields as diverse as nucleosynthesis, the study of cosmic rays and the interstellar medium, pulsar emission mechanisms, active galactic nuclei, compact radio sources, and other areas.

It might be argued that the discipline has not fulfilled its original promise, but perhaps it is not so much that the project has been found wanting as found difficult. The results from the first balloons and satellites revealed a number of difficult and largely unsuspected systematic effects. These have made the analysis of data time-consuming, and the comparison of results from different spectrometers uncertain. This has in turn led to a slowing in the pace of instrumental development.

However the original scientific motives behind the discipline are still as strong — if not stronger — than at the inception, and it may be that if a sufficient number of clear results are demonstrated from the accumulated data then the commitment to advance instrumental design will be found.

With this in mind the author examines confirmed positive line detections, with reference to the instruments, methods of observation and data analysis. There are perhaps two or three non-solar and non-burst lines which are now reasonably established. The data from the 1981 flight of the Durham balloon-borne high energy resolution spectrometer are then examined for the Crab Nebula region and the active galaxy NGC1275. The Crab results offer evidence in support of previous work. The NGC1275 data contain evidence of electron-positron annihilation radiation, perhaps the first detection of an extragalactic line of this sort.

The emphasis in this thesis is on the technical aspects of gamma ray line astronomical observation and on ensuring that the claimed signals have significance. Thus astrophysical models are not dealt with in detail.

In chapter 2 the physical mechanisms for gamma ray line production, energy shifting and broadening are described together with a summary of theoretical predictions regarding potential astrophysical sources. The sources of the continuum fluxes which frequently underlie the nuclear transition energy region are summarised. Finally the interaction mechanisms for gamma rays are discussed — these are relevant to source absorption calculations and also to the understanding of detector responses.

Chapter 3 is a summary of gamma ray line observations. The scope of the review is defined and then the relevant satellite and balloon-borne gamma ray telescopes are described. Each observation is listed together with available details on flight conditions, detector performance and source observation mode. As far as possible the data analysis technique for each observation is described particularly in respect of line-scanning technique and background subtraction. A brief summary of theoretical interpretation of the lines is then given. For the Crab and NGC1275, which were observed in the present work, some of the discussion is deferred to chapter 5, where the Durham results may be placed in context.

The present experiment is described in chapter 4. Details of the Durham mark 1B high spectral resolution gamma ray telescope are given, both in terms of its physical construction and also its detection characteristics. The associated nuclear electronics and telemetry system are described. The telescope orientation system is detailed, the electronics and telecommand interface being the special responsibility of the author during the construction phase. The additional system monitoring electronics and the payload support, environmental containment, power supplies and crash protection are briefly described. Details of the 6–7 June 1981 flight from the National Scientific Balloon Facility, Palestine, Texas, USA are then given; here the author's responsibility was scientific operation of the system for the portion of the flight controlled by the down-range tracking station at Pecos, Texas. Finally this chapter contains a description of the preliminary phase of data processing, that is the validation and ordering of the telemetry data and the removal of corrupt records.

In chapter 5 we move on to the analysis of the Durham flight data for the Crab region and NGC1275. The method of data reduction and its statistical

justification are discussed and the use of the Crab continuum flux to realign the pointing system alt-azimuth coordinates is described. The derived fluxes for the two sources are tabulated and then discussed in terms of previous observations. Finally some suggestions for interpretation are given.

The majority of the computer software used to analyse the source data was written by the author. The following were the sole responsibility of the author:-

i) The overall design of the system of data reduction programmes.

ii) The flight database design, construction and management.

iii) The new command language and hierarchical data storage system which allows programmes to communicate, data to be flexibly stored, and batch processing to be coordinated. This system eases the task of programme maintenance and makes the programmes more straightforward for users unfamiliar with programming details.

iv) Support routines for such matters as calculating geographical position and pointing orientation, and routines for spectral processing and graphical display.

v) The source spectrum scanning system.

These, together with the design and construction of the pointing control system electronics, represent the author's main contributions to this project.

Chapter 2.

Production and interaction of gamma rays.

Gamma ray lines are principally of interest here; and it is to their mechanisms and sites of production, energy-shifting and broadening that most attention is given. However, continuum gamma rays are produced in the line energy region (particularly $< 511\,\mathrm{keV}$) with fluxes detectable by line telescopes from many actual or potential astrophysical line sources, so it is appropriate to describe these mechanisms too. The most common mechanisms for the interaction of gamma rays of this energy are also discussed. This has relevance to the discussion of astrophysical absorption as well as to detection techniques.

The energy range of the Durham spectrometer includes potential gamma ray lines produced by a variety of mechanisms which may be associated with a wide range of astrophysical sites. The mechanisms fall broadly into the categories of nuclear de-excitation, electron-positron annihilation, deuterium formation, charged particle interactions, neutron capture, and cyclotron radiation.

Laboratory measurements of nuclear transition gamma rays having inherently well defined energies are, of course, commonplace. These are slightly shifted and broadened by the recoil of the decaying nucleus, but not to any degree comparable with detector energy resolutions ($1-2\,\mathrm{keV}$ at best). However this is not generally the case with hypothetical astrophysical sites where substantial spectral modification is possible from recoil Doppler shift in gaseous media, and other processes such as gravitational and cosmological redshifting. These effects complicate the interpretation of spectra but may also convey important astrophysical information.

Possible non-solar sites of detectable fluxes include novae and supernovae, supernova remnants, pulsars, active galactic nuclei, Wolf-Rayet stars, accretion sites such as neutron stars and black holes, and the interstellar medium.

Predictions and interpretations of fluxes from specific sources are dealt with alongside the corresponding positive line detections in Chapter 3; here it will be sufficient to examine general theoretical predictions.

2.1 Physical mechanisms of line production.

It is not always possible to make a sharp distinction between some of the mechanisms to be described. For example, deuterium formation might also be described as radiative neutron capture, or even as nucleosynthesis. In some cases the distinction is simply the lifetime of the unstable states involved and hence the different astrophysical sites with which the categories are associated.

2.1.1 Nuclear de-excitation following nucleosynthesis.

A review of the physics of nuclear de-excitation in terms of quantum transitions is given by Chupp (1976). This review is derived from Marmier and Sheldon (1969). Various nuclear models and methods for predicting de-excitation line energies are discussed. However as Chupp (1976) points out, it is the tabulated experimental data to which the gamma ray astronomer should turn out of preference. The present uncertainty in modelling the nucleus makes theoretical prediction a last resort. The extensive tabulations of Lederer and Shirley (1978) and Erdtman and Soyka (1979) were particularly useful in the present work.

Production of nuclear species is the concern of nucleosynthesis theories. The aim is to explain the formation of the elements in their observed relative abundances. A general introduction is given in Clayton (1969), and recent compilations of work in the field may be found in Barnes, Clayton and Schramm (1983) and Arnett and Truran (1985). The general abundances of the elements are inferred from studies of cosmic rays, meteorites, the solar wind, terrestrial abundances and so forth (Cameron 1973).

Briefly, it is the conventional wisdom in nucleosynthesis studies that the cosmic abundances of most of the lighter elements (atomic mass < 60) may be explained by 'burning' processes in the interior of stars. The burning proceeds from one fuel source to another as the star evolves in a fashion which depends upon its mass at formation. Different processes may occur concurrently in different 'shells' of the stellar interior; those involving heavier elements will occur first in the hotter central regions. The established early processes of hydrogen combustion (PPI, PPII, PPIII and the CNO cycle) essentially convert ^{1}H to ^{4}He. The ^{4}He then fuses at higher temperatures to ^{12}C which in turn

is subsequently converted to ^{16}O and thence the unstable $^{24}Mg^{*}$ and $^{32}S^{*}$.

Neutrons liberated in ^{1}H and ^{4}He combustion zones may be absorbed by other elements to produce some of the heavier stable isotopes; this is the slow (s-) process of neutron absorption. However not all heavy elemental formation may be explained by the s-process as some stable elements could only be produced through a β-unstable intermediate stage whilst others are proton-rich. In order to explain the production of the neutron-rich elements, rapid neutron absorption (the r-process) is invoked, whilst the proton-rich elements are probably a result of photo-disintegration (Woosley and Howard 1978) and/or rapid proton absorption (Wallace and Woosley 1981). These processes are only expected in explosive reactions, along with the final burning of ^{28}Si (a decay product of $^{32}S^{*}$) to ^{60}Fe via its radioactive parent ^{56}Ni (Bodansky, Clayton and Fowler 1968). Of the possible sites for such explosive reactions, supernovae are thought to be the most important (eg. Clayton 1983), possibly followed by novae.

It is important to note that the astrophysical sites of some inferred nuclear processes are still uncertain. For example, Cameron, Cowan and Truran (1985) demonstrated that the site of the r-process could not yet be identified unambiguously. The potential of gamma ray line astronomy in this area is very significant. It might provide direct observation of the sites of formation of nuclear species.

Supernovae and novae are possible contributors to a diffuse galactic source of long-lived, nucleosynthetic, gamma-unstable radioisotopes such as ^{26}Al (Leising and Clayton 1985). However, with the demonstration by Arnett (1969) that products of explosive nucleosynthesis would be ejected before decay, then individual supernovae may be viewed as potential sources of gamma rays from short-lived isotopes such as ^{56}Co (Gehrels, Leventhal and MacCallum 1987b) as well as intermediate lifetime isotopes such as ^{44}Ti and ^{22}Na (Clayton 1983).

Another possible source of gamma ray visible radionuclides are Wolf-Rayet stars which, having essentially no atmosphere and strong solar winds, lose nucleosynthetic products to their surroundings. Atomic spectra of He, N, O, Si and C have been detected, but, of course, isotopic abundances could not be determined. This class of object might allow gamma ray line telescopes to view

the more 'normal' (ie. non-explosive) nucleosynthetic processes which proceed in stars.

Supernovae and novae are discussed further as potential astrophysical sites of gamma ray line emission.

2.1.2 Electron-positron annihilation.

This subject has become increasingly important in theoretical high energy astrophysics. With this increased importance has come the realisation that the topic is much more complex than assumed in earlier work, particularly in respect of the dependence of annihilation mode upon ambient temperature, ionization and magnetic field. The various modes of annihilation are summarised in turn. The source of positrons in an astrophysical site is also an important issue and this will be dealt with first.

Sources of positrons.
Lingenfelter and Ramaty (1982) list the possible astrophysical sources of substantial numbers of positrons as follows:-

i) e^+ decay of π^+ mesons produced in high energy nuclear interactions.

ii) e^+ decay of radionuclei produced in low energy nuclear reactions.

iii) $e^\pm$ pair production in electron-electron and electron-nucleus interactions.

iv) $e^\pm$ pair production in photon-electron and photon-nucleus interactions.

v) $e^\pm$ pair production in photon-photon interactions.

vi) $e^\pm$ pair production involving interactions of photons or electrons with intense magnetic fields ($> 10^7$ T).

Consideration of the conservation of stellar field during pulsar formation, and the rate of lengthening of pulsar periods, indicate a magnetic field in the region of 10^8 T, which is adequate for substantial pair production from gamma rays of sufficient energy (ie. $E_\gamma > 2m_0c^2$). Various models of pulsars involve (and some depend upon) production of positrons. The original inner gap model of Sturrock (1971) involved the production of up to 10^{41} positrons per second, whilst the recent, detailed outer gap model of Cheng, Ho and Ruderman (1986)

depends upon vacuum breakdown by pair production in a high voltage (10^{15} V) gap.

Share et al (1988), seeking explanations for diffuse galactic 511 keV positron-electron annihilation, suggest the following as suitable, non-transient sources of positrons:-

i) ^{26}Al, which is a predicted nova and supernova product (Leising and Clayton 1985), and which has actually been detected in the galactic plane by its 1809 keV gamma ray line emission (as will be seen in chapter 3), decays by β^+ emission 82% of the time.

ii) ^{56}Ni, which is suggested by Woosley, Tamm and Weaver (1986) to dominate the ejecta of type I supernovae ('standard' white dwarf detonation model) decays by electron capture, with a mean lifetime of 8.8 days, to ^{56}Co which itself decays 19% of the time by β^+ emission to ^{56}Fe. Production of ^{56}Ni might be several tenths of $M_\odot$.

iii) ^{44}Ti might be produced in quantities up to $10^{-2}M_\odot$ by supernovae. This decays by electron-capture to ^{44}Sc with a mean lifetime of 67.8 years. This in turn decays by β^+ emission to ^{44}Ca. However Cameron (1979) has questioned whether the observed abundance of ^{44}Ca could not be produced directly by the s-process, obviating the need for extensive supernova production of the parent ^{44}Ti.

iv) ^{22}Na might be produced in significant amounts by novae. This might be produced by proton capture on Ne present in the pre-nova atmosphere. It decays by positron emission 90% of the time, with a mean lifetime of 3.75 years. Leising et al. (1988) have recently used SMM (see chapter 3) data to place an upper limit of $4 \times 10^{-7}\ M_\odot$ of ^{22}Na produced from nearby, recent, Ne-rich novae.

Kozlovsky, Lingenfelter and Ramaty (1987) discussed the formation of positrons by the interaction of accelerated particles. They give prescriptions for calculating positron yields from various target compositions and particle spectra. Although this work was essentially concerned with solar positron production, the authors showed how more general predictions may be made. Potential

sources include cosmic ray interactions with the interstellar medium, or particles accelerated in compact sites interacting with the surrounding material. They present data for an extensive range of cosmically abundant target materials (C, N, O, Ne, Na, Mg, Al, Si, S, Ar, Ca, Cr, Fe and Ni), with which they consider all α and proton interactions which might lead to positron production.

We now briefly examine the possible modes of positron annihilation.

Annihilation in flight.
Electrons and positrons may annihilate in flight producing gamma rays with a distribution of energies depending on the particle momenta. There are two classes of events. If the electron and positron spins are aligned then 3 photons are produced, if they are opposed then 2 photons with equal energy (511 keV) in the collision frame are produced. The 2-photon process is 372 (π/α) times more likely than the 3-photon equivalent. (Heitler 1954).

Positronium states.
If the positrons cool and form bound positronium 'atoms' with free electrons (Deutsch 1951) then two modes of decay are possible depending on the spin states of the particles. The singlet $^1S_0$ state, parapositronium, where the electrons have opposed spins, accounts for 25% of positronium, and decays with a lifetime of 1.25×10^{-10} s to give two gamma rays each with a fixed energy of 511 keV. The triplet $^3S_1$ state, orthopositronium, with aligned spins, accounts for the remaining 75% of positronium and decays with a lifetime of 1.5×10^{-7} s to give three photons with a continuous energy distribution.

In an astrophysical environment where positrons may lose energy, there will be a certain proportion which will form positronium and the remainder which will annihilate in flight. The so-called positronium fraction (Brown and Leventhal 1987) determines the intensity and width of the 511 keV annihilation line, and the intensity and spectral shape of the associated continuum flux. It is also an indicator of the incident positron energy spectrum and of the composition, temperature and ionization of the cooling and annihilation medium.

Single-photon annihilation in atomic systems.

It is possible for a positron to form a bound state with an electron in an atom (Heitler 1954). In this case, the nucleus may absorb the momentum and single-photon decay becomes possible. However, as Chupp (1976) points out, the maximum single to double photon production probability is at an incident positron energy of 5 MeV and falls rapidly below this value. This mechanism is therefore unlikely to be significant astrophysically.

Single photon annihilation in magnetic fields.

Daugherty and Harding (1983) point out the possibility of single photon annihilation in intense magnetic fields ($\gtrsim 10^8$ T). In this case the magnetic field absorbs the momentum. Harding (1987) carries on to show that this mechanism might become important and, indeed, inevitable in pulsar magnetospheres. The emitted energy is ($\gtrsim 1$ MeV), but its precise energy is dependent on conditions.

GRASAR action.

Gamma ray amplification by stimulated annihilation radiation (GRASAR) emission was proposed as a potential source of a narrow ~400 keV line from the Crab pulsar by Varma (1977). This involved the condensation of electrons and positrons into rod-shaped droplets ($> 1\,\mu$m long) within a pulsar magnetospheric outer gap such as originally proposed by Cheng, Ruderman and Sutherland (1976). The Fermi energy of the droplet was calculated and found to be greater than the expected temperature (~ 0.5 keV). Degeneracy and hence population-inversion were achieved and amplification of the photon density at ~400 keV by stimulated emission was predicted. The photons would travel along the length of the droplet.

McKinley and Ramaty (1983) point out that though Compton scattering had been ignored in the original work, an adjusted mechanism (Ramaty, McKinley and Jones 1982) was still viable given a minimum pair density of 10^{36} m^{-3}. Varma (1983) determined that when intense magnetic fields were taken into account, the conditions for GRASAR action were much less stringent than determined previously.

As well as being a possible explanation for the Crab results at ~400 keV, this mechanism is now a seriously proposed model for the ~400 keV line emission observed in several gamma ray burst spectra (Ramana Murthy and

Wolfendale 1986, Hurley 1987)

Quarkonium systems.
Kanbach and Schlikeiser (1983) examined the possibility of the production of heavy bound quark-antiquark systems by colliding e^+ and e^- beams in pulsar magnetospheres. Although they concluded that this was indeed possible and that radiative transitions of these systems could produce gamma ray lines, these were predicted to occur in the energy range 120−450 MeV which is beyond the scope of the present work.

2.1.3 Deuterium formation.

The reaction $n + {}^1H \rightarrow {}^2H + \gamma$ yields a gamma ray of energy 2.22 MeV. The cross-section for this reaction is $7.3 \times 10^{-24} v^{-1}\,m^2$, where v is the velocity (in $m\,s^{-1}$), so some form of thermalization is generally required before the reaction takes place.

The neutrons may originate in interactions of energetic particles with matter such as ^{4}He(p,pn)^{3}He, ^{2}H(d,n)^{3}He and ^{3}H(d,n)^{4}He. Possible astrophysical mechanisms are cosmic ray interactions in regions of the interstellar medium where the H density is in excess of $10^{20}\,m^{-3}$ (otherwise the neutrons would decay before interacting), and accretion on to compact objects such as neutron stars.

Brecher and Burrows (1980), in considering the gamma ray lines emitted from accreting neutron stars, suggest the deuterium formation feature to be amongst the strongest emitted lines, along with electron-positron annihilation radiation and lines from ^{12}C (4.44 MeV de-excitation) and ^{16}O (6.1−6.3 MeV spallation). Their calculations assume that the infall energy of the accreted material would be 100−600 MeV per nucleon and that the neutron star material and accreted matter have the same composition. This energy exceeds the thresholds of the following neutron-producing reactions:-

$$p + \alpha \rightarrow {}^3\mathrm{He} + n + p \tag{2.1}$$

$$p + \alpha \rightarrow d + n + p \tag{2.2}$$

$$p + \alpha \rightarrow d + {}^3\mathrm{He} \tag{2.3}$$

$$p + \alpha \rightarrow 2n + 3p \tag{2.4}$$

$$p + p \rightarrow n + p + \pi^+ \tag{2.5}$$

The resulting neutrons are expected to be thermalized by collisions with ambient protons before capture either by a proton or the ^{3}He, produced in (2.1) and (2.3), which can have a 'poisoning' effect on neutron production due to its own high thermal neutron absorption cross section. The mean radiative capture time for the produced neutrons was calculated as 1.5×10^{-4} s which is much less than the decay time ($\sim 10^3$ s).

2.1.4 Neutron capture.

As well as deuterium formation radiation, other gamma ray lines might also be produced by capture of neutrons produced by mechanisms similar to those described in the previous section. Many nuclei form an unstable state after neutron absorption which frequently decays by gamma emission. For neutron stars, the Fe capture process is probably most important:

$$^{56}\mathrm{Fe} + n \rightarrow {}^{57}\mathrm{Fe}^{\star} + e^- \tag{2.6}$$

The excited state decays with the emission of gamma rays at 7.632 and 7.646 MeV.

2.1.5 Charged particle interactions.

Reactions between an energetic charged particle and a nucleus frequently leave the nucleus (which may also be modified in other ways, ie. by spallation) in an excited state which decays by gamma ray emission. Ramaty, Kozlovsky and Lingenfelter (1979) consider reactions of energetic α particles and protons with cosmically abundant target nuclei. The predicted spectra are highly dependent on the energy spectrum of the incident particles and upon the circumstances of the target medium (ie. gas or dust, temperature, composition). These results will be discussed further in the context of the interaction of cosmic rays with the interstellar medium which is the main application of this work.

Kozlovsky, Lingenfelter and Ramaty (1987) examine accelerated particle interactions which might give rise to positron production (and hence gamma ray lines). α and proton interactions are considered with a wide range of targets

(C, N, O, Ne, Na, Mg, Al, Si, S, Ar, Ca, Cr, Fe, and Ni). Although mainly concerned with solar interactions, these calculations may be applied to other source classes.

Higdon and Lingenfelter (1977) and Brecher and Burrows (1980) examine the production of gamma ray lines from matter accreting on to a compact object such as a neutron star. Gamma ray lines are produced either directly by thermonuclear reactions of the infalling matter, or indirectly by reactions of the thermalized daughter products. The former calculations suggest the 4.44 MeV line from the de-excitation of $^{12}C^*$ as the most important, whilst the latter indicate that the indirectly produced 2.22 MeV line from deuterium formation would be dominant, although $^{12}C^*$, along with $^{16}0^*$ (6.1−6.3 MeV de-excitation) and indirectly produced electron-positron annihilation radiation, would also be significant.

2.1.6 Cyclotron radiation.

The classical cyclotron radiation is produced by the helical motion of a charge around a magnetic field line (due to the centripetal acceleration of the Lorentz force). This radiation is isotropic and almost all at the frequency of the motion, which is defined by

$$\nu_L = \frac{eB_\perp}{2\pi m_0 c}, \tag{2.7}$$

where $B_\perp$ is the magnetic field strength perpendicular to the particle motion. The inverse proportionality to the Lorentz factor is neglected in this non-relativistic case. The ratio of the power emitted at successive harmonics of this frequency is given by

$$\frac{P_{s+1}}{P_s} = \frac{v^2}{c^2}, \tag{2.8}$$

where v is the particle velocity and s is the harmonic order. It is clear that, for the low energy particles under consideration, a very large proportion of the power will be emitted at the first harmonic. With magnetic fields of the order of 10^8 T, cyclotron radiation becomes a potential source of gamma ray line emission.

At relativistic particle energies the analogous mechanism is called synchrotron radiation. It produces a continuum of photon energies and is discussed further in that context.

2.2 Continuum production mechanisms.

The various potential sources of continuum gamma ray emission at similar energies to nuclear transitions are described briefly in the following sections.

2.2.1 Thermal radiation.

The intensity, I, of a radiation field in thermodynamic equilibrium with its surroundings is given by Planck's Law

$$I(E_\gamma) = \frac{2E_\gamma^3/h^2c^2}{e^{\frac{E_\gamma}{kT}} - 1} \tag{2.9}$$

(A basic derivation is given in Tucker 1977). Wien's displacement law gives the energy of the emission maximum, expressed in MeV, as

$$E\,(\mathrm{MeV}) = 4.7 \times 10^{-10} T\,(\mathrm{K}), \tag{2.10}$$

from which we see that temperatures of $10^8\,\mathrm{K} < T < 10^{10}\,\mathrm{K}$ are required for nuclear gamma ray production. Such temperatures are frequently invoked in models of supernovae.

2.2.2 Motion in magnetic fields.

Cyclotron radiation refers to photons produced by non-relativistic particles in magnetic fields, the corresponding process for relativistic electrons is known as synchrotron radiation. These effects are also termed magnetobrem s strahlung and gyroradiation. A charged particle moving in a non-parallel, direction with respect to a magnetic field will emit electromagnetic radiation. Also, a charged particle moving parallel to curved magnetic field lines may still emit 'curvature' radiation.

Cyclotron radiation.

Cyclotron radiation is essentially a line emission mechanism and has already been discussed as such. However it is possible for the conditions at an astrophysical site to be such that broadening of the gamma ray lines to a continuum would be inevitable. Cyclotron emission lines might be broadened by non-uniformity in the magnetic field, by Doppler or collisional broadening, or by the effect of self-absorption of the radiation.

Synchrotron radiation.

At relativistic energies, the emitted radiation is beamed in a narrow cone along the instantaneous velocity vector of the particle. The opening angle of the cone varies as the reciprocal of the Lorentz factor of the particle. Most of the radiation occurs at high harmonics, giving a 'quasi-continuous' energy spectrum. There is a critical frequency ν_c above which there is practically no radiation at any angle. Synchrotron radiation is elliptically polarized, the degree of linear polarization increasing as the ratio of the photon frequency to ν_c.

The characteristic frequency, ν_c, is given by

$$\nu_c = \frac{3}{2}\gamma^2 \nu_L \tag{2.11}$$

where ν_L is the rotation frequency. The corresponding frequency for a given pitch angle θ may be evaluated by introducing an additional factor, $\sin\theta$, in the above relation. The emission spectrum is asymmetrical with a maximum at

$$\nu_m = 0.29\nu_c \tag{2.12}$$

For a single particle of mass M and charge Z, the instantaneous power, $P_s(\gamma, B_\perp)$ (in $\mathrm{eV\,s^{-1}}$), for a magnetic field H T and Lorentz factor γ is given by Schwinger (1949) as

$$P_s(\gamma, B_\perp) = 9.89 \times 10^{-16} \left(\frac{E}{Mc^2}\right)^2 B_\perp^2 \left(Z^2 \frac{m_0}{M}\right)^2 . \tag{2.13}$$

It is important to note that the power varies as the reciprocal of the fourth power of the particle rest mass. It follows, therefore, that electrons are likely to be far more important than protons as synchrotron radiators; in fact there is a

difference of the order of 10^{13}. We may now consider (following Ginzburg 1969) the spectrum produced by an ensemble of electrons with a power law distribution of energies, $dN_e = N_0 E_e^{-n}\, dE$, trapped within a magnetic field B T in a region of volume V m^3 at a distance R m from the observer. Under these conditions, the number of gamma rays, $N(E_\gamma)$ m^{-2} s^{-1} MeV^{-1}, is given by

$$N(E_\gamma) = C(n) N_0 V R^{-2} B^{\frac{(n+1)}{2}} E_\gamma^{\frac{(1-n)}{2}}, \tag{2.14}$$

where $C(n) \sim 30$ for indices in the range 1 to 5 (See also Tucker 1977). The validity of this relation for an astrophysical site depends on magnetic field uniformity, Doppler and collisional broadening, and self-absorption of the radiation.

The electron's energy loss due to synchrotron emission is such that it will lose half its energy in $5\gamma^{-1}B_\perp^{-2}$ s. This may be very significant. The Crab Nebula, for example, emits X-rays from 100 TeV electrons in a 10^{-8} T magnetic field. The electrons should have exhausted their energy in a few decades, but the nebula has existed from the 11^{th} century. It therefore follows that there is a source of energetic electrons within the supernova remnant: almost certainly the Crab pulsar (Shklovsky 1970).

Curvature radiation.

Charged particles of energy E MeV travelling along curved magnetic field lines emit electromagnetic radiation with a spectrum peaked at a frequency, ν Hz, given by

$$\nu = 10^{11.2} E^3 R_c^{-1}, \tag{2.15}$$

Where R_c m is the radius of curvature. (See Schlovsky 1960) The power, P_c, is given by

$$P_c = 10^{-14.1} E^4 R_c^{-2} \text{ eV s}^{-1}. \tag{2.16}$$

This form of radiation is essential to all models of pulsar magnetospheres which involve particle acceleration at the neutron star polar cap (inner gap model). The radiation is produced along the curving open field lines and then goes on to interact by the pair production process described in the next section. This important mechanism was first pointed out by Sturrock (1971).

2.2.3 Inverse Compton effect.

Inelastic scattering of high energy electrons by relatively low energy photons (say starlight or the microwave background) is generally termed the inverse Compton effect. When the incident photon energy $E_\gamma \ll m_0c^2\gamma^{-1}$ we may use the classical Thomson formula for the interaction cross-section. However, when $E_\gamma \gg m_0c^2\gamma^{-1}$, we must use the Klein-Nish ina cross-section. In the latter case, the scattered photon takes on the energy of the electron and is essentially independent of the frequency of the scattering radiation. In the former case, it may be seen that (Tucker 1977) the scattered photon energy E'_γ is related to the scattering photon energy E_γ and the incident electron Lorentz factor γ by the approximate relationship

$$E'_\gamma \approx \gamma^2 E_\gamma \tag{2.17}$$

implying that gamma rays might be produced from interaction of cosmic rays with the interstellar radiation fields. Using the Thomson cross-section, $\sigma_T = \frac{8}{3}\pi r_0^3$, we obtain the following expression for the power scattered by a single electron in a region of photon number density ρ

$$P_c = \frac{32}{3}\pi r_0 \gamma^2 \rho c. \tag{2.18}$$

If the incident cosmic rays have a power law spectrum, $dN_e = N_0 E_e^{-n}\, dE$, then the resulting spectrum will be of the form

$$N(E_\gamma) \propto E_\gamma^{-(n+1)/2}. \tag{2.19}$$

The contribution of inverse Compton scattering from the microwave background to the gamma ray and X-ray diffuse backgrounds is discussed by Felten and Morrison (1966), and Silk (1973).

2.2.4 Brems strahlung.

A charged particle, decelerated by the Coulomb field of another, more massive, charged particle, emits brems strahlung photons with a range of energies up to the kinetic energy of the scattered particle. As the differential cross-section is proportional to the ratio of the target mass to that of the incident

particle $M_{\text{target}}/M_{\text{incident}}$ (Heitler 1954), the importance of this effect is normally restricted to electrons scattering from ions.

Fazio (1967) calculated the brem s strahlung spectrum from an ensemble of electrons with a power law energy distribution and found that the output spectrum would be a power law of the same index as the input spectrum. A plasma, which is sufficiently optically thin that the photon spectrum might be non-thermal, may be treated using a thermal electron spectrum input to the brem s strahlung process. This yields an output spectrum of the form $(\exp(-E_\gamma/kT))/E_\gamma$ (Hayakawa 1969).

2.2.5 Neutral Pion decay.

Π_0 mesons (neutral pions) decay with a mean lifetime of $\sim 10^{-16}$ s to produce two gamma rays. Although these are of equal energy (approximately 68 MeV) in the rest frame of the decaying particle, their energies, as measured in the observer's rest-frame may differ by as much as $E_\Pi v_\Pi/c$, where E_Π and v_Π are the energy and velocity of the decaying pion, respectively. The pions may be produced by photomeson production, the annihilation of matter and anti-matter, and p–p or p–α collisions.

The interaction of starlight or microwave photons with energetic protons can produce neutral pions ($p(\gamma, \gamma')\Pi_0$) provided the proton energy exceeds a threshold of approximately 10^{17} eV (see Fazio 1967).

Protons and antiprotons can produce Π_0 s either via boson production at high ($> 10^{11}$ K) temperatures, direct annihilation at intermediate (10^4 K $< T < 10^{11}$ K) temperatures, or rearrangement collisions of neutral Hydrogen and anti-Hydrogen atoms at low ($< 10^4$ K) temperatures. Stecker (1971) reviews these processes and also provides an analysis of the likely relative importance of the various proton-proton and proton-alpha reactions which can give rise to neutral pions. Protons, although far more abundant in cosmic rays, have a lower interaction cross-section with other protons than with alpha particles, hence the latter may still be competitive as a production mechanism.

2.3 Interaction of gamma rays with matter.

This section serves the dual purposes of introducing some mechanisms which might modify the spectra of astrophysical sources, and also of establishing the basic interactions of nuclear gamma rays with detectors. The examples given are in the latter context; astrophysical spectral modification is discussed further in the subsequent section.

Photons cease to contribute to a monoenergetic beam if they are either absorbed or shifted in energy by interaction with a medium. The attenuation of the monoenergetic beam is therefore described simply by

$$I = I_0 e^{-\mu x}, \tag{2.20}$$

where I_0 and I represent the incident and transmitted intensities respectively, x the thickness, and μ the total linear attenuation coefficient in m^{-1}. The quantity μ_m, the mass attenuation coefficient, is often used to characterize the attenuation of a substance regardless of its physical state; it is defined as μ/ρ, where ρ is the density of an absorber of linear attenuation coefficient μ.

The quantity μ represents the effect of several physical processes. For the purpose of analysing gamma ray detector response, it is generally only necessary to consider the photoelectric effect (with atomic electrons), incoherent scattering from free electrons (the Compton effect), and elastic pair production in atomic Coulomb fields. These processes are described in the following sections. The respective linear attenuation coefficients are ${}_a\tau$, ${}_e\sigma$ and ${}_a\kappa$. The total photoelectric, Compton, and pair production linear attenuation coefficients, (from any target), to which the latter are the dominant contributors, are τ, σ and κ. The coherent (Rayleigh) scattering linear attenuation coefficient is denoted by σ_r.

2.3.1 The photoelectric effect.

This is the complete absorption of a gamma ray by atomic electrons, principally in the K shell. The process yields either characteristic X-rays or Auger electrons. The X-ray photons are generally absorbed, but in small detectors, K-escapes (X-rays from K-shell transitions) can become important.

As the absorption process involves the whole atomic electron system, it is not easy to treat theoretically. By making various approximations, Heitler (1954) derived the following formula for the K-shell contribution, ${}_a\tau_K$ $m^2\,atom^{-1}$, to the photoelectric component of the absorption cross-section for photons of energy $E_\gamma \gg m_0c^2$

$$ {}_a\tau_K = 2^{5/2}\psi_0 Z^5 \alpha^4 \left(\frac{m_0c^2}{E_\gamma}\right)^{7/2}, \tag{2.21} $$

where $\psi_0 = 8/3\pi r_0^2$ is the Thomson cross-section, and α is the fine structure constant (1/137). This relationship provides a fairly accurate illustration of the Z and E_γ dependencies for higher energy nuclear gamma rays. At lower energies, there is an approximate E_γ^{-1} dependence.

The photoelectric effect is dominant at low gamma ray energies (100 keV or less). For a particular material, the linear attenuation coefficient due to photoelectric absorption is $\tau = {}_a\tau N\ m^{-1}$, where N is the number density (m^{-3}) of atoms in the substance and ${}_a\tau$, the total photoelectric absorption cross-section, may be approximated by ${}_a\tau_K$. The total linear attenuation coefficient for gamma rays is, to a good approximation, the sum of ${}_a\tau$ and the linear attenuation coefficients for the other two important processes, ${}_e\sigma$ and ${}_a\kappa$.

2.3.2 The Compton effect.

This scattering process is generally dominant between 0.1 MeV and 10 MeV. Unlike photoelectric absorption, the kinematics of gamma ray scattering from free, or nearly free, electrons may be given a complete theoretical description. Given an incident photon with energy E_γ scattering to one of energy E'_γ, and leaving the scattering electron with an additional kinetic energy E_{KE}, then

$$ E_\gamma = E'_\gamma + E_{KE} \tag{2.22} $$

Taking $\alpha = E_\gamma/m_0c^2$ and θ as the angle through which the gamma ray is deflected,

$$ E'_\gamma = \frac{m_0c^2}{1 - \cos\theta + (1/\alpha)} \tag{2.23} $$

or

$$ h\nu' = \frac{h\nu}{1 + \alpha(1 - \cos\theta)} \tag{2.24} $$

gives the scattered energy, and

$$E_{\mathrm{KE}} = \frac{E_\gamma \alpha(1-\cos\theta)}{1+\alpha(1-\cos\theta)} \tag{2.25}$$

is the energy of the scattered electron. The latter has a maximum value at $\theta = \pi$ (ie. when the photon is scattered back along its direction of approach) which is given by

$$E_{\mathrm{KE}}(\max) = \frac{E_\gamma}{1+(1/2\alpha)}. \tag{2.26}$$

The angle subtended by the path of the scattered electron and the projected path of the incident photon ϕ is related to the photon scattering angle θ and the photon energy to electron rest energy ratio α as follows

$$\cot\phi = (1+\alpha)\tan(\theta/2). \tag{2.27}$$

Now the differential cross-section $d({}_e\sigma)$ for Compton scattering of a plane polarized gamma ray such that the scattered photon electric vector is at an angle Θ with respect to the incident electric vector is given by the following equation

$$d({}_e\sigma) = \frac{r_0^2}{4} d\Omega \left(\frac{\nu'}{\nu}\right)^2 \left[\frac{\nu}{\nu'} + \frac{\nu'}{\nu} - 2 + 4\cos^2\Theta\right], \tag{2.28}$$

where ν and ν' Hz are the incident and scattered photon frequencies respectively, and $d\Omega$ is the solid angle element through which the scattered photon emerges. This is the full form of the Klein-Nishina (Klein and Nishina 1929) cross-section, a derivation for which is given in Heitler (1954). For many purposes this may be simplified. Firstly, by summing over the angles of polarization of the scattered photon, we obtain a cross-section in terms of ξ, the angle between the scattered photon path and the incident photon electric field, measured in the plane containing both vectors

$$d({}_e\sigma) = \frac{r_0^2}{4} d\Omega \left(\frac{\nu'}{\nu}\right)^2 \left[\frac{\nu}{\nu'} + \frac{\nu'}{\nu} - 2\cos^2\xi\right]. \tag{2.29}$$

Now, $\cos^2\xi = \sin^2\theta + \cos^2\eta$, where η is the projection of ξ onto the plane normal to the path of the incident photon. It is therefore clear that the differential

cross-section has a maximum at $\eta = \pi/2$ so that the polarization of an incident beam may be deduced by measuring the asymmetry in the frequencies of scattered photon directions. Finally, one may obtain the following differential cross-section for unpolarized incident radiation,

$$d({}_e\sigma) = \frac{r_0^2}{4} d\Omega \left(\frac{\nu'}{\nu}\right)^2 \left[\frac{\nu}{\nu'} + \frac{\nu'}{\nu} - \sin^2\theta\right]. \tag{2.30}$$

Using this equation in conjunction with Equation (2.27), one may obtain the following expression in terms of the energy ratio α

$$\frac{d({}_e\sigma)}{d\Omega} = \frac{1}{2} r_0^2 \frac{\left\{1/\left[1 + \alpha(1 - \cos\theta)\right]^2 \times \left[1 + cos^2\theta + \alpha^2(1 - \cos\theta)^2\right]\right\}}{\left[1 + \alpha(1 - \cos\theta)\right]}. \tag{2.31}$$

At low energies, this reduces to the classical Thomson equation

$$d({}_e\sigma) = \frac{1}{2} r_0^2 (1 + \cos^2\theta). \tag{2.32}$$

Equation (2.31) may be summed over all scattered photon angles to give the total Compton cross-section ${}_e\sigma$

$${}_e\sigma = 2\pi r_0^2 \left\{\frac{1+\alpha}{\alpha^2}\left[2\left(\frac{1+\alpha}{1+2\alpha}\right) - \frac{1}{\alpha}\ln(1+2\alpha)\right] + \ln\left(\frac{1+2\alpha}{2\alpha}\right) - \frac{1+3\alpha}{(1+2\alpha)^2}\right\}. \tag{2.33}$$

As ${}_e\sigma$ is defined per electron, the linear attenuation coefficient due to Compton scattering is $\sigma = NZ\,{}_e\sigma$, where N is the number density of electrons.

2.3.3 Pair production.

A photon of energy exceeding that of the rest mass of two electrons may interact in a Coulomb field to produce a positron and an electron which carry away all the energy of the incident photon in their rest-masses and kinetic energies.

This process requires the presence of a particle of non-zero mass M to conserve momentum. The value of M determines the threshold energy of the interaction as follows

$$E_{\text{th}} = 2m_0c^2\left(1 + \frac{m_0}{M}\right) \tag{2.34}$$

The interaction normally takes place in the Coulomb field of a nucleus, but that of an electron field may also cause a gamma ray to produce electron-positron pairs.

A high energy photon may have a significant chance of interaction outside the K-shell, in which case the charge-screening effects of the atomic electrons become important. For $1 \ll E_\gamma \ll \alpha^{-1}Z^{-1/3}$, the pair production cross-section is well approximated by

$$_a\kappa_p = \alpha r_0^2 Z^2 \left[\frac{28}{9}\ln\left(\frac{2E_\gamma}{m_0c^2}\right) - \frac{218}{27}\right] \times 10^{-4}\,\mathrm{m^2\,atom^{-1}}, \qquad (2.35)$$

where α is the fine structure constant (see Marmier and Sheldon 1969). At higher incident photon energies ($E_\gamma \gg m_0c^2\alpha^{-1}Z^{-1/3}$), it is approximated by

$$_a\kappa_p = \alpha r_0^2 Z^2 \left[\frac{28}{9}\ln\left(\frac{183}{Z^{1/3}}\right) - \frac{2}{27}\right] \times 10^{-4}\,\mathrm{m^2\,atom^{-1}}. \qquad (2.36)$$

Some useful tabulations and plots of attenuation coefficients for common detector, shielding and astrophysical materials are given in Chupp (1976). Other interactions of gamma rays with matter, of less importance in this context, are dealt with by Davisson (1966). For reference, the mass attenuation coefficients of the two most important materials in the Durham telescope, germanium and sodium iodide, are plotted in figure 2.1. Each plot shows the contributions from the three main interaction mechanisms discussed above. It also shows the contribution of coherent (Rayleigh) scattering (σ_r/ρ) and the total mass attenuation coefficient (μ_0/ρ).

2.4 Spectral modification mechanisms.

There are a number of mechanisms by which gamma ray spectra may be modified between production and detection. For line emission this takes the form of attenuation, shifting of the line centroid energy, or a broadening, or higher order modification, of the line shape. High spectral resolution (ie. germanium-based – see chapter 3) detectors are particularly sensitive to these changes. Shifting or broadening $> 1-3\,\mathrm{keV}$ is capable of being detected, depending on the quality, and state of repair of the detector and associated electronics. This can be a problem, particularly in the case of shifting, because it can introduce

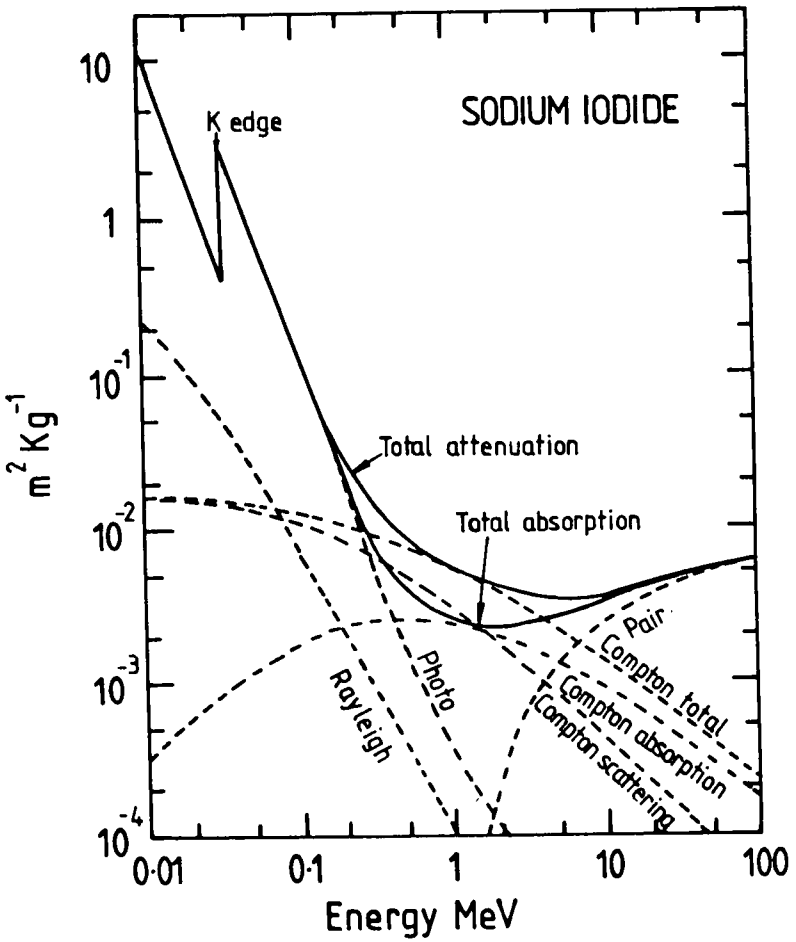

Figure 2.1 The mass attenuation coefficients ($m^2 Kg^{-1}$) for γ-rays in Sodium Iodide.

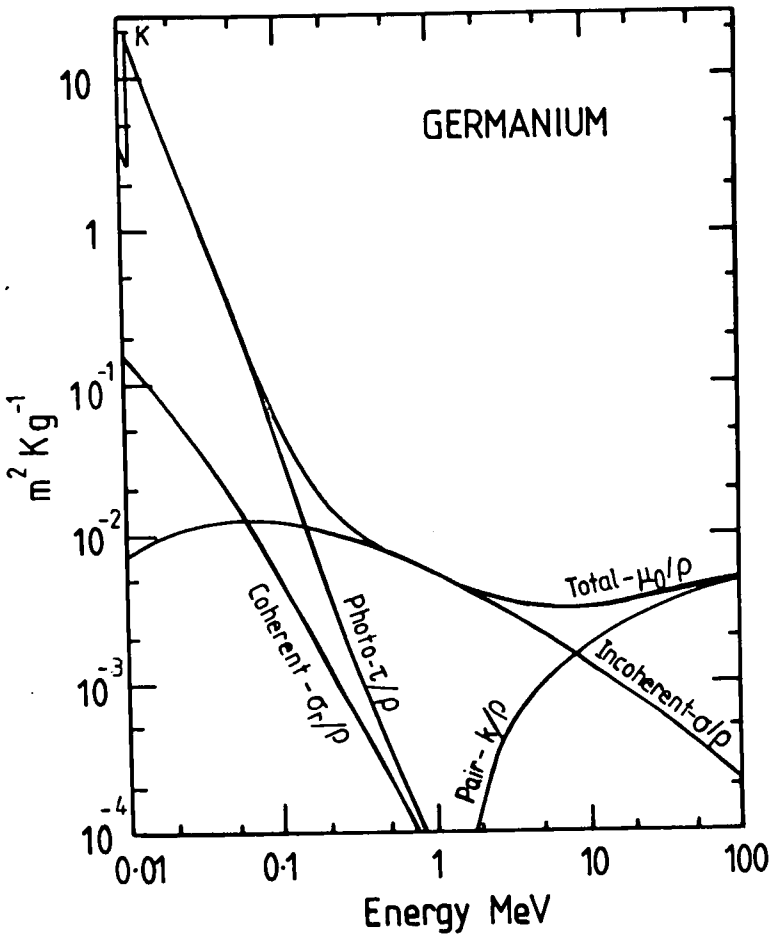

The mass attenuation coefficients ($m^2 Kg^{-1}$) for γ-rays in Germanium.

an *ad hoc* element into the interpretation of spectral lines whereby an otherwise unconstrained shifting mechanism can allow rather arbitrary identification of a spectral line feature, at an unexpected energy, as some astrophysically predicted line 'with shifting'. Conversely, where other constraints exist, measurements of shifting can be highly informative about the intervening media or the production site itself. Such a prospect will be examined following a brief description of likely spectral modification processes.

Chupp (1976) discusses spectral modification in the categories of interstellar and intergalactic absorption, Doppler shifts, and gravitational and cosmological redshifts.

Absorption in the interstellar and intergalactic media.
If the Universe is assumed to be populated by neutral hydrogen atoms with a number density of $\sim 10^{-11}\,\mathrm{m}^{-3}$, then the the mean free path of a photon at nuclear energies would be $\sim 10^{28}\,\mathrm{m}$ which is $\sim 3 \times 10^{11}\,\mathrm{pc}$. This would not generally be a problem, but of course for very long distances one must take into account the following cosmological effects:-

i) The photon was actually emitted with a factor z higher energy than at its detection, where z is the cosmological red shift of the emission site.

ii) The photon path will involve the integration of matter density over previous epochs.

iii) The temperature of the Universe will have varied as $T_0(1 + z)$, where T_0 is the present temperature.

Using standard cosmological models to determine the matter density evolution, Chupp (1976), employing previous work by Arons and McCray (1969) and Fazio and Stecker (1970)), derived a worst-case critical redshift of $z \approx 9$ for gamma rays at nuclear energies. The greatest attenuation occurs at $\sim 100\,\mathrm{keV}$. Beyond this redshift, the Universe is opaque to gamma rays. Calculations for absorption must also be adjusted for sources within or behind regions of higher density interstellar matter.

Doppler shifting of the line centroid energy.

This is due to the relative velocity of the emission site and the telescope. If the production and detection energies are E_γ^0 and E_γ respectively, and the relative velocity vector is of magnitude v at an angle θ with respect to the line of sight, then

$$E_\gamma = E_\gamma^0(1 + (v/c)\cos\theta) \tag{2.37}$$

Doppler broadening.

This effect is due to the temperature of the emission medium imparting a distribution of random velocity vectors to the individual emission systems (radionuclides, positronium, etc.). Generally speaking, this effect is compounded by the decay recoil velocity adding to the initial velocity of the decaying system. The exception is where the decaying system is part of a condensed system such as a dust grain which can absorb the recoil momentum with little change in velocity. These effects are very important when discussing gamma ray line production from the interaction of cosmic rays with the interstellar medium and will be discussed further in this context.

Gravitational red shift (and broadening).

This is red shifting due to emission within the gravitational potential of a compact object. Where emission is not confined to a particular shell or ring, then the range of gravitational potentials at the various emission sites will produce a range of red shifts and hence a broadened line at the detecting telescope. The gravitational redshift z_c, corresponding to a shift of energy ΔE, of a process with emission energy E_γ^0 at a radius R from a compact object of mass M is given by (Chupp 1976)

$$z_g = \frac{\Delta E}{E_\gamma^0} = \frac{GM}{Rc^2}. \tag{2.38}$$

Where the mass of the object is unknown, the emission radius is known, and a line origin can be unambiguously ascribed, then the mass of the object can be determined; a very important measurement in the case of certain compact systems.

Red shifting by the cosmological Hubble flow.
This occurs in exactly the same fashion as at other wavelengths. Clearly, if one knew the distance to an object of a particular redshift then one would know Hubble's constant. A more likely situation is where one can predict the cosmological redshift of gamma ray line emission from an extragalactic source by examining redshift data at other wavelengths.

Magnetic interactions.
Erber (1966) discusses interactions of gamma radiation with magnetic fields, notably pair production. This becomes important near the surface of compact objects, particularly pulsars, where magnetic fields may be intense ($\sim 10^8$ T).

Cyclotron photon energy is linearly dependent on the magnetic field strength, so a distribution of emission energies will be produced by non-uniformity in the magnetic field. As non-uniformity is inevitable in the field of a compact object, this might be thought to lead to inevitable broadening. However, it should be noted that many pulsar models constrain emission to relatively confined, and hence magnetically uniform, inner gaps (eg., Sturrock 1971) or outer gaps (eg., Cheng, Ho and Ruderman 1986).

2.4.1 Importance of spectral modification.

Brecher (1977) makes an important point about the unique potential of gamma ray line astronomy in the study of matter in highly condensed states. The Tolmann-Oppenheimer-Volkoff equation relates the pressure, density and contained mass of a neutron star as a function of radius. If we denote these quantities by $P(r)$, $\rho(r)$ and $M(r)$ respectively then

$$\frac{\mathrm{d}P}{\mathrm{d}r} = -\frac{GM(r)\rho(r)}{r^2}\left[1+\frac{P(r)}{\rho(r)c^2}\right]\left[1+\frac{4\pi r^3 P(r)}{M(r)c^2}\right]\left[1-\frac{2GM(r)}{rc^2}\right]^{-1}. \qquad (2.39)$$

Clearly $M(r)$ and $\rho(r)$ may be simply related as follows

$$M(r) = \int_0^r 4\pi r'^2 \rho(r')\,\mathrm{d}r'. \qquad (2.40)$$

The specification of an equation of state, that is $P = P(\rho)$, a boundary condition (the surface pressure — typically 0), and the central density, produces unique values of the total mass M and object radius R. For a given mass, various

models of neutron star composition, such as interacting neutrons, hyperons, or quarks — see Irvine 1978 for a general discussion, which require different equations of state, predict different neutron star radii. The measurement of a single gravitational redshift from the surface of an object of known mass (eg. a member of a binary system) would therefore distinguish between these models and provide a powerful constraint on the possible states of highly condensed matter.

2.5 Astrophysical sites for line production.

Potential astrophysical sites of gamma ray line emission are discussed by category (eg. pulsars, supernovae, etc.). Where non-diffuse gamma ray lines have been detected, the specific objects are discussed a little further in the context of the observations in chapter 3. The Crab and NGC1275, which were observed by the present experiment, are also discussed in chapter 5.

Although there have been many predictions of fluxes, there is a great deal of uncertainty in the values: not just in the precise level, but sometimes as to whether a particular flux exists at all. This illustrates the considerable potential of experimental gamma ray line astronomy in the testing of astrophysical theories involving nuclear and higher energy processes. The various quantitative predictions themselves are not of so much interest here as the information which their measurement would potentially impart. It may be taken that where a potential gamma ray line is described, its possible detection at levels greater than ~ 0.1 photons $m^{-2}\,s^{-1}$ has been suggested.

Where the emission region may be distributed, as in the case of accumulated supernova ejecta in the interstellar medium, then the 'production site' will be considered to be the ultimate source of the radioactive species: in this case, the supernovae.

The categorization is by observationally defined classes such as 'pulsars' and 'active galactic nuclei' and not by theoretical models such as 'neutron stars' or 'black holes'. The theoretical line flux predictions depend on these models in varying degrees: some are independent (eg., Matteson 1983), some are for generalised objects such as 'accretion sources' (eg., Higdon and Lingenfelter 1979), and some are fully model dependent (eg. Varma 1977).

2.5.1 The interstellar medium.

A very extensive review of gamma ray line emission caused by cosmic ray interaction with the interstellar medium has been given by Ramaty, Kozlovsky and Lingenfelter (1979). The production of gamma rays from interstellar grains was also discussed by Lingenfelter and Ramaty (1977). In both cases some distribution of elemental abundances is required in order to predict fluxes. The work of Cameron (1973) was adopted. This is based mostly on the study of carbonaceous chondrites from meteorites and on cosmic rays.

In a gaseous medium, significant broadening may arise from the recoil Doppler shift of the struck target and from the thermal velocity distribution of the gas. The former would be of the order of 1% for a 10 MeV proton striking an oxygen nucleus, which should be apparent to a good cooled semiconductor detector such as the one used in the Durham instrument. The thermal broadening is of course dependent on the ambient temperature of the target. The broadening would be even greater for a cosmic ray nuclide of higher atomic mass interacting with interstellar gas.

For interactions in interstellar grains (Lingenfelter and Ramaty 1977), it is possible for a very narrow line to be produced provided that the stopping time within the grain is shorter than the nuclear de-excitation lifetime, and that the grain size is greater than the stopping distance. If these conditions hold then the recoil of the target nucleus is effectively absorbed by the grain mass. For a $\sim$10 MeV proton striking a grain nucleus, the recoil energy would be a few keV amu^{-1}. A grain density of 1 g cm^{-2} would stop a particle in $\sim 10^{-12}$ s over a distance of $\sim 10^{-4}$ cm. As this is comparable to grain size, one would expect stopping. Even where complete stopping does not occur one would expect a narrower line than in the gaseous case. Of course the thermal velocity distributions of the grains themselves would still give broadening, but with a typical solid grain temperature of 15 K, this amounts to only a few eV. One of the predicted spectra from the interactions of cosmic rays with dust is shown in figure 2.2.

2.5.2 Supernovae.

Supernovae (and indeed Novae, Wolf-Rayet stars, and other likely de-

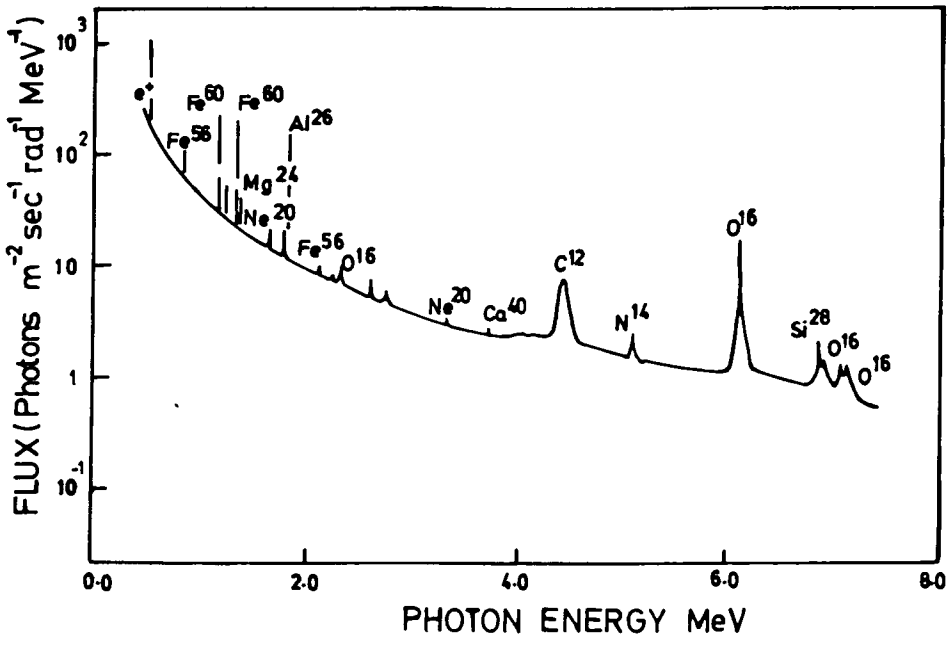

Figure 2.2 Predicted gamma ray spectrum from galactic centre, assuming a low energy cosmic ray density of 1M eVm^{-3} and an exponential size distribution with a characteristic radius of 5×10^{-3}m for dust grains. (from Ramaty and Lingenfelter, 1979)

tectable sources of nucleosynthetic products) can produce both a diffuse emission region of relatively long-lived radionuclides, such as ^{26}Al (mean lifetime $\tau = 1.04 \times 10^6$ yr), which can accumulate from many supernovae, and these may also be compact, but intense, sources of emission from short-lived, but copiously produced, isotopes such as ^{56}Ni and its decay product ^{56}Co, which have mean lifetimes of 8.8 d and 114 d respectively.

The recent predictions of gamma ray line fluxes from individual supernovae by Gehrels, Leventhal and MacCallum (1987b) used recently developed models of type I and type II supernovae to calculate the yields of various isotopes and the opacity of the surrounding material as a function of time from the explosion.

The adopted model of the type I supernova involves a carbon-oxygen white dwarf accreting hydrogen-rich material from a companion at a rate of $> 10^{-9}\,M_\odot\,yr^{-1}$ (see Woosley, Weaver and Tamm 1986 — the first in a series of papers describing type I models). Nuclear burning of the accreted material is thought to occur at the surface which produces a layer of helium. When the white dwarf mass reaches a critical value $M_\odot < M_{WD} < 1.4M_\odot$ then one of two forms of nuclear runaway is predicted:-

i) A supersonic detonation shock starting at the base of the He layer which engulfs the star in $\sim$0.1 s.

ii) A subsonic deflagration wave from the centre of the star engulfing the white dwarf in $\sim$1 s.

In either case the release of $1-2 \times 10^{44}$ J (10^{51} ergs) is predicted. This is an order of magnitude greater than the binding energy of the star which explodes with an average expansion velocity of $\sim 10^4\,km\,s^{-1}$.

Type II supernovae are thought to arise from massive red giant stars $\geq 10^8 M_\odot$ (see, for example, Bethe 1983). This occurs when the $1\,M_\odot$ iron core, the end product of high temperature non-explosive burning, collapses due to degeneracy and then bounces back, ejecting the outer layers. Radionuclides are produced in the central core but the surrounding material has a relatively low expansion velocity and probably remains obscure for $\sim$1.5 yr, by which time

many radionuclides will have decayed.

The studied models of both type I and II supernovae indicated the 847 keV and 1.238 MeV lines from from the decay of ^{56}Ni as being the most intense despite large uncertainty in the production of this isotope (0.4−1.4 $M_\odot$ for type I). Type I models were thought more likely to produce an observable flux than type II. The decay of ^{56}Ni proceeds by the reaction

$$^{56}\mathrm{Ni} \xrightarrow{8.8\,\mathrm{d}} {}^{56}\mathrm{Co} \xrightarrow{114\,\mathrm{d}} {}^{56}\mathrm{Fe} \tag{2.41}$$

where the mean decay times are indicated. The first stage proceeds by electron capture 100% of the time with the emission of a total of 1.72 MeV of gamma rays by various decay paths. These are all thought to be unobservable due to the short mean lifetime and initially high supernova opacity. The second stage proceeds 19% of the time by β^+ decay (a source of annihilation radiation) with a continuum of energies, and 81% of the time by electron capture with a total emitted gamma ray energy of 3.5 MeV distributed over several decay paths. All these paths involve the emission of an 847 keV photon and 68% of the paths produce a 1.238 MeV gamma ray.

Line width, shape and temporal evolution were found to be highly dependent on the density of ejecta and their velocity profiles. The 847 keV emission was expected to peak at approximately 70 days from the initiation of a type I supernova at which time the full spectral width at half maximum intensity (FWHM) would be ~40 keV. An actual measurement would be a direct determination of the nucleosynthetic production rate of ^{56}Fe (optical observations show supernovae to be rich in iron in general). It would also provide the density, velocity structure and total mass of the supernova.

With the discovery of the type II supernova SN1987a, various predictions have been made of gamma ray line fluxes. Applying the techniques described above, Gehrels, MacCallum and Leventhal (1987a) predict a dominant line from ^{56}Ni decay at 847 keV. Assuming a 15$M_\odot$ type II model with 0.01−0.1$M_\odot$ of ^{56}Ni produced, a peak emission of 3−100 $\gamma\,\mathrm{m}^{-2}\,\mathrm{s}^{-1}$ is anticipated. The light curve depends on the particular mass-loss model adopted. Chan and Lingenfelter (1987) also predict the 847 keV line to be dominant.

^{22}Na, as described in the following section on novae, and ^{44}Ti, the decay of which (68.7 yr mean lifetime with positron and 1.157 Mev gamma ray production) is often assumed to account for the natural abundance of ^{44}Ca, have high predicted yields ($\sim 10^{48}-10^{49}$ kg per supernova, Clayton 1983), and might therefore be detectable. This is particularly so given their intermediate lifetimes which would allow time for the reduction in opacity of the outer layers of the supernova. Note, however, that if ^{44}Ca is produced directly by the s-process, as has been suggested by Cameron (1979), then the flux from ^{44}Ti should not be expected.

Gamma ray lines from the long term build up of supernova ejecta are expected to be dominated by those from ^{26}Al and ^{60}Fe. The yields are predicted by Clayton (1983) to be 4.8×10^{47} kg and 3.57×10^{47} kg per supernova of ^{26}Al and ^{60}Fe respectively. These are certainly small compared with, say, 2.16×10^{51} kg of ^{56}Ni, but ^{26}Al decays with a mean lifetime of 1.06×10^{6} yr and ^{60}Fe with 4.3×10^{5} yr. Given a galactic supernova rate of say 1 in 40 years, then an appreciable build-up can occur. The diameter of a supernova remnant after 10^{6} yr could be $\sim$600 light years, so a diffuse source would appear across the galactic plane, but would still follow the supernova distribution.

^{26}Al may be identified by its 1809 keV decay gamma ray, and possibly by annihilation of the positron which accompanies 82% of decays. ^{60}Fe decays with the emission of a 58.6 keV photon followed by the 1.17 MeV and 1.33 MeV gamma rays from its 7.7 yr mean lifetime daughter, ^{60}Co.

2.5.3 Novae.

Novae are probably induced by an accretion process on to a white dwarf much the same as the type I supernova mechanism discussed above. The mass ejected is much less however: $\sim10^{-4}$ $M_{\odot}$. They are, on the other hand, much more frequent. The observation and classification of these phenomena are difficult, so galactic rate distributions are not available; only the distribution of observations. Novae might be sources of emission from ^{22}Na (Clayton 1983) which can accumulate from up to 100 galactic novae within its mean lifetime of 3.75 yr (Leising et al. 1988). This isotope decays 90% of the time by positron emission (leading to annihilation radiation), and also 10% of the time by electron capture, to an excited state of ^{22}Ne which decays rapidly with the

emission of a 1.275 MeV gamma ray.

Clayton (1981) suggested that ^{7}Be might be observed in individual novae by its 478 keV emission during its decay to ^{7}Li. The mean lifetime is 76.9 d, by which time the nova is expected to be quite transparent to nuclear gamma rays. The observation of this line would be enormously important as it could determine whether novae could account for the abundance of ^{7}Li.

2.5.4 Active galactic Nuclei.

Active galaxies are characterized by compact, highly luminous nuclei, often with variable non-thermal X-ray emission (a hard X-ray power index $\sim$1.7 is typical). The category includes Seyferts, BL Lac objects, quasars and Cen A. Matteson (1983) suggested that, due to the high luminosity and small volume of active galactic nuclei, the photon density might be so high that photon-photon pair-production interactions would become important. It should be emphasised that this proposal does not depend upon any particular model of the active galactic nucleus, but is simply a consequence of the observed luminosity and time-variability, which constrains the size of the emitting volume. The criterion for an electron-positron pair-production interaction between two photons of energies E_1 and E_2 is that

$$E_1 E_2 \geq \frac{2\,(mc^2)^2}{1 - \cos\theta} \tag{2.42}$$

where θ is the angle between the incident paths of the photons. The cross section reaches a maximum of 1.7×10^{-21} m^2 when $E_1 E_2$ is twice the threshold value in equation (2.42); for example, two 1 MeV photons interacting at 90°. Assuming that 100% of the positrons annihilate by forming positronium within the active galaxy, and considering pair-production only by 1 MeV photons then the expected flux of 511 keV gamma rays $F(511)$ in photons m^{-2} s^{-1} is

$$F(511) = 4.2 \times 10^{-81} \frac{L^2(> 511)}{D^2\,\Delta t} \tag{2.43}$$

where $L(511)$ is the luminosity in gamma rays of energy > 511 keV, D is the distance to the active galaxy in Mpc, and Δt s is the time-scale of variability. When applied to NGC4151, for which suitable intensity measurements exist,

the flux of photons of energy 511 keV was predicted to be 10 photons $m^{-2} s^{-1}$. This assumes, of course, 100% annihilation as positronium within the galaxy; the effect of positron annihilation in flight may serve to decrease the flux as, indeed, would positron escape. On the other hand, the timescales of variation are probably generally underestimated because of the infrequency of hard X-ray and gamma ray continuum observations. Also the active nucleus might well produce positrons by other means such as nuclear interactions in the accretion disk of a $10^8 M_\odot$ Kerr black hole — a typical active nucleus model (Kafatos and Eilek 1983).

It seems not unlikely that positrons are produced in sufficient numbers in active galaxies to produce an observable flux of 511 keV radiation provided that the conditions for a suitable annihilation mode within the galaxy are met. Marscher et al. (1984) speculate that in highly active galaxies, where non-thermal activity is seen to extend beyond the optical boundary of the galaxy itself, positron escape is quite likely. This picture was derived from the association of positron production with synchrotron radio emission, an assumption which was in turn based on an attempt to extrapolate the 511 keV behaviour of the Galactic Centre to far more intense positron production in active galactic nuclei. Given the recent evidence of Share et al. (1988) (discussed in chapter 3), which undermines the case for a compact Galactic Centre positron source, these assumptions may well be viewed as less secure. This is quite apart from the difference in the scale of positron production required for an extragalactic source to be visible. For an active galaxy at a distance of 50 Mpc, a factor of 2.5×10^7 more positrons would be required for an identical flux to reach the earth as from the same mechanism operating at the Galactic Centre. It is not clear that the flux relationship of annihilation radiation to synchrotron radio, even if it were correctly founded, would hold over such a large scale difference.

The present work involves an observation of the peculiar active galaxy NGC1275. The implications of the results of this observation are discussed at the end of chapter 5.

2.5.5 Pulsars.

The general features of the neutron star interpretation of radio pulsars is described by Irvine (1978). We are concerned with the emission mechanisms

thought to be associated with the pulsar magnetosphere, and the possibility of associated gamma ray line fluxes carrying useful information.

Of all known radio pulsars, only the Crab and Vela have been detected across a wide range of energies; from radio, through optical and X-ray to gamma rays of low, medium and higher energies. Some models of emission suggest that the Crab and Vela pulsation mechanisms are unique amongst pulsars; it is these models which give the best explanations of the observations. Knight (1981) provided a classification of pulsar emission models according to the following scheme:-

i) Wind zone models. These involve radiation from processes occurring outside the light cylinder (ie. the cylinder defined by the radial distance from the pulsar centre at which the corotating magnetosphere would attain the speed of light). This emission is powered by a pulsed stream of electrons from the pulsar. Examples include the synchro-Compton model of Kundt and Krotscheck (1980).

ii) Light Cylinder models. These involve emission processes at the speed of light cylinder, such as proposed in the synchrotron emission model of Hardee (1979).

iii) Inner gap models. These involve the formation of a vacuum gap just above the polar cap where synchrotron and curvature radiation can take place. This type of model was first proposed by Sturrock (1971) and was subsequently developed by Ruderman and Sutherland (1974).

iv) Outer gap models. In this class of models, a gap develops further out in the magnetosphere. These models are not intended to be general, but propose that the Crab and Vela are unique amongst known pulsars. They are however capable of explaining such features as the phase separation of the two pulses in the Crab light curve. This theory was first proposed by Cheng and Ruderman (1979).

Since this classification, da Costa (1983) has further developed the light cylinder model, concentrating on emission from just outside the light cylinder. Morini (1983) has adapted the inner gap model to explain the high energy

gamma ray emission from Vela. This model explained the second pulse of the Vela light curve by a separate mechanism from the first. Various secondary effects at the light cylinder were also invoked. Perhaps the most significant development has been the revised, Crab- and Vela-specific outer gap model of Cheng, Ho and Ruderman (1986). This model differs from the previous one in respect of the position of the gap, its shape, the direction of the emission beams, and the radiation mechanisms which limit the gap potential and contribute to the high energy spectra. It is able to predict accurately the high energy emission in the Crab and Vela and can also explain the pulse structure of the two sources. There is still a degree of uncertainty in the modelling of the Crab pulsar however. The degree to which curvature radiation is important in the Crab spectrum is not constrained, nor are the exact processes occurring deep within the outer gap. There is also considerable freedom in the gap configuration.

All the models involve intense magnetic fields and cyclotron production of gamma ray lines (perhaps not very narrow due to magnetic field non-uniformities) is at least conceivable under all of them. The inner and outer gap models depend on positron production so there is the possibility of a two-photon annihilation line or of GRASAR action. There may be an additional possibility of one-photon decay in the intense magnetic field regions. The models do not make precise predictions of these phenomena. It is possible that high spectral resolution line measurements from these processes might be very constraining of magnetospheric modelling because of the precise knowledge of fields and temperatures which might be obtained.

The present work includes an observation of the Crab region. The implications of the results of this observation are discussed at the end of chapter 5.

Chapter 3.

Review of gamma ray line astronomy experiments.

3.1 Introduction.

The scope of the review is first defined and then a general survey of detector design is given. The relevant telescopes are discussed individually and then each observation, its circumstances, analysis and its interpretation are summarised.

3.1.1 Scope of the review.

The results from the Durham 1981 observations must be placed in the context of previous experiments. This requires a reasonably exhaustive review of high resolution gamma ray telescopes and observations. However, fairly tight constraints may be placed on the scope of the review.

Whilst astrophysical mechanisms are not conveniently delimited in the same way as detector sensitivity régimes, a useful review may be defined by generally excluding experiments outside the energy region of the Durham instrument. Three further restrictions are broadly appropriate. Firstly, solar gamma ray line observations, now a rapidly developing field, do not generally yield information about mechanisms of direct relevance to the rest of gamma ray line astronomy, and are now usually treated separately. Secondly, continuum observations at the same energies as line experiments are not so closely related as might be surmised. Finally gamma-ray bursts, now quite an extensive field are excluded at least as far as observations and observational techniques. An contemporary review of bursts, medium, high and ultra-high energy gamma ray astronomy may be found in Ramana Murthy and Wolfendale (1986). For solar work, Stecker (1971), Chupp (1976) and Hillier (1984) may be consulted.

The dependence of line sensitivity on energy resolution, and of energy resolution on cost, means that detectors with high line sensitivity tend to have relatively low continuum sensitivity. In consequence, though high resolution telescopes detect continuum backgrounds, they tend to make lower significance observations than the continuum spectrum already established by low resolution

telescopes. Additionally, where a relatively substantial continuum contribution must be subtracted from a line flux, the continuum tends to be so well known in comparison to the line flux that it may be treated as an established quantity without a detailed evaluation of various measurements. Furthermore there is not an inevitable direct link between line and continuum production mechanisms. Accordingly, low resolution telescopes and observations will be discussed only when they have direct implications for line observations and interpretations.

Though most line observations have been made with detectors built specifically for that purpose, nevertheless many important results have come from detectors intended for continuum or hard X-ray work. Where such detectors have made contributions, they are described. The overall criterion therefore is that telescopes are discussed in detail if they have made or were intended to make narrow gamma ray line observations at nuclear transition energies. Continuum observations or observations at other energies which are contingent to the interpretation of line measurements are invoked only to the degree in which they are well established; the individual methods are not discussed.

3.1.2 General methods in gamma ray line astronomy.

Gamma ray line telescopes to date have not been capable of sophisticated imaging. Purpose built telescopes have typically used cooled semiconductor Ge(Hp) (hyper pure) or Ge(Li) (lithium drifted) detectors in central energy calorimeters, surrounded by lower energy resolution alkali halide detectors (CsI(Na) or NaI(Tl)) which serve the related purposes of providing active shielding and collimation of the aperture to typically a few tens of degrees, and of providing active Compton spectral background suppression.

Ge(Hp) and Ge(Li) detectors detect impinging gamma rays, interacting as described in chapter 2, by the promotion of electrons or holes to conduction states. A considerable reverse bias of 3−5 kV is required on the detector. The band gap may be of the order of an eV so cooling of the detector is required to prevent overwhelming thermal noise. However the low energies also give high resolution by virtue of the large number of charge carriers produced. The main practical difference between Ge(Hp) and Ge(Li) detectors is the need to keep Ge(Li) at low temperatures permanently in order to avoid the lithium drifting out of the crystal; the lithium compensates for residual impurities in lower cost

crystals.

Alkali halide detectors use scintillation photons in the rôle of the charge carriers in cooled semiconductor detectors. This is an older, cheaper technology and gives line resolutions of the order of a few tens of keV. The lower resolution stems from the greater deposition of energy within the scintillator necessary to produce a detectable scintillation photon, and hence the lower numbers of scintillation photons produced for a given energy of incident gamma ray compared with the corresponding charge carriers in a semiconductor. The Poisson error in the scintillation detector's measurement of the energy is therefore greater. Degradation also arises from non-uniformities in light collection throughout the detector volume, and from the characteristics of the photomultipliers used to detect the photons. The precise contributions to degradation of resolution are highly dependent on design. Lower cost enables higher volume and hence higher continuum sensitivities. However, the lower resolution limits their use in line work both through decreased line sensitivity, and through the inability to distinguish close line features. They are also unable to provide accurate measurement of line energy and broadening. They are therefore used as the main detector in telescopes designed primarily for continuum work. They are generally employed as 'active shielding' in line spectrometers.

The active shielding principle is simply the idea of placing a central detector in electronic, or in the case of the Durham system, software, anti-coincidence with surrounding, collimating detectors. There are several advantages over conventional passive shielding. In an active system it is not necessary to completely stop individual background photons or particles (ie. radiation from outside the collimation solid angle of the telescope). As seen in chapter 2, the highest interaction probability for a gamma ray of say 1 MeV is by the Compton effect. If such an interaction occurred in the shielding this would lead to a scattered photon which would be free to interact with the central detector, registering an unwanted background event. Similar arguments exist for pair production and multiple Compton scattering. If the shield is itself a detector, however, the deposited energy in the shield piece may be used to veto actively the registration of the main detector event.

A less bulky shield is normally adequate under the active rather than

passive system. The precise efficiency of shielding is however highly dependent on shield geometry, material, background spectrum, telescope infrastructure, and it must in any case be balanced against the inevitable propensity of the shields themselves to become sources of additional background radiation when subjected to activating fluxes of neutrons and protons (see Gehrels 1985 and Owens, Myers and Thompson 1986). These considerations will re-emerge subsequently for the Durham detector design. This activation problem is particularly awkward as the activated nuclide might decay some time after the activating particle traversed the telescope. This means that the decay event cannot be eliminated by active shielding.

Only segmented detectors offer the possibility of reducing the problem of detector activation. This technique, which has not yet been incorporated into a functional telescope, is described by Varnell et al. (1984) and Gehrels et al. (1984). A coaxial Ge(Hp) detector is divided into segments by planes cut normal to the cylindrical axis. The principal of operation rests on the fact that induced internal β-decay and elastic neutron scattering events are generally restricted to one segment only (the range of such a β-particle is $\sim$1 mm in Ge; the elastic neutron scattering recoil distance is a few μm). However, contributions to the gamma ray full energy peaks at 0.15–8 MeV are dominated by events involving one or more initial Compton scattering events followed by photoelectric absorption, and the sites of the successive interactions are typically in different segments. Thus, by insisting that more than one segment registers an event in this energy range, it is possible to exclude more background. Reductions in minimum sensitivity (due to improved background suppression) by factors of 2 or 3 are anticipated.

There is an important additional benefit from active shielding and this is the ability to reject non-photopeak events in the main detector where the lost Compton or pair-escape photon is detected in the shields. As seen in the Durham telescope, this leads to considerable spectral background suppression and a decisive increase in line sensitivity particularly at lower energies (Owens 1985c).

If the shield has a reasonable energy resolution, and the event recording system is suitable, there is also the possibility of using the complete telescope as a pair spectrometer. This technique requires that a coincident escape photon

(or photons') characteristic energy is observed in the shield alongside an escape peak event in the main detector.

With an axially segmented shield array there is also the possibility of gamma ray polarimetry based on the polarization dependence of the Klein-Nishina cross-section for Compton scattering as mentioned in Chapter 2.

Most of the detectors discussed are either actively shielded, cooled semiconductor detectors, or larger continuum telescopes using actively or passively shielded central alkali halide detectors. However some important measurements at low energies have also been made using essentially hard X-ray systems based on gas proportional counters. All these are discussed on an individual basis.

Satellite and balloon-borne instruments are discussed separately.

3.2 High Resolution Spectrometers on Satellites.

The two high resolution spectrometers which have so far been flown in satellites are discussed. A brief discussion of the Solar Maximum Mission gamma ray spectrometer is also included. While not strictly a high resolution instrument, this latter detector has made a significant contribution to line studies.

3.2.1 Polar Orbiter (1972–076B).

The Lockheed Palo Alto Research station's satellite-borne gamma ray spectrometer was described by Nakano, Imhof and Johnson (1974), along with some preliminary background measurements. Details of the electronics and data handling are provided in the associated paper under the authorship of Bakke et al. (1974). The spectrometer was part of the payload of satellite (1972–076B) which was launched on 2 October 1972 into a sun-synchronous polar orbit, with an inclination of 98.4° , and an apogee and perigee of 761 km and 736 km, respectively. The satellite had a spin period of 5 s with the spin vector perpendicular to the orbit plane, so that the sun was visible once per spin while the satellite was on the daylight side of the earth.

The payload was two identical gamma ray spectrometers and a variety of particle flux monitoring detectors. The spectrometers were collimated, 0.05 l

Ge(Li) detectors, 44 mm in diameter. The energy range of 40 keV to approximately 2.8 MeV was covered by a 4096 channel Pulse Height Analyzer (PHA) on each detector. The initial energy resolution, full width at half maximum (FWHM), was 3.5 to 4.0 keV at 1.33 MeV. Cooling for the detectors was provided by sublimating CO_2, which gave the somewhat high operating temperature of 130 K. The authors state, however, that the detector resolutions degraded only slowly with temperature up to 130 K (Ge(Li) detectors are normally cooled to $\sim$80–90 K). The detectors were collimated by (passive) tungsten shields (with an aperture of $\pm 45°$) and were shielded by plastic-scintillator detectors, which provided near complete charged particle detection coverage. Any of the photomultipliers on the shield could give an anti-coincidence signal; the shield data could also be used for burst detection. All non-vetoed events were stored internally and later telemetered to the ground. A 32 ms time resolution was provided by the event recording system.

The auxiliary radiation sensors consisted of penetrating radiation spectrometers (sensitive to 0.8–2.1 MeV electrons and 6–400 MeV alpha particles), an electron (plastic-scintillator) spectrometer, a multi-particle channel-multiplier, a low energy (0.2–1 MeV) proton detector, and an omni-directional (> 1 MeV) electron flux monitor. The importance of these detectors was that they permitted studies of the correlation between instrumental background and local particle fluxes.

The two spectrometers were mounted anti-parallel with their axes offset (by a fraction of their opening angles) from the normal to the spin vector. One of the spectrometers failed at launch while the other suffered degradation of resolution shortly afterwards, followed by a mysterious recovery with reduced performance (10 keV FWHM energy resolution and 90% of the original gain).

As well as atmospheric (Imhof, Nakano and Reagan 1976) and sky survey data (Imhof and Nakano 1977), this satellite has also contributed to the study of widespread, episodic, precipitation of charged particles into the atmosphere from the geomagnetic field (Imhof et al 1974).

3.2.2 HEAO C-1 on HEAO 3.

The high resolution gamma ray spectrometer (HEAO C-1) carried on

the third High Energy Astrophysical Observatory (HEAO 3) was described by Mahoney et al. (1980). The satellite was launched on 20 September 1980 into an orbit of altitude 500 km and inclination 43.6°. The satellite had a spin period of approximately 20 minutes, and was oriented so that the spin axis pointed towards the sun. The whole sky could be surveyed in six months in this, the 'normal' scanning mode. The spacecraft could also be placed in 'offset' scanning mode, whereby the aperture scanned along the galactic plane.

The spectrometer, which is illustrated in figure 3.1, comprised four 0.1 l Ge(Hp) gamma ray detectors enclosed by a 66 mm thick CsI(Na) shield defining a 30° (FWHM) field of view. The Ge(Hp) detectors had an initial resolution of approximately 3 keV at 1.46 MeV. The energy range of 0.05 to 10 MeV was covered by individual 8192 channel pulse height analyzers which measured the events recorded in each detector. Cooling was by solid methane, sublimating at 71 K, surrounded by a jacket containing solid ammonia.

Normally, the central detectors operated in anti-coincidence with the shield pieces. However, it was possible to override this veto and to use a telemetry bit-field to flag those events where a shield signal had also occurred. Similar flags recorded multiple Ge(Hp) detector events and the identity of the detector producing the event. Adjustable window discriminators connected to the shield pieces allowed events coincident with the deposition of approximately 511 keV in the shield detectors to be transmitted regardless of the veto condition. (Yet another telemetry flag was used to identify these events). Multiple Ge(Hp) detector events could be analysed to give a 10% increase in the total efficiency.

The flagged data was stored in a 2-level event buffer which served to reduce dead-time. Various rates and housekeeping information were also included in the main data stream.

Laboratory calibration used standard gamma ray sources and, for use at energies > 3.5 MeV, a special 'Neutron Howitzer'. This provided strong lines up to 8 MeV by bombarding a Cr or Ti target with neutrons from ^{235}Cf. The field of view was found to be highly energy sensitive. The FWHM was 27.6° at 2.6 MeV and 43° at 2.6 MeV. The active shield gave a 2–10 improvement over a passive shield and gave Compton event suppression of the order of 70%.

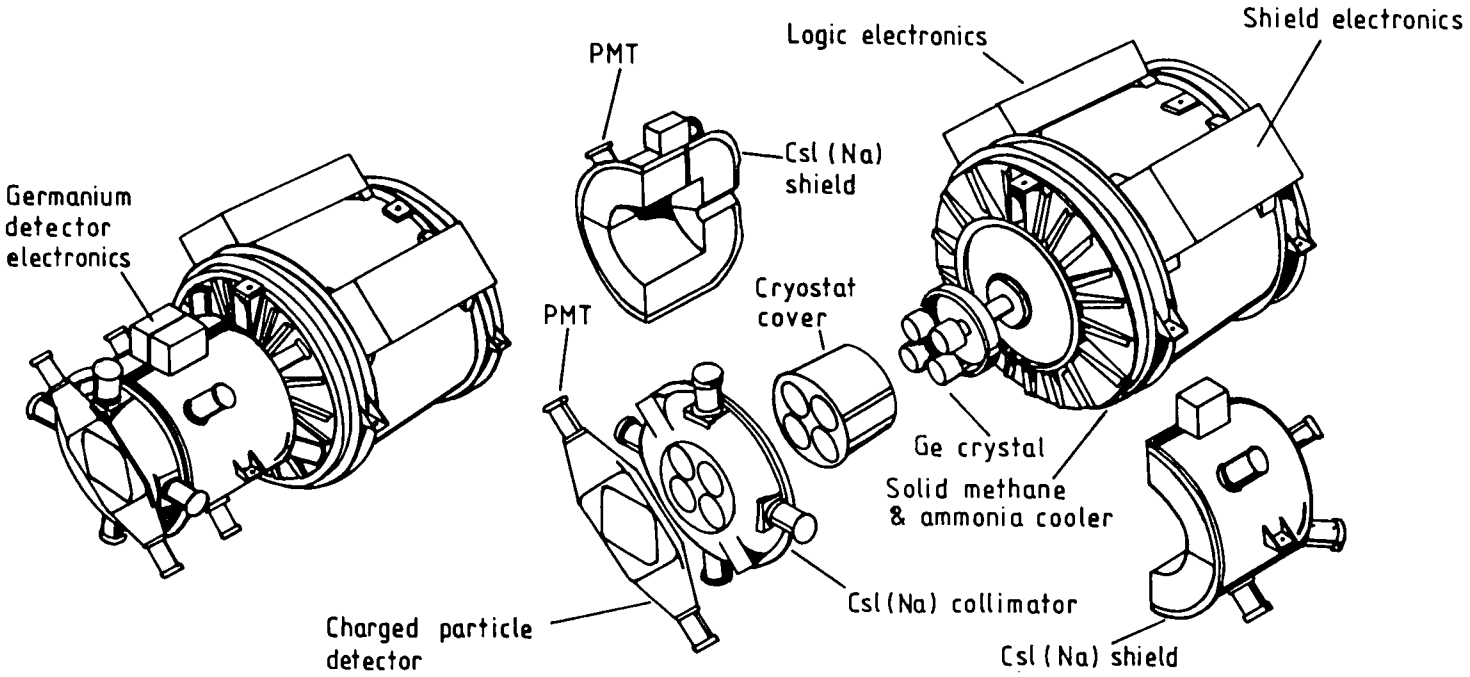

Figure 3.1 Exploded view of the HEAO C-1 spectrometer carried aboard the HEAO 3 spacecraft. (Mahoney, Ling and Jacobson, 1980)

The experiment ended on 1 June 1980 due to exhaustion of the methane coolant. Analysis of the data from this experiment is still in progress at the time of writing. However, a number of important results (some preliminary) have been published, and these are discussed in the context of corresponding balloon-payload data, where available.

Radiation damage to the HEAO C-1 detectors.

Mahoney, Ling and Jacobson (1981) described the effects of radiation damage to the Ge(Hp) detectors while in orbit. The authors estimated that, after 100 days in orbit, each detector had received 3×10^{11} protons m^{-2}. The average FWHM energy resolution had degraded from 3.1 keV to 8.6 keV at 1.46 MeV. The degradation was found to be a linear function of both energy and proton flux, and always occurred on the low-energy side of each line profile. However, the degraded profiles differed between detectors. The analysis was restricted to the 125 days following launch, due to restrictions imposed by the HYPERMET spectral analysis program (see Phillips and Marlow 1976).

Satellites receive Cosmic Ray protons of mean energy ~4 GeV and also trapped (~100 MeV) protons. The total proton flux is of the order of several 10^9 m^{-2} day^{-1}. Both protons and fast neutrons are received, however in laboratory experiments 5.1 GeV protons were found to be approximately 60 times more damaging than neutrons. In both cases, hole traps were created which produced low-energy 'tailing' of spectral peaks. The HEAO 3 spacecraft received its maximum nucleon fluxes during its transitions of the South Atlantic Anomaly, which occurred 10 times each day. Normally the Ge(Hp) and photomultiplier bias voltages were switched off during these transits.

The JPL group were also able to make various prescriptions for reducing damage to future satellite spectrometers. These include using a 'reversed' n-type electrode configuration, and minimizing the operating temperature.

Data reduction for HEAO C-1.

Data reduction for HEAO C-1 has been a complex problem due to the large number of systematic effects encountered. The JPL group have not yet fully defined their standard for data analysis, although through successive developments they seem to have settled on the so-called scan-by-scan method (see, for example, Marscher et al. 1984).

The scan-by-scan method involves fitting the data in each scan individually with a model involving the line flux, a known (or assumed) source position, instrumental angular response function, background, and any other known source which might be interfering. From the best fit of the model to the scan, a source flux f and Poisson error δf is derived. The scans are then amalgamated to form an average flux estimate F and error δF.

3.2.3 The Solar Maximum Mission (SMM) spectrometer.

The gamma ray spectrometer aboard the Solar Maximum Mission (SMM) satellite has made very important gamma ray line measurements, despite having low spectral and angular resolution compared to the cooled semiconductor instruments. It is described in Share et al (1985) and Share et al. (1988).

The spectrometer is illustrated schematically in figure 3.2. It comprises seven (75 mm × 75 mm) cylinders of NaI(Tl) with a total effective area of $7 \times 10^{-3}\,\mathrm{m}^2$. It is collimated to 130° FWHM aperture by an active CsI(Na) anti-coincidence shield. The energy range is 300 keV to 8.5 MeV with a resolution of 41 keV FWHM at 511 keV. Spectra were accumulated by a 476 channel pulse height analyzer and recorded every 16.38 s. There is a 4π sr charged particle anti-coincidence shield.

The data recording system features an active gain compensation unit which has maintained the functionality of the telescope. The excellent gain stability, the long exposure to sources, and advanced data analysis have enabled the extraction of celestial line features despite severe systematic problems.

The SMM is always oriented towards the Sun and therefore scans the celestial sources along the ecliptic with an annual period. A ~11° pointing error developed in late 1980 and was repaired by Shuttle astronauts in April 1984. This problem did not seriously affect the gamma ray spectrometer, but the SMM's recording system was shut down 5 months before the repair. As the earth passed in front of the spectrometer's viewing axis, any celestial source was occulted in a periodic fashion. 'Occulted' is perhaps a rather misleading term, as the earth's albedo at, say, 511 keV is many times more intense than the celestial source (Share et al. 1988). However, this modulation can still be used to derive a net source flux. The SMM passes through the intense radiation

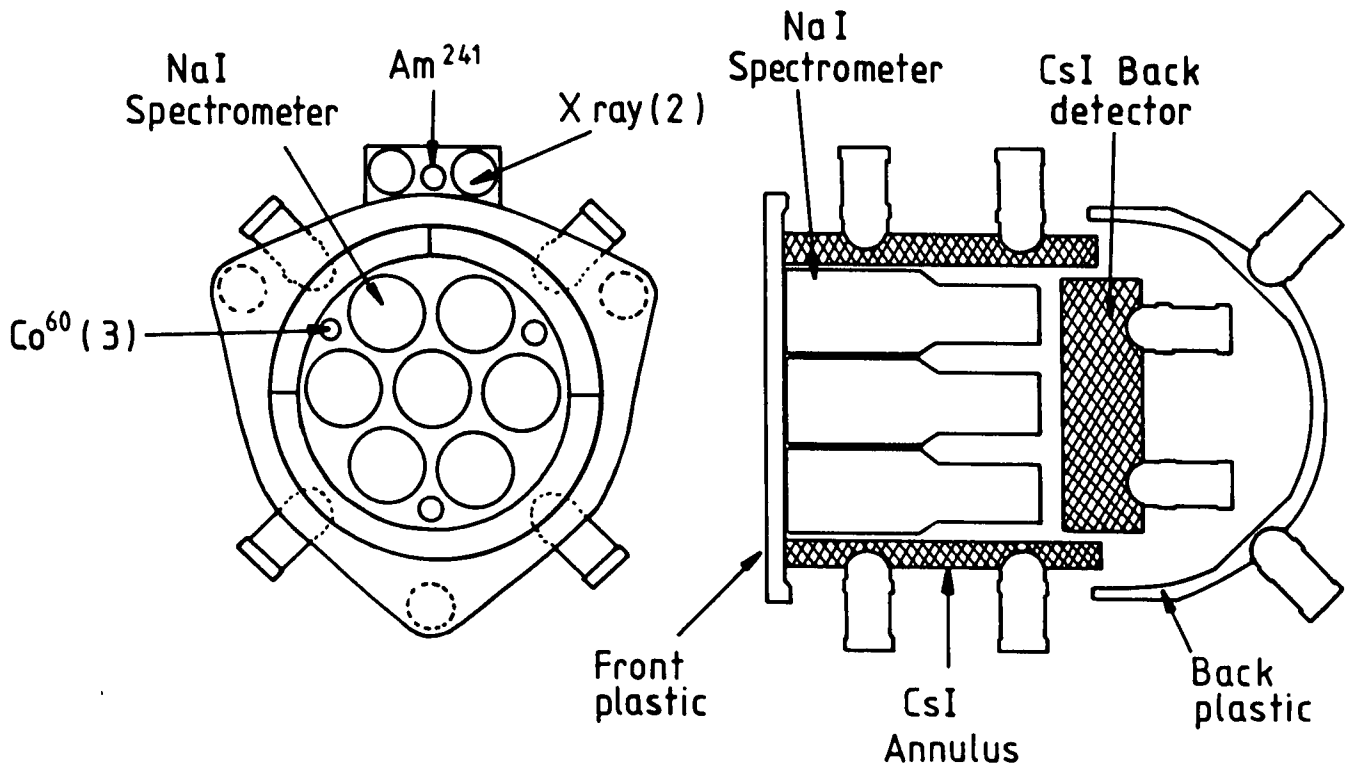

Figure 3.2 Schematic drawing of the Gamma-Ray Spectrometer (GRS) experiment on SMM. (Share et al., 1988)

of the SAA every ~47 days which produces periodic activation and contributes to a long term build up in certain instrumental lines. SAA exposures were not constant and have decreased in severity as the mission proceeded.

Share et al. 1988 have identified 3 parameters as being particularly useful indicators of background (and source) intensity variation:-

i) The time from the last irradiation by the SAA, where the intense proton and neutron fluxes produce activation of the detector and spacecraft materials. During these transits, 511 keV intensity could increase by ~10. Data from orbits containing an SAA traversal were excluded from analysis, and this parameter was used to understand the effect of SAA activation on the remaining data.

ii) The angle between the detector axis and the centre of the earth. This parameter determines both exposure to atmospheric gamma rays and the occultation of celestial sources.

iii) Vertical geomagnetic cutoff rigidity which was used to attempt to understand the effect of cosmic radiation on the instrument.

The spectrometer background spectrum contained 5 strong, partially overlapping background features, which were themselves probably blends of other lines. These features, along with a quadratic background, were studied as a function of the above parameters to establish a basis from which celestial sources could be distinguished.

The tenacious development of data analysis techniques for the SMM gamma ray spectrometer and its own stability have allowed it to make excellent celestial gamma ray line measurements, overcoming the activation problems which would beset any satellite spectrometer, and the spectral confusion which stems from its low energy resolution. However, certain serious problems remain. The low spectral resolution has prevented accurate measurements of line width and position, and this has, so far, restricted the spectrometer to confirmatory detections, although Leising et al. (1988) have recently demonstrated its first use in the exploration of new topics; in this case to provide an upper limit on nova production of ^{22}Na. The low spatial resolution has prevented the identification

of source origins — a problem also common to many high spectral resolution gamma ray telescopes.

3.3 Balloon-borne gamma ray line telescopes.

Ballooning represents a cheap alternative to satellites. A flight at 35–40 km, reduces atmospheric absorption to acceptable levels. At a typical ballooning altitude, the residual vertical column density ('atmospheric depth') might be $\sim 50\,\mathrm{kg\,m^{-3}}$ ($5\,\mathrm{g\,cm^{-2}}$). The highest attenuation will be at the lowest energies; in this case about 63% at 50 keV, falling to about 6% at 10 MeV. A payload of < 1 tonne might be carried, with full telemetry and telecommand facilities, to this altitude for a period of up to 24 hours. There is a residual atmospheric background with strong altitude and zenith dependence (Ling 1974), as was confirmed in the Durham results. There is also considerable detector proton and neutron activation. Though not perhaps as severe as for satellites (depending on the satellite orbit), this still introduces marked secular dependence which varies for different background lines (Ayre et al. 1984, Gehrels 1985, Owens, Myers and Thompson 1986). Accordingly, most observers have employed some form of source/background alternation with a period up to tens of minutes; normally by introducing an azimuthal offset from the current source alt-azimuth coordinates.

The detectors used by the various groups are discussed in turn. Where appropriate each design version is assigned a brief acronym by the author (eg. BS1) for subsequent reference.

3.3.1 JPL balloon-borne telescope.

In addition to experiments with the HEAO C-1 high resolution gamma ray spectrometer carried on HEAO 3, the JPL (Jet Propulsion Laboratory, USA) has also carried out several important observations using a balloon-borne telescope. This instrument was described by Jacobson et al. (1975). It comprised $4 \times 400\,\mathrm{mm^3}$ Ge(Li) detectors in a 63.5 mm thick CsI(Na) active shield. It had an energy range of 50 keV–10 MeV with an energy resolution ≤ 2.5 keV at 1 MeV. The field of view was 0.095 sr. The data system sampled the 2-stage buffers on each detector cyclically for the presence of an event. Flags (individually dedicated telemetry bits) indicated the occurrence of multiple events and the

presence of ~500 keV in the shields. This design of this telescope, which formed the basis for HEAO C-1, is illustrated in figure 3.3.

3.3.2 Bell-Sandia telescopes.

Bell Laboratories and Sandia Laboratories have collaborated in the design, construction and use of a number of high resolution spectrometers which are described individually.

BS1

The first telescope used by the collaboration was reported by Leventhal, MacCallum and Watts (1977). This had a central right-cylindrical Ge(Li) detector 63 mm high and 47 mm in diameter with an active volume of 92 cm^3. It had a 3.4 keV FWHM energy resolution at energies $\leq$ 2 MeV and was contained in a NaI shield collimated to 11° at 50 keV and 13° at 1.33 MeV. The pointing accuracy was $\approx$ 10°. Data recording was via a 4096 channel PHA (pulse height analyzer) with hardware shield veto (ie. the presence of a simultaneous shield event automatically disabled the recording of a Ge(Hp) event). This detector is illustrated in figure 3.4.

BS2

Leventhal, MacCallum and Stang (1978) described a new version of the above with a 130 cm^3 Ge(Hp) replacing the Ge(Li), and with the aperture increased from 12° to 15° at 511 keV. An LiF neutron shield was subsequently added (BS2a) as described by Leventhal et al. (1980).

BS3

A 200 cm^3 Ge(Hp) detector with an energy resolution of 2.4 keV at 511 keV replaced the central detector. This variant is described in Leventhal et al. (1982).

3.3.3 CNRS-CEN-SEP-INPE telescopes.

The *Centre d'Etudes Spatiale des Rayonnements* at CNRS, France, along with co-workers from the *Centre d'Etudes Nucléaires de Saclay*, France and the *Instituto Nacional de Pesquisas Espaciais*, Brazil have made a number of collaborative observations of atmospheric lines and astronomical sources with a series of cooled semiconductor spectrometers.

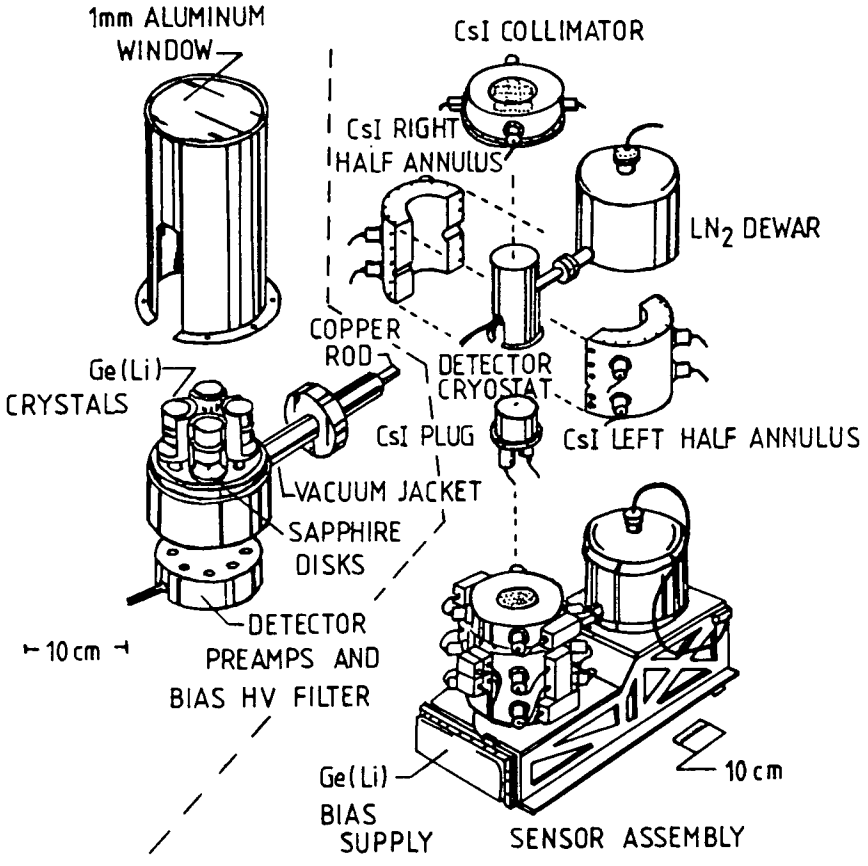

Figure 3.3 The Jet Propulsion Laboratory four-headed gamma-ray spectrometer. [Jacobson et al (1978)] (Balloon-borne)

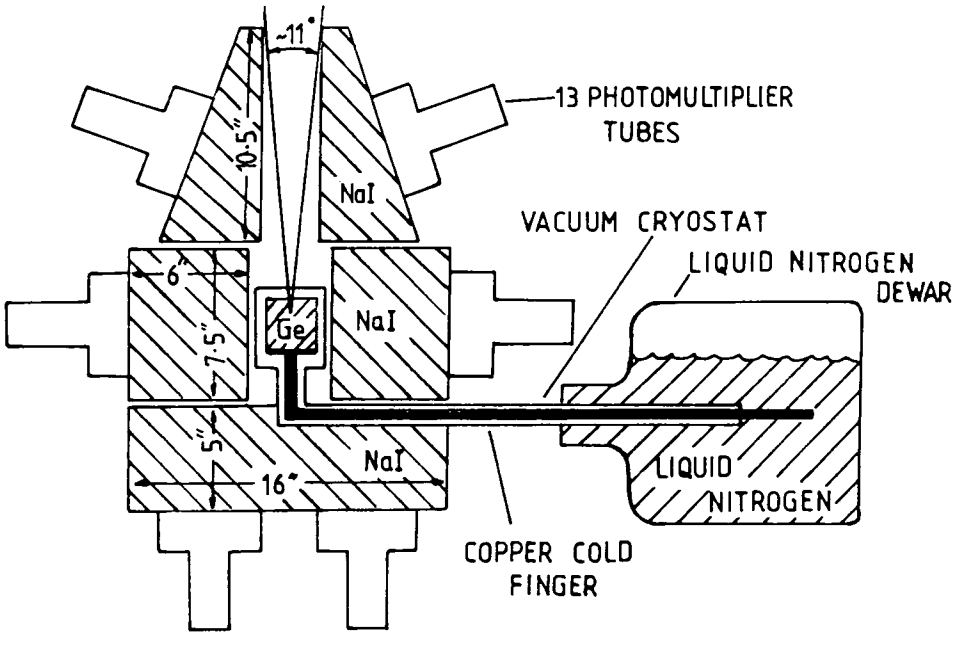

Figure 3.4 A cross sectional view of the Bell-Sandia instrument [BS1]. (Leventhal et al., 1977)

FR1

The first detector described by Albernhe and Vedrenne (1976) used a 25 cm^3 Ge(Li) crystal in a plastic anti-coincidence shield. The shield would have served to reduce charged particle events.

FR2

A much improved telescope is described by Albernhe et al. (1978). This comprised a 140 cm^3 Ge(Li) detector with a 3 keV energy resolution at 1 MeV, and an energy range of 60 keV–8 MeV, collimated by a 50–55 mm thick NaI shield to an acceptance angle of 25°. Two independent encoding systems covered the energy range. Anti-coincidence shield pulses within 80 keV of 511 keV produced a tagged event, rather than a veto, in order to facilitate pair-spectrometry. Some flights of this detector were made with degraded energy resolution.

An omnidirectional detector was also developed as described in Albernhe, Vedrenne and Martin (1979).

FR3

Albernhe et al. (1981) describe a version of FR2 with energy resolution degraded to 5–10 keV and subsequently to 18 keV, and with the aperture increased to 50° FWHM.

3.3.4 The GSFC LEGS spectrometer.

Paciesas et al (1983) describe the LEGS (Low Energy Gamma Ray Spectrometer). This design was produced by a collaboration involving GSFC (Goddard Space Flight Centre), USA; University of Maryland, USA; CENS, France; and Rice University, USA. The original design could be configured with either of two sets of Ge(Hp) detectors. Both configurations are illustrated in figure 3.5. The two detector configurations are:-

a) 3 coaxial detectors with a total volume of 230 cm^3 and a NaI(Tl) shield with a 16° FWHM aperture. The system in this configuration has an energy range of 80–8000 keV.

b) 3 planar detectors with a total effective area of 53 cm^2 within a combination of passive Fe collimators and an active NaI(Tl) shield giving a 5° × 10°

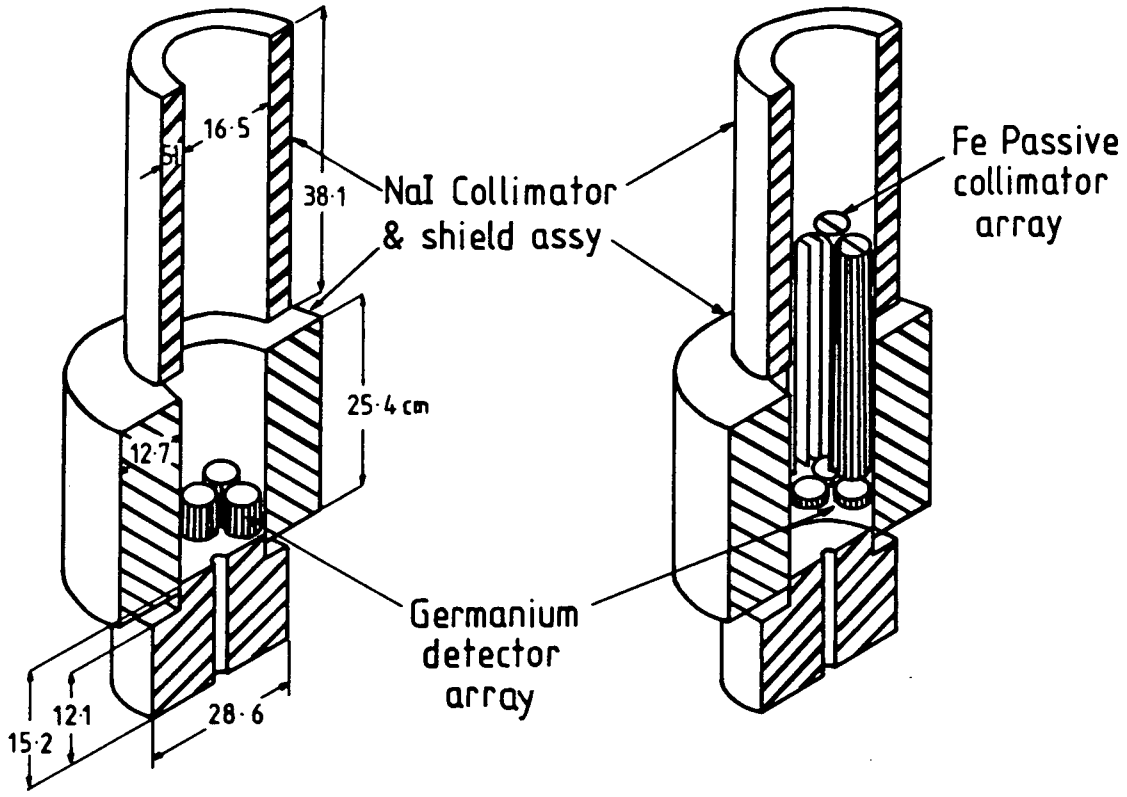

Legs cutaway schematic

Figure 3.5 Schematic views of the two configurations of the GSFC / CENS / RICE Low Energy Gamma ray Spectrometer (LEGS). (Paciesas et al., 1983)

FWHM aperture, and an energy range of 20−200 keV.

Each Ge(Hp) detector has its own 13-bit ADC and a 6-bit ADC is used for shield events which are recorded both in coincidence with the Ge(Hp) and independently. Events are double buffered and transmission priority given to un-vetoed events. A special pulse-pair timing circuit was employed with the planar system to reduce the 54−67 keV feature from neutron activated ^{72}Ge by recording the time between the event and the nearest fast threshold pulse.

3.3.5 Rikkyo University telescopes.

Two Ge(Li)-based spectrometers constructed and flown by the Rikkyo group have made gamma ray line observations of several potential astrophysical sources.

R1

The earlier Rikkyo University high energy resolution gamma ray spectrometer was described by Yoshimori et al. (1979). It comprised a 39 mm diameter by 26 mm long Ge(li) detector in a plastic scintillator active shield defining an aperture of 110°. The Ge(Li) energy resolution was 3 keV FWHM at 1.333 MeV.

R2

A later instrument, which was described by Watanabe (1985), had a central planar Ge(Li) crystal 46 mm in diameter and 8 mm thick. This was surrounded by a 40 mm thick NaI(Tl) shield which defined an aperture of 26° FWHM at 60 keV. The Ge(Li) spectrometer had an energy range of 30−60 keV and a resolution of 5.5 keV at 81 keV, which decreased to 6.8 keV at 356 keV.

3.4 Non-line balloon-borne telescopes.

This section briefly describes gamma ray telescope systems with >5 keV spectral resolution which have been designed for high-sensitivity hard X-ray or low energy gamma ray continuum measurements, but which have nevertheless contributed to the observation of gamma ray lines.

3.4.1 UNH continuum telescope.

The University of New Hampshire developed a continuum detection system with 7 (76 × 76 mm) NaI(Tl) detectors in a 102 mm anti-coincidence shield of crushed NaI(Tl) in silicone oil. This is described by Dunphy et al. (1981).

3.4.2 NRL hard X-ray telescope.

The NRL (Naval Research Laboratory), USA hard X-ray observatory is described in Kurfess and Johnson (1975). It comprised a 5 mm thick NaI(Tl) central detector in a CsI(Na) active shield defining a FWHM field of view of 10°. The effective central detector area was 765 cm^2 and the energy range was 18−240 keV. The energy resolution was 24% FWHM at 60 keV.

3.4.3 Rice University line/continuum telescopes.

The Rice University (Houston, Texas) group have used a variety of alkali halide based, actively shielded, telescope designs to perform a number of pioneering observations. Those designs which have relevance to our present review are briefly described.

RC1

This Rice University apparatus was described by Johnson and Haymes (1973). The instrument comprised two telescopes, each consisting of a 50 mm thick by 100 mm diameter NaI(Tl) central detector surrounded by a "well-type" active shield crystal of NaI(Tl) which gave a FWHM field of view of 24°. The overall energy range was 30 keV to 24 MeV The spectral resolution was approximately 11%.

RC2

This Rice University gamma ray telescope (adapted from previous designs) was described by Walraven et al. (1975). This instrument had a central NaI(Tl) detector, 50 mm thick and 150 mm in diameter, with an energy range 56 keV−12.11 MeV. This was contained in a NaI(Tl) shield giving a FWHM field of view of 13°.

3.4.4 HXR-79 hard X-ray telescope.

The HXR-79 instrument, a balloon-borne hard X-ray telescope, was described by Manchanda et al. (1982). It had an energy range of 22–150 keV and comprised two high pressure Xenon-filled proportional counters giving a total sensitive area of 900 cm^2, 105 mm deep. The detectors were divided into cells with the outside cells used to form an anti-coincidence shield. Passive collimators were used to give FWHM field of views of (7.5° × 7.5°) and (5.5° × 5.5°) in essentially two separate telescopes.

3.4.5 MPI double Compton telescope.

The MPI (*Max-Planck-Institut für Extraterrestishce Physik, FDR*) developed a 'Compton telescope' which used Compton scattering from one plane of alkali halide detectors to another to indicate possible incident photon directions. The detector was described by Schonfelder, Graser and Diehl (1982). The energy resolution was approximately 11% at 1 MeV.

3.5 Gamma ray line observations.

Gamma ray line observations (excluding solar lines) will be discussed in categories determined by the target sources. However it should be noted that some of the detectors described have very large fields of view and source identification is sometimes ambiguous.

Comparison of gamma ray line observations is difficult. The telescopes described above differ in respect of all important parameters, even those used in different observing runs by the same group or collaboration. Furthermore, source/background observation modes are all different, as are flight conditions (geographical location, altitude, source elevation), data analysis (drift correction, spectral summing, background subtraction, detector response correction, peak searching, line fitting, continuum subtraction, temporal variation analysis) and statistical interpretation (significance of excess counts, compensation for number of trials made).

The problem is compounded by lack of complete information in some cases, and by the sensitivity of background line secular evolution to details of detector and gondola construction. Even when considerable effort is made

to make sensible comparisons, caution should be exercised when attempting to draw conclusions.

3.5.1 Crab Nebula and pulsar PSR0531+21.

The Crab Nebula and its associated pulsar have been the subject of numerous gamma ray line experiments. The nebula and pulsar have fairly well known continuum spectra below 1 MeV. These take the form of inverse power laws with somewhat different forms. However, debate exists over the shape of the continuum spectra at ≥ 1 MeV, the existence of an interpulse spectrum, and over whether there is a variation of power law index with light curve phase.

Nebular gamma ray lines might arise from nucleosynthetic supernova debris, whilst pulsar lines might arise from accretion or from interaction of charged particles accelerated at the polar caps. Given the poor angular resolution of gamma ray line telescopes, the only possibilities of distinguishing between nebular and gamma ray emission are timing analysis or interpretation. Nebular emission would be expected at only well defined, predicted nuclear transition energies, whilst in the case of the pulsar, fairly *ad hoc* shifts in energy may be attributed to gravitational redshift or, in the case of cyclotron emission, to the strength of the magnetic field in the emission region.

15 May 1973, RC2

This observation is described by Walraven et al. (1975). The source was observed with North-South reversal every 11 minutes in order to obtain background. Upper limits of 10 photons $m^{-2}\,s^{-1}$ were obtained for various predicted lines as summarised below. Timing analysis allowed the differentiation of nebular and

pulsar upper limits.

Source	*Energy (keV)*	*Origin*	2σ *Upper Limit*, $m^{-2}s^{-1}$
Nebula	180	$^{251}Cf^*$	13
Nebula	390	$^{249}Cf^*$	9.6
Nebula	511	β^+ annihilation	11
Nebula	847	$^{56}Fe^*$	14
Nebula	1330	$^{60}Co^*$	18
Nebula	1630	$^{20}Ne^*$	14
Nebula	4430	$^{12}C^*$	11
Nebula	6130	$^{16}O^*$	8.9
Pulsar	511	β^+ annihilation	7.7
Pulsar	847	$^{56}Fe^*$	10
Pulsar	1330	$^{60}Co^*$	13
Pulsar	1630	$^{20}Ne^*$	10
Pulsar	4430	$^{12}C^*$	7.2
Pulsar	6130	$^{16}O^*$	6.4

These trial energies were chosen from theoretical predictions by Clayton and Craddock (1965) which were in all cases at least an order of magnitude less than the upper limits.

10 June 1974, JPL balloon telescope.
Data from this observation of the Crab are described in Ling et al. (1977) and Ling et al. (1979). The former paper is a negative retrospective search for the 'Leventhal effect' at 400 keV (illustrated in figure 3.6) which, as its observation was actually later, is described subsequently in this chapter. The latter paper described positive evidence for a line at 73 keV.

The Crab was observed by transit. 104 minutes of live time were taken as Crab source data, and 128 minutes before and after as background. The average exposed area (at 400 keV) was 5.62 cm^2. If the Leventhal effect had been present at the Leventhal rate (22.4 photons $m^{-2}\,s^{-1}$) then it should have given a 1.26×10^{-2} counts s^{-1} increase; a $3.9\,\sigma$ excess. Instead (-2.85 ± 3.27) counts s^{-1} were obtained. This negative result is illustrated in figure 3.7.

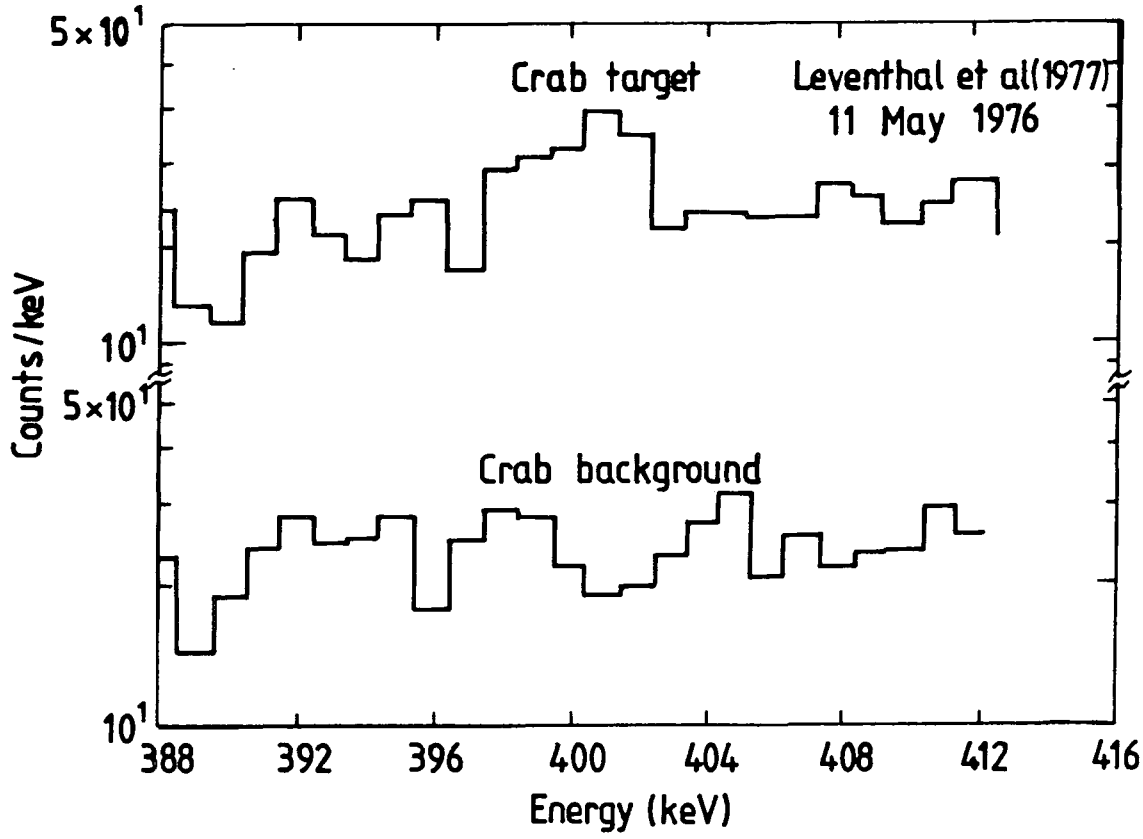

Figure 3.6 The Crab target energy spectrum in the vicinity of 400 keV. From Leventhal et al. (1977)

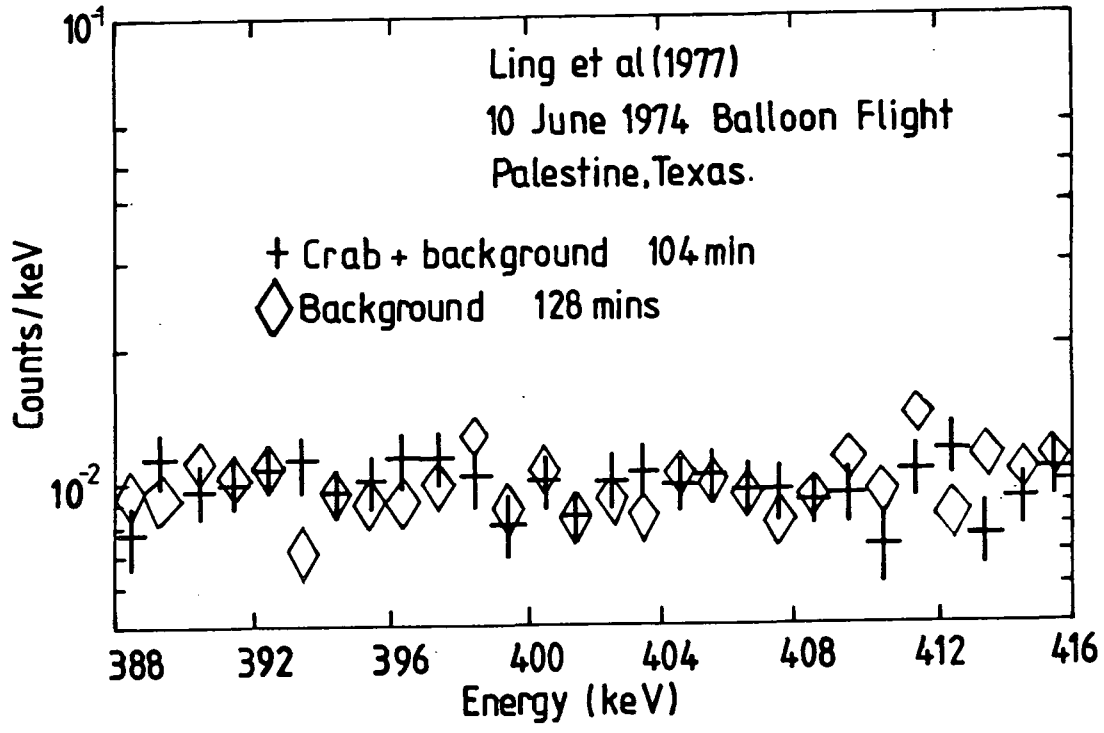

Figure 3.7 The Crab target energy spectrum in the vicinity of 400 keV. From Ling et al. (1977)

The following criteria were employed for a general line search in 5 keV bins:

(i) A $3\,\sigma$ excess over the underlying continuum of the summed spectra.

(ii) A similar feature in the spectra for each crystal.

The only suitable feature was in the 71−76 keV bin which is illustrated in figure 3.8 The total excess spectrum was fitted with a model comprising an inverse power law and a gaussian line centred at 73.3 keV. A fit of $\chi^2 = 44.5$ for 37 degrees of freedom. This is compared with $\chi^2 = 41.4$ for 27 degrees of freedom with the inverse power law alone. From the former fit a line intensity of (38 ± 9) photons $m^{-2}\,s^{-1}$ with width < 4.9 keV is derived. The authors examined the possibility that this line might be either the first harmonic of cyclotron radiation in an $\approx 8 \times 10^{12}$ G magnetic field, or that it might be K_α X-rays of Pb.

10 May 1976, NRL telescope.
This work is described in Strickman, Kurfess and Johnson (1982). The telescope reached a float altitude having an average atmospheric pressure of 2.3 mb. Nine 15 minute source observation segments were obtained. Each source segment was followed by a 5 minute background sample obtained with a 15° azimuthal offset. The offsets were taken alternatively clockwise and anti-clockwise from the source. The authors successfully extracted a continuum Crab spectrum and pulsar light curve, they found some suggestion of a variation of pulsar power law index with light curve phase.

This telescope had six energy bands in the energy range 18−240 keV. The authors found a 'flare' effect in the 70−89 keV band occurring only in pulsed emission. The flare was apparently in progress at the start of the observation and returned to 'normal' over ≈ 25 minutes. This was a $5.1\,\sigma$ effect obtained after 4536 trials. Assuming a δ-function centred on (76.6 ± 2.5) keV, the instantaneous (not pulse-averaged) flux was (41 ± 12) photons $m^{-2}\,s^{-1}$.

The authors examined a cyclotron model for this emission. If $z = 0.2$ then 77 keV implies a magnetic field strength of 8×10^8 T. If beamed with a longitudinal electron Lorentz factor of 10^3 and a blueshift 10^3, then a 10^6 T

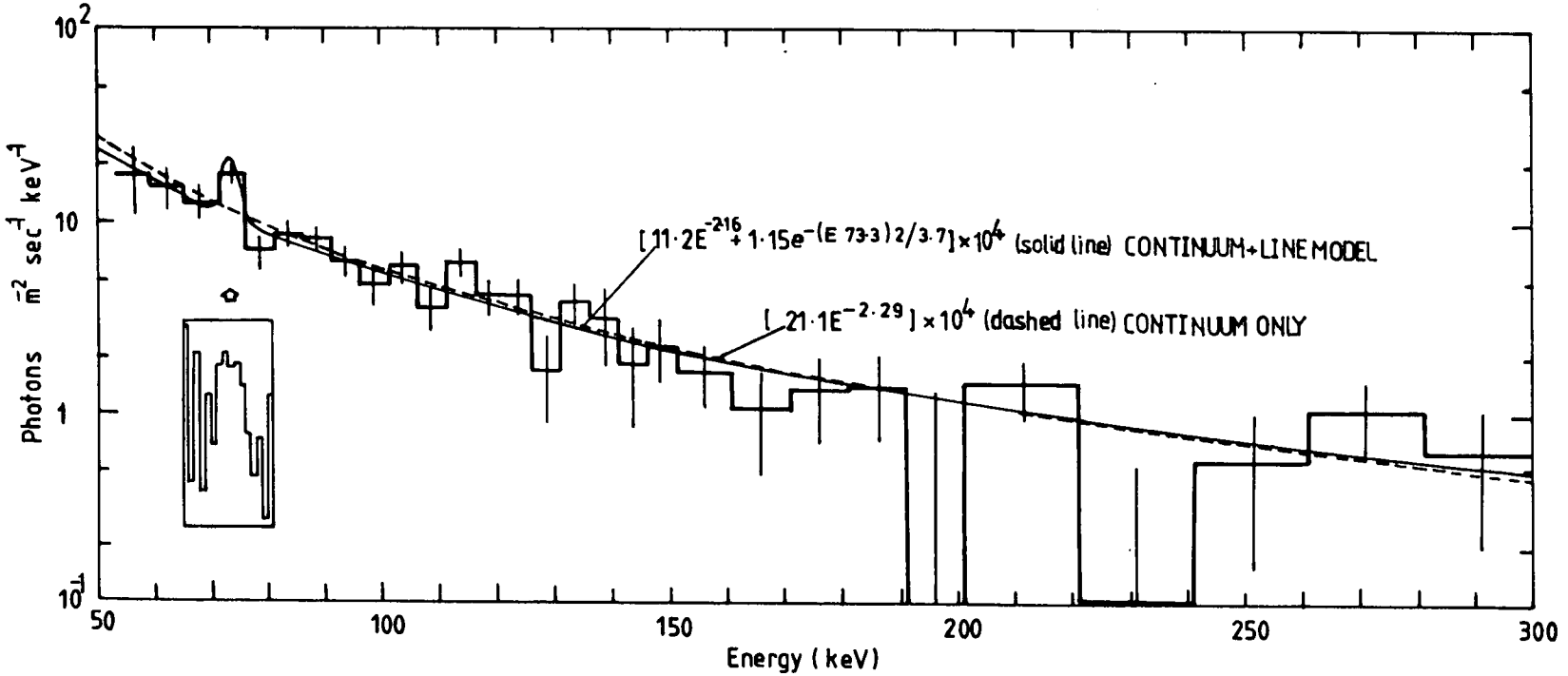

Figure 3.8 The net photon spectrum from the Crab Nebula in the energy range 50keV to 300keV, measured on June 10, 1974. From Ling et al., (1979).

magnetic field would be required. The line is narrow implying very similar Lorentz factors for all the electrons which must all occupy low Landau levels — this is difficult to conceive. If we assume 10^8 T and a dipolar configuration, then the emission regions must be at ~50 km from the neutron star surface. The narrow line implies little variation in magnetic field strength and hence a small emission region; it also requires very little thermal Doppler broadening. The timescale of the flare would require continuous injection of energy.

10–11 May 1976, BS1

This observation with the BS1 detector is described by Leventhal, MacCallum and Watts (1977). An altitude of 36–39 km was maintained whilst the Crab region was observed using a 20 minute target/background alternation period. Background was sampled by a 180° offset in azimuth with no change in zenith. Seven complete cycles and one shortened one were obtained by this method. The authors describe the weighting of each run pair for changes in atmospheric depth, and also recalibrating the detector against gain changes.

The continuum was detected and fitted with the usual power law

$$I(E)dE = 12.2E^{-2.08}dE \tag{3.1}$$

(the fit gave $\chi^2 = 11.4$ for 8 degrees of freedom). This is quite consistent with the world continuum data. The authors used a simple efficiency calculation to derive this rather than the matrix inversion often prescribed. Calculations on active Compton background suppression in the Durham instrument, which is of a similar class to BS1, show this decision to be well justified.

Line searching was performed by searching the source spectra for an excess of $\geq 3\sigma$ within a 5 keV window over a background determined by averaging over an adjacent 10 keV wide window of the spectrum. This method will of course find background lines as well as any source lines present, so the authors simply looked for lines that were present in the source and not the background.

Twelve background lines were indeed found and mostly interpreted as being due to (n,γ) reactions in the detector materials and telescope infrastructure. One line, however, was found in most of the target segments but none of the background and is illustrated in figure 3.6. This was at (400 ± 1) keV and gave

a $4\,\sigma$ deviation from adjacent averaged bins (1000 attempts were made in order to find it, however). The width was $\leq 3\,\mathrm{keV}$ and the flux corrected to the top of the atmosphere (ATA) was $(22.4 \pm 6.3)\,\mathrm{photons\,m^{-2}\,s^{-1}}$. The authors tentatively suggested gravitationally redshifted positron annihilation radiation as a possible cause, this would mean $Z_{\mathrm{Crab}} = 0.28$.

30 September 1977, R1.
This flight of the Rikkyo University high energy resolution gamma ray spectrometer is described by Yoshimori et al. (1979). The Crab was observed by transit. 6 hours 6 minutes of Crab data were compared with 3 hours 7 minutes of background. An uncorrelated excess was seen at 400 keV with width $\leq 3\,\mathrm{keV}$. This is a comparatively weak signal, being only a $1.4\,\sigma$ deviation above background and representing a flux of $(74 \pm 54)\,\mathrm{photons\,m^{-2}\,s^{-1}}$.

26 August 1979, HXR-79.
This observation is described by Manchanda et al. (1982). The payload attained an altitude of 2.9 mB, and the Crab was observed by transit. 30 minutes of on-source data were obtained using the $7.5° \times 7.5°$ field of view detector (the $5° \times 5°$ detector had malfunctioned). Background was taken whilst the source was just outside the field of view.

The Crab light curve and non-pulsed continuum spectrum were obtained and found consistent with world data apart from an apparent line in the latter at $\sim$73 keV. The line, which was found by visual inspection of the spectrum, was a $3.8\,\sigma$ excess in the energy channel 67–79 keV. The reported spectrum is shown in figure 3.9. There were 12 energy bands in the continuum spectrum so in effect 12 attempts were made to find a line. The observed excess represents an intensity of $(50 \pm 15)\,\mathrm{photons\,m^{-2}\,s^{-1}}$. The observed width was consistent with a narrow line ($E < 4\,\mathrm{keV}$).

Due to the low number of counts it was not possible to say definitely whether the line was pulsed or not. However, the energy band containing the line did have a higher pulsed fraction than would be expected from the world data (30% rather than 15%).

The authors discuss a possible cyclotron origin for the line, and rightly comment on the number of unknown parameters involved in trying to model

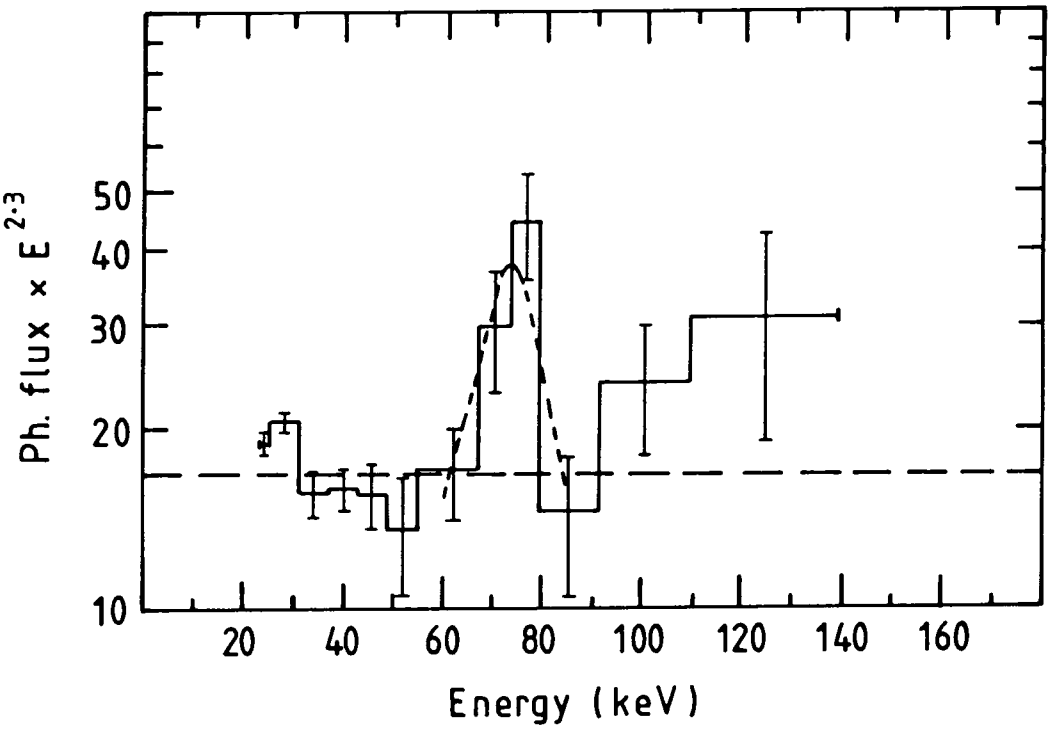

Figure 3.9 HXR - 79 detection of Crab line feature at ~73keV. (Manchanda et al., 1982)

this emission using current knowledge of pulsar magnetosphere topology.

25 September 1980, LEGS(Planar).
This observation is described in Hameury et al. (1983). It was made using the planar Ge(Hp) version of LEGS (20–800 keV). A residual atmospheric depth of 4.5 g cm^{-2} was attained. Observation was by alternating 20 minute source and background segments. The latter were obtained with an azimuthal offset of 30°, with the source elevation < 65°, taken alternatively clockwise and anti-clockwise. Actual rates were computed by subtracting each 20 minute source segment from a sum of 10 minutes of background from both before and after the source period.

The transient X-ray source A0535+26 (see Fishman and Watts 1977 and references therein), which — like the Crab — is in Taurus, turned out to be active at the time of observation, and confused the Crab continuum spectrum. However, the authors successfully deconvolved power law spectra from both sources.

The data were examined for lines at the specific energies 73 keV and 400 keV. No significant excesses were found and respective 3 σ upper limits at 6.2 photons m^{-2} s^{-1} and 17 photons m^{-2} s^{-1} were derived. The authors divided their data into 10 minute intervals and looked for a transient at 77 keV; again nothing was found.

A general line search was conducted using a 2.5 keV 'sliding window' which was subtracted from an averaged sample of adjacent spectral background. The background regions were adjusted so that strong instrumental lines were excluded. No positive detections were claimed.

HEAO C-1.
HEAO C-1 observations of the Crab pulsar are described by Mahoney, Ling and Jacobson (1984). The source was observed for 18 days in Autumn 1979 (23 September – 10 October) and 41 days in Spring 1980 (24 February – 4 April). During these periods the Crab was within 20° of the telescope aperture central axis. The JPL data reduction technique has been the subject of continuous development and has probably not yet reached its definitive form. In this case a pulsar phase-determined background subtraction was employed. This paper

must therefore be regarded as specifically about the Crab pulsar.

A comparison with Arecebo confirmed that photon arrival times were accurate to 1 ms. The data were treated as multiple spectra: 60 phase bins × 4 detectors × 8192 channels. Four spectra were then formed: the two peaks of the light-curve, the interpulse spectrum and the sum of these three. Net spectra were normalised by dividing by (phase-dependent) live time and (energy-dependent) transmission function.

The Autumn and Spring light curves were found to be the same and to be consistent with all other observations. There was no evidence of variation of power law index with pulsar phase, and no evidence of line emission. The following specific $3\,\sigma$ upper limits were obtained:

$$\begin{aligned} 73\,\text{keV} &: 2.8 \quad \text{photons}\,\text{m}^{-2}\,\text{s}^{-1} \\ 400\,\text{keV} &: 1.8 \quad \text{photons}\,\text{m}^{-2}\,\text{s}^{-1}. \end{aligned}$$

2-day interval searches revealed no evidence of flaring emission at 77 keV (The 'Strickman effect'). The authors state, however, that a ~25 minute flare would not have been detected.

Line searches were performed using a 'sliding filter'. This used an N channel source region, where $N \approx 1.2 \times \text{FWHM}$, from which is subtracted a $2N$ background taken from either side.

29 September 1982, R2

This observation of the Crab which is described in Watanabe (1985) with the R2 Rikkyo spectrometer was made from a float altitude of 4.1 mBar. The Crab Nebula region was observed for 2 hours and 50 minutes using a constant zenith angle of 15° and a 17 minute periodic alternation between points set at +60° and −60° in azimuth from the South. The effect was that as the source made its meridian transit it was observed alternately with an azimuthally offset background. Ge(Li) pulse height information was transmitted along with timing information and accompanying shield detector pulse height information (if any).

The vetoed background spectra were subtracted from the vetoed source spectra, the 17 minute time-segments were then summed together and the result transformed to compensate for the detector response. The data were found to be consistent with previous inverse power law observations.

The authors examined the 73−79 keV region indicated as possible emission energies by Ling et al. (1979) and in preliminary reports of the present work in Ayre et al. (1983). They found a weak excess at ~78 keV corresponding to a photon flux at the top of the atmosphere of (35 ± 19) photons $m^{-2}\,s^{-1}$. Because of the low statistics the authors did not derive an exact linewidth.

Discussion.

Most observers have used some variant of the 'sliding window' line search. Regions of the source spectrum are compared with averaged adjacent 'background' taken from the source spectrum itself. A similar procedure is then carried out on the genuine 'off-source' background spectrum. A positive detection would then be an excess in the 'on-source' scan which had no corresponding effect in the background spectrum.

This technique may not be ideal, however. Analysis of the Durham data reveals a great number of atmospheric background and instrumental lines. Automated spectral analysis revealed significant background line fluxes which are not visible to the eye. Doubt therefore is cast on the use of an averaged adjacent part of the source spectrum to calculate fluxes in a scan. These adjacent regions might well contain background lines just below the detection threshold, therefore they do not provide a reliable basis for comparison. It might be thought that the use of the background spectrum as a 'control' would eliminate this problem, however this is not so. A source line would still be missed if the adjacent spectral background contained an undetected instrumental line. Such lines vary between experiments making comparison of such scans dubious.

Li and Ma (1982) give a careful analysis of the statistics of scanning. They point out that the normal assumption that the Poisson error on an observed count may be calculated as if it were the parent population mean is undermined by the act of scanning, which will tend to pick out low background and high source sample fluctuations about the parent mean at each energy. Any scanning technique should take account of the effect of this on calculations of significance, as well, of course, as the effect of the number of independent trials involved in the scan.

Many experimenters report periodic recalibration of spectrometer gain to

eliminate drift. The errors involved in realignment are difficult to assess.

These general problems are particularly important in the comparison of data from the Crab, where *ad hoc* gravitational redshifts mean that lines cannot be predicted to occur at fixed energies; hence the adoption of scanning techniques. The existing world line data will be compared to the Durham observations of the Crab described in chapter 5, but precise comparisons of results are difficult.

3.5.2 Galactic Centre Region.

The majority of high spectral resolution observations of the general region of the Galactic Centre have concentrated on an apparent source of 511 keV gamma rays. Several observations of time variability on the order of months have given rise to the general acceptance of a compact source in Sagitarius, although this has recently been challenged. No spectrometer has had sufficiently precise angular resolution to identify this unambiguously with any known feature at the Galactic Centre.

25 November 1970, RC1

This flight is described by Johnson, Harnden and Haymes (1972). The flight included a 7 hour observation of the Galactic Centre. Background was sampled every 10 minutes by offsetting the telescope from the source by 180° in azimuth. When the background data were subtracted from the source data, and the residual corrected for atmospheric absorption, then a power law with spectral index 2.37 ± 0.5 was found. Superimposed upon this was evidence for a line feature in the 0.5 MeV region with a flux of 18 ± 5 photons $m^{-2}\,s^{-1}$.

20 November 1971, RC1

This observation, which was described by Johnson and Haymes (1973), produced 8.5 hours of data for the Galactic Centre region, all but one hour of which was obtained with the same observing mode as the 1970 flight. The remaining hour involved a lunar occultation of the Galactic Centre. The data proved to be precisely consistent with the previous flight. The lunar occultation produced a $2.3\,\sigma$ decrease in the 511 keV flux level.

2 April 1974, RC2.

This flight of the Rice University telescope was described by Haymes et al. (1975) and Walraven and Haymes (1976). The source was observed using a 10 minute on-source, 10 minute off-source cycle. The background was obtained using azimuthal offsets. In total 219 minutes were obtained on-source and 217 minutes off-source.

An inverse power law continuum was observed together with evidence of line emission in three energy bands:

Energy (MeV)	*Flux* (photons $m^{-2} s^{-1}$)	*Suggested origin*
0.5	9 ± 3	e^+e^- annihilation
1.2–2.0	26 ± 6	unknown
4.6 ± 0.1	8 ± 2	$^{12}C^*$

14 and 17 February 1977, FR3

These two flights are described in Albernhe et al. (1981). For the second the spectral resolution of the instrument was degraded to 5–10 keV then to 18 keV. Both observations were by drift-scan with the Galactic Centre transitting at 2° from zenith; 2–3 hours were obtained with the source transmission fraction (ie. the probability of a 511 keV photon from the Galactic Centre direction penetrating the collimator and reaching the central detector) at ≥ 0.5.

The data from both flights gave a total of 5 hours on-source and 2 hours, 40 minutes of background. The measured flux at 511 keV was 41 ± 15 photons $m^{-2} s^{-1}$. 3σ upper limits were also derived for a number of theoretical lines; they were all ≤ 18 photons $m^{-2} s^{-1}$.

11–12 November 1977, BS2

Leventhal, MacCallum and Stang (1978) describe a long balloon flight during which the Galactic Centre region was observed for 17.3 hours from a mean atmospheric depth of 3.6 g cm^{-2}. Source and North-South reflected azimuth offset background segments were alternated on a 20 minute period.

A near doubling of the 511 keV rate for the on-source segments; a 4.5σ effect. The results are illustrated in figure 3.10 and in more detail in figure 3.11. The data were fitted with a three-component model:

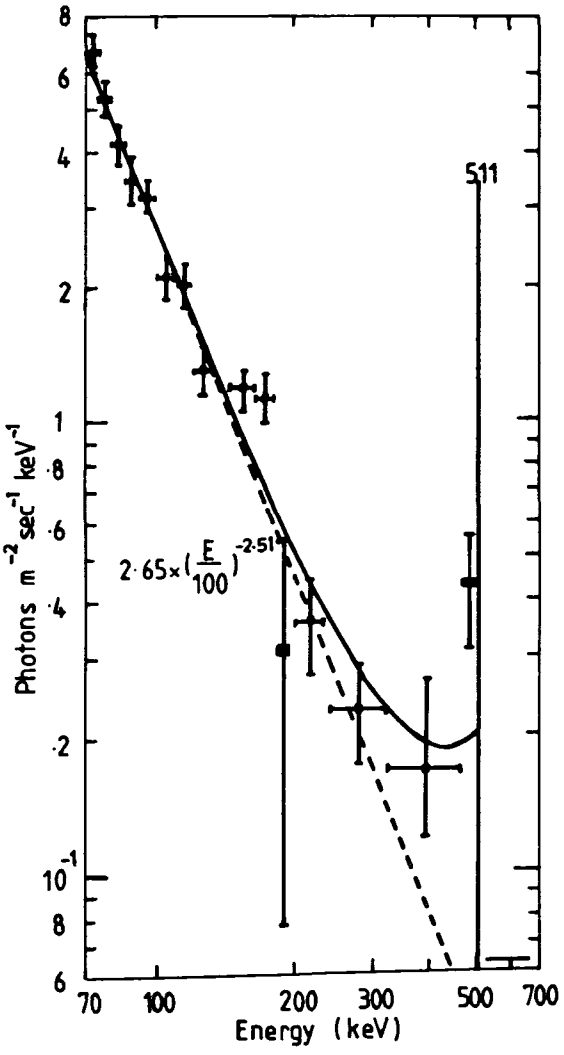

Figure 3.10 Differential photon spectrum from the galactic centre. From Leventhal et al.,(1978)

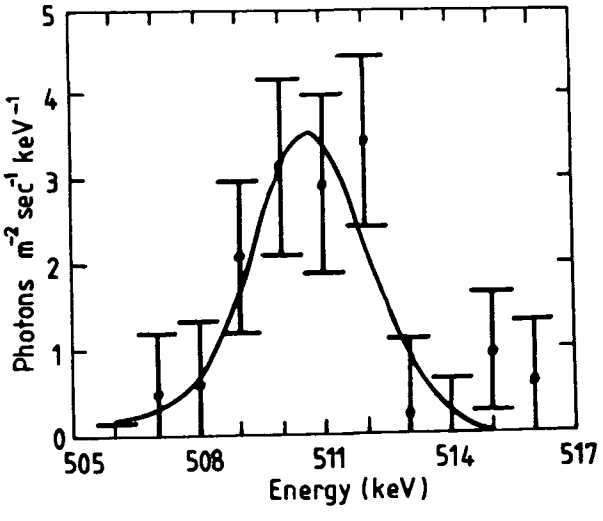

Figure 3.11 An expanded version of Fig. 3.10 in the vicinity of 511 keV. From Leventhal et al.,(1978)

(i) A Gaussian 511 keV line; fitting parameters: width, intensity, location.

(ii) A 3-photon positronium decay spectrum; fitting parameter: intensity.

(iii) An inverse power law continuum, fitting parameters: intensity, exponent.

When the χ^2 of the fit was plotted against the positronium fraction f (ie. the fraction of the positrons which decayed via positronium formation rather than in flight), they found a minimum at $f = 1.0$ (ie. 100% via positronium). This result, if correct, would mean that 75% of positrons in the source decay to the 3-photon continuum and 25% to the 511 keV annihilation line. A result of $f = 0.0$ would have meant that all positrons would have decayed into the line.

If this all came from the Galactic Centre at 10 kpc it would require 8.1×10^{42} annihilations s^{-1} at $f = 0.0$ (the luminosity would be 1.4×10^{37} erg s^{-1}). If we accept that $f = 1.0$ then only 2.5×10^{43} annihilations s^{-1} are required.

21–22 November 1977, UNH

This flight of the University of New Hampshire large NaI(Tl) detector was described by Dunphy et al. (1981) and by Gardner et al. (1982). The latter report actually discussed the 511 keV result. On the first day of observation 9 hours of data were accumulated with the Galactic Centre within the field of view. This was whilst the telescope axis was pointed in three different directions, presumably to make observations of other suspected sources. Background data were then accumulated whilst the Galactic Centre was below the horizon. This was followed by an 8 hour drift-scan of the source on the second day.

Evidence for 511 keV emission with a flux of 40 ± 6 photons m^{-2} s^{-1} was found. The exact flux value is dependent on the assumed positronium fraction.

HEAO C-1

HEAO C-1 observations of the Galactic Centre region are described in Riegler et al. (1981) and Riegler et al. (1985). Data collection and flux analysis are reported in the first paper, with further interpretation given in the second. The data were recorded in September and October 1979, and March and April 1980. There were two classes of data:

(i) 'Nominal' scans within approximately 10° of the Galactic Centre.

(ii) Scans along the galactic plane. These were conducted on 27 September for 14 days, and then from 4 March to 4 April, 15 days were accumulated interwoven with nominal scans.

Unfortunately HEAO C-1 suffered from large orbital variations in the intensity of the background 511 keV feature. Accordingly three different analyses were used:

(a) Correction for the magnetic latitude effect on the 511 keV flux by an empirical fit.

(b) Subtraction of background on a scan-by-scan basis.

(c) Accumulation of a PHA spectrum for each scan angle (×4 detectors and the sum). A net 511 keV signal was derived from the difference between 511 keV channels and adjacent PHA channels.

All three were found to be in agreement and (c) was used to derive the reported flux values.

Method (c) gives an array of 511 keV flux values versus scan angle (galactic longitude). This array was then fitted by looking for features similar to the instrument's 1 dimensional angular response function. When applied to the Autumn data, this gave a best fit of $\chi^2 = 1.36$ per degree of freedom to a flux of (18.5 ± 2) photons $m^{-2}\,s^{-1}$ from galactic longitude $l^{ii} = 3°.9 \pm 4°.0$ assuming a point source. The net source spectrum for the Autumn 1979 data is shown in figure 3.12. The equivalent data for Spring, however, showed a corresponding flux of (6.5 ± 2.7) photons $m^{-2}\,s^{-1}$, a $3.5\,\sigma$ decrease of (12 ± 3.5) photons $m^{-2}\,s^{-1}$. For the Autumn data the intrinsic line width was $1.6^{+0.9}_{-1.6}$ keV. The Spring and Autumn accumulated galactic plane scans are shown for comparison in figure 3.13.

Single scan values with Compton scattering contributions removed were subsequently fitted with a four-component model comprising:

(i) An inverse power law continuum from known hard X-ray sources.

(ii) An orthopositronium (3-photon decay) continuum.

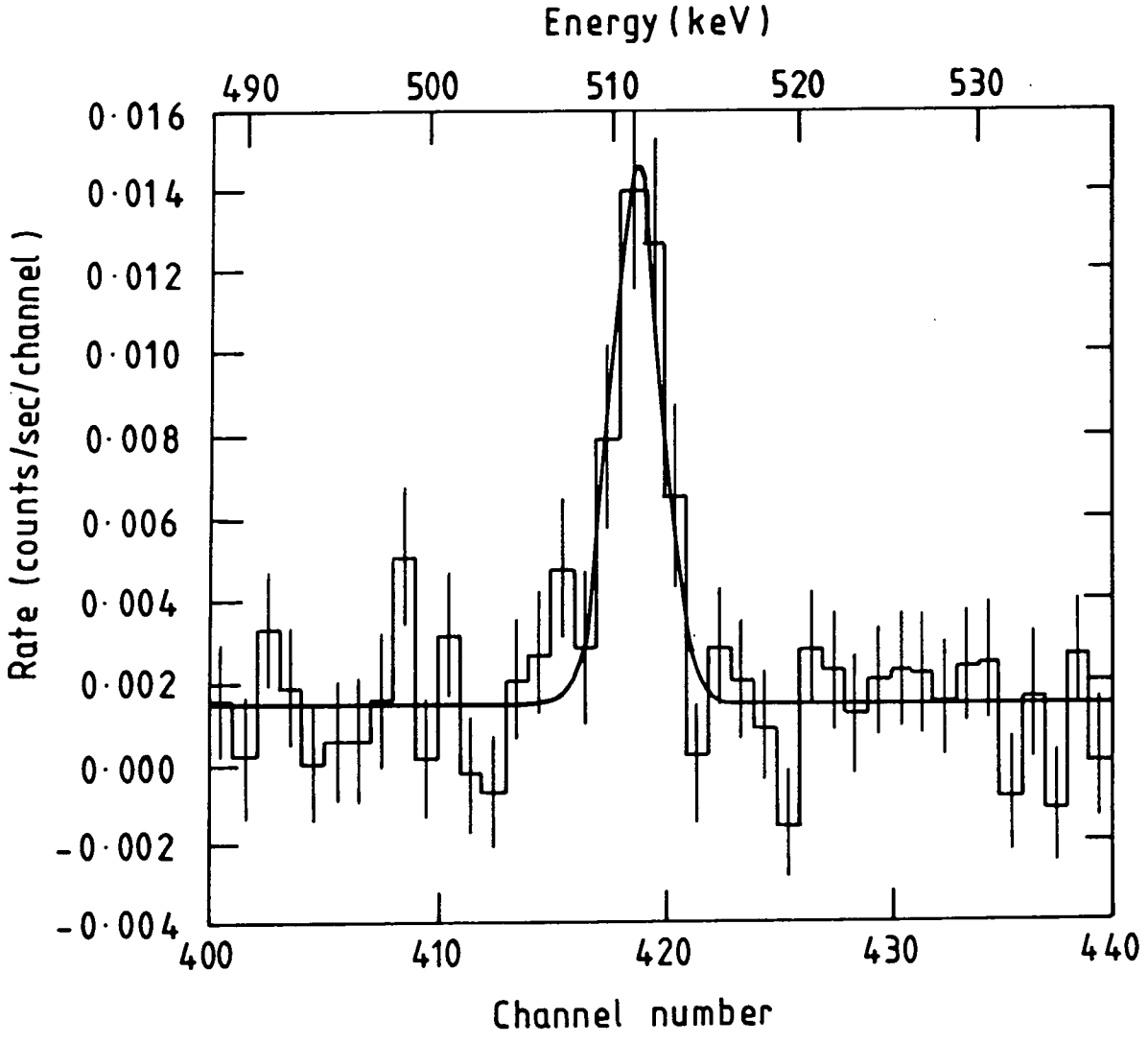

Figure 3.12 HEAO-C Autumn 1979 observation of annihilation radiation from the galactic centre. Net source spectrum. (Riegler et al., 1981)

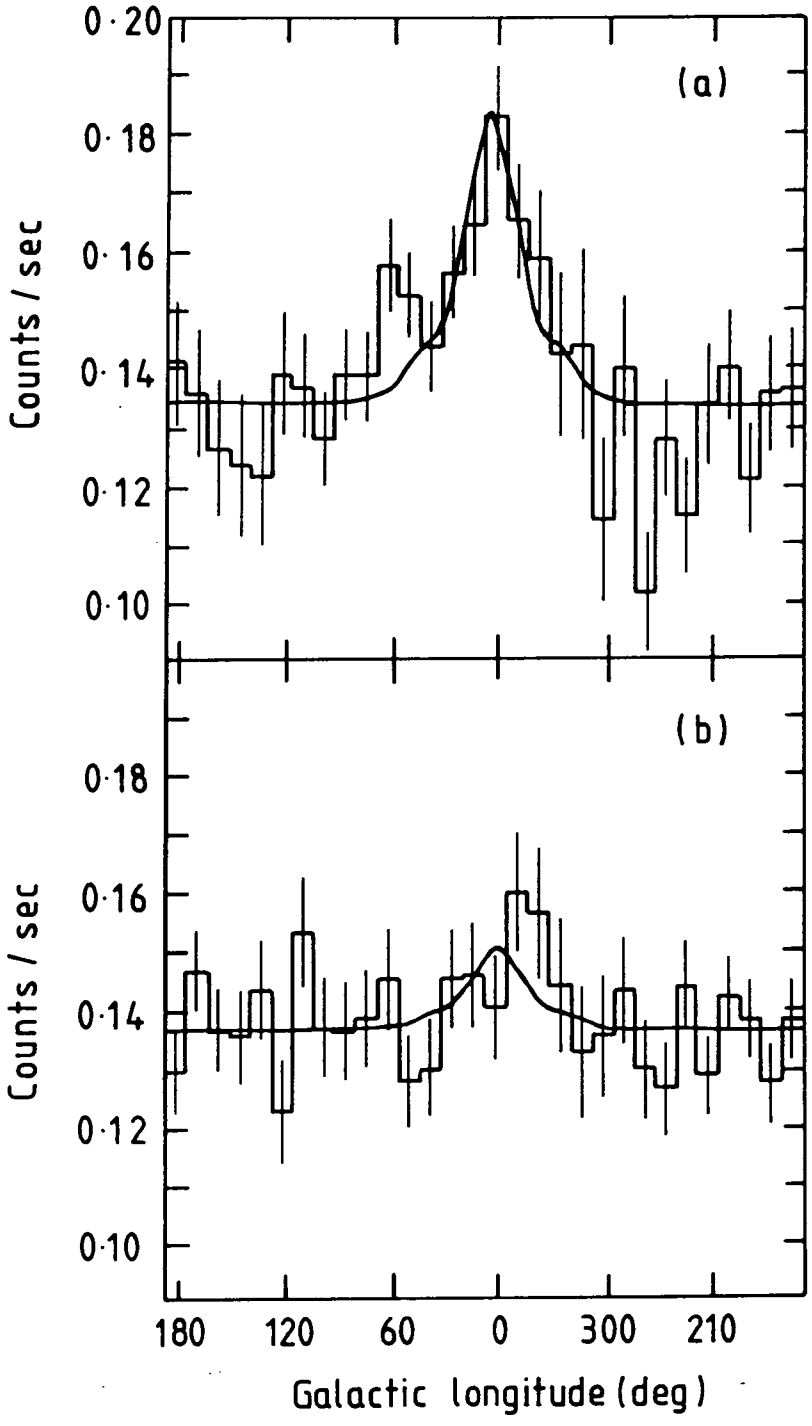

Figure 3.13 HEAO - C total galactic scans of 511keV line flux for (a) Autumn 1979 and (b) Spring 1980 (Riegler et al., 1981)

(iii) A 511 keV line.

(iv) A hot plasma comptonized thermal emission spectrum.

From fits to Spring and Autumn data, which are illustrated in figures 3.14 and 3.15, it was concluded that

(1) The high energy (> 511 keV) luminosity had decreased.

(2) The intensity of the 511 keV line intensity had decreased.

(3) The positronium fraction for Autumn 1979 was $f = 0.39$.

20 November 1981, LEGS (coaxial)

Paciesas et al. (1982) describe this flight of the LEGS (coaxial variant) instrument. A pointing system malfunction during the Galactic Centre meridian transit forced a switch to drift-scanning, although 'normal' operation (20 minute target-background alternation using 180° azimuthal offset) resumed later. 2 hours 15 minutes of normal were followed by 3 hours 50 minutes of drift-scan, and then a further hour of normal observation.

The drift-scan data were divided into 20 minute intervals which were individually compensated for the azimuthal dependence of collimator transmission.

Although continuum emission was detected at energies > 100 keV, no line flux was seen at 511 keV. The continuum emission was expressed by the authors in the form

$$\frac{dN}{dE} = A\left(\frac{E}{100}\right)^{-\alpha}, \tag{3.2}$$

where E is the energy in keV, $A = (1.9 \pm 0.4)$ photons $m^{-2}\,s^{-1}$ and $\alpha = 2.35^{+0.5}_{-0.4}$. The 98% upper limit on 511 keV line emission was given as 12 photons $m^{-2}\,s^{-1}$.

21 November 1981, BS3

This flight is described by Leventhal et al. (1982) (note that it was nearly simultaneous with the flight of the GSFC LEGS instrument on 20 November 1981 reported by Paciesas et al. 1982). 15 minute target-background alternation was used with 180° azimuth reversal for a total observation of 7 hours.

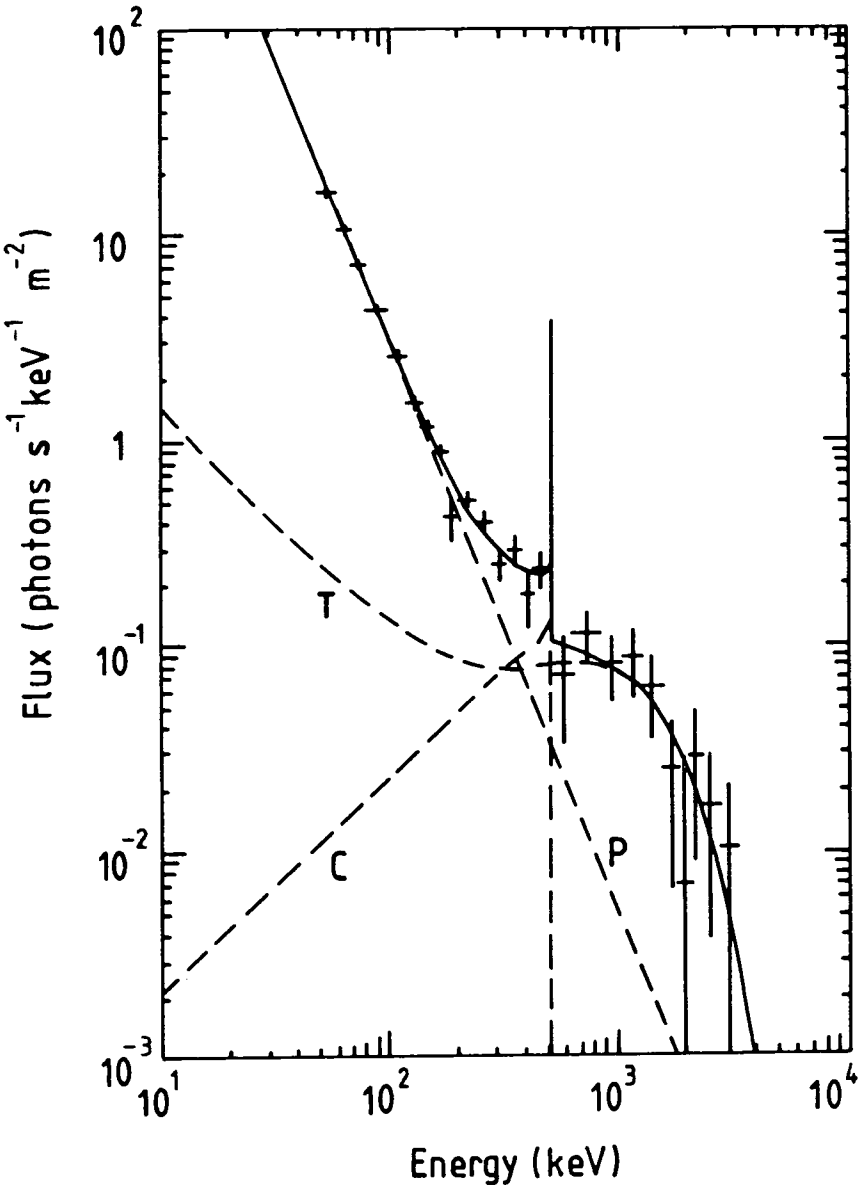

Figure 3.14 HEAO - C Autumn 1979 Galactic centre observation. Data points between 500 and 520 keV were omitted for clarity. Solid line: best-fitting four-component spectrum. Broken lines: orthopositronium continuum (C), power law (P), and thermal spectrum (T) components. (Riegler et al., 1985)

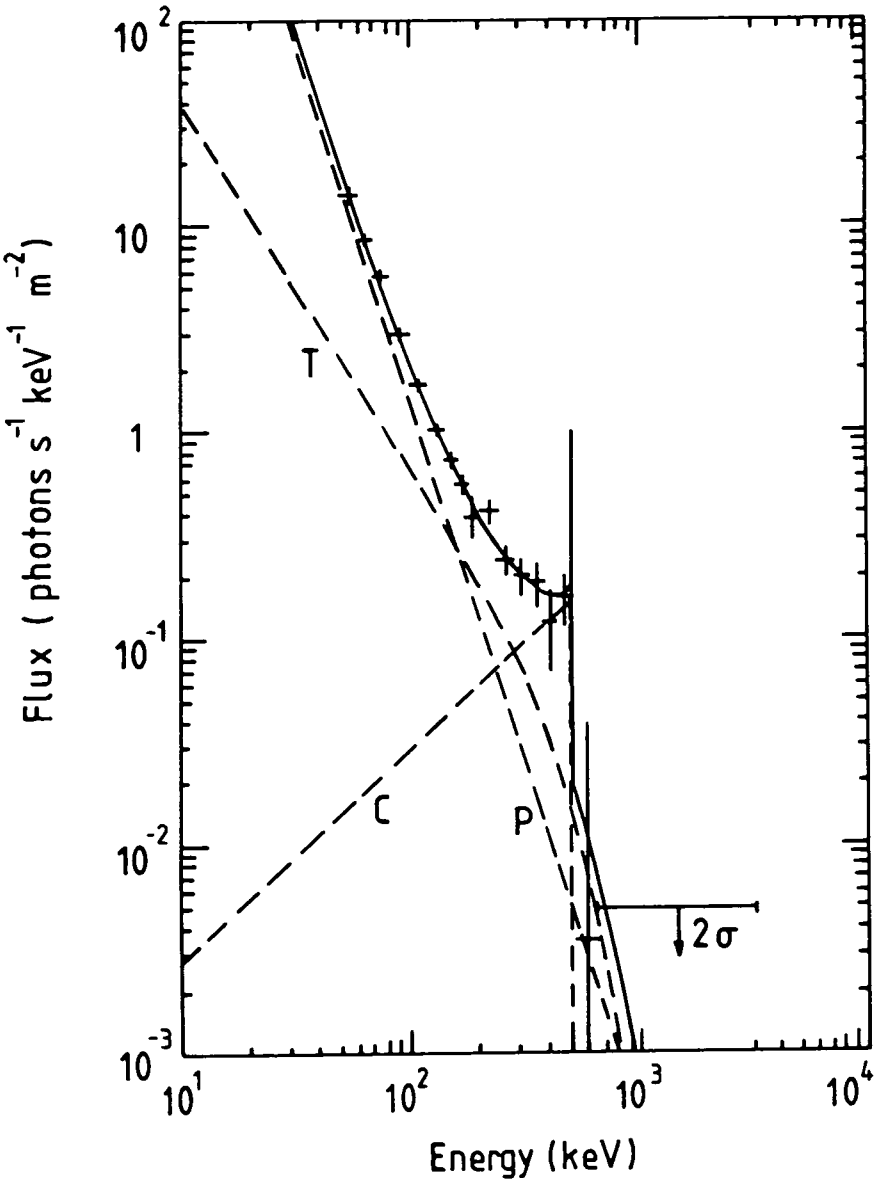

Figure 3.15 HEAO - C Spring 1980 Galactic centre spectrum. Fit as figure 3.14 (Riegler et al., 1985)

The best fit to the Galactic Centre 511 keV flux was in fact zero. A $1\,\sigma$ upper limit of 3 photons $m^{-2}\,s^{-1}$ was calculated.

20 November 1984, BS3

This flight was described by Leventhal et al. (1986). 7.5 hours of observation were obtained. The observation was divided into source and background segments by a 180° azimuthal reversal every 15 minutes. The flux at 511 keV was found to be $(0.6 \pm 4.4) \times 10^{-4}$ photons $m^{-2}\,s^{-1}$, hence confirming the apparent "off" or "low" state.

1980–1986, SMM

The SMM spectrometer has observed the galactic plane from 1980 to 1986 (Share et al. 1988) during the annual scans of the ecliptic. The data analysis for the SMM gamma ray spectrometer is rather complicated, as described previously. By modelling the evolution of the background spectral features in the sky-viewing data and by excluding the worst effects of SAA activation, it has been possible to produce a net spectrum from the galactic plane, and to confirm this by examining the effects of earth occultation in terms of the 511 keV albedo, and the time dependent instrumental 511 keV line.

The result has been a $30\,\sigma$ cumulative detection of 511 keV flux from the Galactic Centre region, with an intensity of $21 \pm 4\,m^{-2}\,s^{-1}$, assuming a point source. The maximum year to year variation in intensity was less than 30%. Given the accumulated HEAO-C and balloon evidence for variability, this is an astounding result. To explain this, a diffuse source following the galactic CO distribution has been postulated. The SMM observation would require such a flux to be normalised to $16 \pm 3\,m^{-2}\,s^{-1}\,rad^{-1}$ at the centre. The 130° aperture of the SMM spectrometer was unable to determine whether this flux was an inherently better or worse fit to its own data than a point source. However, when this hypothetical diffuse flux was folded with the aperture responses of the telescopes which made the observations described above, then impressive agreement was obtained.

The results of this SMM analysis and corresponding predicted and measured fluxes for the other telescopes are illustrated in figure 3.16. This analysis assumed a positronium fraction of 90% which was used to adjust the UNH $\sim$32 photons $m^{-2}\,s^{-1}$. The fit to the HEAO-3 Autumn 1979 galactic plane

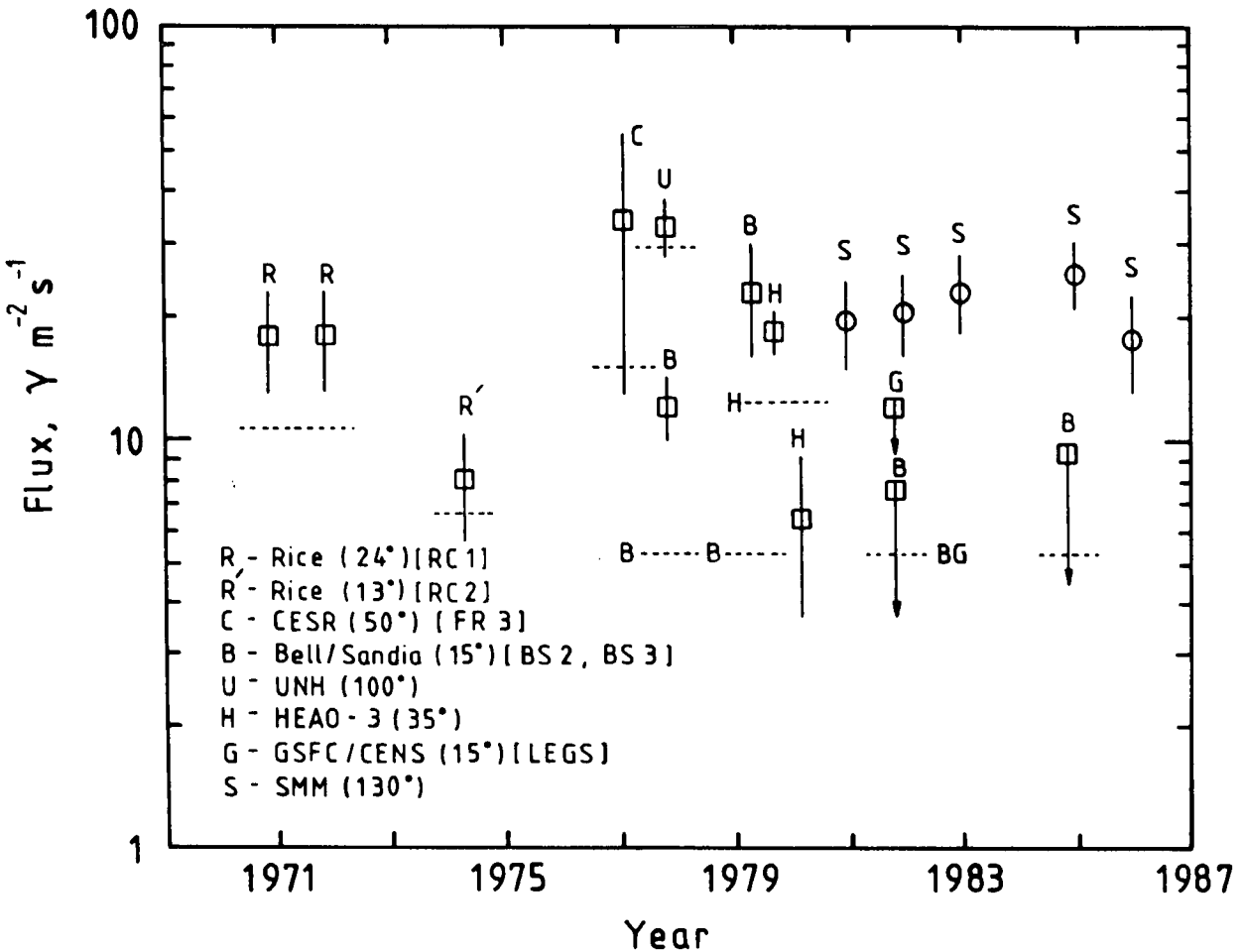

Figure 3.16 History of Galactic centre 511keV line measurements. Dashed lines are estimates of the contribution to measured intensities from a normalized distributed source proportional to Galactic CO. (Adapted from Share et al., 1988)

scans shown in figure 3.13was only marginally worse for the SMM postulated CO distribution (χ^2/DOF = 1.45) than the best fit of Riegler et al. (1981) (χ^2/DOF = 1.34). To quote Share et al. (1988): "In summary we conclude that the SMM measurements, when compared with earlier observations, suggest the presence of an intense flux of annihilation radiation distributed relatively broadly along the Galactic plane. When such a diffuse contribution to the other Galactic 511 keV observations is taken into account, the evidence for a time variable source at the Galactic Centre is weakened.".

Discussion.

The work of Share et al. (1988) has a profound effect on the interpretation of the 511 keV line. All interpretations since the HEAO-C report of flux variability have assumed a point source. The SMM report is so recent that no detailed analyses have been made in the light of the new evidence. It seems likely, in any case, that the lack of angular resolution would preclude unambiguous interpretation of the source, or indeed sources, of this radiation (see the discussion of a corresponding problem with the diffuse 1809 keV radiation by Leising and Clayton 1985). A variable point source (in addition to the diffuse flux) is not excluded, so some point source interpretations may be briefly described. However, the weakening of the evidence for such a source should be borne in mind.

Lingenfelter and Ramaty (1982) suggested that the most likely model for a compact source of positrons involved photon-photon collision, and indeed that all other mechanisms could be excluded, given the width of the line and the requirement that the production region must be optically thin. The suggestion for the compact object was a $< 500\,M_\odot$ black hole.

In interpreting the fall in 511 keV flux values, Riegler et al. (1985) proposed a model with two observed states. The first state has intense higher energy (> 511 keV) luminosity, low positronium fraction f, and intense 511 keV emission. The second has faint high energy emission, high f, and moderate 511 keV line emission. This implies a high energy luminosity source with an efficient source of positrons and substantial orthopositronium suppression. There was no high energy flux in the Spring 1980 HEAO C-1 observations suggesting that the Spring orthopositronium and annihilation line were due to previously

generated positrons. Bildstein and Zurek (1987) argued that the apparent discrepancy between the high energy and 511 keV behaviour, and that of the lower energy continuum can be reconciled by 'Cheshire cat' Compton scattering (ie. Compton scattered radiation continues to be re-directed towards earth after the source has stopped emitting) of the high energy and line emission.

Brown and Leventhal (1987) reviewed observations of the 511 keV effect and argued from their own laboratory simulations and calculations that the observed positronium fraction could be consistent with annihilation in a neutral medium. They also discuss other models involving an ionized or dusty medium.

With the advent of the SMM evidence for a diffuse origin for much — if not all — of the flux, attention has been focussed on nucleosynthetic production sites such as red giants, novae, supernovae and Wolf-Rayet stars. 15% of the observed flux can be associated with the diffuse ^{26}Al if it is assumed that 90% of the positrons from its decay (a positron is emitted in 82% of ^{26}Al decays) form positronium. ^{56}Ni is expected to be plentifully produced in supernovae and its ^{56}Co daughter decays with positron emission 19% of the time. With conventional yields of ^{56}Ni, this can account for the flux if sufficient positrons escape from supernovae and can build up a diffuse flux. Similar arguments apply to supernova production of ^{44}Ti which decays to ^{44}Sc and thence by positron emission to ^{44}Ca. Nova production of the positron emitting ^{22}Na seems inadequate if predicted yields of $2 \times 10^{-7}\,M_{\odot}$ per nova are correct. Similarly the predicted positron production from cosmic ray interactions with the interstellar medium can account for no more than 5% of the flux (Ramaty, Kozlovsky and Lingenfelter 1979).

3.5.3 Galactic ^{26}Al.

A diffuse source of 1809 keV line emission attributable to ^{26}Al has been strongly indicated by the HEAO C-1 and SMM satellite spectrometers. Balloon results from the MPI double-Compton telescope whilst confirming flux suggested a point-source origin. However in a retrospective analysis of previous balloon flights, the Bell-Sandia group found supporting evidence for the diffuse emission model.

This discovery of this line flux has strong implications for theories of

nucleosynthesis, though no clear interpretation has emerged.

HEAO C-1

Mahoney et al. (1984) report the discovery of the 1809 keV emission by the HEAO C-1 high resolution spectrometer, although preliminary results had been reported earlier.

Using a scan by scan analysis of all suitable data from the mission, the authors find a $4.8\,\sigma$ excess in a narrow line at (1809 ± 0.41) keV. The Autumn 1979 spectrum in the line region (ie. before the degradation in resolution) is shown in figure 3.17. There were insufficient counts available to produce a map of the source distribution. However some distribution had to be assumed so the authors adopted the distribution of supernova remnants in the galactic disk as represented by the > 70 MeV diffuse gamma radiation measured by the SAS 2 (Fichtel et al. 1975) and COS B (Mayer-Hasselwander et al. 1982) satellites. The derived flux value of (4.8 ± 1.0) photons $m^{-2}\,s^{-1}$ should therefore be treated with a degree of caution as the supernova origin is not certain.

1980–1982, SMM

Share et al. (1985) describe the confirmation of a galactic 1809 keV line using data from the SMM spectrometer taken over the period 1980–1982 during transits of the Galactic Centre. The source spectrum ('sky-viewing') and corresponding Earth-occulted data are shown in figure 3.18. Note, the arbitrary vertical scales: at this stage in the development of the SMM spectrometer data reduction method it was not possible to define the sky-viewing continuum from earth occulted data. The systematic background variations were not sufficiently well understood. The net flux value of $4 \pm 0.4\,m^{-2}\,s^{-1}\,rad^{-1}$ was derived by subtracting the galactic anticentre sky-viewing spectrum and assuming that the emission followed the > 100 MeV galactic gamma ray distribution.

The net detection significance was $10\,\sigma$ with no evidence of time variation. The centre of the data was consistent with the centre of the emission being at the Galactic Centre. However it was not possible to resolve the source or sources. The flux, line width and energy were consistent with the HEAO C-1 data.

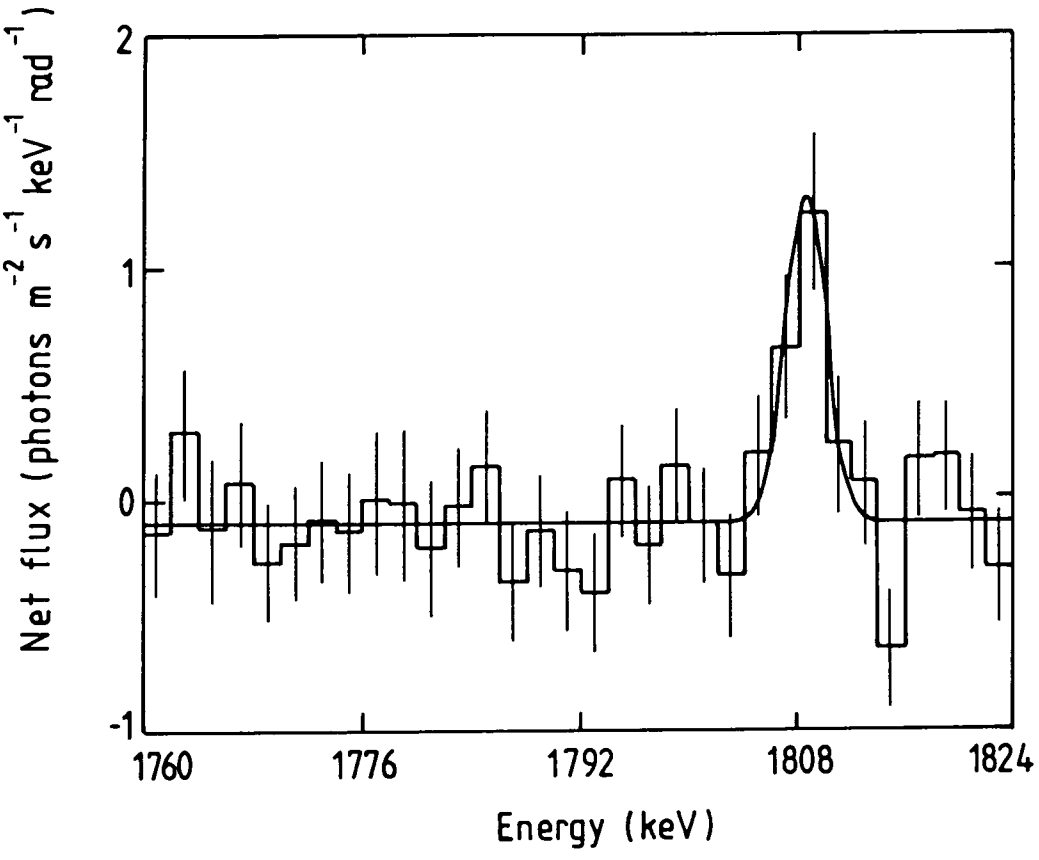

Figure 3.17 HEAO-C Autumn 1979 net galactic plane spectrum around 1809 keV. (Mahoney et al., 1984)

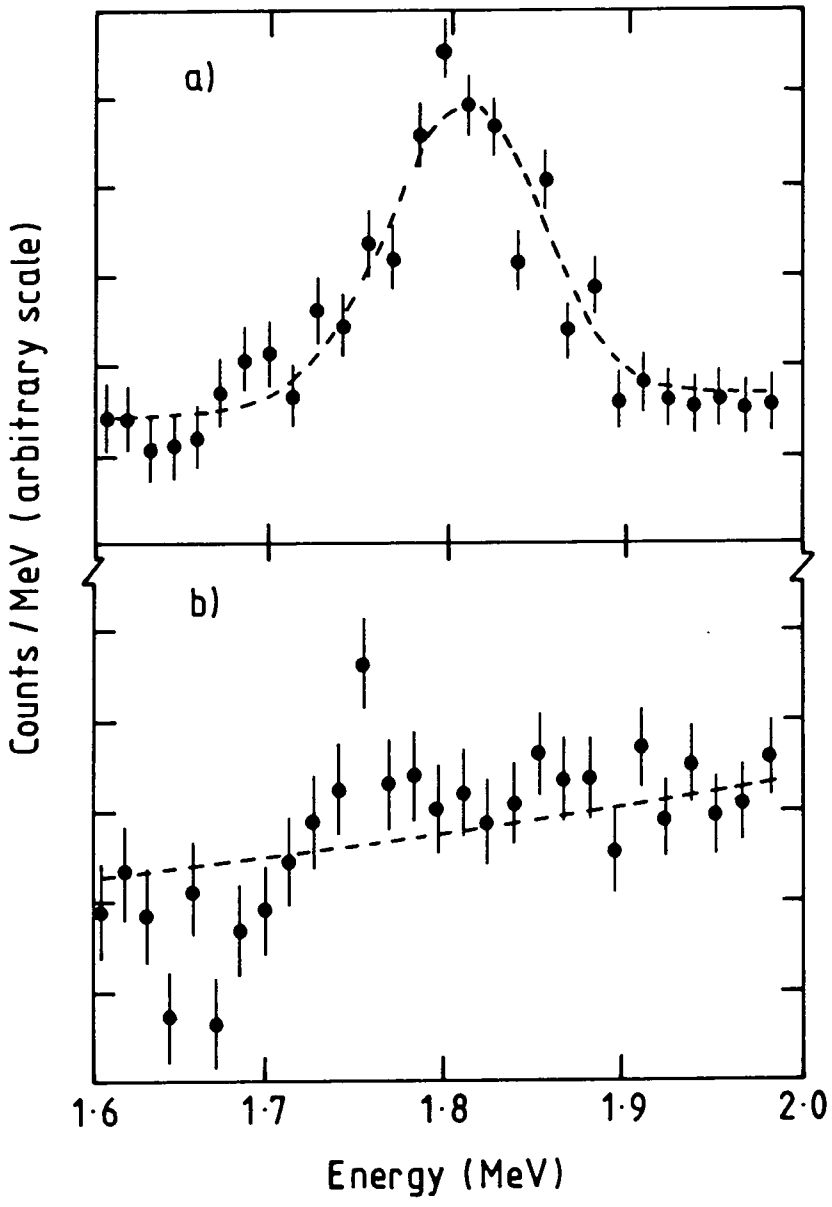

Figure 3.18 SMM net spectra from 1980 to 1983, a) sky viewing data. b) earth occulted data. (Share et al., 1985)

31 October 1982, MPI

The use of the MPI Compton telescope to map the 1809 keV line flux is described in von Ballmoos, Diehl and Schonfelder (1987). The line detection was confirmed at $3.8\,\sigma$, however the authors report that the flux distribution was consistent with a point-source at the Galactic Centre. Such a source would have produced a 10° angular profile in the MPI telescope.

1977–1984, Bell-Sandia

The Bell-Sandia group searched the data from previous flights as described in MacCallum et al. (1987) and found evidence confirming the diffuse distribution indicated by HEAO C-1 and SMM, but not supporting the point source reported by MPI.

Discussion.

The 1809 keV line corresponds to the decay of ^{26}Al. Mahoney et al. (1984) suggest a supernova origin for this line. Using the ratio of ^{26}Al to ^{27}Al suggested by Woosley and Weaver (1980) for supernova nucleosynthesis ($\sim 10^{-3}$) and making various assumptions about the ratio of solar and galactic metallicities, the authors were able to obtain a sufficient production rate of ^{26}Al to account for the line intensity. The mean lifetime of ^{26}Al is 1.06×10^6 yr so the mechanism involves the build up of ejecta from many supernovae. However the metallicity ratio suggested was not appropriate for population I stars, which are made from supernovae products, and which should therefore have been the one adopted. A shortfall of a factor of 10 in the supernova production of ^{26}Al with respect to that indicated by the line intensity is therefore possible and the deficit might be attributed to nucleosynthesis in novae or red giants.

Leising and Clayton (1985) point out that the origins of the ^{26}Al which gives rise to the 1809 keV flux cannot be unambiguously determined without information on the angular distribution. Distribution information could, for example, distinguish between Novae and Supernovae as the principal sources. This information is still not available. The authors present various models to aid data analysis and future mission planning.

3.5.4 SS433.

Some evidence of line emission from the unusual object SS433 was found by

the HEAO C-1 satellite-borne spectrometer. The observation was subsequently investigated by the Bell-Sandia group. A number of interpretations have been produced.

HEAO C-1

The original discovery of apparent emission from SS433 was reported by Lamb et al. (1983). Net spectra for SS433 from the the above dates were produced by selecting events from within $\pm 15°$ of the scan angle of the source. These data were then subtracted from a 78° wide control region.

The data were then searched by eye for line emission and the statistical significance of any excess calculated using a relative likelihood method. This involved calculating the difference ($\Delta\chi^2$) in the χ^2 of the data fits obtained using models with and without a line flux; the relative likelihood $\approx \exp(-\Delta\chi^2/2)$. The probability values obtained were reduced to take account of the number of energy bins scanned (2000) and the number of allowed line widths (10).

'Preliminary evidence' was found for a $6\,\sigma$ effect at 1.5 MeV over 18 days. There was also some evidence for emission at 1.2 MeV. Both were variable on a timescale of days. The 46 day average, respective flux values were 15 ± 3 and 11 ± 2 photons $m^{-2}\,s^{-1}$. The Autumn 1979 non-degraded line spectrum is illustrated in figure 3.19.

29 September 1983, BS3

An investigation of the HEAO C-1 discovery by the Bell-Sandia group is reported in MacCallum et al. (1985). Nine hours of observation were made using alternate 20 minute target-background segments separated using 180° azimuthal rotation. An intermittent loss of veto due to saturation of shield amplifiers by cosmic rays was corrected *post-facto* using rate-bursts to identify the non-veto 4 ms time-slices.

The data were searched using Cash's 'C' statistic (Cash 1979). Nothing was found. There were six $> 3\,\sigma$ events (as expected); the best was a $4.6\,\sigma$ event at 1298.5 keV with a FWHM of 5.4 keV. Using HEAO C-1 time-averaged fluxes, the authors expected to see the 1.2 MeV effect at $2\,\sigma$ and the 1.5 MeV at $3\,\sigma$.

The authors note that if the gamma ray line output is correlated with

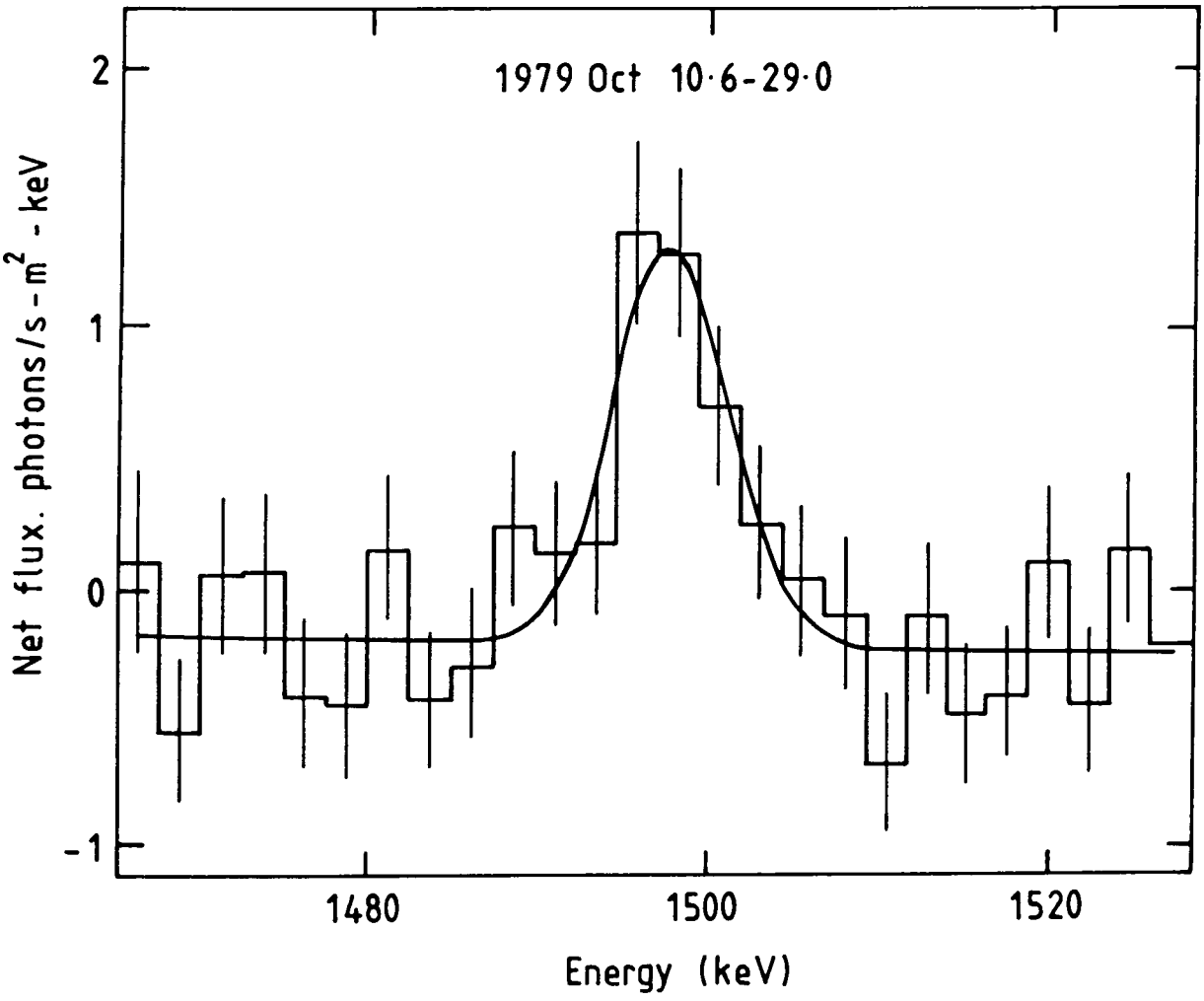

Figure 3.19 HEAO - C Autumn 1979 net spectrum from SS433. (Lamb et al., 1983)

radio flare activity then their negative result might be expected: SS433 was very radio quiescent at the time of the Bell-Sandia observation.

Discussion.
The original interpretation of the HEAO C result given by Lamb et al. (1983) was the de-excitation of $^{24}Mg^*$ populated by inelastic collision with protons in the jets of SS433. The 1.5 MeV and 1.2 MeV lines corresponded to respective blueshift and redshift caused by the motion of the opposed arms.

An alternative interpretation was suggested by Boyd et al. (1984). They questioned whether the kinetic power of the beams could produce the observed gamma ray line fluxes ($> 10^{37}$ W would be required). They considered thermonuclear reaction models and support proton radiative capture on ^{14}N as the source of the line emission. This would, however, require fairly substantial overlap of the N and H relative velocity distribution and the rather narrow resonance for this reaction.

Yet another model was proposed by Ramaty, Kozlovsky and Lingenfelter (1984). They argue that the narrowness of the observed spectral lines and the absence of other lines from abundant elements favour grains as the site of emission. Excited states of the ^{24}Mg in the grains would be populated by inelastic collisions with the ambient medium.

3.5.5 Active and mildly active galaxies and QSOs, HEAO C-1.

Two surveys of HEAO C-1 data were made in order to investigate the possibility of an extragalactic analogue of Galactic Centre annihilation radiation. Such a flux would occur with a suitable cosmological redshift from 511 keV. This would in fact generally aid detection, the redshifts are well known and, if reasonably substantial, would serve to move the line away from the strong instrumental line hence increasing sensitivity.

The first survey, of mildly active galaxies, was reported by Marscher et al. (1984). This covered M81/M82, NGC4278, M104, NGC6500, NGC2911 and NGC262. The second, described by Wheaton et al. (1987), investigated NGC1068, NGC1275, NGC4151, 3C273, M87 and Cen A; this was a selection of more strongly active galaxies and QSOs.

Both surveys used the scan-by-scan technique on data obtained during the HEAO C-1 survey. This was used to derive upper limits on the fluxes from these sources, in no case do the authors claim a positive detection.

Mildly active galaxies.

The reasoning behind the first selection was that if positron production is linked to relativistic electron production, then 511 keV flux should scale linearly with synchrotron radio emission. The candidate source must therefore have a suitably intense non-thermal radio source. However the source must be compact and confined to the central regions of the galaxy. If it were too extended then positrons might be able to escape without annihilating sufficiently promptly. That is, the positron cooling and hence annihilation timescale might exceed the lifetime of the activity (say a few M yr), no steady state of production and annihilation would be reached, and the observed 511 keV flux would be reduced from the expected value. This criterion ruled out intensely active galaxies and QSOs and prompted the selection of galaxies of intermediate activity.

The first survey gave 98% confidence level upper limits of < 7.9 photons $m^{-2} s^{-1}$. If the scaling law had been correct then each source would have produced fluxes between 2 2 and 3 9 photons $m^{-2} s^{-1}$. The investigators suggest a number of possible explanations:

(1) The approximations used in deriving the scaling law were invalid, this might be resolved by more accurate radio mapping.

(2) The time variability of the Galactic Centre placed the flux at an infrequent 'high', so the value was incorrect for general scaling.

(3) Positron production is in fact decoupled from relativistic electron generation.

(4) A steady state of production and annihilation of positrons has not been attained.

(5) There is an evacuated region around the active centre so the positrons must travel a long way before annihilating.

Strongly active galaxies and QSOs

The second survey produced a series of 2σ upper limits which were $<$ 6.2 photons m^{-2} s^{-1}. Of particular interest here is of course the observation of NGC1275, for which evidence of 511 keV emission is presented in chapter 5. Remarkably, the HEAO C-1 group do observe an excess flux but it is at $\sim$502$-$510 keV, a little higher than the predicted redshifted line centre at 502 keV. The net spectrum in this region, and a fit to an apparently non-existent line at 502 keV, are shown in figure 3.20. To quote the authors: "The positive fluxes observed for NGC1275 and NGC4151 near 511 keV would perhaps be of greater interest [than NGC1068], although still not compelling, but appear at incorrect energies.".

The excess is in two bins from 502$-$508 keV with fluxes of $\sim(.5 \pm .2)$ and $\sim(.3 \pm .3)$ photons m^{-2} s^{-1}. In describing the data reduction method, the authors make the following specific point: "Because the data for NGC1275 spanned a time interval during which the scan plane moved a large distance, the analysis for this source only was broken down into segments with sources [for scan-by-scan modelling] chosen for each as necessary to avoid interference.". It is tempting to speculate whether these procedures could produce the energy shift from the predicted value (and indeed the reduction in flux compared to the Durham results). This source will be discussed further in chapter 5.

3.6 Summary.

Although direct quantitative comparison of the results of gamma-ray line astronomy experiments is difficult, particularly where line-scanning techniques have been employed, there does now seem to be strong evidence for the following:-

i) Positron-electron annihilation radiation from the galactic plane.

ii) A diffuse source of 1809 keV radiation from ^{26}Al in the galactic plane.

iii) A time (and possibly energy) variable line at 73$-$80 keV from the Crab Nebula region, very probably from PSR0531+21.

The other confirmed or individually strong results from the Crab at $\sim$400 keV and from SS433 must probably await further observation, preferably

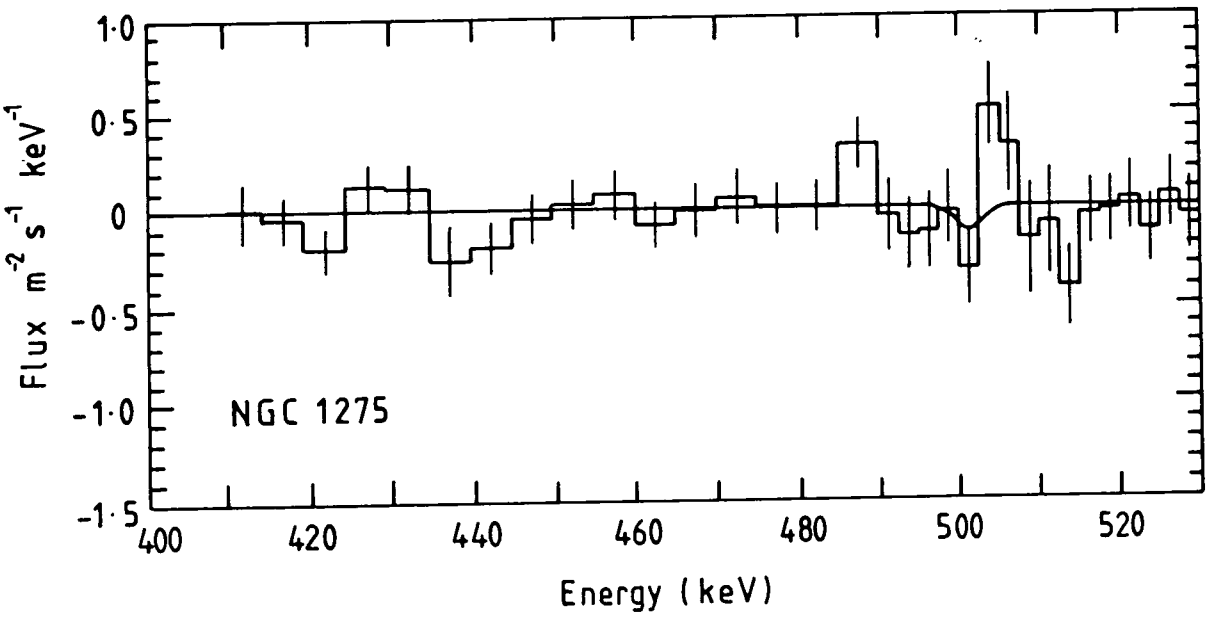

Figure 3.20 HEAO - C observation of NGC1275.(1979 - 1980)
(Wheaton et al., 1987)

with improved instrumental sensitivity, spatial resolution, background control, and some reasonably standardised method of source observation and data analysis.

Chapter 4.

The Durham Mk. 1B telescope and 1981 flight.

4.1 Introduction.

The Durham gamma ray telescope was designed for high spectral resolution gamma ray spectrometry of compact sources in the approximate energy region 50 keV to 10 MeV. Accordingly, an actively shielded, cooled semiconductor detector was employed to provide superior energy resolution (2.52 keV at 1.33 MeV), and also to provide suppression of Compton spectral background.

A relatively small aperture (4.78° geometrical) was used so that sources could be studied in reasonable isolation, and so that background could be sampled close to the source. The latter capability is important as it may be used to reduce the systematic temporal and sky background variation effects which hinder observation with this class of telescope. Background/source observation switching may be done more rapidly, hence reducing the effect of temporal variation and the loss of data during slewing. When an azimuthal scan technique (ie. moving the telescope between source and background by azimuthal variation alone) is used together with an aperture response function cross-correlation data reduction method (Hermsen 1980), then a degree of source imaging is possible (~5° FWHM). Crude this may be, but it would have been sufficient to overcome the inability of wider aperture telescopes to distinguish between a novae or supernovae origin for the 1809 keV line from galactic ^{26}Al (Leising and Clayton 1985). The disadvantage with respect to, say, a 30° aperture telescope is simply that the telescope pointing system must be more accurate.

The design of the data aquisition system allowed for studies of source spectra and also of the shielding mechanism and instrumental background. This was made possible by the selective telemetry transmission of coincident shield spectra as well as un-vetoed central detector events.

The telescope was intended for use with stratospheric balloons, so a gondola with suitable pointing direction controls, payload insulation and protection was constructed. Electronic circuits, actuators and transducers for data transmission, remote control and payload monitoring, respectively, were also built.

Current balloon technology allows payloads in excess of 1000 kg to maintain altitudes greater than 35 km for periods longer than 24 hours. There is, however, considerable uncertainty in the flight duration which is most frequently limited by geographical drift of the balloon. This may cause either an encounter with a national border or a loss of communication between balloon and tracking station.

The Durham 1A detector flew as a balloon payload from the National Scientific Balloon Facility (NSBF) in Palestine, Texas, USA in 1979 and suffered some minor damage on landing. Ayre et al. (1981) describe some aspects of this early flight. The detector and balloon gondola were modified significantly on return to Durham. Refinements were also made to the data acquisition strategy and to the associated electronics. The new 1B detector was mounted on a redesigned alt-azimuth platform capable of being steered to a precision of 10 arcminutes in azimuth and 0.25° in zenith.

The telescope, it s auxiliary systems, and the details of the 1981 flight at NSBF, from which the data in this thesis were derived, are discussed in the remaining sections of this chapter.

4.2 The Durham Mk. IB spectrometer components.

The spectrometer comprises an intrinsic, high-purity, germanium (Ge(Hp)) detector in an active sodium iodide, (NaI(Tl)) shield. A cross sectional view of the spectrometer is shown in figure 4.1. The collimator and the side and rear elements of the active shields are viewed by a total of 10 photomultipliers. The spectrometer is symmetrical about its central axis.

4.2.1 The Ge(Hp) detector.

The central intrinsic Germanium crystal, its container, cryostat, dewar and pre-amplifier, form a single unit. This was manufactured by Princeton Gamma Tech (PGT), Princeton, New Jersey, following a design specified in Durham. The position of the pre-amplifier is unusually far from the detector in order to accommodate the close-fitting shielding array. No increase in the noise level over that found with a conventionally positioned amplifier was encountered when the amplifier was moved to this relatively distant position from the Ge(Hp)

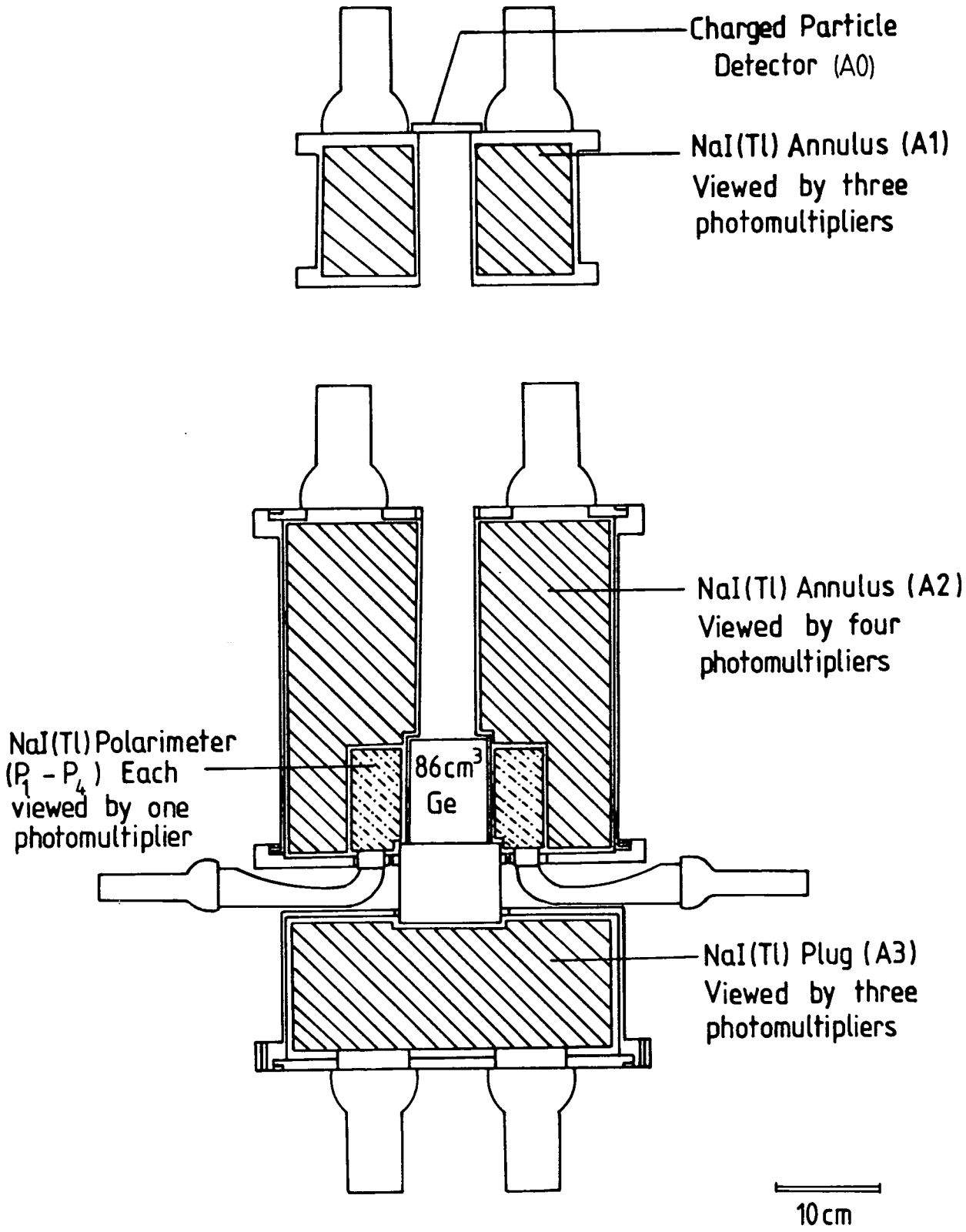

Figure 4.1 Cross-sectional view of the Durham MK.1B gamma ray telescope.

crystal.

Ge(Hp) was employed in preference to Ge(Li) because it does not suffer damage if allowed to warm up to around 20°C, an occurrence which is very likely during payload recovery.

A cross-sectional view of the Ge(Hp) crystal and its containment is shown in figure 4.2. The coaxial, right-cylindrical, 0.086 l crystal was thermally coupled to an enclosing aluminium can. Electrical connection was made to the central electrode by a lead passing through the wall of the can and then along the centre of the cold finger containment tube to the FET input stage of the pre-amplifier. The vacuum cryostat, also aluminium, enclosed the inner can and provided some external protection.

The EHT bias used for the detector was 3.8 kV. This gave a FWHM (full width at half maximum) resolution of 2.62 keV at 1.33 MeV and a detection efficiency of 23% relative to that of a 76.2 mm by 76.2 mm right-circular cylinder of NaI(Tl) irradiated by a point source, on the axis 250 mm from the top surface. The cryogenic system could maintain a crystal temperature of less than 135 K for a 10 day period following the filling of the liquid nitrogen dewar.

The detection characteristics are discussed further in section 4.3.

4.2.2 The Anticoincidence shields.

The anticoincidence shield consisted of units of NaI(Tl): A1, A2, and A3, P1, P2, P3 and P4, manufactured by *Harshaw Chemie BV, Stnijkvientel 67, DeMeeon*, Netherlands. Each detector comprised a crystal, hermetically sealed inside an aluminium can (this prevents hygroscopic dissolution of the NaI) with optical windows to allow the photomultipliers to view the NaI(Tl). The choice of NaI(Tl) scintillator was influenced by its relatively high light output, low self absorption of scintillation photons, good temperature stability and low decay time constant (compared to other inorganic phosphors). Particularly important considerations were cost and a high cross-section for gamma ray interactions.

A0 charged-particle shield.

The charged particle event rejection shield A0 was a circular disk of Nuclear Enterprises NE102a plastic scintillator 75 mm in diameter and 3 mm thick.

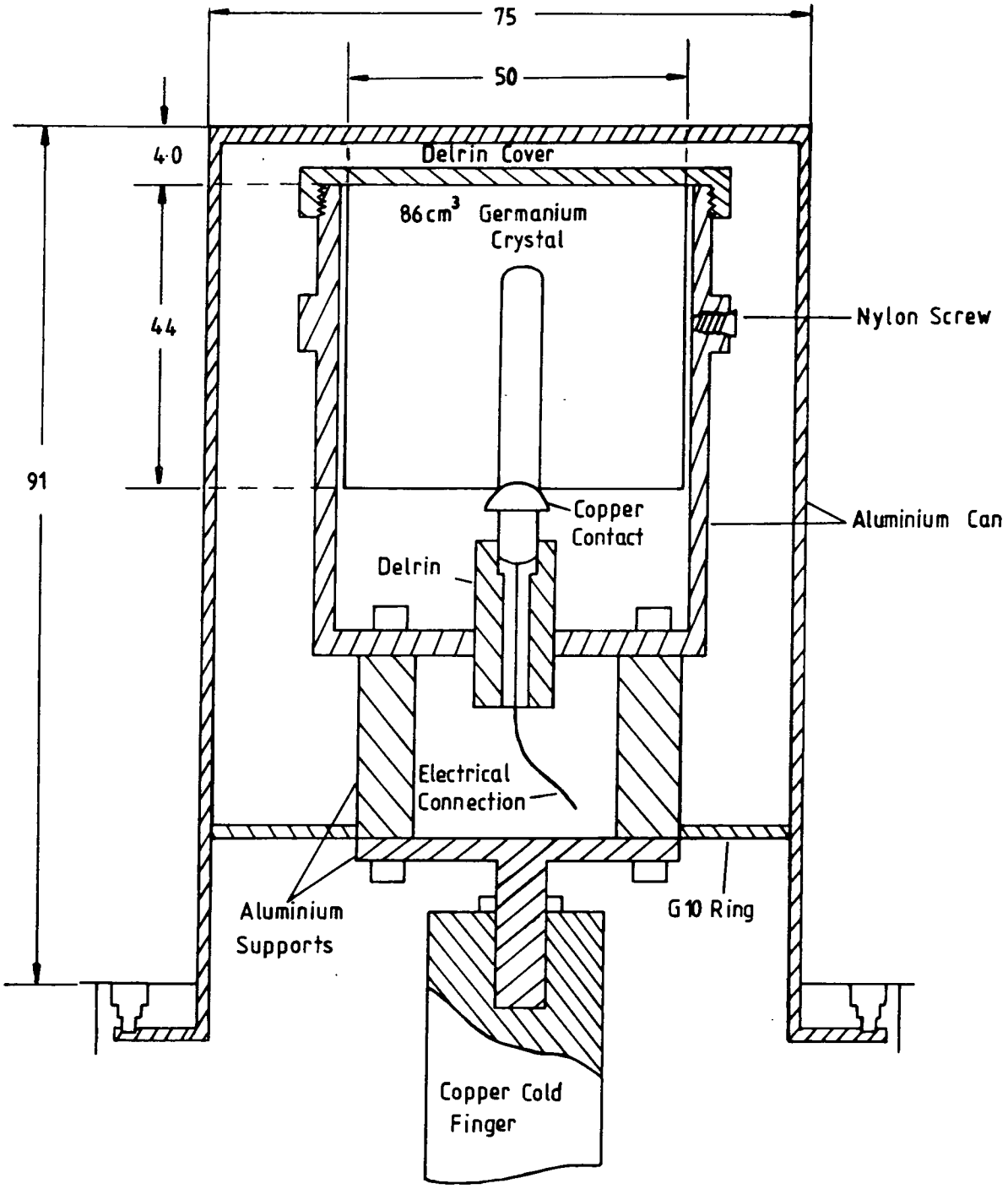

All dimensions in mm.

Figure 4.2 A cross-sectional view of the Germanium detector cryostat.

It had a high cross-section for charged-particle detection and a low cross-section for gamma ray photons of energy greater than 50 keV. The main data acquisition system was in anticoincidence with this unit. It therefore acted to reject coincident triggers produced in the Ge(Hp) crystal by charged particles travelling down the collimated aperture of the instrument. This unit was viewed by a single photomultiplier which was optically coupled to the scintillator by an adiabatic perspex light-pipe.

A1 collimator.

This detector was a right-cylindrical annular crystal of NaI(Tl) 225 mm in diameter and 140 mm high. An aperture, 50 mm in diameter, extended cylindrically through the crystal and defined the acceptance of the detector. The acceptance was slightly energy dependant and not sharply defined as the gamma ray photons penetrated the shield with a probability depending on their energies (see section 4.3). Three 140 mm diameter optical windows were provided through which photomultipliers might view the crystal. (See figure 4.3).

A2 coaxial shield.

This was an annular right-cylinder of NaI(Tl) viewed by four photomultipliers. The cylinder was 300 mm in diameter and 300 mm high. The bore was 50 mm in diameter, but this increased to 76 mm at 95 mm from the crystal base and again to 180 mm for the final 92 mm. As illustrated in figure 4.4, this allowed the insertion of the Ge(Hp) crystal and its encompassing polarimetry sectors.

P1–P4 polarimetry units.

These units, which were intended to detect Compton scattered photons from the Ge(Hp) crystal, were mounted around the Ge(Hp) and comprised four optically isolated sectors of an annular right-circular cylinder of NaI(Tl) (external diameter 180 mm, internal diameter 76 mm and length 92 mm). These were installed inside the A2 detector as illustrated in figure 4.4. Light-pipes guided the scintillation photons to four photomultipliers, the axes of which were orthogonal to the aperture axis of the telescope.

A3 base shield.

This was a right-circular cylinder 300 mm in diameter and 125 mm deep. On the lower face three photomultipliers were mounted and on the opposite face was a shallow circular depression to accommodate the base of the Ge(Hp) housing.

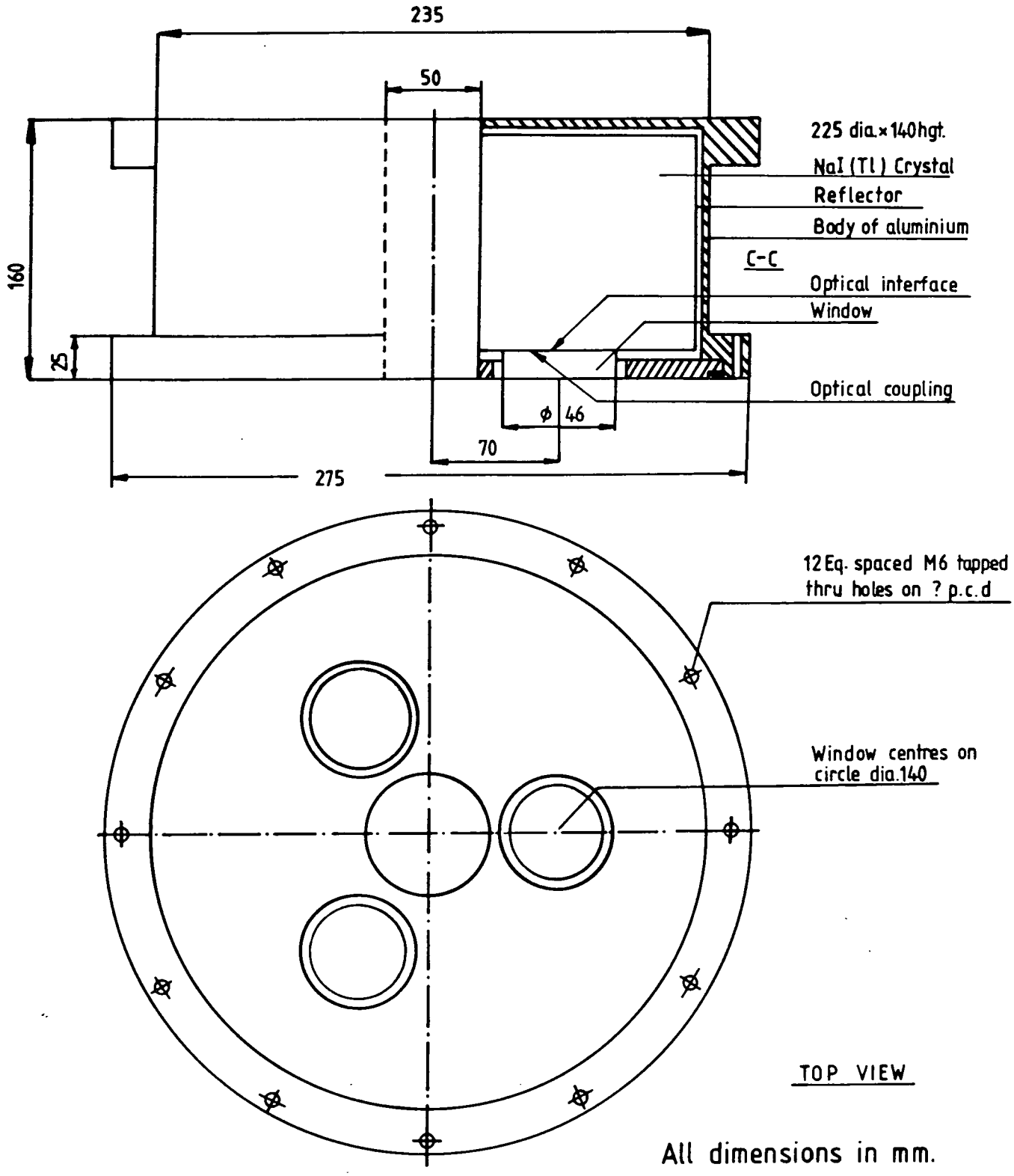

Figure 4.3 Cross-sectional view of the A1 collimating shield detector unit.

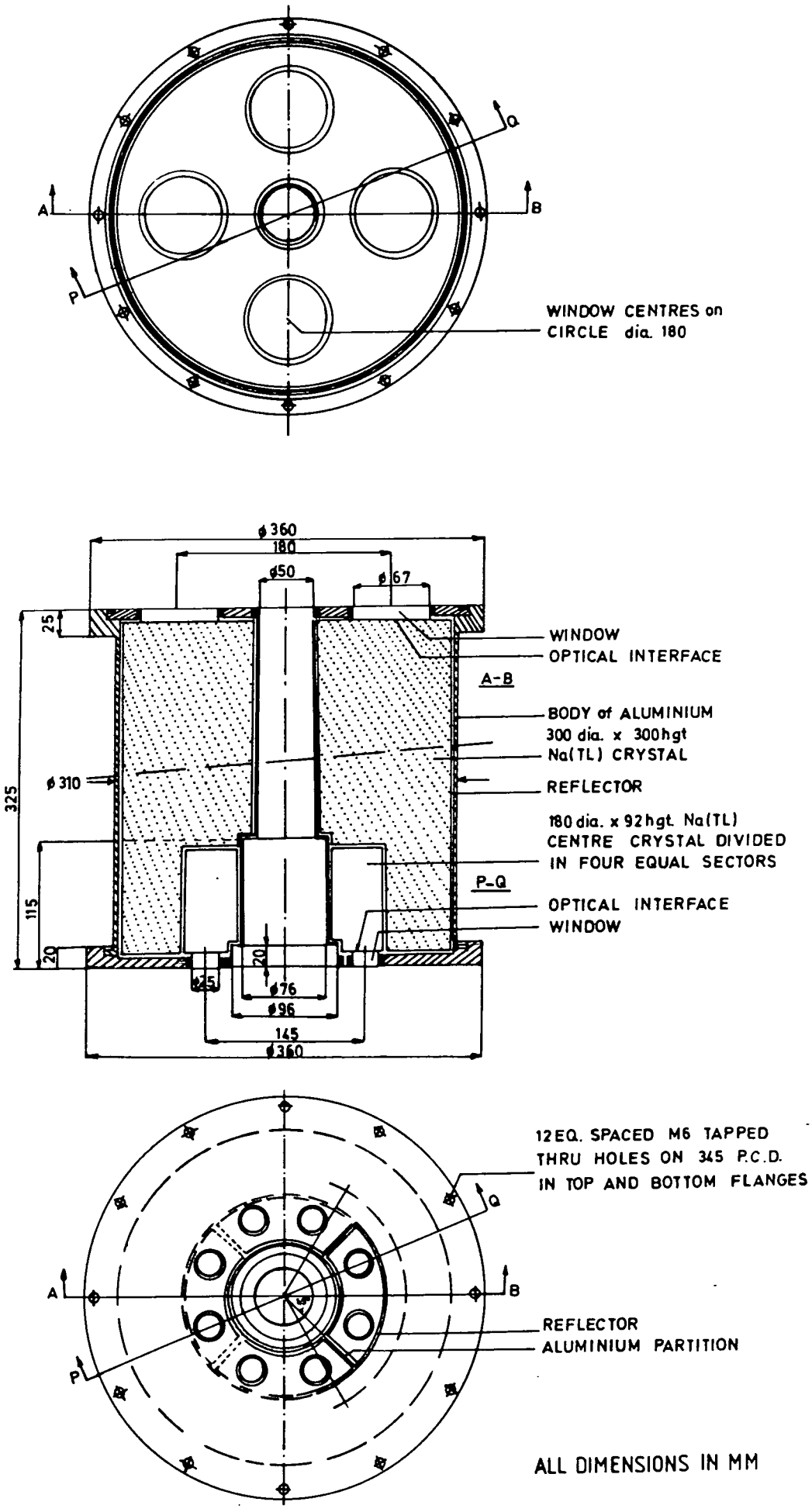

Figure 4.4 The A2 annular crystal assembly.

(See figure 4.5).

4.2.3 Photomultiplier assemblies.

The photomultipliers were mounted on to the detector windows (with intermediate light-pipes in the case of A0 and P1–P4) as individual assemblies, each including a base, dynode resistor chain, pre-amplifier and mu-metal magnetic screen. The assemblies were made light-tight and the electronics were encapsulated in silicone rubber (Dow Corning Silastic 9161).

4.2.4 Neutron shield.

The detectors A2 and A3 were surrounded by 30 mm thick paraffin wax shields containing materials with high neutron absorption cross-sections. These substances were considered unlikely to give troublesome gamma ray line emission. The reduction of the neutron flux is important because it produces activation of the detector which subsequently decays producing gamma rays which contribute to the background of the experiment.

Neutron absorption cross-sections are larger at thermal than at higher energies. The shield operated by thermalizing incoming neutrons by collisions with the nuclei in the wax, and this resulted in increased absorption of the neutrons by the added absorbers.

The collisions of the neutrons with the hydrogen nuclei of the paraffin wax are responsible for most of the neutron moderation; a 'head-on' collision with a carbon nucleus only reduces the neutron energy to 0.715 of its original value whereas a similar collision with a proton will stop the neutron. The absorption cross-section for neutrons with hydrogen is, however, very small; it is only 0.33 barns at 1/40 eV (approximate thermal equilibrium kinetic energy). Cadmium has a very high absorption cross-section but the process entails the emission of 3–4 gamma rays of total energy 9.1 MeV which would increase the background of the spectrometer. Boron, on the other hand, has a thermal neutron cross-section of 755 barns and produces stable nuclides according to the reaction

$$^{10}\mathrm{B} + \mathrm{n} \rightarrow {}^{6}\mathrm{Li} + {}^{4}\mathrm{He} \qquad (4.1)$$

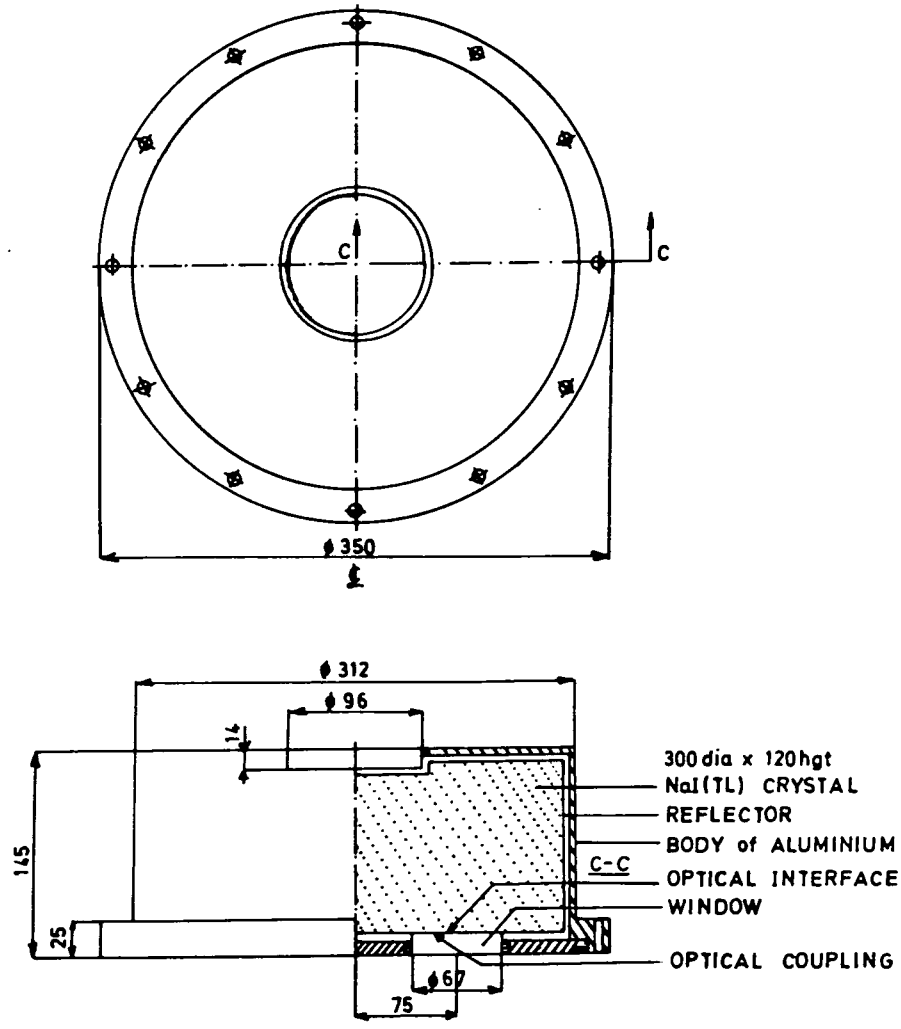

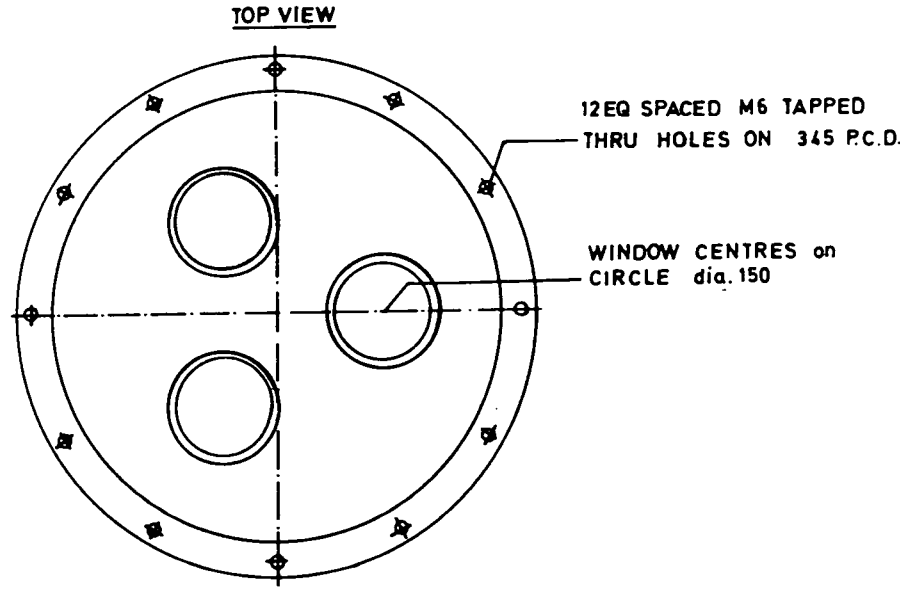

Figure 4.5 The A3 crystal assembly.

The composition finally employed was:

Compound	proportion in grams per kg of wax
Li_2CO_3	15–20
WO_3	20–25
HBO_2	20–25

Theoretical and laboratory studies using similar absorbers indicated that the 5 MeV neutron flux was reduced by a factor of 10 and the 1.8 MeV flux by a factor of 100. The performance of this shield in flight was discussed by Owens, Myers and Thompson (1985) and the conclusions are summarised in section 4.3 of this thesis.

4.3 Characteristics of the Durham spectrometer.

The responses of the Ge(Hp) detector and individual shield piece detectors together with the system aperture angular response function were measured in the laboratory, and could be checked to some extent during the flight. A series of supporting calculations were made by Summers (1983) and Owens (1985d) which are used together with the laboratory parameters in the analysis of atmospheric and astronomical data. A very full discussion of these matters is given in Owens (1985a-d) and Owens, Myers and Thompson (1986). This includes a series of calculations and simulations by Dr. A. Owens supported by data from the 1981 flight processed by the author, and laboratory measurements by the Durham group.

The use of flight data to calculate detection parameters is, of course, essential but it does anticipate somewhat the descriptions of flight data processing at the end of this chapter and in chapter 5. However this should be offset by the advantages of keeping the discussion of flight parameters alongside the discussion of physical dimensions, manufacturers specification, laboratory measurements, and simulations.

External diameter	50 mm
External length	44 mm
Operating bias	3800 V
Active volume	72.2 cm^3 (7.22×10^{-5} m^3)
Dead layer depth	1.128 ± 0.02 mm
Efficiency (at 1.333 MeV)	10.1%
Resolution (at 1.333 MeV)	2.52 keV
Effective area (at 100 keV)	14 cm^2

Table 4.1. The characteristics of the Ge(Hp) detector.

4.3.1 The Ge(Hp) detector.

The principal characteristics of the Ge(Hp) detector are summarised in table 4.1.

Ge(Hp) energy resolution.
The energy resolution may be approximated by the semi-empirical formula,

$$\Delta E(\text{keV}) = [(2.16 \times 10^{-3})E + (1.82 \times 10^{-6})E^2 + 1.042)]^{1/2}, \qquad (4.2)$$

where ΔE is the energy resolution and E is the gamma ray energy in keV. The quadratic term arises from incomplete charge collection and charge trapping. The linear term is simply the statistical fluctuation in the number of charge-carrying pairs produced. The constant represents ADC (analogue to digital convertor) channel width and electronic noise effects. Charge collection was the dominant noise contribution for energies $>$ 200 keV. For energies $<$ 200 keV electronic noise dominated; it also made significant contributions up to 1 MeV. The measured and calculated energy resolutions are shown in figure 4.6.

Ge(Hp) detection efficiencies.
Various methods for producing functional and semi-empirical fits to the measured full energy peak efficiency (FEPE) were compared. The full energy peak includes

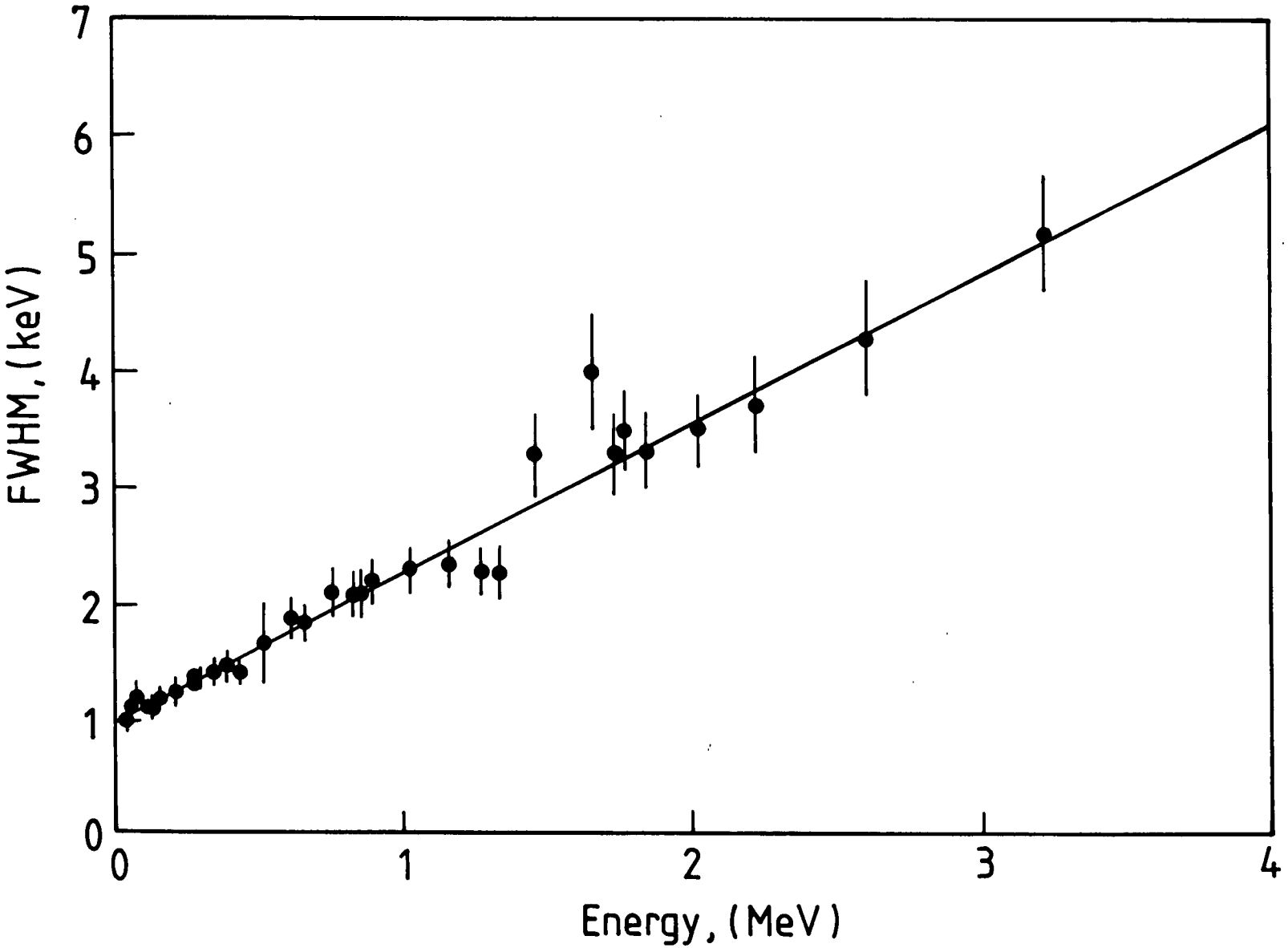

Figure 4.6 The Ge(Hp) Energy Resolution FWHM as a function of energy.

photoelectric absorption events, single and multiple Compton scattering where the final scattered gamma ray is photoelectrically absorbed, and initial pair-production events where the 'escape' photons are absorbed. The absolute efficiency is the probability of any form of interaction. This is of course not used for line studies where only full-energy events contribute. Indeed, with efficient shield Compton suppression, we shall see that it may be ignored for continuum spectra also.

A method of Hajnal and Klusek (1974) was adopted as the most satisfactory semi-empirical fit technique. This involved fitting an expression for the FEPE comprising terms for:

i) The attenuation in the detector window.

ii) The detector outer dead layer, that is the volume of Ge(Hp) at the top of detector which is not sensitive to interacting gamma rays.

iii) The total initial interaction probability.

iv) The probability of direct photoelectric absorption.

v) Single Compton scattering followed by either:

   a) Photoelectric absorption.

   b) A further Compton scatter and absorption.

vi) Pair production followed by absorption.

Some ten empirical constants were included which were determined by a fit to experimental data which yielded a minimum χ^2 of 10.6 with 13 degrees of freedom (possibly the experimental errors were overestimated, making the χ^2 a little low). The advantage of this technique is that it yields Compton and pair production cross sections as well as the initial interaction term which may be simply multiplied by the window and detector dead-layer attenuations to give the absolute efficiency.

Figure 4.7 shows the measured and calculated FEPE, together with the semi-empirically derived contributions and window attenuation. Also shown are the measured absolute efficiency and corresponding values calculated from the

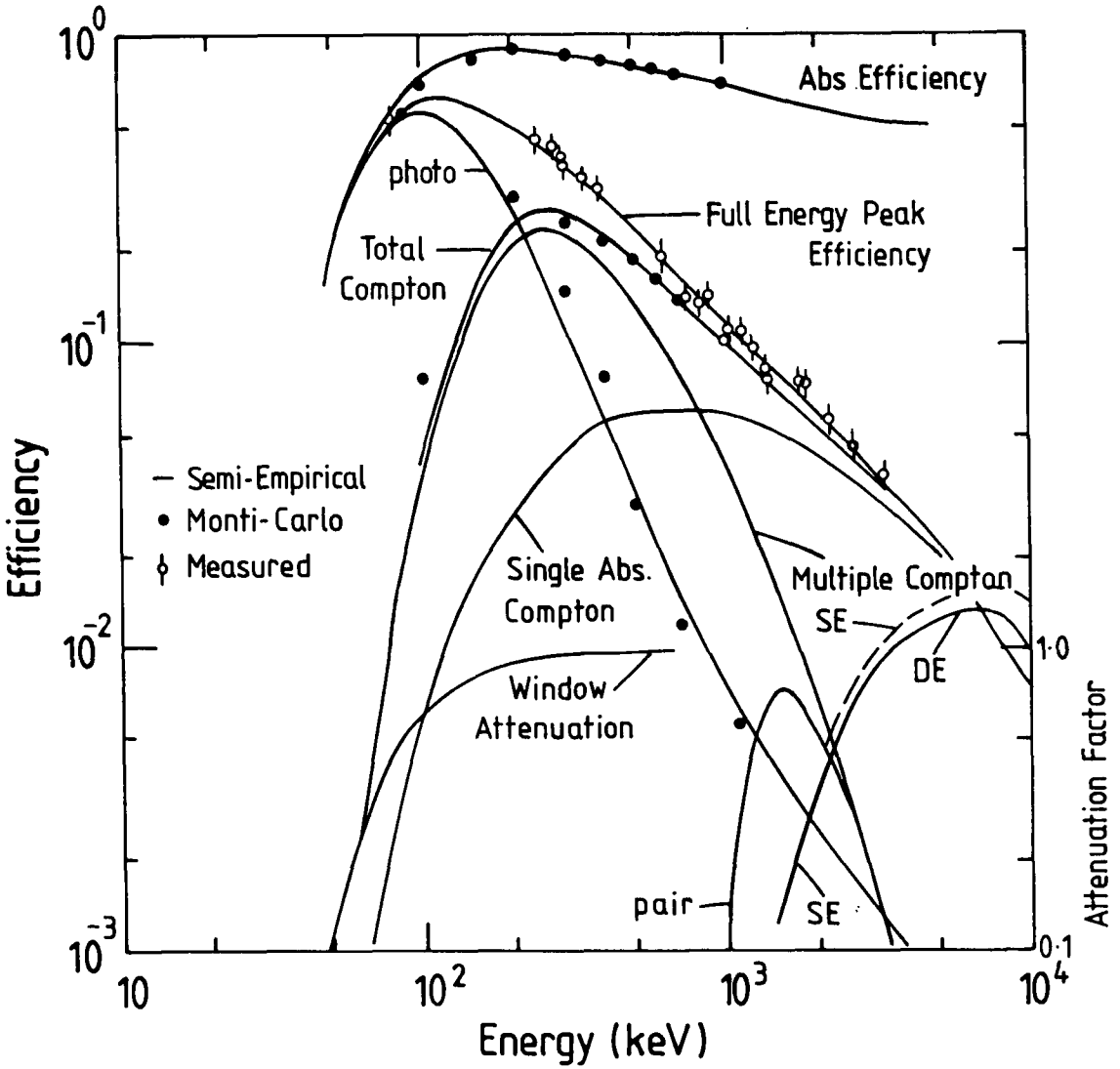

Figure 4.7 The experimental and calculated efficiencies for the MK1B telescope. Note: Photo, total Compton single absorbtion Compton, multiple Compton and pair refer to the various contributions to FEPE, SE and DE denote single and double escape peak efficiencies respectively. (Owens, 1985 d)

calculated contributions to the FEPE fit.

4.3.2 The shield pieces.

The energy resolution of A1, A2 and A3 is approximated by

$$\Delta E(\%) = 12.74 E^{-0.33}. \tag{4.3}$$

where E and ΔE are the energy resolution and gamma ray energy respectively; both are measured in keV. The measured detection efficiencies for the A2 and A3 detectors are shown in figure 4.8, which also shows calculated values based on the sodium iodide response and absorption in the aluminium casing. The polarimeter quadrant resolutions are ~25% at 662 keV. The collimator is discussed further in the context of the telescope angular response function.

4.3.3 Compton suppression in the assembled telescope.

Using the semi-empirically derived single and multiple Compton scattering cross-sections for the Ge(Hp) detector together with the 'veto efficiency' (ie. the probability of such a non-photopeak event being suppressed by detection of the scattered gamma ray in the shield pieces), it was found that for the Durham telescope, or indeed any similar actively collimated telescope having a veto efficiency $> 0.5\%$, the contribution of non-photopeak events to energy loss spectra may be ignored. This was confirmed by calculating the non-photopeak component of the Durham observation of the Crab continuum (shown in Chapter 5), which was a factor of at least 20 less than the measurement errors in the flux at all energies. The greatest relative contribution of unvetoed Compton events was at the lowest energies.

4.3.4 Effective collimator aperture of the telescope.

If the collimator (A1) were completely opaque to gamma rays, then the effective area exposed to a distant point source may be determined by a simple geometric calculation of the exposed area of the detector and a term $\cos\theta$ (where θ is the angle between the telescope axis and the source direction) to account for the projection of the illuminated area on to the perpendicular to the source direction.

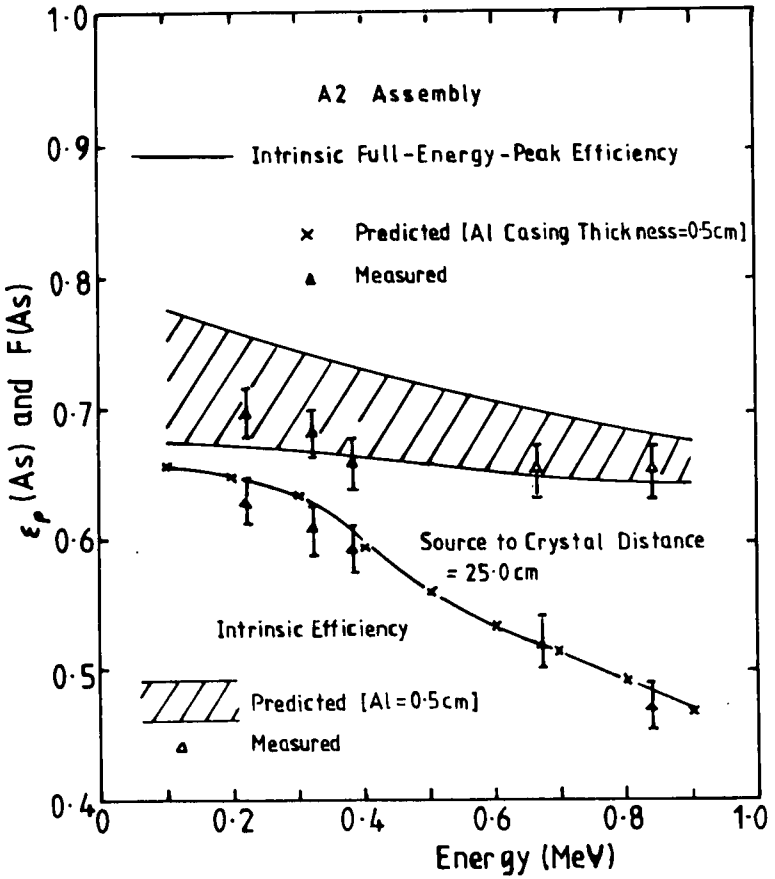

Figure 4.8 Predicted and measured values of intrinsic efficiency and intrinsic full-energy-peak efficiency for the A2 shield assembly as a function of source energy.

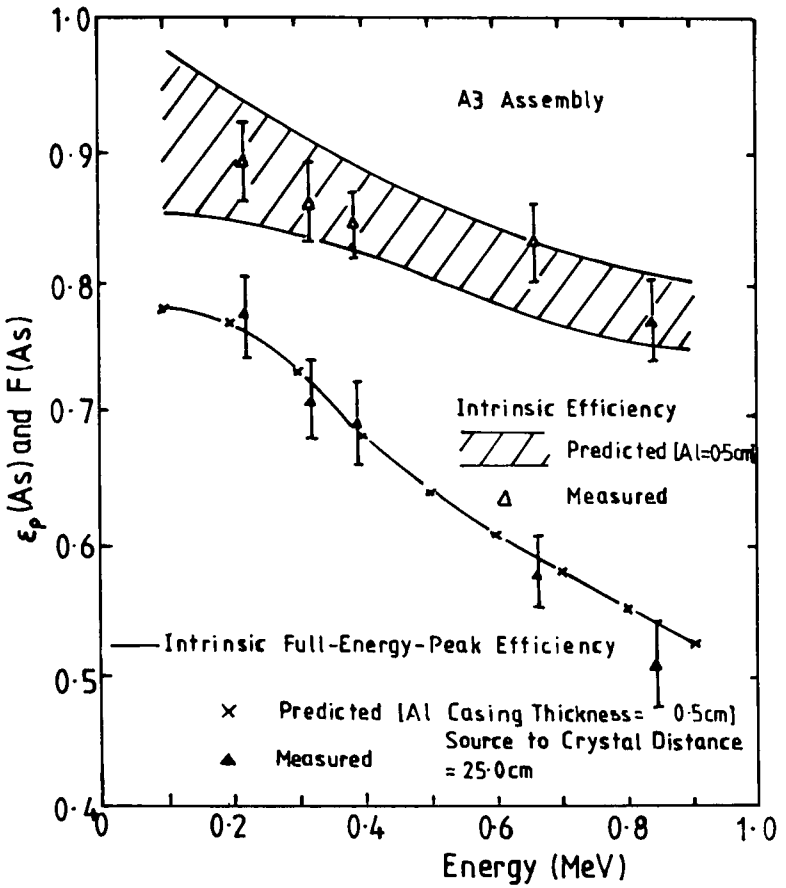

Predicted and measured values of intrinsic efficiency and intrinsic full-energy-peak efficiency for the A3 shield assembly as a function of source energy.

Above ~300 keV, one should also take into account leakage of the collimator. The method used to achieve this was to make predictions for a laboratory point source and to compare these with measurements made by the Durham group with IAEA gamma ray sources set at various angles to the detector axis at a fixed distance above the collimator top face. Having established agreement, the calculations were then adjusted for a distant point source and the energy dependent exposed area functions shown in figure 4.9 were derived.

For the purpose of analysing astronomical point sources, the author has included the computer routines used to derive these effective areas in the main source analysis programmes, so that the effective area is calculated for each specific energy and cumulative distribution of source-detector angles rather than by interpolating the curves in figure 4.9, which are simply given to illustrate the energy and angular dependence.

4.3.5 Instrumental background.

The measured instrumental background continuum (with coincident shield-Ge(Hp) events removed by software veto) during the flight has been fitted by a semi-empirical model based on that described by Dipper (1979) which includes contributions from various mechanisms:

i) A contribution from atmospheric flux observed through the aperture of the telescope. The vertical gamma ray spectrum of Schonfelder, Graser and Daugherty (1977) was used to calculate this component.

ii) The atmospheric gamma ray flux which leaks through the shield without producing a detectable interaction. The angular dependent flux values calculated by Costa et al. (1984) were employed.

iii) Production of gamma rays by radioactive nuclei in the anti-coincidence shield detectors (Owens, Myers and Thompson 1986). These radioactive species may be produced by neutron or proton interaction with the shield material. Both atmospheric neutrons and those produced by cosmic ray interactions with the apparatus were considered. Radioactive nuclides may also be generated by spallation interactions of atmospheric charged particles. Neutron fluxes were obtained from the review of world data

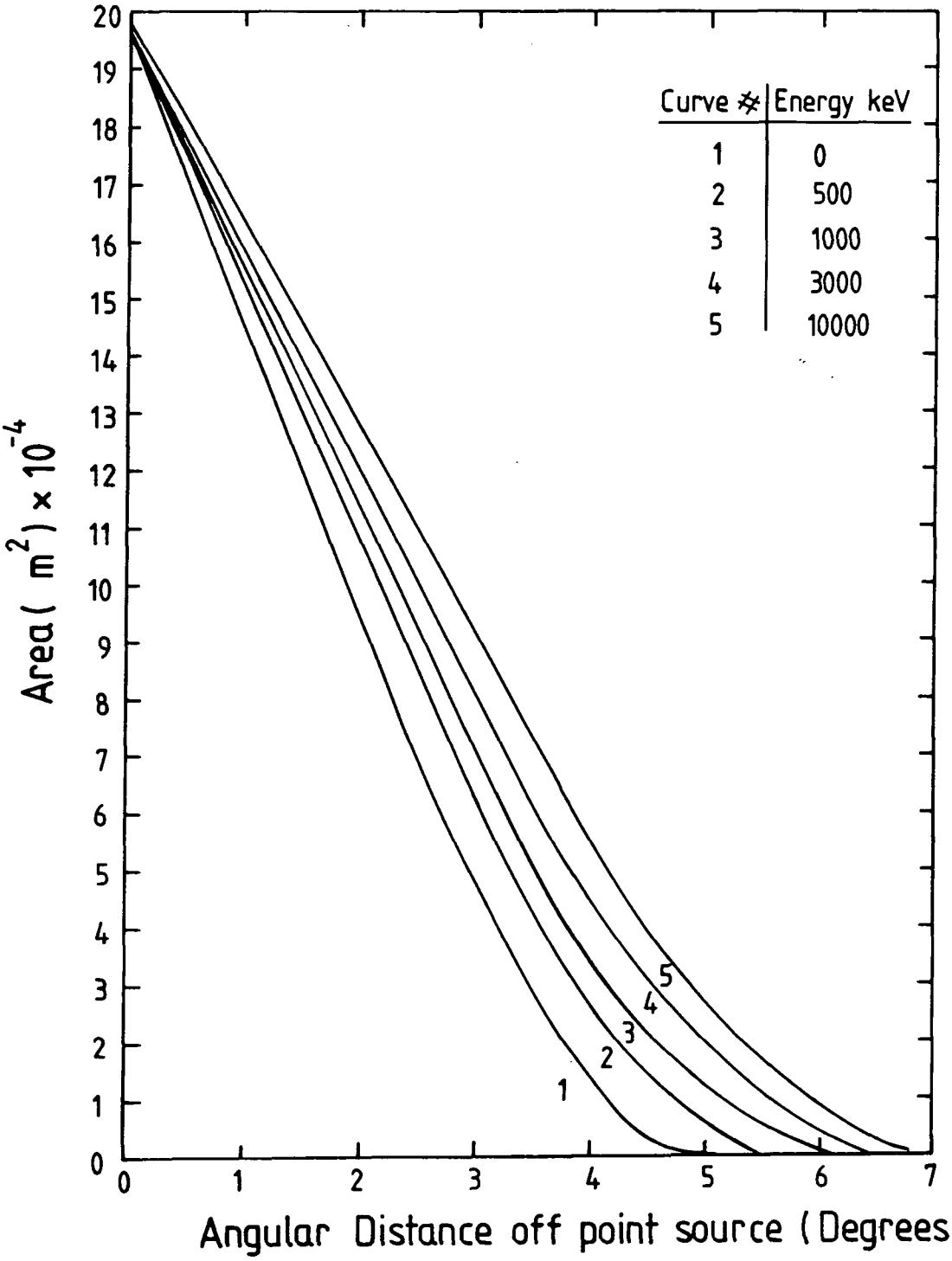

Figure 4.9 The angular response of the MK1B telescope to a distant point source.

by Dean and Dipper (1981), whilst a proton flux of 0.3 protons m^{-2} s^{-1} (Hayakawa 1969) at a rigidity of 4.5 GV was used to approximate the charged particle flux.

iv) The production of β^--unstable nuclides within the Ge(Hp) detector itself. These may be produced by either neutrons or atmospheric energetic protons.

The results of the fit, together with the flight measurements are shown in figure 4.10.

The effectiveness of the neutron shield was evaluated by Owens, Myers and Thompson (1985). Without the neutron shield, the telescope was expected to receive 1974 n s^{-1} at an atmospheric depth of 5.4 g cm^{-2} and a further 1983 n s^{-1} from cosmic ray interactions with the active shield detectors (within the neutron shield). So if the neutron shield removed all external neutrons (the best possible performance), a decrease by a factor of $\sim$2, in neutron-induced background would be expected. Just such a decrease is indicated by the reduction in the Ge(n, γ) induced 139 and 198 keV background line fluxes (see appendix B) from their 1979 values (Ayre et al 1981). The reduction factors are actually 2.4 ± 0.6 and 2.7 ± 0.5 for the two lines respectively, as compared with 1.4 ± 0.2 for the 511 keV line. The continuum background is neutron dominated, as seen in in figure 4.10, so a corresponding reduction would be expected over 1979 values — a reduction factor of 2.1 was actually measured. The performance of the neutron shield was therefore, apparently, excellent.

The measured background line features are discussed in appendix B of this thesis and by Ayre et al. (1984). They demonstrate the stability of the system and provide the energy calibration of the detector and its associated electronics.

4.3.6 Line sensitivity.

Using the observed atmospheric background continuum, the telescope sensitivity to narrow lines was calculated using the method described in Jacobson (1975). The calculated fluxes required for a 3σ narrow line detection during a 1 hour on-source and 1 hour off-source observation are shown in figure 4.11.

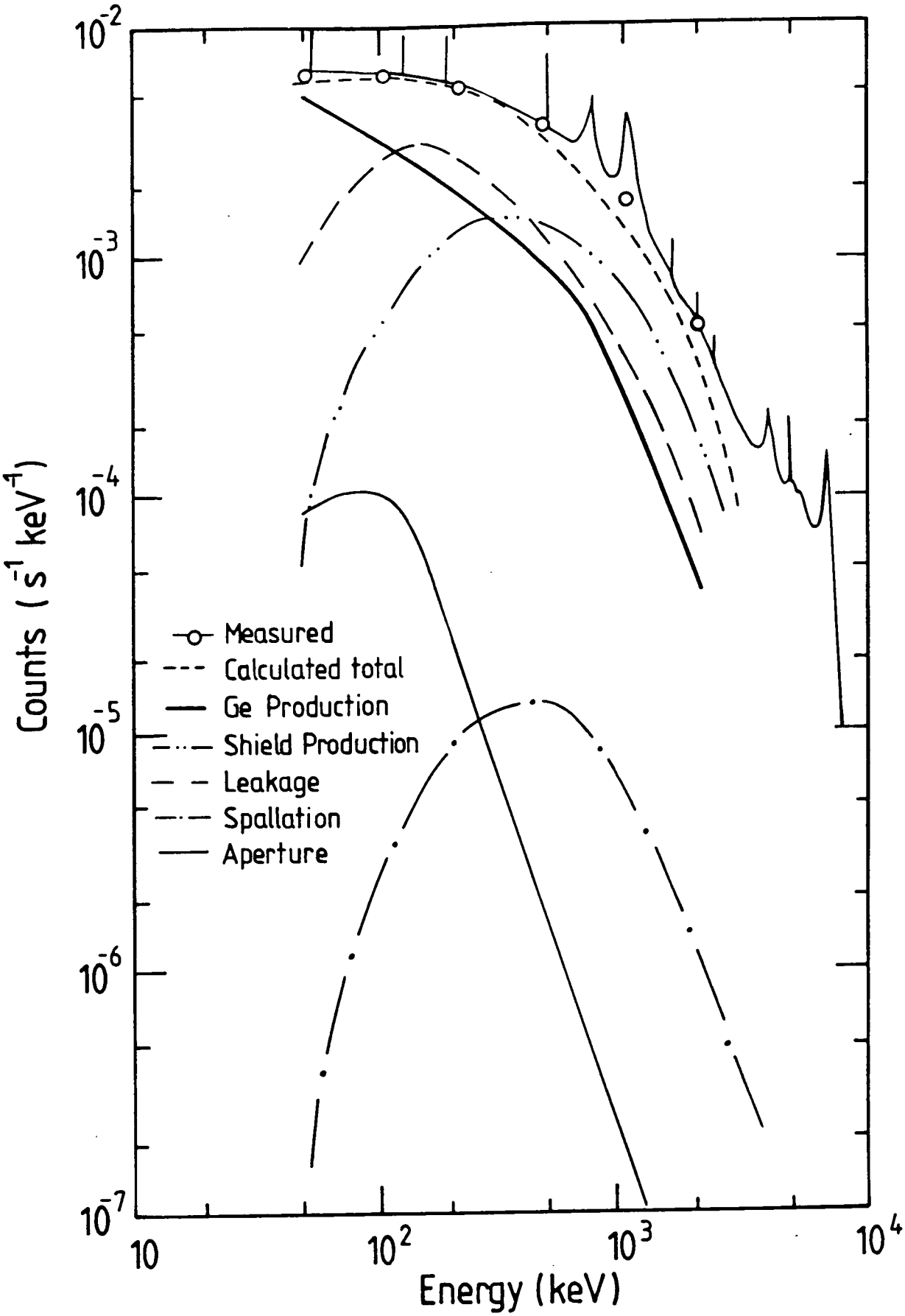

Figure 4.10 The measured and predicted instrumental background (with full veto) at a mean atmospheric depth of 5·4 g cm^{-2} over Palestine Texas. The aperture flux, shield leakage, shield production, Ge production and spallation components are shown separately. The typical uncertainty in the sum of these components (the sum is shown by the short dashed line) is 50%.

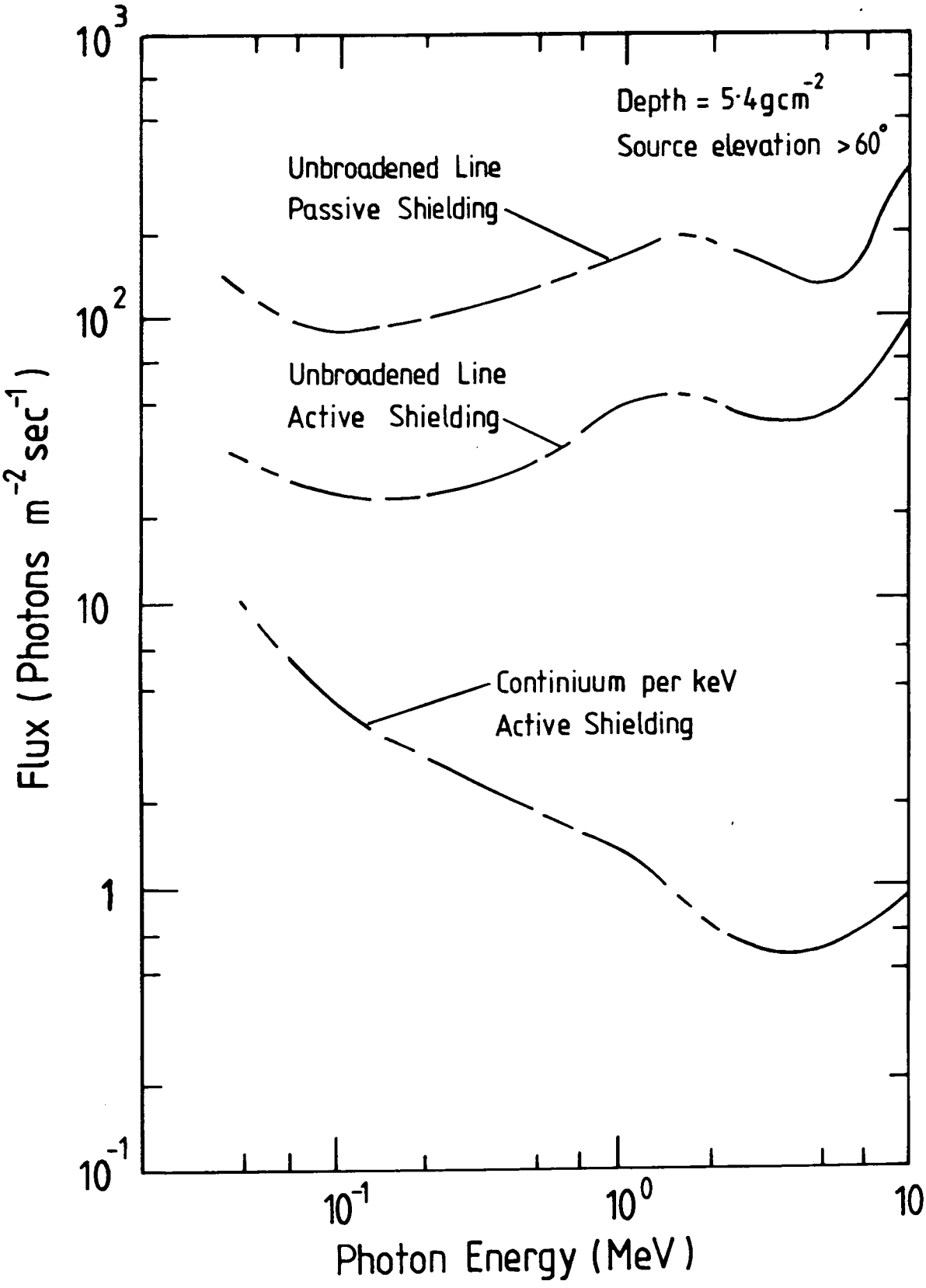

Figure 4.11 The sensitivity of the spectrometer for a 1 hour 'on-source' 1 hour 'off-source' observation and 3σ significance in the detected flux. The gaps in the curves indicate the presence of strong background lines; consequently the sensitivity in these regions will be considerably worse than shown.

Also shown are the line sensitivity when the active veto system is not used (ie. 'passive' shielding only), and the continuum flux sensitivity. The improvement due to active shielding is basically due to suppression of the Compton scattered component of the background. Note the exclusion of strong background lines which seriously and adversely affect the sensitivities.

4.4 Durham 1981 payload.

The payload for the June 1981 flight of the spectrometer comprised the Mk. IB detector with modified acquisition electronics (i.e. amended from 1979 designs), new command and monitoring circuits, modified thermal shielding and environmental dome, environmental sensors, new pointing control and sensing equipment, power supplies, a newly designed crash protection frame and an NSBF Consolidated Instrument Package (CIP).

4.4.1 Data acquisition.

The data acquisition system is the electronic system responsible for the transfer of information in the form of electronic pulses from the Ge(Hp) or the shield photomultipliers to the telemetry unit. The overall process is illustrated semi-schematically in figure 4.12.

The operation of the event recording system was governed by the organisation of the telemetry data transmission sequence. The CIP provides a telemetry encoding system with a flexible transmission format. The experimenter may determine, within certain limits, the order in which data are transmitted and the time between such transmissions. Corresponding strobes were provided to synchronize the data acquisition system with data transmission times. The Durham electronics used these strobes to perform detector sampling, locking, timing and resetting.

Providing the event rate is not too high compared with the data transmission rate, this approach dispenses with the need for elaborate on-board data reduction and does not incur excessive dead time. A fixed sampling cycle was therefore used to convey event data to the ground without prior processing. It is best if the sampling cycle is complete before there is a high probability of another event arriving, and further sufficient information must be transmitted

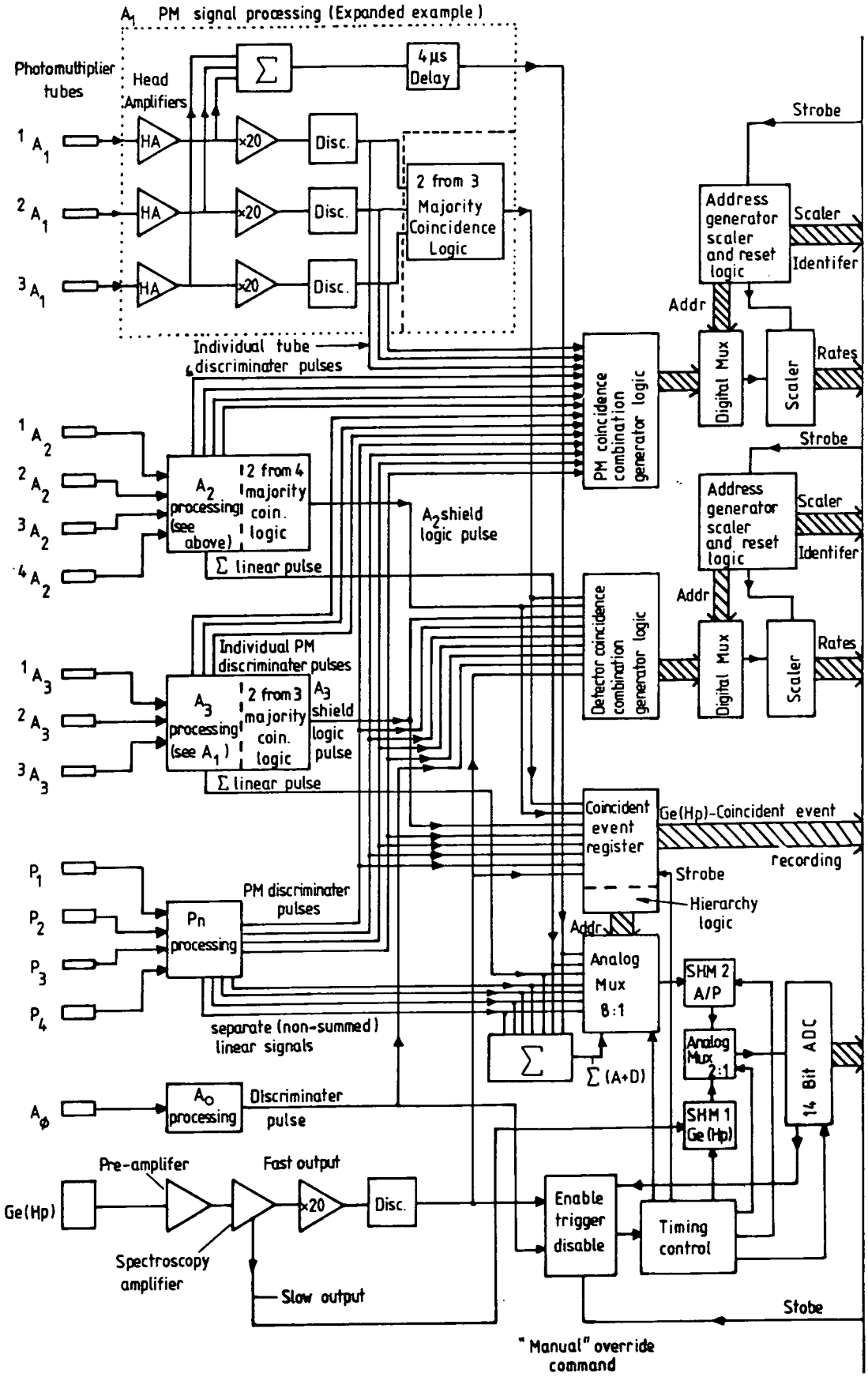

Figure 4.12 Schematic summary of detection event processing electronics.

with each event to characterize it 'unambiguously'. If these criteria are met then this technique is ideal. By transmitting the primary data associated with each detected event, one retains the maximum flexibility in the analysis of the experimental results.

Data were acquired by the CIP either as parallel 10-bit 'reads' or as analogue signals. The parallel reads were made using 12 groups of 10 lines, each line sampling one logical state. A group of 10 bits then formed a single telemetry transmission word. These 12 sets of sampled lines are referred to as 12 distinct digital channels. The analogue signals were sampled using single lines with a common return, these entered a data acquisition and ADC system which selected a single line and generated a 10-bit word corresponding to the voltage on the selected line. These 10-bit words were then transmitted in the same way as the parallel digital channels.

Either type of channel may be sampled with arbitrary frequency. The sampling order is called the telemetry format and was controlled by a programmable read-only memory (PROM) in the CIP. The format was repeated every 0.25 s. The selected data transmission rate was 40.96 kbits s^{-1} and 1024 10-bit words were transmitted during each repetition of the format.

There was a formal arrangement of the telemetry format, or data transmission frame, into 32 subframes of 32 words each. (The terms frame and subframe are reversed in some technical literature.).

Each subframe within the frame normally consisted of an identical pattern of channels to be sampled, however it was possible to arrange for certain positions within each subframe to be occupied by cycles of differing channels on successive appearances. Such cycles must repeat an integral number of times within each frame. So far as the CIP is concerned each frame is identical. This process of less frequent sampling is called subcommutation and its use in the Durham telemetry format is illustrated in figure 4.13 which shows a single frame of words along the top with transmission time advancing from left to right. The subcommutated positions are indicated with channels for successive substitution arranged as vertical columns.

The subcommutated channels were generally used for relatively slowly

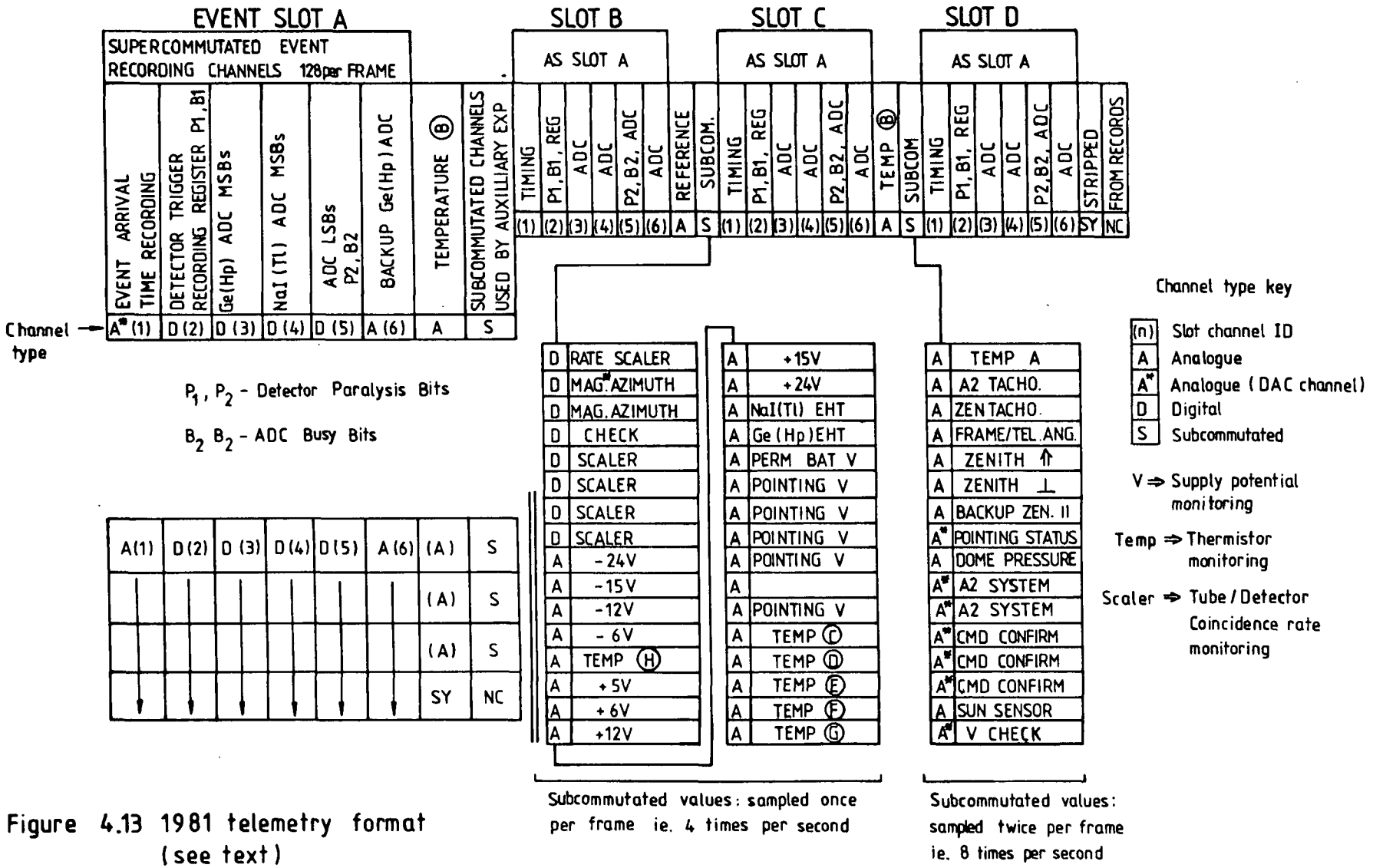

Figure 4.13 1981 telemetry format (see text)

varying quantities such as temperatures, pressure, system voltages and payload pointing angles. These are known collectively as 'housekeeping' information. The maximum time between successive sampling of any channel was 0.25 seconds (i.e. one complete frame). If even less frequent sampling was desired then the experimenter had to multiplex several quantities into one CIP channel and use a frame-synchronized strobe to switch between the various strobes. This technique was used by the Durham scaler system to provide for the sampling of a large number of coincidence counting rates of the various detector and photomultiplier combinations.

Figure 4.13 shows that not all words within each subframe were samples of distinct channels. On the contrary, a pattern of six channels was repeated four times during each subframe, that is 128 times in each frame. Each of these groups of channels is a 'slot' which may hold an event description. This process of cyclic repetition within a subframe is known as supercommutation.

It should be noted that the last two words of each subframe were dedicated to a predefined bit-pattern which was used by NSBF ground station equipment for subframe synchronization. At the end of each complete frame, this code was replaced by its compliment for the purposes of frame synchronization.

The six-word slots were the mechanism for event recording. An 'event' took place when at least one of the detector systems fired. That is, electronic pulses were produced which exceeded noise discrimination criteria and conformed to photomultiplier majority logic conventions (see the subsequent section on event signal processing electronics). Typically, several detectors would fire within the allowed 1 μs resolving time and their identities would be recorded in a register (one bit per detector). Two criteria were imposed for an event to be so recorded: firstly, the set of firing detectors had to include the Ge(Hp) and secondly, it had to exclude A0, the axial charged particle detector. (Coincident firing rates which were independent of these criteria were measured by the scaler recording system).

The structure of the slots was determined by an assessment of the likely usefulness of the various pieces of information available when an event took place. The most frequently occurring class of multiple-detector events involved the Compton scattering of a gamma ray from the Ge(Hp) detector, with the

scattered photon being recorded by one of the shielding detectors. As such events deposited a continuum of energies in the Ge(Hp) it was desirable to exclude them from the Ge(Hp) spectrum.

The approach taken with most actively shielded detectors (see Chapter 3) has been to use electronic anti-coincidence to select events in which only the central detector was triggered. This provided a preferential aperture response for the detector and suppression of the 'Compton continuum' from the recorded data. The disadvantage of the 'hardware' anti-Compton approach was that a substantial amount of information was lost. It is clear that Compton scattering may reveal information about primary polarization. Also, it might be possible to use the central detector and shield pulse heights to recover some information from Compton or pair-production initiated events. Further still, one may use such data to investigate the active shielding mechanism in the stratospheric radiation environment. Such investigations require shield detector pulse-height information. Accordingly, the Durham system was designed to analyze the pulse-height from one of the shield pieces alongside the Ge(Hp) event. The identity of this shield detector was determined from the pattern of detectors which actually fired during a particular event. If only the Ge(Hp) fired then the summed output from all the shield photomultipliers was analyzed. Where just one detector fired in coincidence with the Ge(Hp), this was naturally selected for analysis. If more than one fired then they were selected according to a fixed hierarchy. This was devised to reflect the relative likelihood of their being connected with the Ge(Hp) event.

Two pulse-heights, one from the Ge(Hp) detector and one from a shield element, had to be recorded along with the contents of the register showing which detectors fired. It was also important to record the time of the event arrival within the recording slot. This information may be used in, say, pulsar timing analysis. A backup analysis of the Ge(Hp) pulse-height was also made in case the main nuclear pulse-height analysis system (i.e. the main ADC) malfunctioned.

After an acceptable event had been detected the apparatus was paralyzed until the slot into which the events was stored had been read into the CIP. The paralysis of the apparatus was indicated by a single bit, P and recorded in

the slot with the event data. An accompanying 'busy-bit', B, indicated when the pulse height analysis was complete.

The CIP provided a separate strobe pulse before each channel was read. The main ADC system reset was derived from the strobe corresponding to one of the channels within the slot group. The timing of the reset is indicated in figure 4.14 which is a detail of figure 4.13. The system reset was not always enabled, it depended upon the paralysis state during the previous slot. When it was present, however, it cleared the paralysis state, reset the event timing clock and restarted it.

The arrival of an acceptable Ge(Hp) event (with the system in an un-paralyzed state) stopped the timing system, initiated analysis of the Ge(Hp) and shield pulse-heights, triggered the backup ADC, and put the system into a paralyzed state. The busy flag was set during analysis, indicating that the accompanying data was unreliable (i.e. if the busy-bit was seen to be set in the recorded data set then the data in that slot had been read before analysis was complete). The appearance of $P\bar{B}$ (paralysis-bit set, busy-bit clear) in the data-set therefore indicated that valid data was present at the time of the PB sample.

PB was actually sampled twice in each slot (P_1B_1 and P_2B_2) in order to allow events to be distinguished according to arrival time. The event data was placed in the slot as indicated. The exact placement of the main pulse-heights and the detector firing register were not important, but the positions of the backup Ge(Hp) pulse height and the timing word were important as will be seen.

In figure 4.14 one may distinguish three classes of event according to arrival time relative to the reset strobe.

Timing region A.

The arrival of a pulse in region A (see figure 4.14) would set $P\bar{B}$ at the second sampling in slot 1 but not at the first. This would indicate that the data in slot 1 was invalid. The system would not reset in this case and the data would be read at slot 2 where $P\bar{B}$ would be present at both samplings. The slot 2 timing value would also correctly refer to this event but note, however,

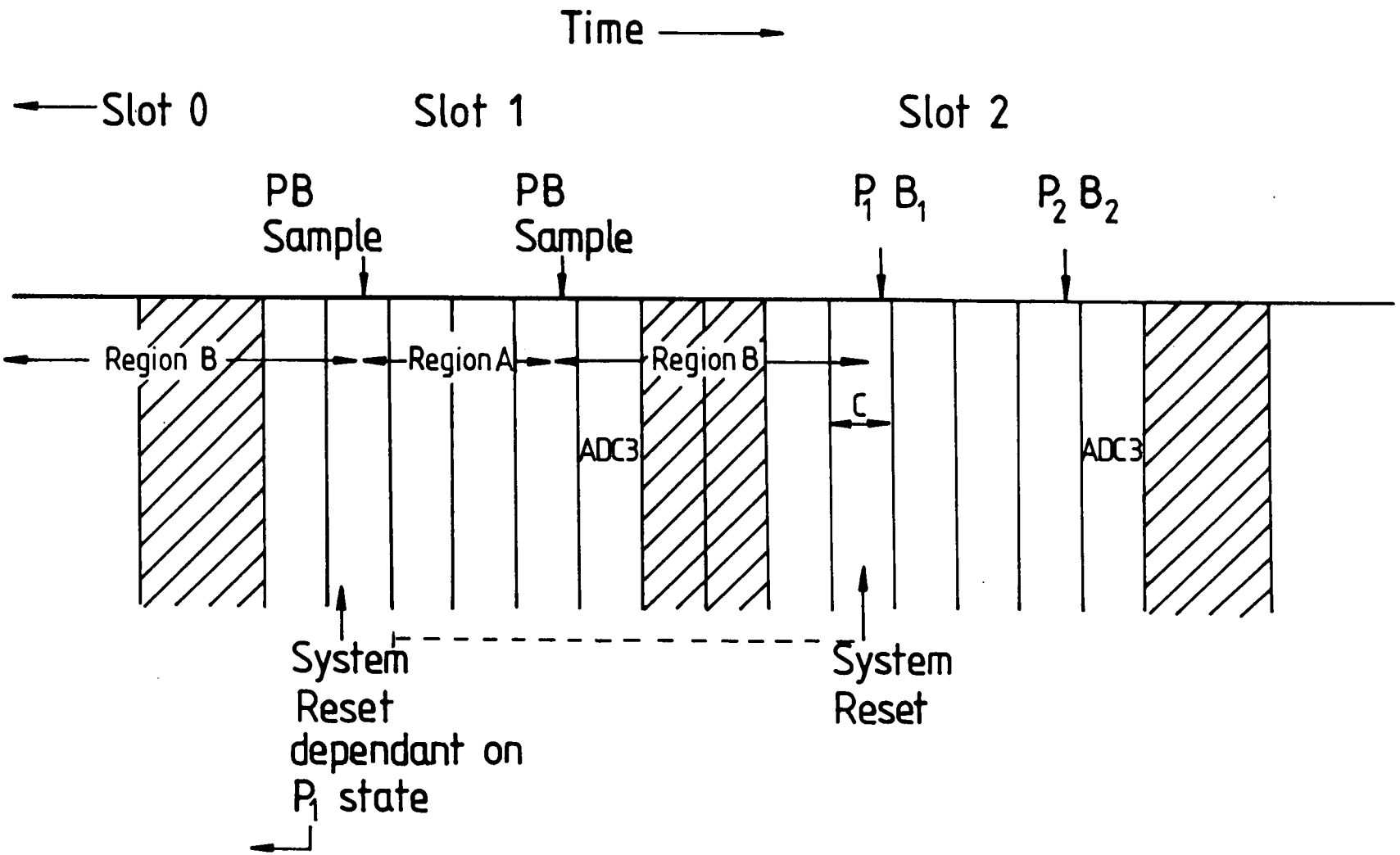

Figure 4.14 Detail of event recording supercommutated cycle of the 1981 telemetry format.

that the backup Ge(Hp) ADC, having an independent reset, would present its data at slot 1 and would have cleared before being read again at slot 2.

Timing region B.
If the event arrived in region B then $P\bar{B}$ would be present at both samples in the next slot and the timing and backup Ge(Hp) ADC data in this slot would correctly refer to this event.

Timing region C.
There was a narrow timing window between the main reset and the first PB sample An event arriving here would be correctly read out in the current slot, but its timing value would not appear until the next slot.

The overall rule is that if $P\bar{B}$ was present at both samplings then the data in that slot was valid. The system reset was therefore conditional upon the presence of P at the first sampling in the previous slot. The second PB sample is used to inform the analysis software of the condition where the backup Ge(Hp) ADC value must be saved for use with the data in the next slot.

4.4.2 Nuclear instrumentation.

The operation of the electronics will now be considered in the context of the preceeding discussion and figure 4.12. Signals from the Ge(Hp) dedicated pre-amplifier were passed to a spectroscopy amplifier, which provided a prompt trigger and a delayed proportional pulse. The photomultiplier assemblies on the NaI(Tl) crystals had integral head-amplifiers which acted as input buffers and line drivers. The pulses from these head-amplifiers were available for discrimination (with prior amplification by a factor of 20 to change the effective discrimination threshold if necessary) or for summing and analysis. Both the Ge(Hp) and the shield detector electronics were adjusted so that $0 \rightarrow 10\,\mathrm{V}$ output pulse height corresponded roughly to $0 \rightarrow 10\,\mathrm{MeV}$ of deposited energy.

The discriminator pulses, where there was more than one photomultiplier on a given detector, were subject to 'majority logic' in establishing that the detector had fired. That is, the majority of the photomultipliers on a particular detector had to trigger their discriminators in coincidence in order for the detector to register an event.

All discriminator circuits were set to operate at a 1 volt input level. Amplification by a factor of 20 at the previous stage made this threshold effectively 50 mV. This allowed the discriminator circuits to operate at an optimal threshold while providing a discrimination level at the appropriate fraction of the ADC input voltage range. The signals used for pulse-height analysis bypassed the factor of 20 amplification. The shield and Ge(Hp) discriminators were therefore operating at threshold voltages equivalent to approximately 50 keV of deposited energy in the detectors.

The analogue signals from all the photomultipliers on each detector were summed and passed to the analogue multiplexor inputs of the main analysis unit. Suitable linear delays were provided for these summed pulses to allow the logic circuits to respond to the discriminator pulses before the analogue signals arrived.

4.4.3 Main ADC system.

The primary analogue to digital convertor (ADC) was an Analogic MP8014 14-bit (16384 channel) unit with an 8.4 microsecond conversion time. The inputs were selected by Analogic MN4708 analogue multiplexors from one of two SHM60 Burr-Brown sample-hold units. One of these 'held' the Ge(Hp) pulse. This would be the first Ge(Hp) pulse, with height exceeding the discrimination threshold, to arrive since the last ADC reset pulse. The ADC reset pulse was derived from the telemetry system and the state of completion of the last analysis; its timing was therefore locked into the main supercommutated sampling cycle.

The other sample-hold module held either the summed pulse heights from all the photomultipliers on a particular detector (which fired in coincidence with the Ge(Hp)) or, in the absence of any shield piece triggering, the summed output from all shield detectors other than A0.

The voltages from the two sample-hold modules were analyzed in turn and the output digital words were entered into the telemetry frame. The multiplexing of signals into the shield sample hold module (sometimes referred to as the ADC2 channel) was done using Analogic MN4708 analogue multiplexors.

The ADC output values increased from a zero corresponding to an input

voltage of less than the discriminator level to a maximum value at approximately 10 V (ie. ~10 MeV). The precise energy calibration of the Ge(Hp) was determined by background line measurements in flight as described in appendix B.

4.4.4 Scaler recording.

Several subcommutated channels were committed to the recording of the coincidence rates of various photomultiplier and detector combinations. The measurement of these rates was independent of the state of the main ADC system. This information served to confirm that the various photomultipliers were operating correctly and that the shield-pieces were undamaged.

As there were many coincidence combinations, they were contrived to occupy only five subcommutated words within the telemetry frame by appropriate multiplexing. This was controlled by successive frame strobe pulses. Ambiguity in subsequent analysis is avoided by the provision of scaler identifier words. These record the digital multiplexor addresses which selected each coincidence permutation for rate measurement. Therefore, in the absence of telemetry 'drop-outs', these counts are seen to increment, or to be reset after a maximum, at successive appearances in the telemetry stream.

4.4.5 Auxilliary Monitoring

Other than the Main ADC and scaler monitoring, provision was made to record data associated with the following:

- Eight regulated supply voltage levels.
- Eight pointing system supply voltages.
- Eight temperatures obtained using pre-calibrated thermistors attached to various points on the payload. (See figure 4.15 for details of their locations).
- Internal environmental-dome pressure.
- EHT voltages for the Ge(Hp) detector and NaI(Tl) crystals.

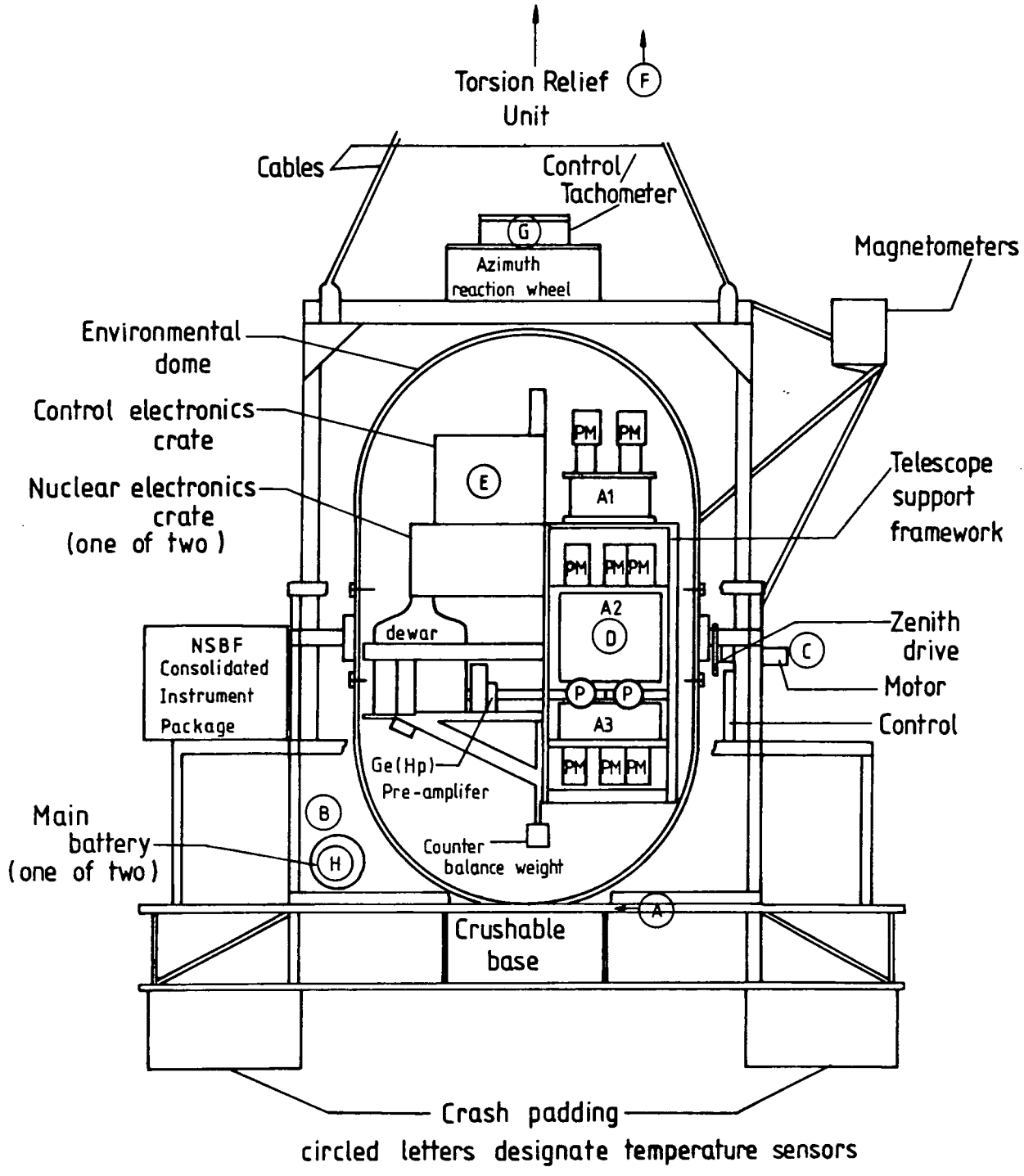

Figure 4.15 Cross-sectional view of the 1981 payload.

- Various pointing system indicators showing the zenith and azimuth orientation.
- Command confirmation.

4.4.6 Payload control.

Remote control of the payload used transmission mechanisms provided by the CIP. 42 were available together with a 16-bit parallel discreet command word and strobe. Logic circuits were constructed to register and buffer the command states and to provide a reset to inactive states either at power-on or by using the 'master-reset' command.

Those circuits responsible for switching the main system power supplies (Lithium-organic batteries with DC/DC convertors) had separate, external power.

The 'manual' (ie. non-automatic) telescope pointing commands had special logic circuits to prevent an immediate transition between opposed slewing actions. This prevented motor or gear damage through inadvertent command transmission.

The data word had two possible meanings: either a zenith or an azimuth telescope pointing demand angle. Part of the command was used to distinguish between these and other, unused, destinations. The spare capacity was intended for future on-board microprocessor control of pointing functions. Confirmation of the parallel commands was recorded in the telemetry format.

Facilities were provided for the transmission of control data from the Palestine base, from a down-range tracking station (in this case located in Pecos, Texas.) and from mobile transmitters.

4.4.7 Power Supply.

The system power was derived from two banks of Lithium-organic cells giving in total 30 V. Separate batteries were provided for certain pointing system motors, and for the main power on/off command decoder and relays, which were permanently powered. Precise voltages for the operation of the electronics were derived from the 30 V batteries using DC/DC convertors.

4.4.8 Environmental dome.

The components of the apparatus external to the spectrometer were concerned with providing protection from mechanical shock and extremes of temperature and pressure and also with providing the alt-azimuth alignment of the spectrometer axis.

The detectors and the data acquisition and control electronics were contained within an environmental dome which was hermetically sealed and thermally insulated. The EHT supplies, photomultiplier dynode chains and head amplifier electronics and lead connections were individually 'potted' in silicone rubber to prevent breakdown at low external pressures. It was not expected that these elements would experience a low pressure environment, due to their being within the environmental dome, but, in the event of the environmental dome pressure falling, the potting of the high voltage system would ensure that the detectors would continue to operate. The pointing system motors, servo-amplifiers, batteries and the CIP were external to the pressurized dome. The overall arrangement of the gondola is illustrated in figure 4.15.

4.4.9 Pointing control.

The telescope, together with the electronic equipment and environmental dome, was mounted so that its altitude (compliment of zenith distance) could be adjusted by tilting it with respect to the gondola frame. The azimuth of the telescope was adjusted by rotating the entire gondola. Motors and control electronics were provided to drive the alt-azimuth mount either 'manually' (i.e. by transmitting commands to switch the drives on and off) or 'automatically' (i.e. by transmitting encoded azimuth and zenith 'demand' angles which the control system would then realise).

Using the Omega navigation latitude and longitude information to obtain the instantaneous geographical position of the payload, and, by estimating the local geomagnetic declination (the horizontal plane angle between true North and the geomagnetic field direction) at that point, the alt-azimuth coordinates of a given celestial object could be calculated for any particular time as described in, for example, Smart (1977). The ground control personnel might then elect either to command the payload to this orientation, so that the aperture axis

aligned directly with the object, or, to command the payload to an offset orientation for background sampling.

An electric motor and gears provided powered adjustment of the zenith angle. A directly driven reaction-wheel together with a suspension cable torsion relief system provided the corresponding facility in azimuth.

The orientation was sensed and transmitted to the ground where it formed both a permanent record in the telemetry data and a display for the experimenter's use. In the zenith tilt plane, an inclinometer together with two auxiliary sensor systems (a geared pendulum with potentiometer and a friction driven, frame telescope angle sensor) provided orientation monitoring. Additionally, an inclinometer was used in the plane orthogonal to the tilt axis. The azimuth angle was monitored using digitally resolved fluxgate magnetometers and also by a sun-sensor. As may be seen in figure 4.15, care was taken to fix the magnetometers in regions free of ferromagnetic materials.

The sensors were calibrated before launch and the alignment of the zenith angle sensors with the plane of tilt was checked. The azimuth sensors were calibrated in an area free of magnetic materials. Sightings of the transit of the sun were used to establish the direction of true North.

The automatic systems are illustrated in figure 4.16 and figure 4.17. It may be seen that both systems use binary comparison of an encoded demand angle with a digitized sensor signal. In the case of the zenith angle drive, the sensor was the 60° inclinometer and the outcome of the comparison was used to provide signals for the drive motor.

The azimuth system was a little more complicated. Here, the sensor signal was proportional to the rotary angle of a positioning table with respect to the plane in which the zenith angle control system operated. The results of the comparison were used to provide signals for a stepper motor which moved a table carrying a pair of fluxgate magnetometers (these magnetometers were distinct from the main confirmatory magnetometers). The processed signals from the magnetometers drove the reaction wheel. Hence the whole gondola was driven to a position where the magnetometer axes lay at the geomagnetic orientation which gave a stable zero-crossing in the motor signal. By moving

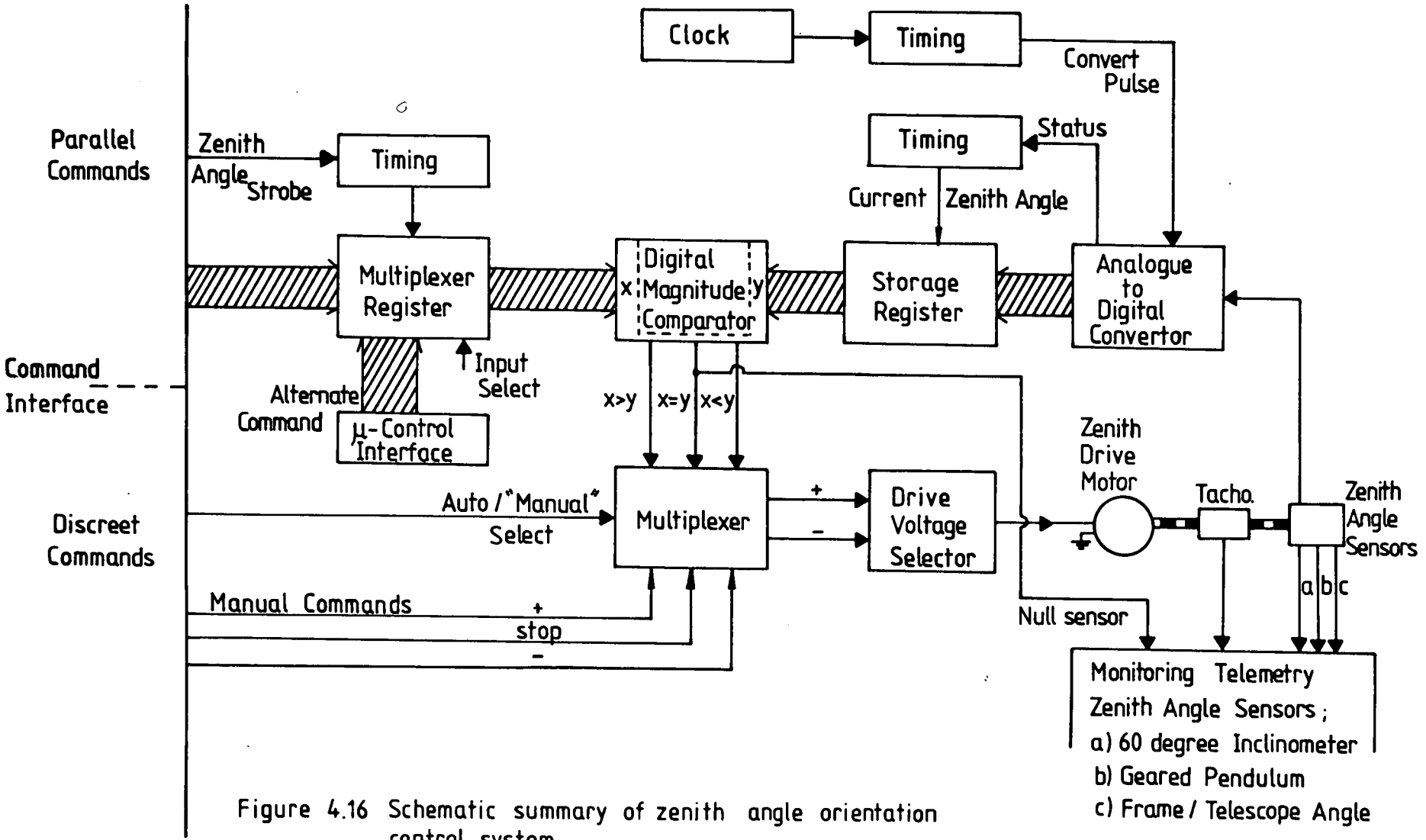

Figure 4.16 Schematic summary of zenith angle orientation control system.

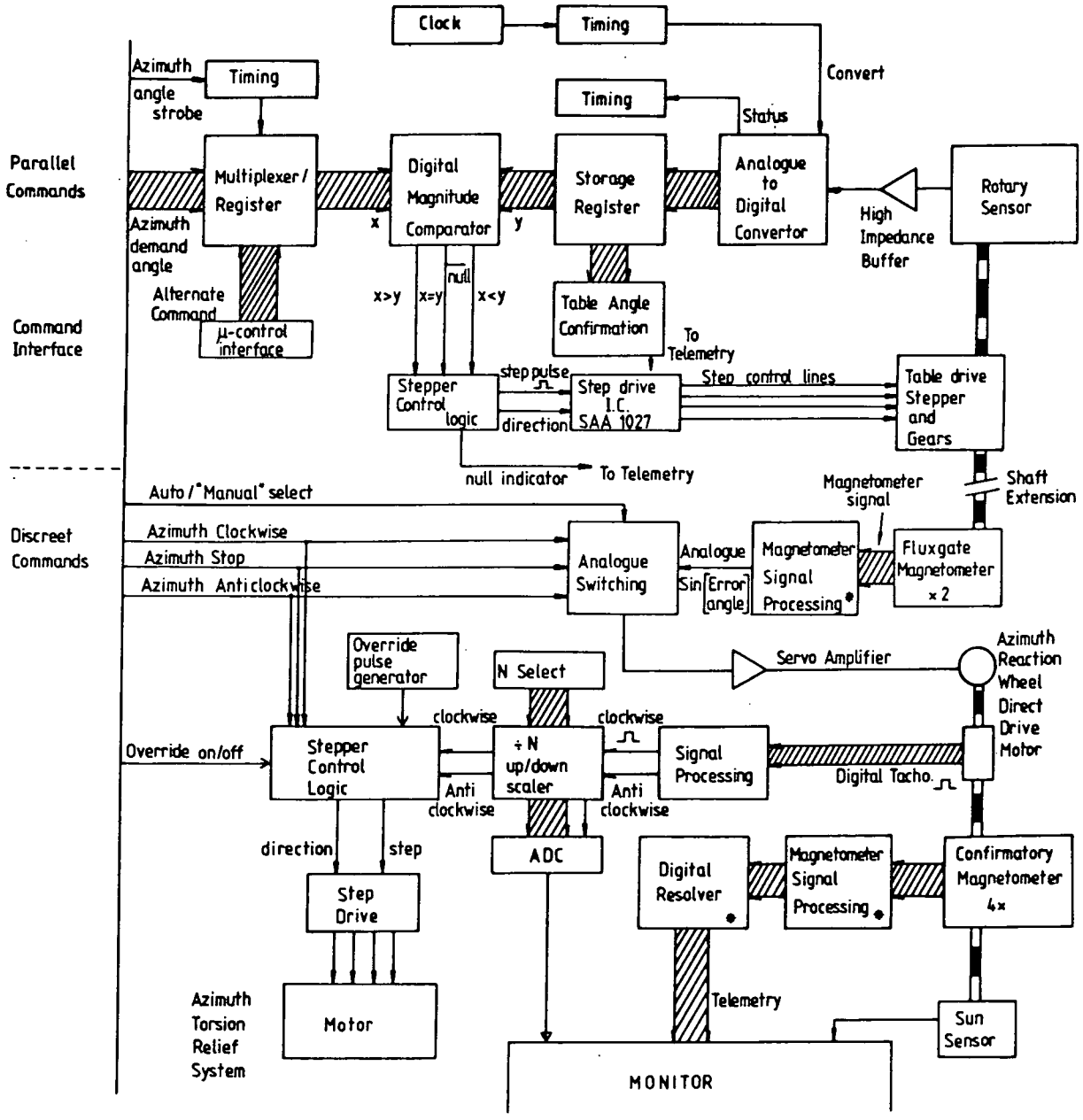

* Circuits by T. Jackson, EWS, Physics Dept, Durham.

Figure 4.17 Schematic summary of azimuth orientation control system.

the table, the whole gondola could be set to a different azimuth angle.

Pulses for a stepper motor providing cable torsion relief were derived from an incremental optical encoder on the reaction wheel. The stepper motor drove the two parts of the suspension swivel with respect to each other.

4.4.10 Payload superstructure.

The gondola was constructed principally from aluminium alloy scaffolding tubing which formed a protective cage around the environmental dome. The dome could tilt up to a maximum zenith angle of approximately 45° without the telescope axis being obstructed. The cage was attached to the rectangular frame supporting the environmental dome and contents. The frame was itself constructed from aluminium alloy channel. The frame also provided a support platform for the CIP.

Finally a large-area, crushable crash frame, constructed from thin aluminium alloy angle beams, was attached to the lower struts of the cage. Crushable cardboard crash packs were attached to the underside corners of this frame in order to provide further impact impulse absorption.

4.4.11 The NSBF consolidated instrument package (CIP).

The standard flight unit provided by NSBF comprised the following items:

- Spacetac 2100 Pulse Code Modulation encoder. The sampling sequence was PROM controlled; a maximum of forty-eight analogue channels and twelve ten-bit digital words were available. A transmission rate of 40.96 kBits per second was employed.
- Command receiver. This provided remote control of the payload, ballast jettison and flight termination.
- Omega Navigation system. This located the balloon within a four square-kilometer area using standard transmissions from international ground stations.
- Rosemount altimeter. This could detect an altitude change of less than 0.1% at 120000 feet.

- FM/FM telemetry system. This transmitted the telemetry data. The side bands were used for the Navigation and altitude information.

4.5 1981 Flight

Long-duration, high-altitude balloon flights made using presently available technology are normally scheduled for the period of reversal of the stratospheric wind direction over the launching site as this is likely to give a relatively slow drift rate when the payload reaches float altitude (ie. when it reaches equilibrium and ceases to climb).

The spring wind 'turn-around' season at the National Scientific Balloon Facility at Palestine, Texas, USA afforded a good opportunity for a Crab observation (the primary objective of the planned campaign), provided that the payload was at float altitude for at least two hours before and after the Crab transit. Accordingly launch was scheduled for this season in 1981. The payload was therefore transported in advance to allow assembly and testing to be completed.

4.5.1 Data recording.

The launch took place at 12.35.23 UT (Universal Time, equivalent to 7.35.23 local) on 6 June 1981. the payload reached float altitude (approximately 36.5 km) at 14.26.0 UT. The course proved to be West and slightly North, permitting a long flight with appropriate use of the down-range tracking station at Pecos, Texas. approximately 500 miles West of Palestine. The flight was terminated when the payload left telemetry range of Pecos at 10.55.00 UT on the following day.

At the two ground stations the data were received, decoded, displayed and recorded and the steering commands were computed and transmitted.

As the PCM encoded frames were received at the ground station at Palestine, they were decoded, their synchronization checked and the results passed to one of two Digital Equipment Corporation PDP-11 minicomputers for recording on 800 BPI magnetic tape. The two computers were available to allow instantaneous switching during tape changes. The computers appended

'ground-frame' information to each frame. It consisted of the frame reception time (to within 0.0001 s relative to the clock initialisation), the Omega navigation system geographical balloon position and the CIP pressure.

At Pecos, the PCM was recorded directly as analogue signals on magnetic tape with time-code being recorded on parallel tracks. These tapes were subsequently translated by the computers at Palestine. Positional information for the Pecos monitored portion of the flight had to be obtained 'manually' from Omega printouts.

Failure to receive a frame correctly due, say, to bad transmission conditions produced a 'drop-out' and the frame should not have been recorded in the ground computer. However, it was found subsequently on analysis of the data that a great many demonstrably corrupt frames had actually been written to the tapes, especially during times of known bad reception. Particularly degraded telemetry conditions were noted at the following times: Firstly, during ascent and shortly afterwards (Indeed the data is missing completely for the first nine minutes of ascent); secondly, during the switch of control and recording from Palestine to Pecos; and finally, towards the end of the Pecos recording. Also a whole data set (5.24.00 UT to 6.42.00 UT) is missing from the Pecos recording period.

There were, in all, 38 final magnetic tapes of data; tape switching was effected by parallel recording, however this system did not always work perfectly and there are some gaps in data at tape boundaries.

4.5.2 Data validation.

The criterion for satisfactory operation was that the main ADC system was working with active veto from the shields and that the transmitted record showed no corruption.

Vetting the data for corruption was essentially a two-stage procedure. Firstly, simple checks (frame time sequence and fixed check bits) were used to remove some corrupt frames (each frame formed a single one-record block on the original tapes). The results from the temperature and system voltage monitoring were then analysed for the entire flight using the simple checks as a data filter. It was established that the only recorded deviations from normality

were associated with periods of data corruption (that is where there were a large number of records rejected by the simple checks). Normal ranges were then obtained for these quantities which were then used in the second stage of data filtration. That is, records with unrealistic temperature or voltage indications were rejected.

It was noted that corruption often began part-way through the transmission of a frame (due, presumably, to loss of subframe synchronization); it was therefore fruitful to reject the frames immediately prior to those in which corruption had been detected.

4.5.3 System monitoring.

Analyses of the various 'housekeeping' data were carried out. Non-pointing system electronic supply voltage levels were all found to be stable.

The temperature sensor data showed that the main electronic systems rack and crystal temperatures remained within the limits 10° C to 30° C. Outside the environmental dome, a much larger variation was recorded by similar sensors. A point on the frame, distant from heat sources, encountered a minimum of $-36°$ C and a maximum of $+52°$ C. Various other strategically placed external sensors yielded data which were appropriately correlated with sunset and the dissipation of power by the pointing system.

The pressure inside the environmental dome stayed within 25 mBar of 1 Bar. The variations in this quantity seemed to be correlated with the internal temperatures.

The Omega latitude and longitude information from the ground frame, flight report and Pecos Omega printout were mutually checked and organised into machine-readable tables for efficient use; obviously unphysical values were removed. The altitude data were treated in a similar manner.

Pointing system data were accumulated for the entire flight in order to verify the agreement of the various transducers. The inclinometer which was set orthogonal to the zenith tilt-plane gave a maximum variation of 4 arcminutes, which was correlated with the zenith tilt, implying a negligible miss-alignment.

Azimuth data were corrected for magnetic declination (that is, the local

angle between magnetic and true North) at Palestine. As the magnetic declination varied over the flight, it was necessary to compute the change at any given time in order to interpret the azimuth pointing sensor data.

Magnetic declination values were obtained from U.S. aeronautical charts compiled by the National Oceanic and Atmospheric Administration, USA. The intersections of lines of constant magnetic declination with lines of latitude were used to construct a projected rectangular grid of magnetic declination values lying on a set of parallel lines. The grid area was chosen to cover the flight path. These were then fitted with a third order by third order Chebyschev polynomial surface. The least squares fit coefficients provided a means of rapidly interpolating the magnetic declination surface. Test interpolation points agreed with actual values to within one arc minute.

In conclusion, the environmental dome functioned extremely well and the orientation transducers gave agreement to within 20–40 arcminutes.

4.5.4 Detector monitoring.

Photomultiplier/detector rates confirmed that all photomultipliers and crystals had functioned normally. The Ge(Hp) counting rate in an auxiliary monitoring channel was found to be approximately twice that expected from the Main ADC triggering rate; this was probably due to 'double-pulsing' in this channel. It was found that the rates of all coincidence combinations which involved the Ge(Hp) were similarly affected.

Having verified the correct functioning of the telescope, electronics and support systems, and having also devised a technique for the rejection of corrupt data, it is possible to proceed to analysis of the experimental results as discussed in the next chapter.

Chapter 5.

The 1981 Durham data.

5.1 Introduction.

The steps required to produce the net fluxes and to perform line searches on the Durham flight data will be described. The principal results from the flight are evidence for three lines from the Crab Nebula and evidence for annihilation line emission from the unusual active galaxy NGC1275. This thesis is basically experimental and concerned with obtaining and reporting these results but some brief suggestions for interpretation will be presented.

Of the Crab line features, two are possible confirmation of previous results, whilst the third and strongest is a new result. The NGC1275 flux has not been reported previously but it is argued in chapter 3 that it may have been detected to some extent in the HEAO C-1 data (Wheaton et al. 1987).

Additional information has also been produced on atmospheric and instrumental background lines, on the continuum emission from the Crab and NGC1275, and the Crab pulsar continuum flux light curve. Although none of these data are important astronomically, they can serve important purposes in analyzing astronomical data. The background lines are used to calibrate the instrument and to monitor the gain stability and the correct functioning of the nuclear instrumentation. The continuum fluxes and the Crab pulsar light curve are useful indications of the validity of the data and of the reduction techniques. In particular they indicate that the pointing system and the interpretation of orientation transducer data were within tolerable bounds of accuracy.

Databases were constructed from the original data tapes in order to facilitate data retrieval. A system of library routines and applications programmes was written to access these data bases and to perform the required analyses. Various techniques were developed for the uniform control of these programmes, intercommunication between programmes and for the flexible storage of operational data structures. Some of these techniques may have applications outside gamma ray line astronomy.

The majority of the software was devised and written by the author; the following exceptions are very gratefully acknowledged. The first stage of the data filtration was performed by Dr. P.N. Bhat and the initial analysis (prior to the database construction) was performed jointly by Dr. P.N. Bhat and the author. Many concepts in subsequent programmes were derived from Dr. Bhat's original work. Dr. K.C. Yau devised and wrote the barycentric reduction and period search software. Dr. A. Owens provided various detector response correction routines, utility fitting programmes, and made many important suggestions.

5.2 Preliminary processing and background analysis.

This section briefly describes the construction of the databases from flight telemetry records and the use of a background line analysis to establish the Ge(Hp) energy calibration. These constitute the prerequisite steps for the analysis of celestial source fluxes.

5.2.1 Data Filtration.

As described in section 4.5.2, the recorded flight telemetry data showed considerable corruption. The techniques used to reject invalid data were improved during the development of preliminary source analysis techniques, and consequently the results from these early efforts show some small variations (say, one or two counts in a line feature containing $\geq$70 counts). However, with the construction of the primary database, the data filtration method was 'frozen'. This means that the primary database has not been revised since its original generation. The filtration methods employed at this stage used all available techniques to ensure the most efficient rejection of corruption. These included the examination of all 'housekeeping' variables within a frame to check that variations were physically realistic, and also the rejection of any frame prior to one showing demonstrable corruption.

The inputs to this final filtration programme were versions of the flight telemetry records which had already undergone preliminary checks on the consistency of ground frame information (see section 4.5.1). The output consisted of variable length records which began with a fixed length header containing telescope pointing information (the azimuth and zenith transducer values), the frame time (local hours, seconds and 100 μs units), two bits indicating the

correction functioning of the Ge(Hp) and shield detector EHT systems, and information from the scaler monitors. This fixed header was then followed by a variable number of 'event cycles', each describing an individual event. The event description comprised the event register bit pattern which described which detectors fired during the event (one bit per detector: A1, A2, A3, P1, P2, P3, P4; Ge(Hp) was always present), the Ge(Hp) and (selective) shield pulse heights from the main ADC, the contents of the secondary Ge(Hp) ADC (along with two status bits indicating a 'normal', 'delayed', or 'uncertain' event — see section 4.4.1), and the event clock value for use in pulsar timing analysis.

In addition to the scientific information, the record headers also contained a 'logical record sequence number', a physical record number indicating which original telemetry record the data were derived from (to aid in investigating any processing problems), and a 'logical record length'. These numbers had a bit set to differentiate them from data fields. The event cycles also included a cycle number indicating the ordinal cycle position within the frame. The reason that these variable length output records are described as 'logical' is that they were not actually output as separate physical records but were packed into fixed length 16000 byte blocks for storage efficiency. Logical records could span physical block boundaries for greater efficiency, and considerable internal packing of bit fields within records was also done. The storage efficiency was such that the entire flight data in this format, together with separately stored geographical data and housekeeping summaries could be stored on four 1600 BPI tapes. The use of differentiated sequence numbers and logical record lengths provided for the checking of logical record unpacking during data retrieval.

This system constituted a 'transport format' which was used for transferring filtered data between computer systems. It was optimised for efficient storage and not for speed of retrieval. From this format, the databases were constructed; these were intended for fast and/or random access.

5.2.2 Database construction and access routines.

The transport format data were divided into 33 files corresponding to the original telemetry data tapes. The primary database consisted of 33 corresponding sequential files consisting of unblocked and expanded versions of the 'logical records' within the transport format. An index file was also

constructed which contained entries for each of these sequential files, describing the transmission time for the telemetry frames corresponding to the first and last record within each file. These files, together with the geographical data files (which contained balloon latitude, longitude, altitude and magnetic declination information) constituted the primary database which was physically stored on a 300 MByte dismountable magnetic disc pack.

Library routines were written to provide sequential access (including transparent logical reads across physical file boundaries) and pseudo-random indexed access seeks for record groups starting at a particular time (typically the observation period for a particular celestial source). The effective random access was achieved by using the index file to find the required data file and then by sequentially searching that file to find the desired starting record. Corresponding library routines were written for accessing the geographical data. In the case of latitude, longitude and altitude, this was achieved by interpolating tables which were read in at the start of an analysis run. In the case of magnetic declination, a functional fit to the magnetic declination data was evaluated.

The main use of the primary database was where information from other detectors besides the Ge(Hp) was required. For example, it was used to study the consistency of the relative firing rates of detectors in coincidence with the Ge(Hp). However, for the analysis of celestial source spectra, with which we are principally concerned here, this information is not normally required. Accordingly, a secondary database was constructed which contained only those events which involved the Ge(Hp) and no other data (ie. it contained 'actively vetoed' data). This secondary database was a single true indexed file (only about 8 MByte long) which contained celestial coordinates for each frame in a pre-processed form. These pre-processed Right Ascension and Declination values used an assumed transformation from frame time, alt-azimuth coordinates, and geographical position. This transformation was subsequently re-examined as will be seen. For such examinations, programmes had to revert to the more basic retrieval routines and recalculate the celestial coordinates. The file was indexed using a single primary index derived from the local frame time. A program could therefore access the reduced information from a specific frame simply by specifying its transmission time.

The secondary database gave efficient access to partially reduced data. It was possible to access the data from the entire 5 hour Crab observation, and derive and scan spectra, in under 10 minutes of CPU time on a DEC VAX 11/750. A number of access systems were developed for this database, including the possibility of 'registering' a 'frame envelope' describing restrictive limits on various frame variables. The access routines would then return only data from frames which passed these restrictions. The frame variables (not all independent) were universal time of transmission, zenith angle, azimuth angle, Right Ascension, Declination, latitude, longitude, altitude, pressure, residual atmospheric depth (vertical column density), geomagnetic declination, galactic longitude, galactic latitude and the number of events within the frame. Provision was made for only loading tables and accessing data which were actually needed for the calculation of results which had been registered as being required for a particular run. Several such runs could be executed concurrently within the same program.

5.2.3 Instrumental and atmospheric background lines.

The float spectrum for the entire flight was accumulated with no constraints on the data included in the spectrum (apart from the rejection of corrupt data and the requirement for Ge(Hp)-only events). This spectrum was then analysed with the HYPERMET line feature analysis programme which is discussed in appendix A.

The resulting Durham 1981 background lines are listed in appendix B and in Ayre et al. (1984). This is by far the longest such atlas yet produced. The reasons for this are the length of the flight, the stability of the instrument, the use of the HYPERMET spectral search program (see Phillips and Marlow 1976), and the efforts made to interpret the line origins. The background spectrum up to 700 keV is shown in figure 5.1. The total number of instrumental lines detected was 62, of which only 5 could not be ascribed to an atmospheric or instrumental origin.

The relevance of the background lines here is that they provide the energy calibration of the detector and establish the stability of the detection system; a vindication of the use of an environmental dome for the detector and nuclear electronics. There was no detectable change in the position of the 511 keV or

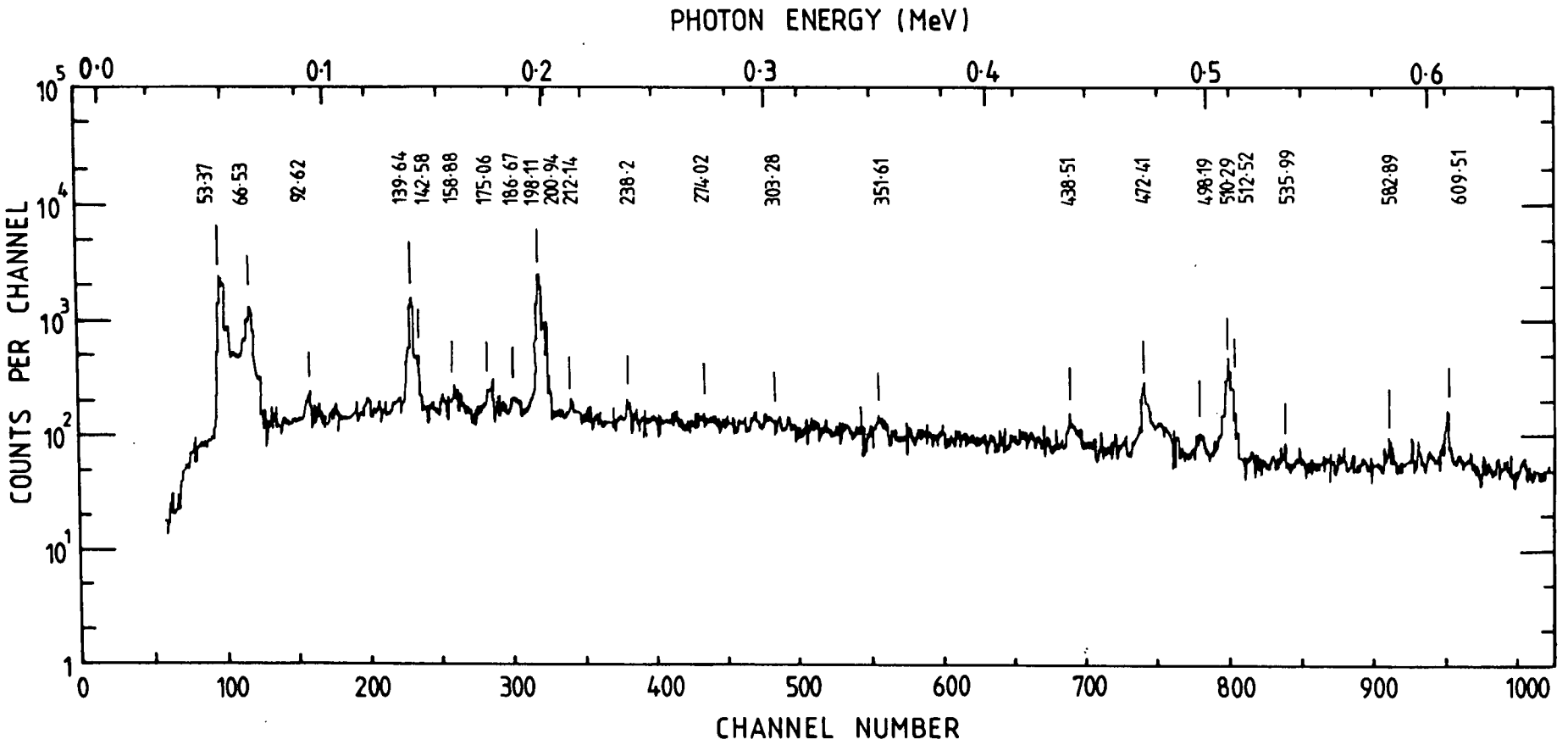

Figure 5·1 The measured background spectrum for an exposure of 5×10^4 secs at 5·4 mb over Palestine, Texas. From Ayre et al. (1984)

any other line throughout the flight. No gain drift compensation procedures were therefore necessary. In order to illustrate the gain stability, the 511 keV background line for the entire flight, including ascent, is illustrated in figure 5.2. Two components are resolved, one arising from atmospheric positron annihilation and one from the decay of ^{209}Tl. The table in appendix B gives the parameters of these two components.

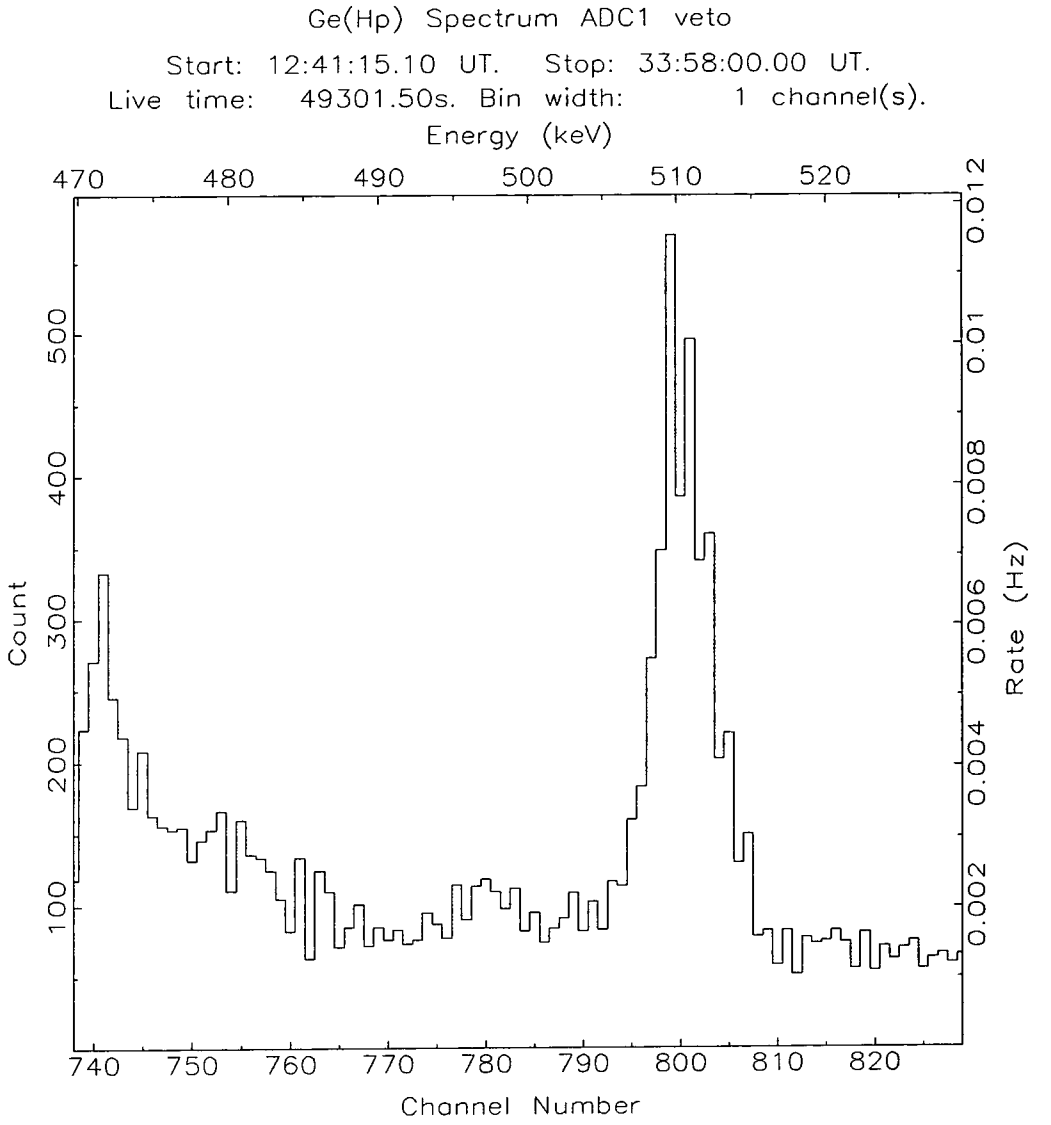

Figure 5.2. The 511 keV background line accumulated over the entire flight. The events were selected with the software active veto criterion operating: ie. events involving detectors other than the Ge(Hp) were rejected. Note that Universal Times (UT) on 7 June 1981 (the morning on which the flight ended) are represented by allowing UT to exceed 24.00. This technique simplified database construction.

As discussed in appendix B, the calibration technique can only be applied with certainty up to 2 MeV and this restriction was imposed on all analyses which required precise knowledge of energy; most notably it was used to restrict searches for celestial spectral lines. This is rather drastic, but the need for precise calibration will be clear when energy shifting of source emission lines is discussed subsequently. The need to reject data in order to eliminate systematic effects has been evident in analyses performed by other workers, notably in the reduction of HEAO C-1 and SMM data. Unless these effects can be understood, and it is entirely possible that the flight data itself does not contain the information for this, then data rejection is the only method of ensuring confidence in astronomical results.

5.3 Celestial source spectral analysis methods.

The methods for deriving and analysing celestial source spectra are described. This includes the calculation of continuum spectra, pulsar timing analysis, cross-correlation imaging, and scanning source spectra for line features. Various 'application programmes' were written to perform these analyses by accessing the flight databases using the methods described in the previous section.

It should also be noted that programmes were also written to perform various other analyses not directly connected with celestial source spectra. For example, the variation of background spectral features with azimuth, zenith, residual atmospheric depth and local time were investigated in order to eliminate systematic effects which could interfere with source observations. The results of these analyses were used in the correction of source spectra. No unexpected results were found (ie. nothing inconsistent with the results of previous workers, or theoretical predictions), although the varying atmospheric depth dependency of background lines, as described in appendix B, should be noted.

5.3.1 Source observation and net flux extraction.

Celestial sources were observed by azimuthal scan; that is, by causing the telescope to alternate between the celestial coordinates of the source to be observed and the coordinates of a 'background' region or regions displaced in azimuth angle alone from the source. As seen in chapter 3, some form of

azimuthal offset is the invariable choice for non-drift-scan telescopes; this is due to the strong zenith angle dependence of the atmospheric spectrum. The term 'background' is a little ambiguous, as the background — in the sense of the summed instrumental, atmospheric and diffuse celestial spectra — is still being measured when the celestial source is within the field of view. Accordingly the terms 'on-source' and 'off-source' are used to describe the observational modes and corresponding spectra acquired when the celestial source is respectively within and outside the field of view.

The off-source spectra have been used by all workers to derive net continuum spectra. The exception is timed observation of a pulsed source, where timing can be used to separate the flux within the pulse phase (which will clearly include a non-pulsed contribution) from the rest of the light curve. The off-pulse flux then may be subtracted from the pulse flux in order to remove the non-pulsed contribution and derive a net pulsed spectrum. In the present work, comparison of the on-source and off-source spectra is also used in celestial line searches. This can overcome uncertainties involved in attempting to search the on-source spectrum alone (sliding window analysis). Without a full spectral fitting algorithm such as HYPERMET, the sliding-window method is susceptible to the presence of unresolved instrumental lines close to a celestial line. (The reason why HYPERMET itself cannot be used for celestial sources is discussed in appendix A). However, when the off-source spectrum is to be used for this purpose great care must be taken that systematic effects are not allowed to introduce false differences between the on-source and off-source spectra. To an extent the analysis is self checking, as such false differences would be likely to involve the strong atmospheric lines. For example, an inadequate constraint on the allowed zenith angle difference between on-source and off-source spectra, will produce a spurious detection of net 511 keV flux due to the strong zenith angle dependence of the atmospheric 511 keV line.

The smaller aperture of the Durham telescope made it possible to sample off-source spectra much closer to the source than other telescopes. The off-source spectra were sampled with the detector axis offset from the celestial source direction by $5°-10°$. At this angular separation, the source would still have been well within the field of view of virtually all the other telescopes described in chapter 3. As discussed in chapter 4, close sampling of the off-source spectrum

is preferable because it reduces any hypothetical azimuthal or celestial variations in background, and, because the smaller azimuthal amplitude makes it possible to chop more quickly between source and background it can reduce temporal and altitude variations. The balloon's altitude varied as the flight progressed, which produced detectable spectral changes. Other temporal change arose from instrumental activation processes which did not reach secular equilibrium during the course of the flight. The rapid switching ($\sim$1 minute) between on-source and off-source meant that the off-source was effectively sampled concurrently with the on-source spectra because this period was much less than the characteristic timescale of any known systematic temporal variation.

As the detector axis scans across the source in azimuth, then the corresponding change in celestial coordinates depends upon the hour-angle of the source (Smart, 1977). Sources were observed while transitting in order to reduce zenith angle dependent background intensity. Therefore, throughout the course of the observation, the detector axis was scanned across a range of celestial coordinates. This permitted a degree of source imaging to be made with the Crab continuum flux.

In order to produce the on-source and off-source spectra, the data were examined frame by frame. The telemetry frame period (0.25 s) was the most frequent sampling of the pointing system transducers. From these transducer values, the zenith and geomagnetic azimuth angles were calculated from the pre-flight calibrations. The geographical position indicators from the telemetry ground frame were then used used to obtain an estimate of the geomagnetic declination by interpolating a fit to aeronautical chart data (this could well be the most error-prone part of the process). The true azimuth angle was computed by subtracting the geomagnetic declination from the telescope geomagnetic azimuth angle. The local siderial time (LST) was computed from the instantaneous geographical position of the balloon and the universal time (UT) at which the frame was transmitted. Using the standard formulae of spherical trigonometry (Smart 1977), the LST, azimuth and zenith angles were used to compute the instantaneous celestial coordinates of the detector viewing direction. Using the source coordinates, the angular separation of the detector axis and the source were computed; this is the so called polar angle. In fact, all the spherical trigonometry calculations were already present in the secondary database, only

the actual polar angle value for a particular celestial source had to be derived during a particular run. The exception to this was then the coordinate transformation itself was being investigated, in which case the calculations had to be effectively re-done.

Using the instantaneous polar angle, the information within the telemetry frame could then be assigned as either on-source or off-source, according to whether or not the polar angle exceeded a certain threshold. The threshold could be based either on the geometrical opening angle of the detector, or, when only events of a given energy were being examined, the energy dependent angular response function (see chapter 4). The events within the frame could then be selected on the basis of the detector event register; normally this would mean selecting events where only the Ge(Hp) detector had fired, hence producing actively vetoed on-source and off-source spectra. The instantaneous altitude and zenith angle were also required for correcting net fluxes (the difference between on-source and off-source rates in a particular energy channel) for atmospheric absorption. Using these parameters it was possible to compute the projected column density of air through which the detector was viewing the celestial source during any on-source frame.

In order to derive a net flux from a celestial source it was necessary to compensate not only for the atmospheric absorption but also the exposure factor obtained during the on-source periods. The exposure factor is the integral of the area of the detector, presented perpendicular to the source direction, with respect to time. This was again calculated on a per-frame basis, and — for the final source flux calculations — also included compensation for the energy dependent aperture response function (see chapter 4). Each energy region of the net spectrum was therefore calculated using a different exposure factor accumulated on a per-frame basis taking into account the transmission of the collimator for gamma rays of that particular energy at the calculated polar angle for that frame. The full energy peak efficiency of the Ge(Hp) detector, as described in chapter 4, was used to compensate the net spectrum for the response of the telescope. Allowance was also made for the energy-dependent absorption of gamma rays by the aluminium of the environmental dome and also for absorption by the column of air trapped within the dome, through which the collimated Ge(Hp) detector viewed celestial sources. The mass attenuation

coefficients for these corrections were obtained from Chupp (1976).

5.3.2 The spectral line search technique.

In the light of the problems with previous line search, methods particularly the 'sliding window' technique as discussed in chapter 3 and the fourth section of this chapter, a different technique was developed.

Li and Ma (1983) analysed the statistics of line searches involving the comparison of separate on-source and off-source spectra. If N_{on} is the on-source count obtained in some channel over a time period T_{on}, and the corresponding background N_{off} was obtained over a period T_{off}, then the significance S is approximated by $-2\ln\lambda$ where λ is given by

$$\lambda = \left[\frac{f}{1+f}\left(1+\frac{N_{off}}{N_{on}}\right)\right]^{N_{on}} \left[\frac{1}{1+f}\left(1+\frac{N_{on}}{N_{off}}\right)\right]^{N_{off}} \qquad (5.1)$$

and where $f = T_{on}/T_{off}$. The expression is derived by calculating the relative likelihood of the observed counts in the two spectra arising, within the observation times, from a) background fluctuations and b) the best estimate of the source flux (simply the difference of the two rates $N_{on}/T_{on} - N_{off}/T_{off}$). The relative likelihood is then used to estimate a significance as if the probability of the particular relative likelihood had arisen under a gaussian probability distribution. The expression was specifically designed, and tested using Monte Carlo simulations, for accuracy during line searching, which undermines the usual approximation that the parent value of a Poisson distribution is well estimated by the observed count, and that the error can be estimated by its square root. A line search invalidates this assumption by effectively picking out high fluctuations from the parent level in the on-source data and low fluctuations from the parent level in the off-source data.

This expression was applied to the on-source and off-source spectra at successive energies using a starting line width based on the known energy-dependent instrumental resolution. Once a threshold 'trigger' significance had been found at a particular energy, the width was adjusted to optimise the significance. The use of a trigger threshold keeps down the number of independent trials made to find a significant excess (as opposed to repeatedly scanning the spectra for excesses of various widths). The spectral regions over which the scan was

applied were constrained to energy ranges which were relevant either to specific physical processes or to previous line observations. A constant scan range of 10 keV was used in these cases. A general scan from 50 keV to 10 MeV was also performed. Naturally anything found in the constrained scans also appeared in the general scan. In each case the significances were reduced to account for the number of trials made. If P_r is the probability that an effect is due to a random fluctuation during one trial (this is derived from the significance given by the Li-Ma formula), then $1-(1-P_r)^n$ is the probability of it being produced by a random fluctuation in any of n similar trials. The scan result tables show $1-P_r$, the inferred probability that the feature was not produced by a random fluctuation at a specific energy. Also shown is $(1-P_r)^n$ the correspondingly reduced probability when the number of trials is taken into account. Where a feature has been found in a constrained search, the reduced probability is shown for both the constrained and general searches. The distribution of line significances (for positive and negative fluctuations) were accumulated in each scan and the result checked against the expected distribution of random excesses.

Temporal variation analysis.

Where there were sufficient data at both on-source and off-source positions, it was possible to break down an observation into temporal sub-sections or segments, and to re-run the line scan on each of these portions individually. In this way it was possible to check for variation of the flux, position or width of the line during the course of the observation. The independent detection of a flux in several sub-sections was also a check on the detection significance.

Line flux profiles.

Once a line had been found by the scanning technique, a flux profile was derived by producing a fully corrected spectrum in the peak region (using all the energy-dependent corrections required for a net source spectrum) and then fitting the resultant data with a function of the following form

$$F(E) = a_1 + a_2E + a_3E^2 + A\exp\left(\frac{E-E_0}{2\sigma^2}\right) \tag{5.2}$$

where $F(E)$ is the estimated flux value at energy E. This comprises a quadratic fit to the background (with parameters a_1, a_2 and a_3) and a superimposed gaussian peak with amplitude A, centroid energy E_0 keV and width σ. The

best values of a_1, a_2, a_3, A, E_0 and σ were found by selecting those which produced the minimum χ^2 fit to the flux profile and its associated channel by channel error estimates.

Although this is not sophisticated by the standards of, say, HYPERMET, it does provide a reasonably good centroid value and a feature width from which the instrumental resolution can be subtracted to obtain an estimate of the intrinsic width of the source line.

5.3.3 Additional source analysis techniques.

It was also possible to examine a source flux by pulsation timing analysis and by cross-correlation imaging. In practice, these could only be effectively applied to the Crab continuum flux for which sufficiently good statistics were available. These methods are therefore described in the specific context of the Crab observation.

5.3.4 Reduction Programmes.

The above analyses were performed by a set of programmes which scanned the databases and produced results directly, or which used a two-stage process of producing partially reduced data from the databases for input to separate programmes.

Common elements such as database access, detector calibrations, standard spherical trigonometry, line scanning, graphics etc., were provided as library routines which were shared between reduction programmes. The library currently contains some 265 routines (all but about 10 were written by the author), which clearly precludes their being described individually.

In order to provide a common means of controlling these programmes, a new command language was developed. The decoding of the language was in three stages. Firstly a number of 'pragmats' (42 at present) were available to the user which were processed first. These provided a number of facilities including nested indirected command files with parameters, local and global symbols, indefinitely nested, structured conditional input, the writing of control scripts to taylor the user interface, batch job control, interfacing with the operating system, command verification, and logging to produce a runnable

command script. The next level allowed physical values to be associated with units; for example, channel numbers could be specified directly, or in MeV, or in keV. Support was also provided for a number of time and angle formats at this level. Input was also checked for numerical range and validity; interactive error correction was available at all levels, including a facility to fix errors from within nested command files. The final level of processing was essentially a language for the description of hierarchical heterogeneous data by a consistent set of named fields with data types, multiple tagged fields of the same type, unions of several data types, vectors and matrices of homogeneous subsets and bulk (binary) stored homogeneous subsets. This system is transportable and versions have been coded in both the FORTRAN 77 and C programming languages. The detailed description of this system is outside the scope of the present work.

5.4 The Crab observation.

The Crab was observed from 17.01.15 to 21.51.52 UT on the 6 June 1981 using the observational technique described above. The continuum flux and pulsar light curve were derived for the purpose of confirming that the system was indeed observing the Crab and that the data processing technique was correct. A cross-correlation imaging method was used with the Crab continuum flux to check the pointing accuracy of the telescope. The Crab spectrum was then analysed for line features, both for the whole observation and for three temporal sub-sections.

5.4.1 The Crab continuum flux.

The Durham telescope was designed specifically for line detection. Nevertheless, it can still measure continuum spectra; not with a significance that can contribute greatly to the world data but to a degree which provides a useful indication of correct instrument function, pointing alignment and data reduction. It might also be employed to provide recalibration of the pointing system using the limited imaging capability to be demonstrated.

The total geometrical exposure factor to the Crab was 52203.7 cm^2 s, accumulated during 4413.0 s of on-source data along with 3756.25 s of effectively

concurrent azimuthally offset off-source data. The energy loss spectra for on-source and off-source ('background') are shown in figure 5.3. From these two spectra, a net continuum spectrum at the top of the atmosphere was calculated. This is presented along with the results of other workers in figure 5.4 which also shows a weighted best-fit to a power law of the form

$$\frac{dN(E)}{dE} = \beta \left(\frac{E}{E_0}\right)^{-\alpha} \tag{5.3}$$

The contour in fitted parameter space is at $\chi^2_{\min} + 2.3$, that is at a 68% confidence level for both parameters. The best values of $\alpha = 2.5^{2.7}_{1.2}$ and $\beta = 8.6 \pm 3.4$ photons $\mathrm{m}^{-2}\,\mathrm{s}^{-1}\,\mathrm{keV}^{-1}$, with E_0 set to 80. The use of E_0 was simply a device to provide circular χ^2 contours for the fitting routine.

Cross-correlation analysis.

A cross-correlation analysis (eg. Hermsen 1980) of the continuum data may be used to obtain the uncertain image which is shown in figure 5.5. Also shown is corresponding data from Schönfelder (1979) obtained with the MPI Compton telescope (see Chapter 3). The figure shows the location of AO535+26, which when flaring can complicate the Crab spectrum for wide aperture telescopes (see Hameury et al. 1983); as can be seen it may be ignored in the Durham observation.

The figure was obtained by simply moving the hypothetical source location around a grid of celestial coordinates and performing a complete analysis and correction of the total Crab data at each coordinate. The analysis was exactly the same as that described in the previous section, the only difference being that the source coordinates were changed. For each pair of source coordinates, the net flux from the Crab was derived and an intensity value was added to the map at the corresponding coordinates. As the corrections are based on the angular aperture response function, it follows that the most significant value in the 'image' should be obtained where the data most matches the instrument response function.

It will be noted that there is a discrepancy $\sim 1.4°$ between the expected peak of the distribution and the position of the Crab. This must be due to some form of error in the pointing system. Clearly this cannot be simply an offset error in celestial coordinates because the telescope has an alt-azimuth

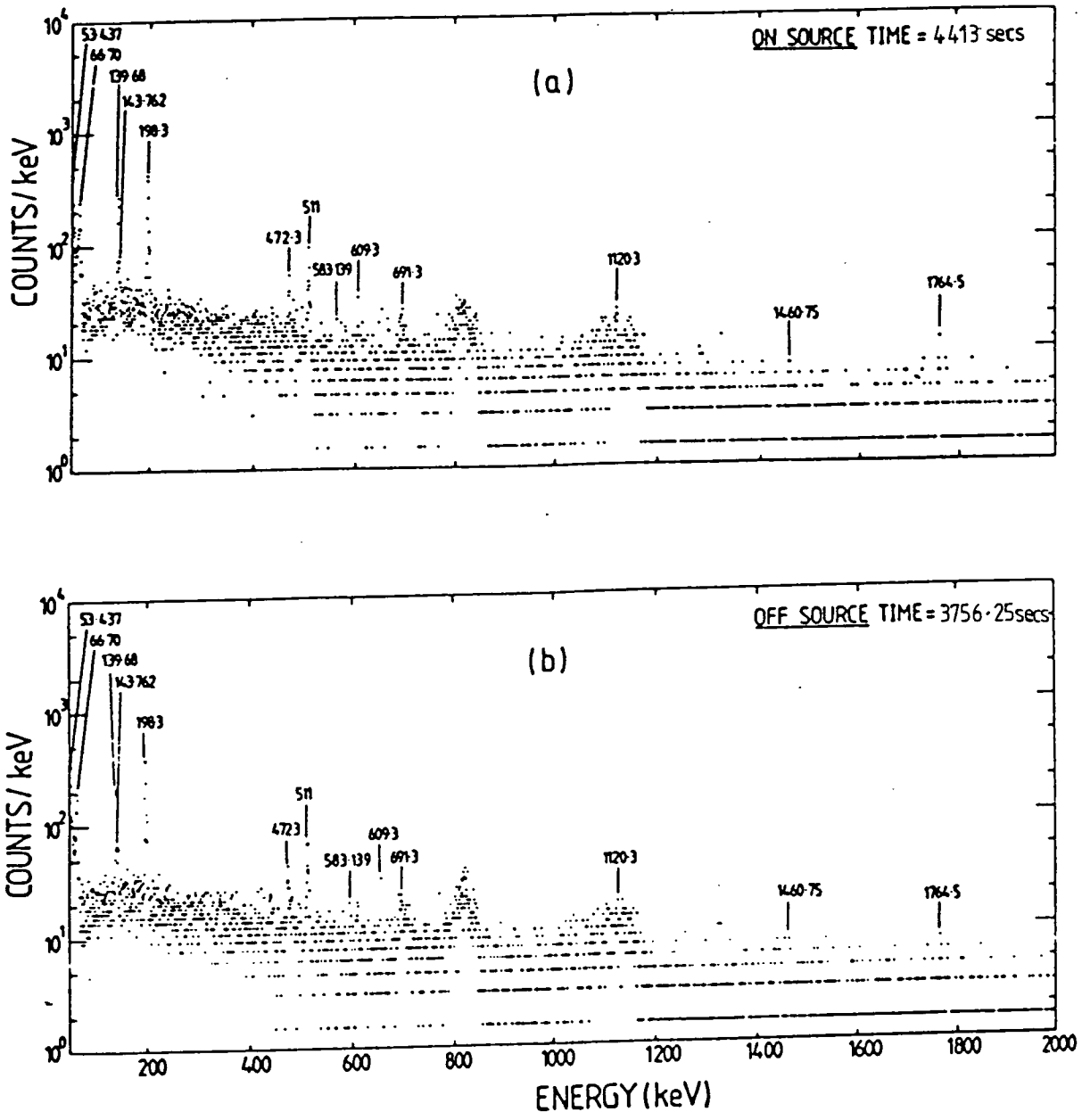

Figure 5·3 (a) The total energy spectrum – on source measurements,

(b) the energy spectrum for the background – off source measurements.

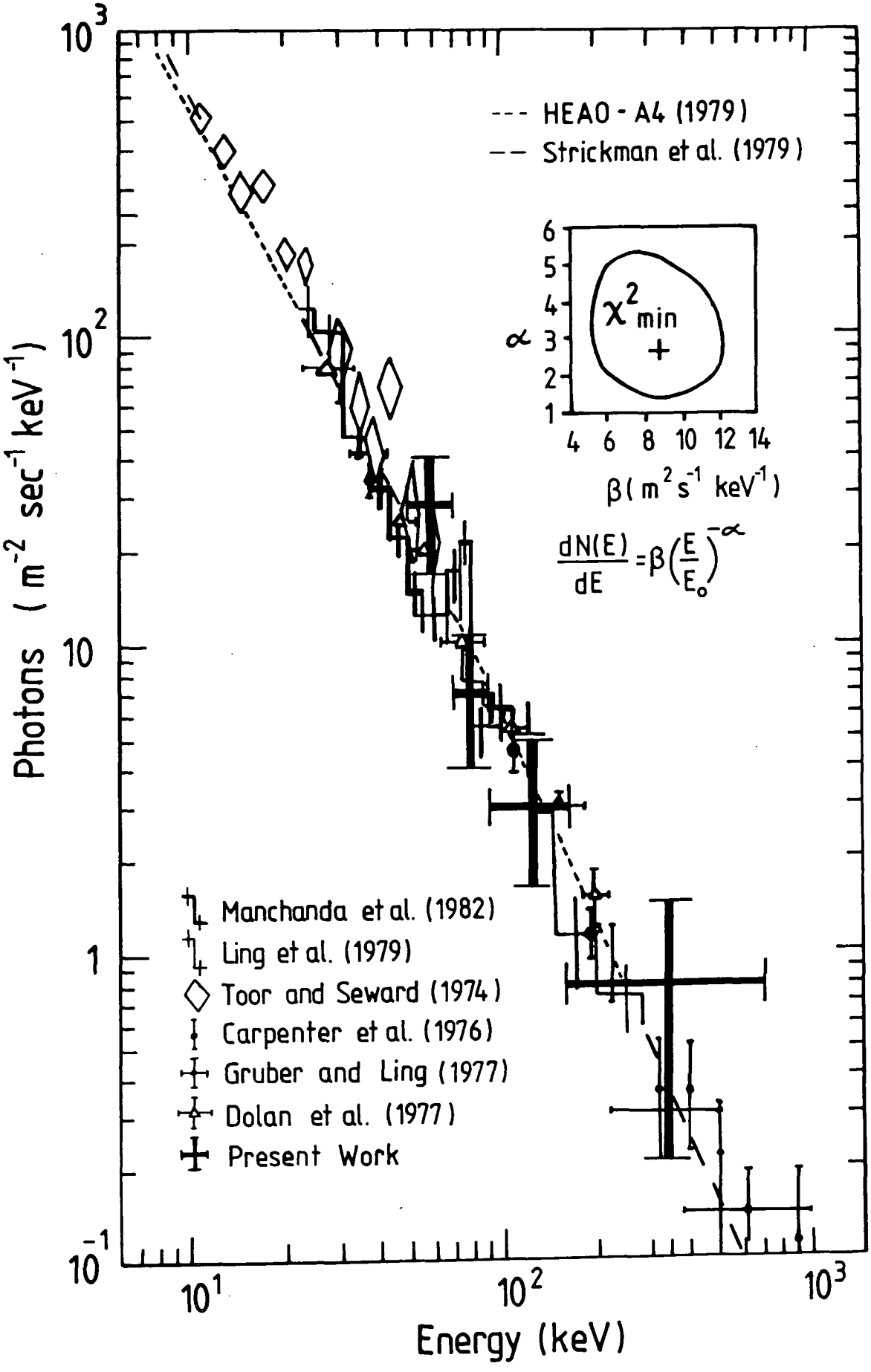

Figure 5·4 The net Crab Nebula photon spectrum measured on June 6 1981. The 68% confidence contour for a single power law fit of the form $dN(E)=\beta(E/80)^{-\alpha}$ is shown in the inset.

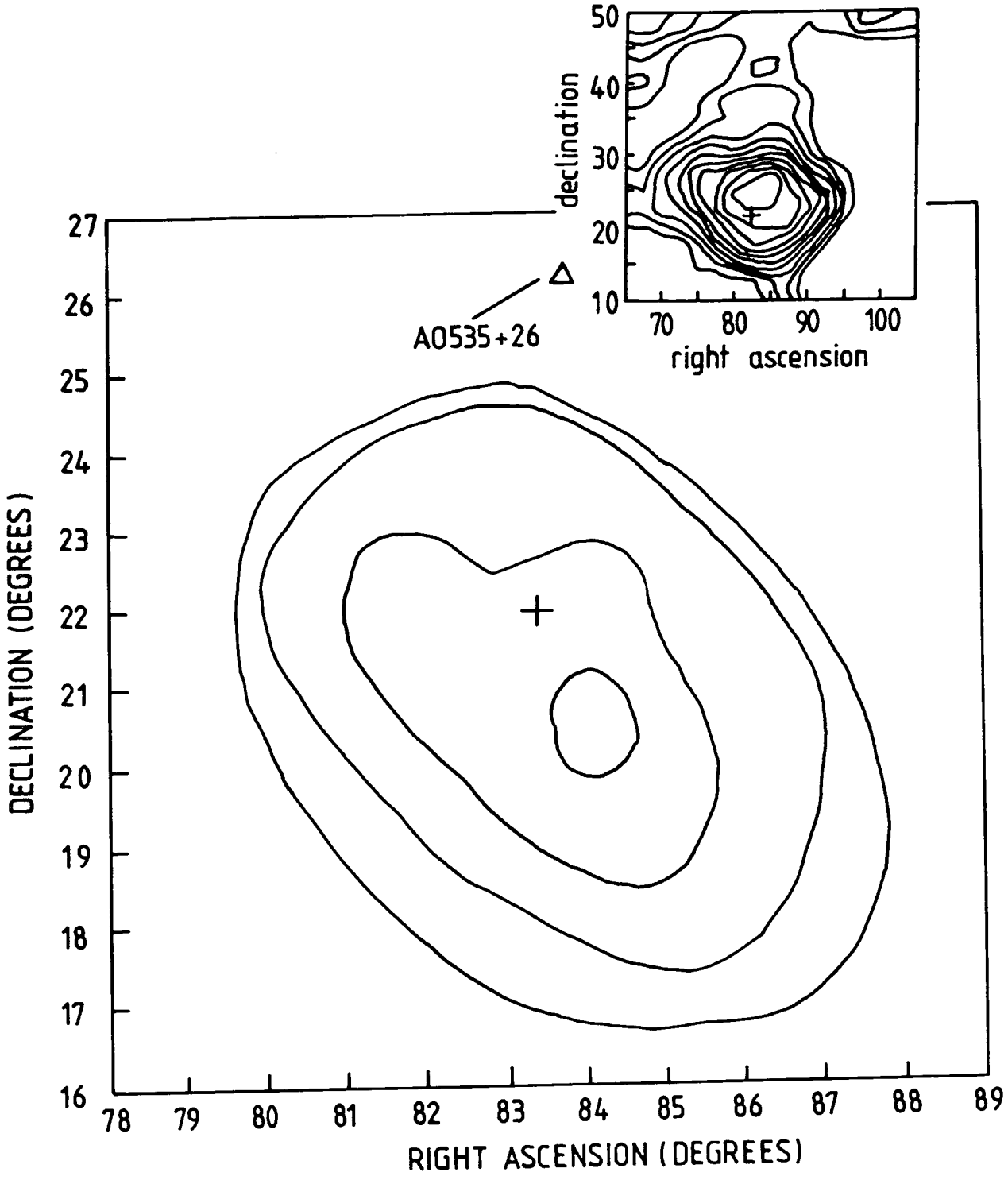

Figure 5·5 Results of a cross-correlation analysis for the field of view containing the Crab. The energy interval of accepted events is 50 to 350 keV. The contours represent positions where the correlation function has constant values at the nσ level. The cross denotes the true position of the Crab in 1950 coordinates. From the graph the error in the orientation system is estimated to be 1·4° rms. For comparison the inset shows the Crab imaged in 3-7MeV gamma-rays (Schonfelder, 1979).

mount and the celestial coordinates are obtained by a time dependent non-linear transformation of the alt-azimuth coordinates. The error has therefore probably been folded into this transformation throughout the observation and will have distorted the map in a non-linear way. Whatever the cause of the error, it would not be legitimate to use this map to correct the Crab data itself without some compensation for the number of statistical trials made to find as large a flux as possible by moving the hypothetical source location around the celestial, or any other, coordinate grid.

It is legitimate to attempt to correct the pointing system for the independent observation of another source, ie., NGC1275. The simplest hypothesis was that there were constant offsets in the azimuth and zenith pointing variables, perhaps caused by problems with alignment at calibration (such as a failure to find true North) or more likely by payload 'snatch' during launch. In order to investigate this idea, the above cross-correlation analysis was repeated using alt-azimuth instead of celestial coordinates. This was not expected to produce a sensible map, of course, but the peak of the distribution should correspond to the best estimate of the zenith and azimuth offsets if the hypothesis is correct. The derived values were 1° in zenith and 3° in azimuth. The azimuth value might seem large but it should be remembered that it has been derived from the discrepancy in polar angle which it has hypothetically produced. As the azimuthal offset translates to a polar angle offset as the sine of the instantaneous zenith angle, and the Crab was observed near transit, it follows that azimuth has little effect on the polar angle, therefore this determination of the azimuth offset has a large uncertainty (~2.5°). When these offsets were applied to the analysis of the 502 keV line from NGC1275 (to be described subsequently), the detection significance improved from $3.3\,\sigma$ to $4.4\,\sigma$. However, when a celestial map of this line was computed using these corrections (a dubious process in itself given the poor statistics of trying to image a single line), the peak of the distribution ($4.9\,\sigma$) was still offset by ~1° (though possibly subject to a large relative error).

The constant zenith and azimuth offset error hypothesis is therefore at best incomplete. There is probably another additional source of systematic error (perhaps a longitude dependent error in the geomagnetic declination). It may well be that the data do not contain sufficient information to correct this

remaining error. Indeed a protracted search for a suitable model would be illegitimate without an independent check. No doubt *something* could be found which would bring both the Crab and NGC1275 correlation functions to their expected positions. But the search for this would effectively be an attempt to maximise the apparent flux from NGC1275, as this would have been used as a figure of merit in the search.

Given the above problems, the alt-azimuth corrections have not been used for the basic analyses. However, it is still legitimate to note that the actual detection significance for the 502 keV emission line from NGC1275 is probably higher than the uncorrected determination. This suggestion is based on the independent determination of an error in the Crab analysis which seems to affect the Crab and NGC1275 data in the same way.

5.4.2 Crab pulsation analysis.

The Durham Mk. 1B spectrometer did not have the benefit of sufficiently accurate absolute timing to establish the absolute pulsar phase of an event. However relative pulse phase could be calculated and a light curve produced. This limitation restricted the basic utility of the exercise to a confirmatory rôle, as the number of trials introduced by the relative nature of the timing undermined the significance of any analysis which might be made of, say, the content of line features.

The event times were corrected to the solar system barycentre using a technique devised by Yau (1984). A period search was then performed by shifting the period over a range of values such that the total number of cycles which were included in the observation was varied by two. Each period value was tested by calculating the χ^2 of each resulting 'folded' trial light curve. The events used were obtained with the telescope look-axis within 3.8° of the Crab, and with strong background lines excluded.

The maximum light-curve χ^2 obtained (assumed to correspond to the best period) was 43 for 24 degrees of freedom. Using a pulse duty cycle of 60%, derived from Boldt et al. (1971), the expected value of χ^2 is 41. Given the trials involved the confidence level for this result is 61%. Figure 5.6 shows the total Crab observation for events from 50–2000 keV with an exposure factor

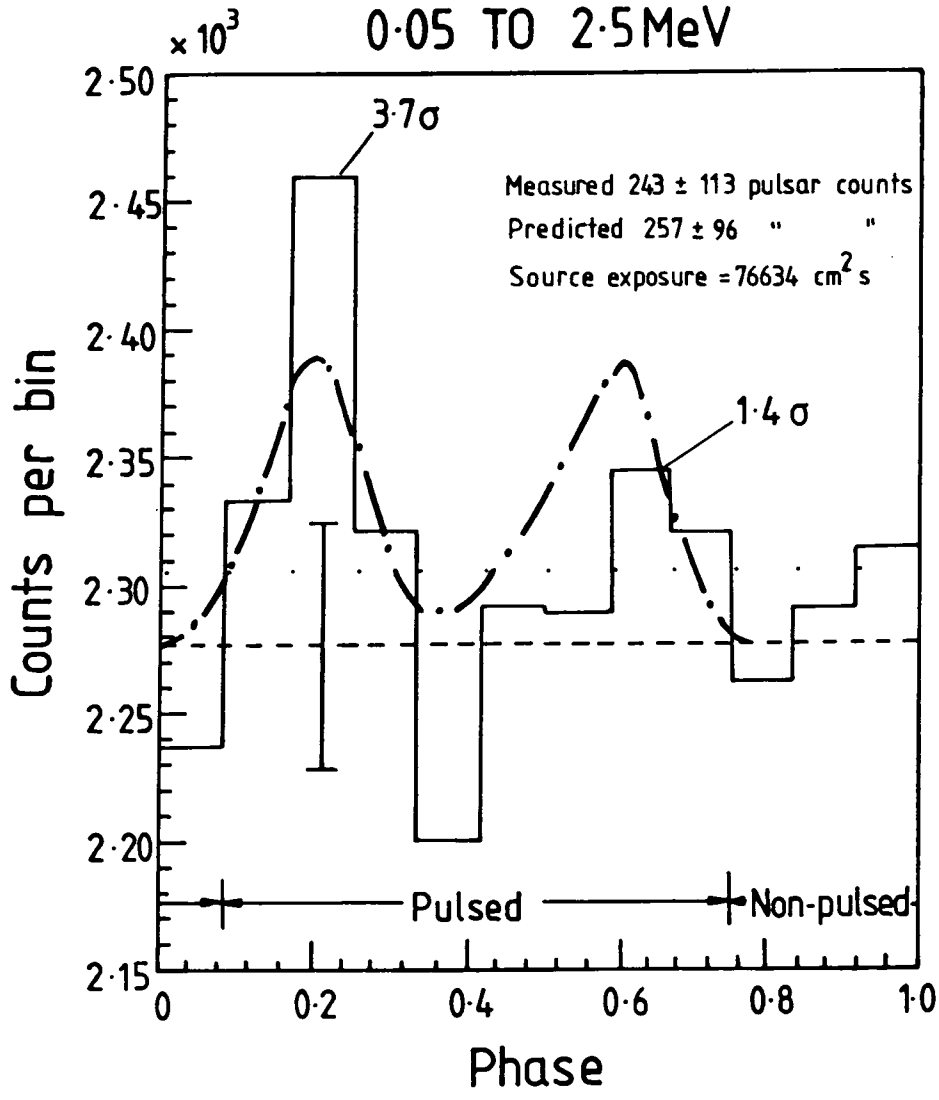

Key :-

..... mean number of counts per bin

– – – mean background

—·— predicted response assuming the power law source flux given in Mahoney et al. (1984)

Figure 5·6 Light curve in the energy range 50 keV to 2·5 MeV with 12 bins.

of 76634.2 cm^2 s. The expected response curve was obtained using the data of Mahoney, Ling and Jacobson (1984).

It is possible to produce a pulsed continuum spectrum by subtracting events whose pulse phase falls outside the pulse from those within (with suitable weighting of each flux by the fraction of the light curve from which it was drawn). The resulting spectrum is shown alongside other results in figure 5.7. This is obviously not of high significance but shows agreement with previous results.

5.4.3 Crab line Fluxes.

The data obtained using the on-source, off-source separation described previously were searched for line emission using the Li-Ma technique. The $> 3\sigma$ effects found in this scan are shown in table 5.1. Constrained searches were conducted in the energy ranges 395−405 keV and 70−80 keV where previously reported lines had been grouped (see chapter 3).

Table 5.1. Spectral line search results for the total period of the Crab observation.

Energy (keV)	Number of events		Li-Ma signif-icance ($n\sigma$)	Probability of non-random effect	Search Range (keV)	Degrees of freedom in search.	Reduced Probability of non-random effect
	On-source T_{on} = 4340.5 s	Off-source T_{off} = 3808.25 s					
328.7–331.3	73	31	3.5	0.999767	50-2000	2985	0.499
401.8–406.4	93	45	3.4	0.999663	395–405	14	0.995
					50–2000	2985	0.336
1044.6–1053.1	81	26	4.8	0.999999207	50–2000	2985	0.998
1954–1965	21	4	3.3	0.999517	50–2000	2985	0.236
1974–1980	12	1	3.1	0.999032	50–2000	2985	0.056
77.8–79.8	32	11	4.1	0.9999793	70–80	14 x 3	0.999
segment	T_{on} =	T_{off} =			50–2000	2985 x 3	0.831
3 only	1571.75 s	2019.5 s					

The table shows the specific significances and probabilities of the line if no trials had been made. There is then a predicted range for the peak which is based on previous observations in the case of the $\sim$ 400 keV and $\sim$ 77 keV lines (see chapter 3), or is simply the full scan range 50−2000 keV for the others. The number of trials associated with this scan range is then given along with a corrected confidence level taking it into account. This eliminates all line features

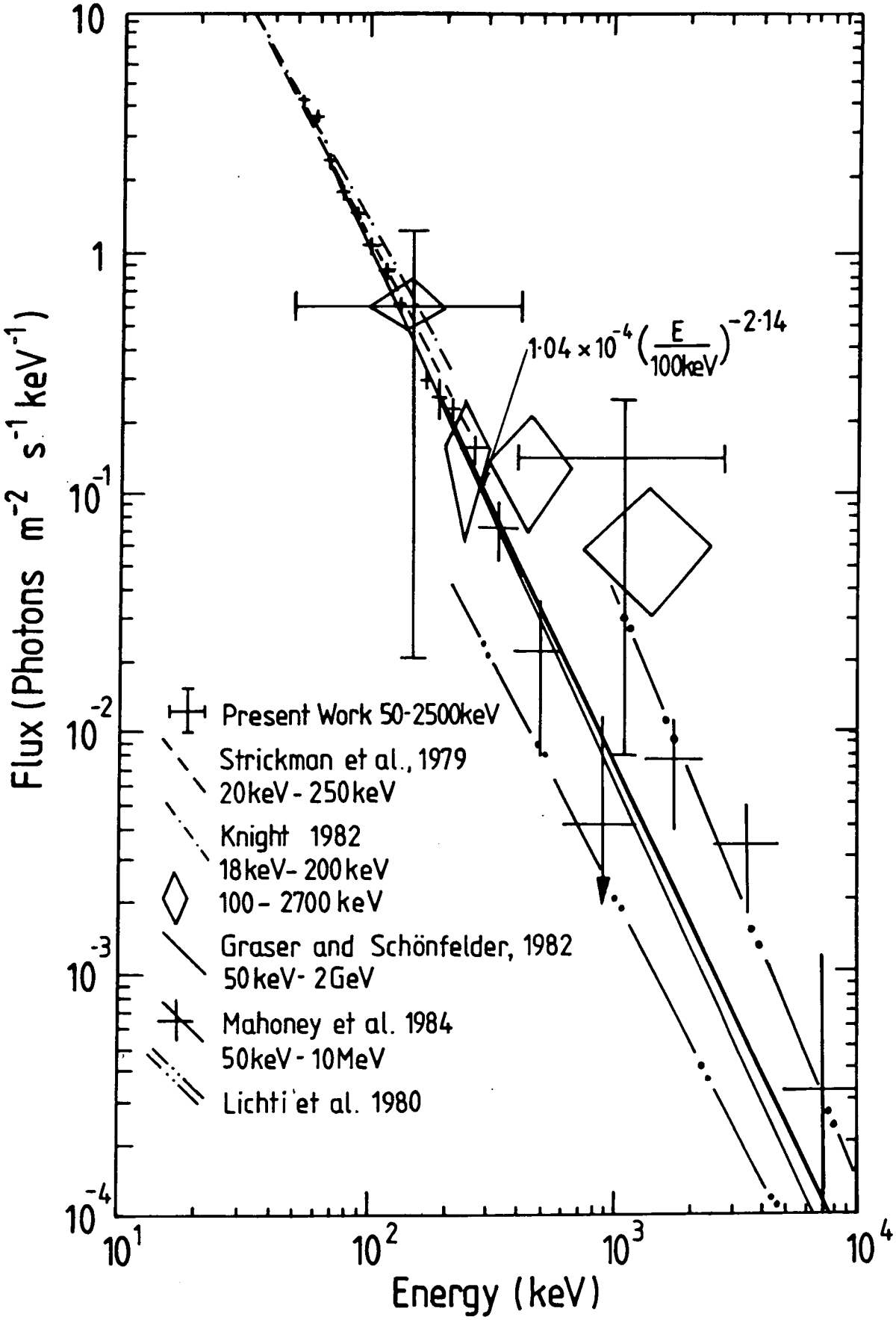

Figure 5·7 The net Crab pulsar spectrum measured on June 6 1981. An extrapolation of the COS-B data (Lichti et al., 1980) show that the data are consistent with a single power law from the x-ray to the high energy gamma-ray region.

apart from one at 403 keV (within the constrained scan range) and a second at 1050 keV. The table also shows a significant effect found at 78.8 keV in only a temporal subset of the Crab observation from 20.17.57 UT to 21.52.52 UT (the end of the observation). This was found as a result of a temporal variation analysis which is described in the following section. In order to take account of the extra trials made by dividing the data into three temporal segments and searching them individually, a factor of 3 has been included in the number of trials for this line.

Temporal variation analysis.
The data were divided into 3 time segments in order to investigate any temporal variations. These segments were then searched for lines using the technique described above. An apparently significant effect was then seen in the 77 keV region during the last segment, even when a factor of 3 had been introduced to allow for the number of trials. This line was therefore added to the other two for subsequent analysis. No additional significant lines were found, when judged by the criteria used for the search of the total data. The 1049.8 keV feature appeared at $> 3\sigma$ in each of the segments. The intensity variations of the three lines are shown in figure 5.8. A χ^2 test for variability of the data in this figure yielded percentage variabilities of <50% for the 404.7 keV feature, <35% for the 1049.8 keV feature, and $125 \pm 39\%$ for the 78.8 keV feature. Further subdivision of the data was not attempted due to the poor counting statistics which would have been produced.

Line profiles.
The flux profiles of the three lines corrected to the top of the atmosphere are shown in figure 5.9 along with best fit gaussian peaks superimposed on a quadratic fit to the background. The parameters of these fits, along with estimated luminosities for the Crab at a distance of 2 kpc, are shown in table 5.2.

The results are discussed further in the context of previous measurements.

5.4.4 Comparison of Crab results.

The observational status of the gamma ray line spectrum of the Crab region is complex, and the Durham results, though not inconsistent, add to the complexity. If we examine only positive results (including the present

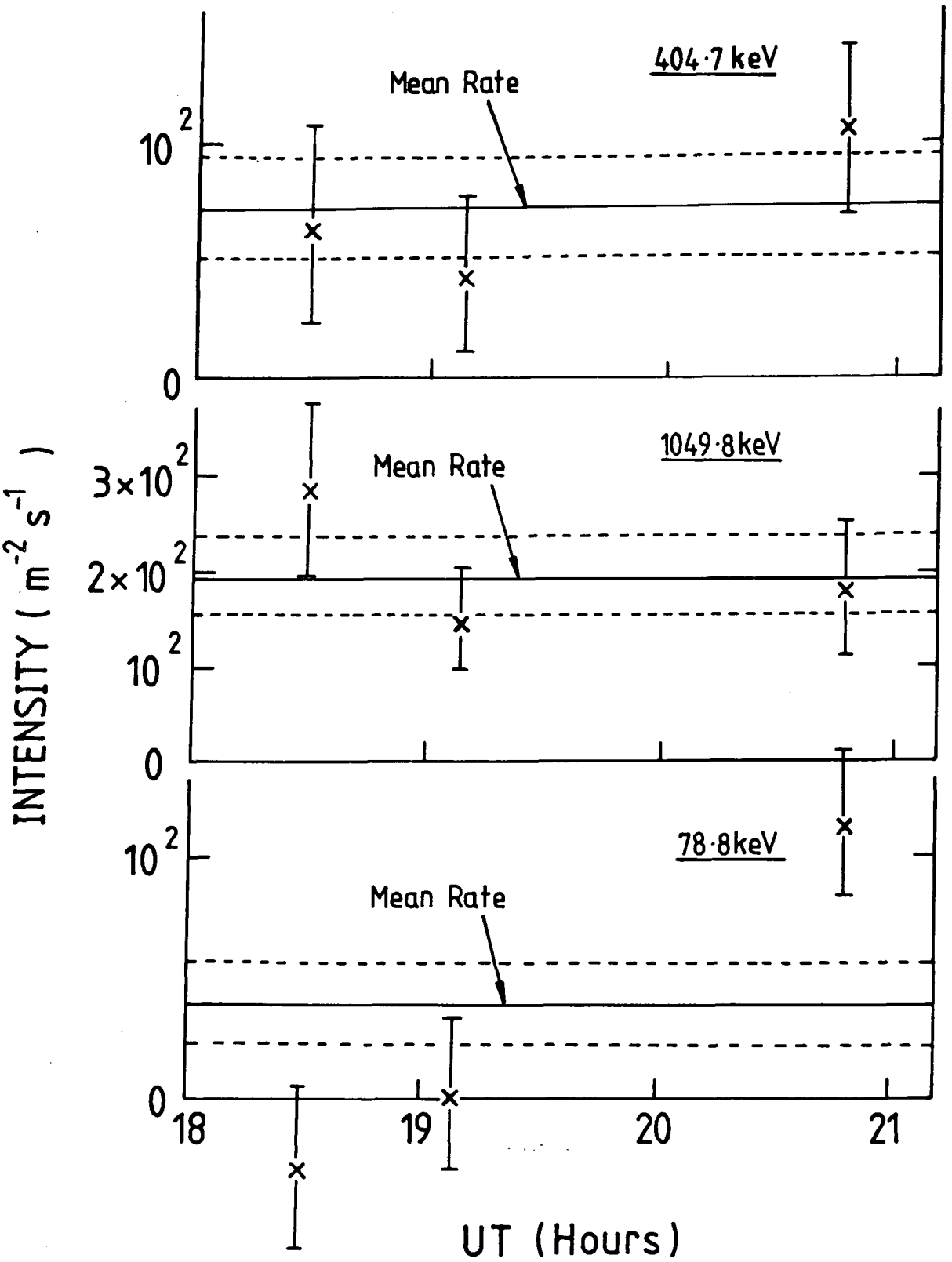

Figure 5·8 Variation in the intensity of the 78·8, 404·7 and 1049·8 keV line features during the observation period.

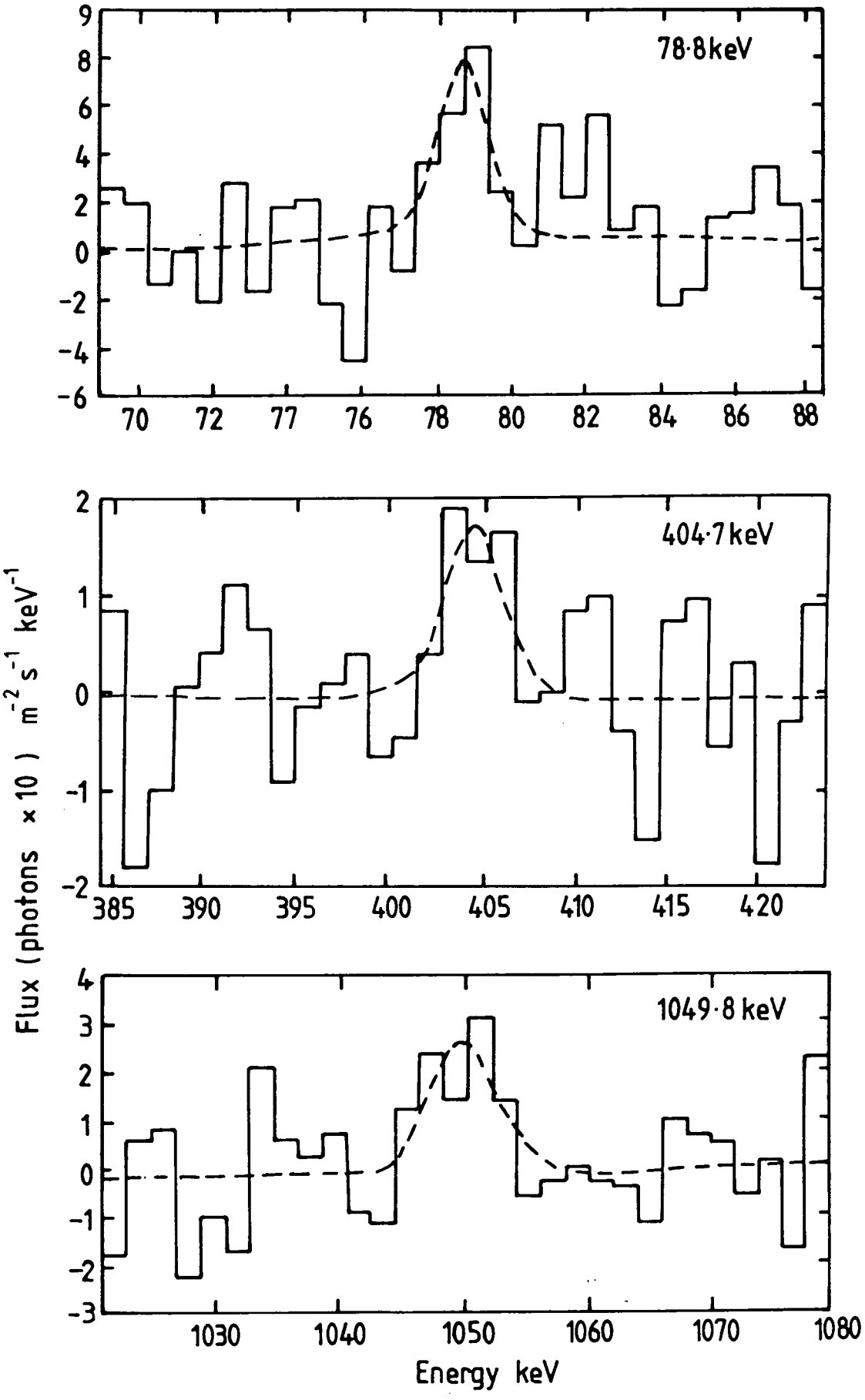

Figure 5·9 Line profiles of the three detected features after correcting to the top of the atmosphere. The dashed line on each profile is a best fit polynomial plus a Guassian peak.

Table 5.2. Parameters of the significant lines from the Crab. The 78.8 keV feature occurred only in the final temporal segment.

Centroid Energy (keV)	Flux $m^{-2}s^{-1}$	Measured width (keV)	Intrinsic width (keV)	Luminosity Watts
78.8 ± 0.2	110 ± 30	1.5 ± 0.4	< 1.5	6.3×10^{28}
404.7 ± 0.7	72 ± 21	3.8 ± 1.2	3.5 ± 1.4	2.1×10^{29}
1049.8 ± 0.8	200 ± 50	6.7 ± 1.4	6.3 ± 1.6	1.5×10^{30}

work), there are 5 reports of emission between 73 and 79 keV as summarised in table 5.3.

Table 5.3. Observations of Crab lines in the region 73 to 79 keV.

	Authors	Date d/m/y	Energy (keV)	Width (keV)	Intensity $m^{-2}s^{-1}$	Variable	Pulsed
A	Ling et al. (1979)	10/6/74	73.3	< 4.9	38 ± 9	No	—
B	Strickmann et al. (1982)	10/5/76	76.6	—	41 ± 12	$\sim$ 25 mins.	Yes
C	Manchanda et al. (1982)	26/8/79	~ 73	< 4	50 ± 15	No	—
D	Present work	6/6/81	78.8	< 1.5	110 ± 30	< 2 hours	—
E	Watanabe (1985)	29/9/82	~ 78	—	35 ± 19	No	—

There have been three reports of line emission between 400 and 405 keV as summarised in table 5.4. None of the observations involved a test for pulsation and none observed variability.

Table 5.4. Observations of Crab lines in the region 400 to 405 keV.

	Authors	Date d/m/y	Energy (keV)	Width (keV)	Intensity $m^{-2}s^{-1}$
F	Leventhal et al. (1977)	10/5/76	400	≤ 3	22.4 ± 6.3
G	Yoshimori et al. (1979)	30/8/77	400	≤ 3	74 ± 45
H	Present work	6/6/81	404.7	3.5 ± 1.5	72 ± 21

The first problem is how to treat the various negative searches for these lines which are described in chapter 3. Some of the searches were made with high resolution detectors and the resulting spectra were examined only at the originally reported energies, the analyses having been conducted before energy variability

had been suggested. These searches may therefore have missed the lines if they had been present and shifted. Other searches were made by comparing a 'sliding window' of the source spectrum with an adjacent spectral 'background' region. This technique does not provide for the correct continuum fitting and feature separation required by a spectrum analysis program such as HYPERMET, which is described in appendix A. The sliding window technique would therefore be susceptible to the presence of unresolved instrumental background lines adjacent to a celestial line. As many of these are specific to instrumental designs (see appendix B for some examples) they cannot be easily anticipated. It is therefore not possible to be definite about the negative results, however for the 73−79 keV result there are the explicit observations of variability (B and D). This adds another problem of interpretation, in that some negative observations may not have been sensitive to flaring effects. An important example being HEAO C-1, where the scanning observation mode might have prevented the detection of such a source.

The energy variability is well established in the sense that A and D for the lower energy line, and F and H for the higher energy line, were $>3\,\sigma$ detections conducted with Ge detectors. The line centroids were therefore accurate to within 1 keV. We have, therefore at least a $5\,\sigma$ measurement of shifting in both cases if all observations are assumed to be true. There are insufficient data to attempt to analyse the pattern of energy variability, however, because B and C, being lower spectral resolution observations, are compatible with more or less the whole observed range of source energies.

The 1049.8 keV result is the first such observation, but due to its high significance, and independent detection at $> 3\,\sigma$ in the three time segments, it may be considered along with the others. Continuum spectral excesses in the 1 MeV region have been reported by Baker et al. (1973) and Gruber and Ling (1977), but were not confirmed by Schonfelder, Lichti and Moyano (1975) and Carpenter, Coe and Engel (1976). For other high resolution spectrometers, no spectral searches at this energy have been reported.

5.4.5 Implications of the Crab results.

Ling et al. (1979), Strickman, Kurfess and Johnson (1982) and Manchanda et al. (1982) all suggest a cyclotron origin for the 73−79 keV line. Given

the pulsed and time variable nature of the line, this seems reasonable. This implies an intense magnetic field which would arise only close to the pulsar and therefore some gravitational redshift must be inevitable. Given a gravitational redshift $z = 0.2$, then a magnetic field strength 8×10^8 T would be required. However, Strickman, Kurfess and Johnson (1982) show that if an allowance is made for beaming towards the observer with an electron Lorentz factor 10^3 then only 10^6 T is required. The fundamental difficulty with this interpretation is the narrowness of the line, which constrains the emission region to a very small volume.

Leventhal, MacCallum and Watts (1977) suggested redshifted positron-electron annihilation as the origin of the 400 keV effect. The line energy does not correspond to any predicted de-excitation line which might be expected to come from the nebula, so the attribution to the pulsar is again probably reasonable. The present work would be consistent with 10^{42} positrons annihilating each second. The difficulty is again the narrowness of the observed lines. The constraints on temperature and the radial extent of the emission region are again problematic. The GRASAR mechanism (see chapter 2), suggested by Varma (1977) and later refined by Ramaty, McKinley and Jones (1982) and Varma (1983), offers the possibility of producing a narrow line in the 400 keV region without redshifting. The mechanism involves stimulated annihilation in a relativistic electron-positron pair plasma. This mechanism is also suggested for the 400−460 keV lines observed in burst spectra (Hurley 1987).

The 1049.8 keV line does not correspond to any of the lines predicted for supernova nucleosynthesis, as discussed in chapter 2, so it seems reasonable to rule out the nebula as a source. Equally, this line does not correspond to any of the predicted lines from accretion on to the neutron star surface (Higdon and Lingenfelter 1979, Brecher and Burrows 1980), even when allowance is made for a gravitational redshift. It does however seem consistent with the prediction by Harding (1987) of a narrow feature in the 1 MeV region from single photon annihilation in intense magnetic fields $\gtrsim 10^8$ T. To quote the author: "The one-photon annihilation spectra have a fine structure near threshold, ~1 MeV... in other words the kinematics of the one-photon process preserves narrow lines even in the presence of strong thermal broadening. The possibility of observing this fine structure, which is a direct consequence of quantum effects

in superstrong fields, may be possible with high resolution detectors." In order to achieve as narrow a line as observed, the positron temperature must be <100 keV. This is less than the lower limit of the range of hypothetical pair temperatures to which the theory was originally applied. Whilst a more or less convincing explanation can be found for each of the lines individually, when they are examined collectively and placed in the context of pulsar high energy emission models, it becomes clear that the theories, though the most sophisticated and successful available, are too limited to be able to model the electron-positron structure of the magnetosphere in the detail required. For example, the assumptions in the theory of Ramaty, McKinley and Jones (1982) explicitly prevent it being used to study a beamed effect or to study a pair plasma in an intense magnetic field. It is therefore impossible to place this mechanism convincingly in the context of, say, an outer gap pair production region.

Obviously, as two of the lines actually require positrons to produce them, there is considerably more support for the gap models, which actually require pair production, than for the wind zone and light cylinder models, which do not. The requirement for intense magnetic fields $\sim 10^8$ T for the 73–79 keV and 1049.8 keV lines might mitigate somewhat for the adapted inner gap model of Morini (1983) rather than the outer gap of Cheng, Ho and Ruderman (1986) where fields of only 100 T are present in the pair production region. The gap widths implied by the naive application of the GRASER theory of Ramaty, McKinley and Jones (1982) would also generally support this. It should be noted that the model of Cheng, Ho and Ruderman (1986) explicitly forbids the existence of pairs outside the gap region. The width of the lines is a severe constraint on the size of the emission region in all cases. However, given the difficulties in applying the emission theories to the magnetospheric models it is probably wise to treat these ideas carefully. It should also be noted that there is no particular reason to assume that all the emission lines, if real, occur in the same region, particularly given the apparently uncorrelated temporal behaviour of the 73–79 keV effect with respect to the other two.

The important point is that the theories are strained by these observations, something which has not been true since the successful explanation of the high energy emission and the pulse structure of the Crab and Vela. If

these lines can be confirmed by further observation and their pulsation and temporal variability investigated, then they might provide extremely useful, if not otherwise unavailable, information on the the magnetospheric structure, the rôle of positron-electron pairs in pulsar emission mechanisms and the physics of intense magnetic fields. It would be necessary, if the lines were confirmed, to extend not only the generality of the emission theories, but to include specific gap widths and locations, magnetic and electric field uniformities, pair temperatures, and the ultimate disposition of the positrons and electrons; within the pulsar emission models themselves.

5.5 The NGC1275 observation.

Observations of NGC1275 were made between 14:55:00 and 16:55:00 UT on 6 June 1981. Observation and data reduction techniques were as described for the Crab.

5.5.1 NGC1275 continuum flux.

The total source exposure factor was 53836.5 cm^2 s, with T_{on} = 3852.7 s and T_{off} = 1150.8 s. The continuum flux was calculated and is shown in figure 5.10 together with previous work. Though mostly upper limits, the results do demonstrate some broad agreement with the other results, bearing in mind the variability which the other authors report.

5.5.2 NGC1275 line flux.

The data were searched for line emission in the same way as the Crab. In this case, the only constrained search region was a 10 keV window around the expected cosmologically redshifted energy of the positron-electron annihilation line which is 502.17 keV The results are presented in table 5.5. Only one significant result emerges, that is at the predicted redshifted annihilation line energy. The corrected flux at the top of the atmosphere was (71 ± 22) photons m^{-2} s^{-1}, the line centroid energy (derived from a gaussian fit) was 501.9 ± 0.7 keV, and the intrinsic line width was (3.27 ± 1.3) keV. The corrected flux profile and best fit gaussian peak (with quadratic background) are illustrated in figure 5.11. Due to the general undersampling of the off-source data in this observation (only 1150.8 s as opposed to 3852 s of on-source data), it was not possible to

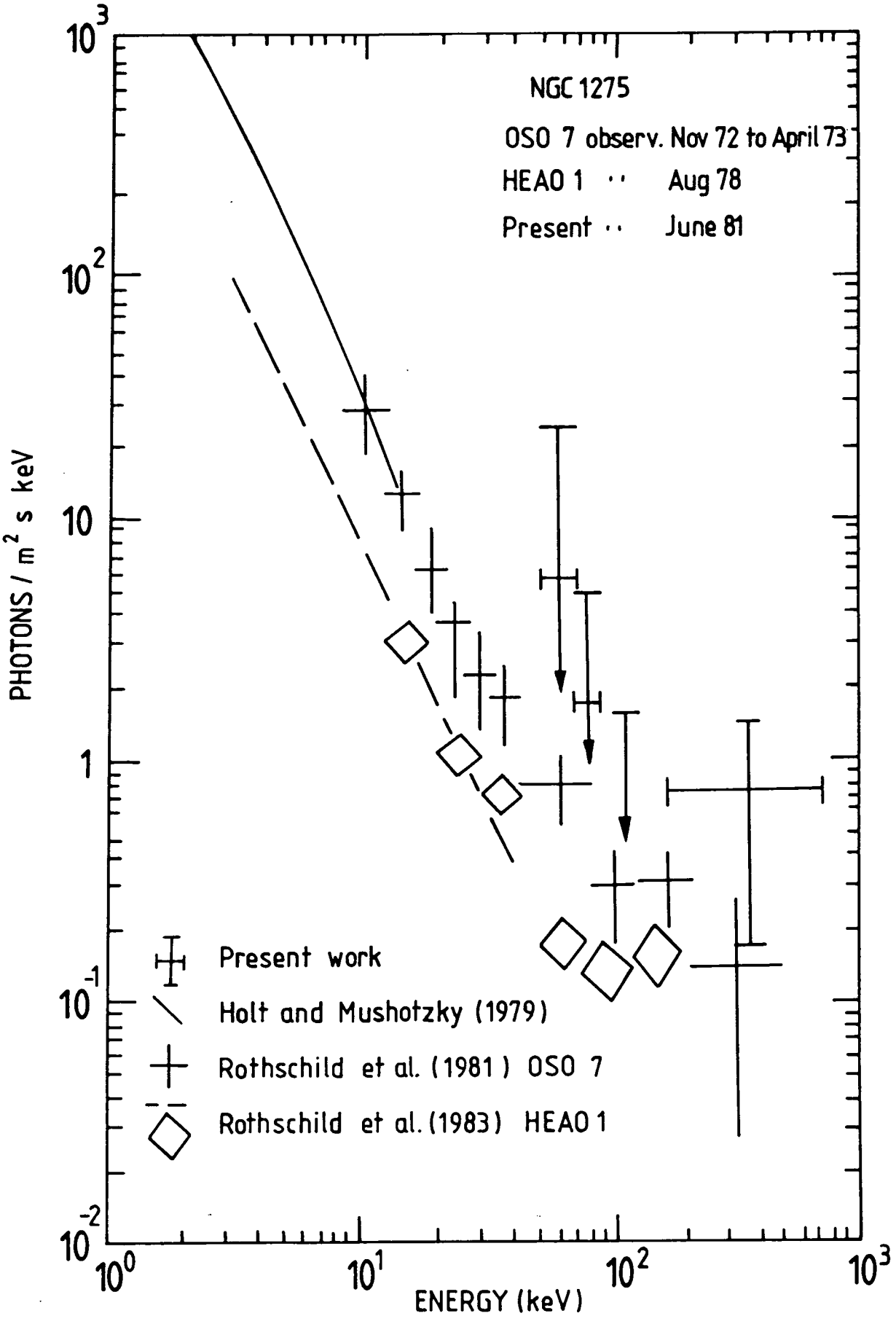

Figure 5·10 Energy spectrum of the Seyfert galaxy NGC1275 in the direction of the Perseus cluster. The upper limits obtained by the present experiment are at the 1σ level. Variability is evident.

construct suitable temporal subdivisions for the analysis of temporal variation is in the case of the Crab observation. The techniques used to derive these results were identical to those used in the analysis of the Crab lines. The 502 keV result is discussed further in the last section of this chapter.

Table 5.5 Line search results for the total period of the NGC1275 observation.

Energy (keV)	Number of events		Li-Ma signif-icance ($n\sigma$)	Probability of non-random effect	Search Range (keV)	Degrees of freedom in search.	Reduced Probability of non-random effect
	On-source T_{on} = 3852.8s	Off-source T_{off} = 1150.8s					
500.47–503.73	41	2	3.3	0.999517	497–507	14	0.993
					50–2000	2985	0.236
618.05–623.93	56	5	3.1	0.999032	50–2000	2985	0.056
909.41–912.68	32	1	3.3	0.999517	50–2000	2985	0.336

It is worth noting that when the (flawed) alt-azimuth offsets derived from the cross-correlation analysis of the Crab continuum flux were applied to the analysis of this line, the effective detection significance increased to $4.4\,\sigma$ with a celestial map peak at $4.9\,\sigma$.

5.5.3 Implications of the NGC1275 result.

The peculiar active galaxy NGC1275 is A426 in the Perseus cluster, of which it is the optically brightest member. It was originally classified as a Seyfert galaxy; in fact the nucleus is of BL Lac type. This means that it has the nonthermal optical continuum characteristic of Seyferts but lacks the usual strong broadened emission lines. Optically, the flux from the nucleus is extremely variable.

The VLBI radio-frequency map shows the nucleus to occupy $<10^{-14}$ of the volume of the galaxy (Preuss et al. 1979). The galaxy itself is peculiar and optically shows filaments around the nucleus. Einstein satellite data show that the soft to medium X-ray emission also follows the filaments (Grindlay, Branduardi and Fabian 1979). It is possible that these filaments are ejected from the nucleus, or they may consist of accreting cold gas such as seen in Cen A.

Spectrophotometry of the rest of the galaxy shows a very high supernova formation rate of approximately 1 per year. The proportion of B stars is very

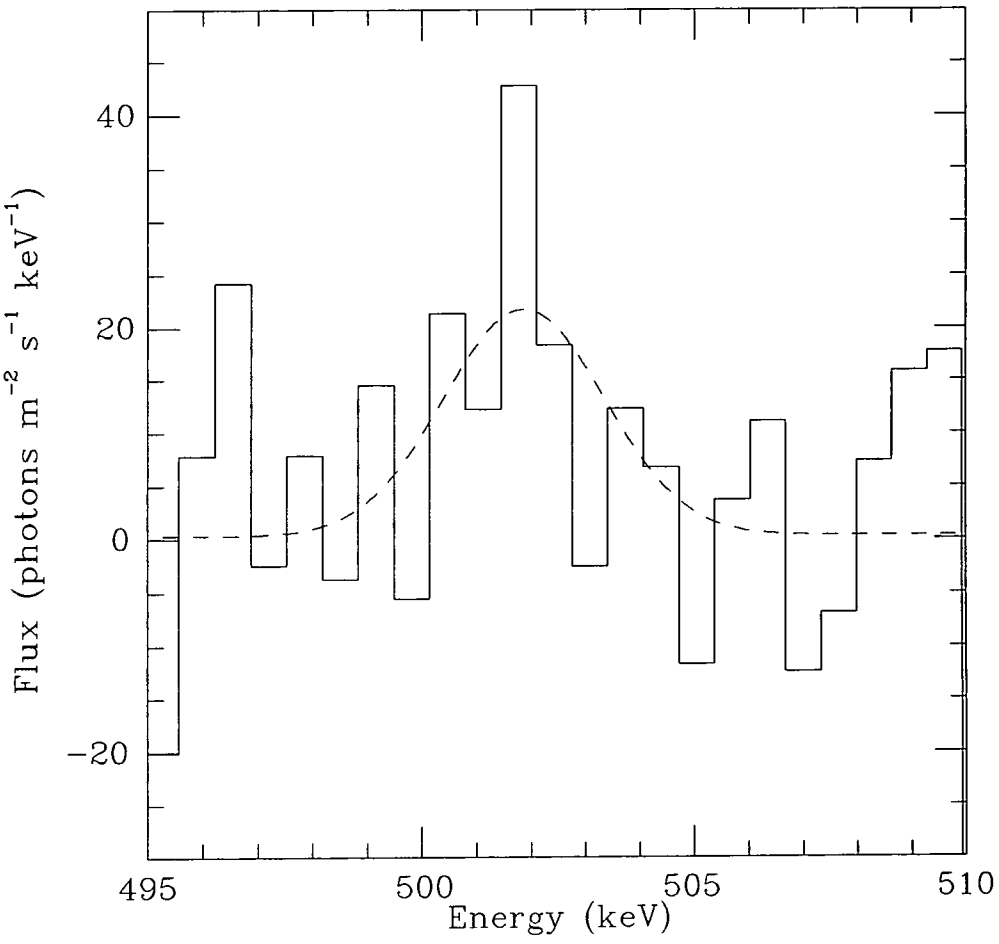

Figure 5.11. The corrected flux profile for NGC1275 in the region of 502 keV. The dashed line is a best fit (minimum χ^2) gaussian peak and quadratic background.

high and seems to indicate a star formation rate of $30\,M_\odot\,yr^{-1}$ (Wirth, Kenyon and Hunter 1983). There is also evidence that intracluster gas is accreting into the galaxy (Fabian and Nulsen 1977).

Rothschild et al. (1981) examine the hard X-ray data from the HEAO 1 (1978) and OSO 7 (1972) satellites. The thermal component ($kT \approx 6.6$ keV) becomes unimportant at the present sensitivities above 20 keV. However there is a non-thermal component with spectral index ~ -1.5 which shows variability on timescales less than 1 year. The authors attribute this to synchrotron self-

Compton radiation linked to the radio emission. The hard X-ray measurements lack the sensitivity and spectral resolution to have detected the Durham 502 keV gamma rays, although there does seem to be evidence of a consistent upturn in the spectra. On the other hand, the Durham telescope lacked the continuum sensitivity to constrain the hard X-ray emission. Had this been possible, the relationship of the annihilation line to the non-thermal continuum flux could have been investigated. Additionally the positronium fraction could have been determined, or at least constrained. Simultaneous hard X-ray and high spectral resolution gamma ray studies of this object could be very valuable indeed.

Even without a firm knowledge of the continuum, the apparent existence of extremely narrow, unshifted (at source) positron-electron annihilation radiation from this source might still be a powerful constraint on understanding the source. The first question is the origin of the radiation: the nucleus or the outer galaxy. This could easily be established by a study of the temporal variation or lack thereof. Unfortunately the only other high spectral resolution measurement, the HEAO C-1 observation of Wheaton et al. (1987) is difficult to understand (see Chapter 3). There does seem to be some evidence of emission but it is shifted to a slightly higher energy. There were apparently difficulties with the analysis of this source, and if we speculate that this (perhaps coupled with line and/or continuum variability) might have created the shift, then we cannot rely on the flux measurement. This is a factor of 35 ± 10 smaller than the Durham result and was taken about 18 months before, so it would have indicated variability and constrained the source to just over a parsec in extent.

Even without the direct evidence of variability, it is difficult to conceive of a diffuse mechanism to produce the Durham measured intensity. If we examine the mechanisms offered by Share et al. (1988) to explain their measurement of diffuse 511 keV radiation within our galaxy, such as supernovae, novae, Wolf-Rayet stars, and attempt to extrapolate these to NGC1275, we see that optical spectrophotometry would support an increase by a factor $\sim$40 in these phenomena (Wirth, Kenyon and Hunter 1983). If we take the Hubble constant to be $H_0 = 50$, then the redshift of NGC1275 places it at 70 Mpc. Taking the point source model flux value for our own galaxy from Share et al. (1987) ($21 \pm 4\,\mathrm{m^{-2}\,s^{-1}}$) and placing this at 10 kpc, we see that a corresponding source in NGC1275 must be $\sim 10^8$ times more intense in order to produce the Durham

result. Likewise such an increase in the cosmic ray intensity in NGC1275 with respect to our own galaxy, where a cosmic ray/ISM source of positrons was predicted by Ramaty, Kozlovsky and Lingenfelter (1981), is difficult to conceive.

If we tentatively take the source of the positrons as being the active nucleus, say under the model-independent photon-photon mechanism of Matteson (1983), then it is interesting to speculate on how cooling to produce an unbroadened line could take place. Dallaporta (1984), reviewing active galactic phenomena, describes the two current models of BL Lac type nuclei. One model explains the absence of broadened line emission by proposing that the rapidly moving clouds surrounding the nucleus (the broad line region, BLR) is absent in BL Lac type objects. Another model proposes that the continuum producing emission mechanism in Seyferts involves directed jets at the nucleus, which in the case of BL Lac types simply happens to be oriented in the line of sight of the observer, hence multiplying the continuum intensity and overwhelming any line emission. The electron-positron annihilation line observation would appear to support the former model, as the presence of the BLR would certainly lead to a broadened annihilation line component, which is not observed. However, the cool filaments would appear to provide a possible annihilation medium for positrons flowing from an unshielded nucleus (see Brown 1985 and Brown, Leventhal and Mills 1986).

The present result alone is not sufficient to make such a distinction, however it illustrates very clearly the potential of further observations of this feature, preferably with simultaneous hard X-ray and radio observation. A determination of line variability in relation to other energies and a measurement of the positronium fraction, could constrain the production and annihilation modes of the positrons sufficiently well to profoundly influence our understanding of NGC1275 and possibly of active nuclei in general.

Appendix A.

Description of the HYPERMET programme.

The HYPERMET computer programme was written at the Naval Research Laboratory, Washington, D.C. and is now available at a number of installations. The main documentation is the report by Phillips and Marlow (1976). The purpose of the programme is the analysis of gamma ray spectra from high resolution (germanium) detectors. The output of the programme is a list of parameters of all detected narrow peaks which conform to various preset constraints. The algorithm is sophisticated and can achieve very high performance in virtually automatic operation. It is easily able to distinguish features so confused as to be invisible to a search by eye.

The use of the programme in the present work was restricted to the analysis of background lines (see appendix B). The programme is fundamentally unable to deal with lines which have an inherent width other than that imposed by the detector resolution (see, for example, Mahoney, Ling and Jacobson 1980). It has therefore been found unsuitable for astrophysical sources. The author has examined the programme and believes it would have to be completely rewritten in order to deal with potentially broadened lines. When more sensitive instruments are employed, this rather considerable investment of effort may well be worthwhile.

HYPERMET in its original form was of course designed to use punched cards for control input, and now appears dated, even in respect of the coding techniques which were employed. These are, however, only minor problems; the actual algorithms are still superb by modern standards and it is these which will now be described.

The HYPERMET analysis process consists of three basic stages. Firstly the spectrum is searched quickly but sensitively for potential peaks. Once a suspected peak is located the region is fitted with a semi-empirical model of a germanium detector response to a fine line source. The residual (ie. the data with the calculated fit subtracted from it) is then examined and if another peak is suspected in the region then the fitting process is repeated with a 2-peak model; the first fit is discarded. The residual is then examined again and yet

another peak added to the model if required. This process is repeated until the residual is satisfactory. The program then recommences the peak search which continues until another suspected peak is found, or until the specified search range has been covered.

Spectral search.
The spectral search method is to evaluate the second difference of the spectral data using a bin width based on the estimated energy resolution of the detector. This evaluation is carried out at successively higher energies until a certain threshold is exceeded. This would correspond to a change in slope of the spectrum of the order expected for a peak with the approximate shape expected from the estimated detector resolution at the energy currently being searched. This has been found in practice to be a very useful search method for inherently monoenergetic lines.

Peak model.
The parameters of the semi-empirical peak model which is fit (multiply, if near-superimposed peaks are indicated in the residual) to the data are as follows (in order of decreasing importance) :-

1. The peak amplitude Γ and idealised (Gaussian) energy resolution δ of the detector.

2. The normalising amplitude α and index factor $(1/\beta)$ of an exponential function representing charge-straggling and pile-up which is folded into the gaussian function (1) and produces tailing at the low-energy side of the peak.

3. The corresponding parameters, τ and μ, of a much longer exponential, also folded into the gaussian, which represents incomplete charge collection.

4. The amplitude of a step Σ folded with a gaussian to give $\Sigma\,\mathrm{erfc}(x/\sigma)/2$ (where x is the spectral position with respect to the peak) which represents the effect of Compton back-scattering of photons from surrounding material, or escape peaks summed with Compton scattered energy from the escape photons.

5. The parameters a, b, c of a quadratic fit to the background $a + bJ + cJ$,

where J is the channel number.

All the effects are proportional to the peak amplitude Γ (except the quadratic) so $\alpha = A\Gamma$, $\tau = T\Gamma$ and $\Sigma = S\Gamma$ where A, T and S are amplitude independent parameters. Letting $\gamma = -\sqrt{2\beta x}$, $\mu = -\sqrt{2\nu x}$, and $x(I,J) = J - P(I)$ the fitting function $Y(J)$ for channel J in a subregion containing m peaks in positions $P(I)$ (where $I = 1, m$) is

$$
\begin{aligned}
Y(J) = \sum_{I=1}^{m} \Gamma(I) \Big[& \exp\left(-(x(I,J)/\delta(I))^2\right) && (1)\\
& + (A/2)\exp(x(I,J)/\beta)\,\mathrm{erfc}(x(I,J)/\gamma + \gamma/2\beta) && (2)\\
& + (T/2)\exp(x(I,J)/\nu)\,\mathrm{erfc}(x(I,J)/\mu + \mu/2\nu) && (3)\\
& + (S/2)\,\mathrm{erfc}(x(I,J)/\sigma)\Big] && (4)\\
& + a + bJ + cJ^2 && (5)
\end{aligned}
\qquad (A.1)
$$

The fit is performed by minimising the following expression

$$\chi^2 = \sum_J \left[(K(J) - Y(J,X))/K(J)^{\frac{1}{2}}\right]^2 \qquad (A.2)$$

where $K(J)$ is the actual spectral count in channel J.

Once the fit has been performed, the residuals (normalised to the estimated Poisson error in the counts, ie. $(K(J) - Y(J))/K(J)^{1/2}$) are checked for evidence of additional peaks by searching the smoothed second difference of these values over the fitting region. If an additional peak is detected then it is added to the model and the fitting process is repeated.

Appendix B.

1981 flight background lines.

The table of background lines in this appendix was derived from the total float altitude data, corresponding to 50613 s of elapsed time. The HYPERMET program (Phillips and Marlow 1976) was used to search for lines in the region 50 keV to 4000 keV. The table list those features for which the calculated count was $> 2\sigma$ above the continuum background. The tabulated data of Lederer and Shirley (1978) and Erdtmann and Soyka (1979) were used in interpreting the line origins. These results are also reported in Ayre at al. (1984).

There is no compensation for energy calibration drift as this was essentially zero ($\ll$ 0.2 keV around 511 keV). Above 2000 keV an increase in the fitted line widths is seen together with and an increasing failure to ascribe an origin for the features. It was therefore decided to make 2000 keV the upper limit for astronomical spectral work unless and until a better understanding of the spectrum at higher energies could be reached. Below 2000 keV our knowledge of the energy calibration and resolution of the detector, as derived from measurement of these lines throughout the flight, is excellent.

Many of the lines in the table are seen to arise from n-Ge or p-Ge reactions within the central detector, together with corresponding lines from the Na and I of the shield detectors and the Al of the support structure. Some aspects of the 1981 background are discussed briefly in chapter 4 of this thesis; a more full discussion is given in Owens, Myers and Thompson (1986) whilst general background problems for balloon-borne gamma ray spectrometers are discussed at some length by Gehrels (1985).

Members of the Uranium, Thorium and Actinium series are seen to be present in the data, particularly the lines from ^{214}Bi which is in the Uranium series. When the tabulated relative intensities were compared to those detected, generally good agreement was found at higher energies, but lower than expected fluxes at lower energies. This was particularly true for the 609.31 keV line for which the measured count was half that which would be expected from the measured intensities of the higher energy lines, and the known relative decay rates. When, however, compensation was made for attenuation in the shielding

Measured energy (keV)	Tabulated energy (keV)	Counts	Line width (keV)	Possible nuclides	Origin/comments
53.32 ± 0.16	53.437	6694 ± 1641	1.91 ± 0.27	$^{32}Ge^{73m}$, $^{33}As^{73}$	$^{32}Ge^{72}(n,\gamma)$, $^{32}Ge^{74}(p,d)$, $^{32}Ge^{73}(p,p')$
66.53 ± 0.12	66.737	4269 ± 451	2.34 ± 0.16	$^{32}Ge^{73m}$	
92.62 ± 0.38	92.80, 93.35	348 ± 111	2.15 ± 0.76	$^{90}Th^{234}$, $^{92}U^{235}$	
139.64 ± 0.08	139.687	3749 ± 488	1.72 ± 0.22	$^{32}Ge^{75m}$	$^{32}Ge^{74}(n,\gamma)$, $^{32}Ge^{76}(n,2n)$
142.58 ± 0.18	143.762	923 ± 171	1.68 ± 0.28	$^{92}U^{235}$	nat. $^{92}U^{235}$
158.88 ± 0.42	159.71	307 ± 118	2.10 ± 0.96	$^{32}Ge^{77m}$	$^{32}Ge^{76}(n,\gamma)$
175.06 ± 0.39	174.9	334 ± 115	1.95 ± 0.38	$^{33}As^{71}$	$^{32}Ge^{70}(p,\gamma)$
186.67 ± 0.59	185.72,186.0	180 ± 90	2.33 ± 0.87	$^{92}U^{235}$, $^{33}As^{71}$	nat. $^{92}U^{235}$, $^{32}Ge^{70}(p,\gamma)$
198.11 ± 0.09	198.3	9084 ± 774	2.08 ± 0.23	$^{32}Ge^{71m}$	$^{32}Ge^{70}(n,\gamma)$, $^{32}Ge^{70}(d,p)$, $^{32}Ge^{72}(p,d)$
200.94 ± 0.34	202.84	1585 ± 341	2.08 ± 0.32	$^{53}I^{127}$, $^{54}Xe^{127}$	$^{53}I^{127}(n,n'\gamma)$, $^{53}I^{127}(\gamma,\gamma')$, $^{53}I^{127}(p,n)$
212.14 ± 0.20	212.19	117 ± 36	1.16 ± 0.58	$^{53}I^{121}$	
238.20 ± 0.30	238.63	156 ± 72	1.62 ± 0.81	$^{82}Pb^{212}$	nat. $^{90}Th^{232}$
274.02 ± 0.77	272.97	109 ± 42	3.49 ± 0.79	$^{32}Ge^{66}$	
303.28 ± 0.67		153 ± 58	3.51 ± 0.80		
351.61 ± 0.57	351.99	134 ± 61	1.96 ± 0.61	$^{82}Pb^{214}$	nat. $^{92}U^{238}$
438.51 ± 0.38	438.0	122 ± 51	1.21 ± 1.1	$^{12}Mg^{23}$	$^{11}Na^{23}(p,n)$
472.41 ± 0.26	472.3	665 ± 99	2.11 ± 0.36	$^{11}Na^{24m}$	$^{11}Na^{23}(n,\gamma)$, $^{13}Al^{27}(n,\alpha)$
510.29 ± 0.16	511.0, 510.72	1172 ± 175	2.35 ± 0.22	e^+/e^-, $^{81}Tl^{209}$	positron annihilation, nat. $^{92}Th^{232}$
512.52 ± 0.25	511.0	774 ± 148	2.35 ± 0.3	e^+/e^-	positron annihilation
535.99 ± 0.17	536.09	40 ± 16	0.89 ± 0.18	$^{53}I^{30}$	$^{53}I^{129}(n,\gamma)$
582.89 ± 0.15	583.139	56 ± 21	0.87 ± 0.17	$^{81}Tl^{208}$	nat. $^{90}Th^{232}$
609.51 ± 0.10	609.312	310 ± 49	1.80 ± 0.38	$^{83}Bi^{214}$	nat. $^{92}U^{238}$
643.77 ± 0.33	641.0	61 ± 27	1.68 ± 0.70	$^{33}As^{72}$	$^{32}Ge^{72}(p,n)$
655.87 ± 0.04	654.4	190 ± 35	0.87 ± 0.09	$^{33}As^{82}$	fission
693.60 ± 0.25	691.3	200 ± 65	2.34 ± 0.50	$^{32}Ge^{72}$	$^{32}Ge^{72}(n,n'\gamma)$
697.06 ± 0.38	696.07	187 ± 61	2.34 ± 0.50	$^{33}As^{82m}$	double escape peak of 1718.07 keV
708.86 ± 0.06	709.31	492 ± 115	8.54 ± 1.49	$^{33}As^{82}$	double escape peak of 1731.31 keV
740.08 ± 0.18	739.48	31 ± 11	1.01 ± 0.28	$^{53}I^{130}$	$^{53}I^{129}(n,\gamma)$
763.33 ± 0.19	768.356	63 ± 31	0.88 ± 0.23	$^{83}Bi^{214}$	nat. $^{92}U^{238}$
842.33 ± 0.3	843.76	167 ± 65	1.57 ± 0.73	$^{12}Mg^{27}$,$^{13}Al^{27}$	$^{13}Al^{27}(n,n')$
910.48 ± 0.58	911.226	120 ± 36	2.36 ± 1.04	$^{89}Ac^{228}$	nat. $^{99}Th^{232}$
970.65 ± 0.85	968.33	119 ± 32	5.13 ± 1.46	$^{89}Ac^{228}$	nat. $^{90}Th^{232}$
1032.00 ± 0.15	1029.9	37 ± 15	1.01 ± 0.23	$^{33}As^{82m}$	single escape peak of 1540.9 keV
1120.84 ± 0.52	1120.287	215 ± 67	2.82 ± 0.61	$^{83}Bi^{214}$	nat. $^{92}U^{238}$
1238.60 ± 0.20	1238.11	95 ± 18	2.58 ± 0.42	$^{83}Bi^{214}$	nat. $^{92}U^{238}$
1294.51 ± 0.33	1293.538	57 ± 21	2.41 ± 0.69	$^{51}Sb^{116}$	
1375.99 ± 0.51	1377.669	52 ± 20	2.64 ± 0.74	$^{82}Bi^{214}$	nat. $^{92}U^{238}$
1406.99 ± 0.32	1407.98	57 ± 20	2.73 ± 1.26	$^{83}Bi^{214}$	nat. $^{92}U^{238}$
1432.46 ± 0.21	1434.08,1434.06	22 ± 9	1.20 ± 0.29	$^{24}Cr^{52}$, $^{25}Mn^{52m}$	
1460.84 ± 0.21	1460.75	102 ± 14	3.21 ± 0.49	$^{19}K^{40}$	
1507.14 ± 0.19	1509.228,1509.0	25 ± 10	1.24 ± 0.27	$^{83}Bi^{214}$, $^{33}As^{70}$	nat. $^{92}U^{238}$, single escape peak of 1540.9 keV
1541.29 ± 0.23	1540.9	23 ± 10	1.25 ± 0.32	$^{33}As^{82m}$	fission
1583.00 ± 1.97	1581.8	33 ± 15	5.08 ± 1.3	$^{33}As^{82m}$	double escape peak of 2603.8 keV
1660.83 ± 0.25	1661.28	25 ± 8	1.37 ± 0.24	$^{83}Bi^{214}$	nat. $^{92}U^{238}$
1730.93 ± 0.66	1729.60	67 ± 18	5.52 ± 0.82	$^{83}Bi^{214}$, $^{33}As^{82}$	nat. $^{92}U^{238}$, fission
1764.62 ± 0.12	1764.50	256 ± 19	3.05 ± 0.13	$^{83}Bi^{214}$	nat. $^{92}U^{238}$
1779.15 ± 0.29	1778.7	93 ± 15	3.05 ± 0.27	$^{13}Al^{28}$	$^{13}Al^{27}(n,\gamma)$
1810.71 ± 1.08		44 ± 16	5.52 ± 1.07		
1847.77 ± 0.35	1847.42	26 ± 10	1.44 ± 0.38	$^{83}Bi^{214}$	nat. $^{92}U^{238}$
2020.30 ± 0.23	2020.0	15 ± 5	1.48 ± 0.27	$^{33}As^{70}$	$^{32}Ge^{70}(p,n)$
2094.18 ± 3.27	2092.8	37 ± 17	10.24 ± 4.3	$^{33}As^{82m}$	single escape peak of 2603.8 keV
2128.86 ± 0.24	2127.50	18 ± 7	1.52 ± 0.34	$^{33}As^{82m}$	double escape peak of 3149.5 keV
2205.26 ± 0.57	2204.21	94 ± 17	6.29 ± 0.64	$^{83}Bi^{214}$	nat. $^{92}U^{238}$
2223.24 ± 0.28	2223.35	202 ± 13	6.29 ± 0.41	$^{1}D^{2}$	$^{1}H^{1}(n,\gamma)$
2450.49 ± 2.00	2447.81	39 ± 16	7.78 ± 4.09	$^{83}Bi^{214}$	nat. $^{92}U^{238}$
2616.57 ± 0.40	2614.47	129 ± 16	7.03 ± 0.49	$^{81}Tl^{208}$	nat. $^{92}Th^{232}$
2664.97 ± 0.39		29 ± 12	7.03 ± 1.58		
3053.76 ± 1.2		23 ± 10	7.76 ± 1.95		
3156.05 ± 1.5	3149.5	28 ± 12	7.98 ± 2.08	$^{33}As^{82m}$	fission
3442.80 ± 1.5		26 ± 12	8.40 ± 2.11		
3525.38 ± 1.4		30 ± 12	8.40 ± 1.80		

detectors, excellent agreement was found overall. It was therefore concluded that the ^{214}Bi was external to the spectrometer. If the source is natural ^{222}Rn decaying to ^{214}Bi within the air of the environmental dome, then a concentration of $\times 1000$ normal levels of ^{222}Rn must have been present at the pre-launch dome sealing. If the source is stratospheric, then, allowing for 20 km horizontal and 8 km vertical attenuation lengths at float altitude, a ^{214}Bi concentration of $5.5\,\mathrm{pCi\,m^{-3}}$ is required. Rn amongst the balloon He is a possible source but would require a concentration of $\sim 86\,\mu\mathrm{Ci\,m^{-3}}$; an unacceptably high figure.

The variation of some of the principal lines with residual atmospheric depth is illustrated in figure B.1. The 53, 67, 139, and 198 keV lines arise mainly from n-Ge interactions, unlike the mainly atmospheric 511 keV line. The different depth dependence of the 511 keV line illustrates its different origin. The neutron induced fluxes might be expected to likewise fall below the Pfotzer maximum, but this is clearly not the case. The continued neutron activation at high altitudes is believed to be caused by neutron production due to cosmic ray interactions in the shields. A more detailed discussion of neutron production and activation within the Durham system is given by Owens, Myers and Thompson (1986).

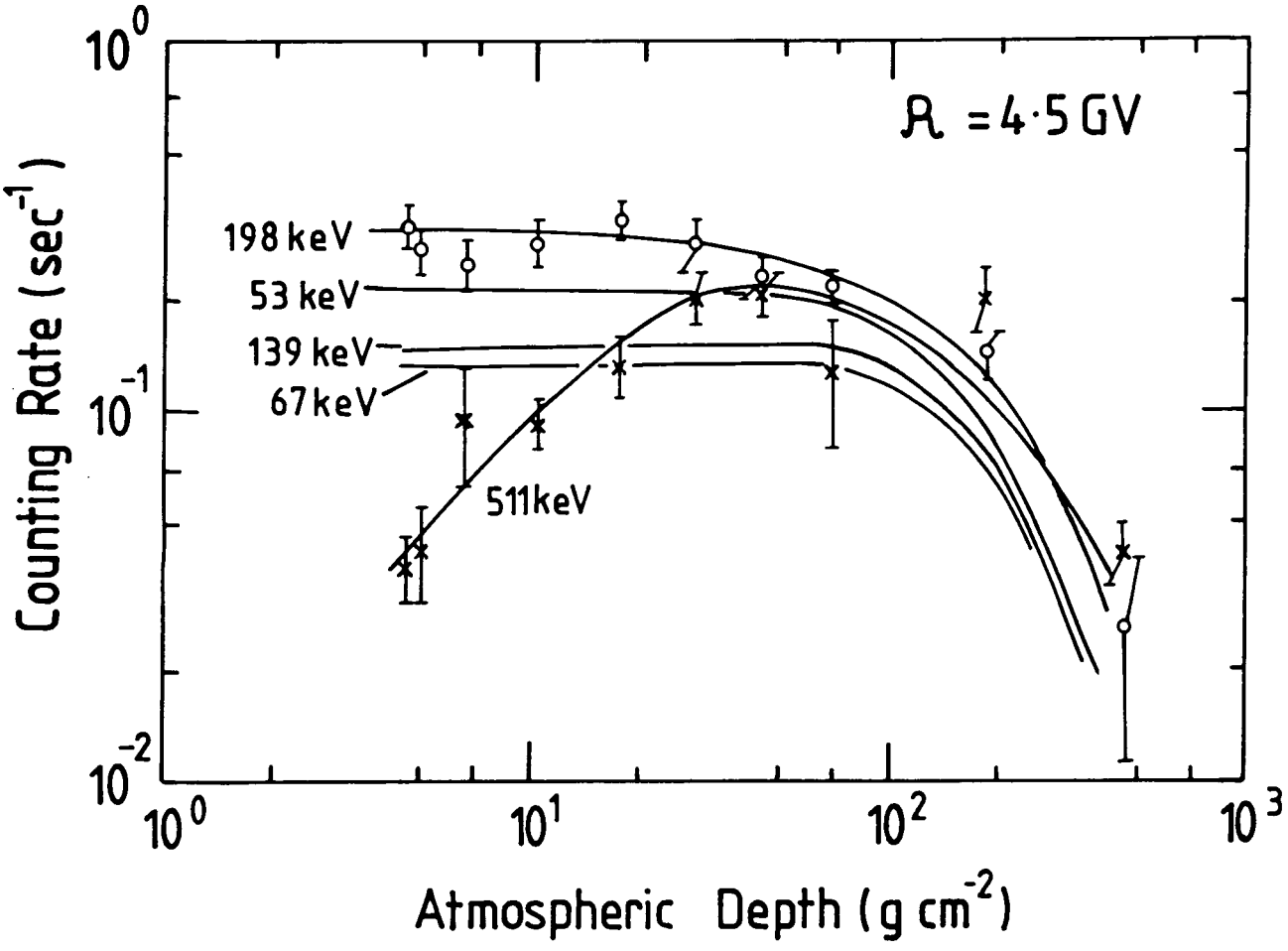

Figure B·1 The variation of intensities of the 53, 67, 139, 198 and 511keV lines with atmospheric depth over Palestine Texas.

[1 g cm^{-2} = 10 Kg m^{-2}]

Acknowledgements.

I would like to thank Professors A.W. Wolfendale and B.H. Bransden for the use of the facilities of the Physics Department and for their encouragement and support of this work.

I am very grateful to my supervisor, Dr. M.G. Thompson without whose unfailing help and invaluable advice and expertise this project would certainly not have been possible. Many thanks are also due to the other members of the gamma ray astronomy group: Dr. C.A. Ayre, Dr. P.N. Bhat, Dr. Y.Q. Ma, Dr.A. Owens, Mr. W.M. Summers and Dr. K.C. Yau; all of whom made invaluable contributions. Particular thanks are due to Dr. A. Owens, presently of the University of New Hampshire, who has maintained a constant interest in this work, especially in the area of the detector response, and has also made invaluable suggestions for processing the flight data.

The fine work of Mr. K. Tindale and Mr. A. Turnbull on the telescope and payload hardware and also the excellent work by the departmental workshops supervised by Mr. D. Jobling, Mr. W. Hogg and the late Mr. W. Leslie, is gratefully acknowledged. I also thank the staff of the NSBF, Palestine, particularly Mr. M. Poarch.

Special thanks are due to Mr. T. Jackson of the electronics workshop for his excellent work on the magnetometers and at Palestine and also for his help and guidance on all electronics matters. Thanks also to his staff, particularly Mr. T. Adamson.

Special thanks again to Mr. A.P. Lotts, the Durham starlink node manager who has been a constant and completely invaluable source of expertise, help and advice on all aspects of computing. Mr. M. Munro, then of the Computer Unit and Mr. P.R. Baxendale of the Microprocessor Centre are also thanked for their kind help with this work.

It is a great pleasure to express my gratitude to my mother and my late father for their unfailing support and love without which this, and much else, would not have been possible.

Mrs. P.A. Russel is thanked for her excellent work with the diagrams (and

wire-wrapping!). Finally the SERC is thanked for provision of a studentship and its support for this work.

References.

Albernhe, F., Vedrenne, G.; J. Geophys. Res., **81** (1976) 2433

Albernhe, F., Bochet, D., Chabacid, J.P., Vedrenne, G.; NIM, **155** (1978) 171

Albernhe, F., Vedrenne, G., Martin, I.M.; J. Geophys. Res., **84** (1979) 6658

Albernhe, F., Leborgne, J.F., Vedrenne, G., Boclet, D., Durouchoux, P., Da-Costa, J.M.; Astron. Astrophys., **94** (1981) 214

Arnett, W.D.; Ap. J., **157** (1969) 1369

Arnett, W.D., Truran, J.W.; *Nucleosynthesis: Changes and New Developments*, University of Chicago Press, Chicago, London (1985)

Arons, J, McCray, R.; Ap. J. Lett., **158** (1969) L91

Ayre, C.A., Bhat, P.N., Owens, A., Summers, W.M., Thompson, M.G.; Phil. Trans. R. Soc. Lond. A, **301** (1981) 687

Ayre, C.A., Bhat, P.N., Ma, Y.Q., Myers, R.M. Thompson, M.G.; MNRAS, **205** (1983) 285

Ayre, C.A., Bhat, P.N., Ma, Y.Q., Myers, R.M. Thompson, M.G.; NIM, **220** (1984) 549

Baker, R.E., Lovett, R.R., Orford, K.J., Ramsden, D.; Nature Phys. Sci., **245** (1973) 18

Bakke, J.C., McDaniel, J.D., Mathews, J.D., Reagan, J.B.; IEEE Trans. Nucl. Sci., **NS-21** (1974) 164

von Ballmoos, P., Diehl, R., Schönfelder, V.; Ap. J., **318** (1987) 654

Barnes, C.A., Clayton, D.D., Schramm, D.N.; *Essays in Nuclear Astrophysics*, Cambridge University Press, Cambridge (1983)

Bethe, H.A.; in *Essays in Nuclear Astrophysics* [Ed: Barnes, C.A., Clayton, D.D., Schramm, D.N.] Cambridge University Press, Cambridge (1983) 439

Bildstein, M.L., Zurek, W.H.; AIP conference proceedings, **155** (1987) 184

Bodansky, D., Clayton, D.D., Fowler, W.A.; Phys. Rev. Lett., **20** (1968) 161

Boldt, E.A., Holt, S.S., Serlimitsos, P.J.; Ap. J. Lett., **164** (1971) L9

Boyd, R.N., Wiescher, M.; Ap. J., **276** (1984) L9

Brown, B.L.; Ap. J. Lett., **292** (1985) L67

Brown, B.L., Leventhal, M., Mills, A.P.,Jr.; Phys. Rev. A., **33** (1986) 2281

Brown, B.L., Leventhal, M.; Ap. J., **319** (1987) 637

Brecher, K.; Ap. J. Lett., **215** (1977) L17

Brecher, K., Burrows, A.; Ap. J., **240** (1980) 642

Cameron, A.G.W.; Space Science Review, **15** (1973) 121

Cameron, A.G.W.; Ap. J. Lett., **230** (1979) L53

Cameron, A.G.W., Cowan, J.J., Truran, J.W.; in *Nucleosynthesis: Changes and New Developments* [Ed: Arnett, W.D., Truran, J.W.] University of Chicago Press, Chicago, London (1985) 190

Carpenter, G.F., Coe, M.J., Engel, A.R.; Nature, **259** (1976) 99

Cash, W.; Ap. J., **291** (1979) 939

Chan, K.W., Lingenfelter, R.E.; Ap. J. Lett., **318** (1987) 51

Cheng, A.F., Ruderman, M., Sutherland, P.; Ap. J., **203** (1976) 209

Cheng, K.S., Ho, C., Ruderman, M.; Ap. J., **300** (1986) 500

Chupp, E.L.; *Gamma Ray Astronomy*, Reidel, Dordrecht (1976)

Clayton, D.D., Craddock, W.L.; Ap. J., **142** (1965) 189

Clayton, D.D.; *Principles of Stellar Evolution and Nucleosynthesis*, University of Chicago press, Chicago, London (1969)

Clayton, D.D.; Ap. J. Lett., **244** (1981) L97

Clayton, D.D.; in *Essays in Nuclear Astrophysics* [Ed: Barnes, C.A., Clayton, D.D., Schramm, D.N.] Cambridge University Press, Cambridge (1983) 401

Costa, E., Massaro, E., Salvati, M., Appolloni, A.; Astron. Astrophys., **17** (1984) 165

Da Costa, A.A.; MNRAS, **204** (1983) 1125

Dallaporta, N.; in *Relativistic Astrophysics and Cosmology* [Ed: Sabatta, V. de, Karade, T.M.] World Scientific, Singapore (1984) 1

Daugherty, J.K., Harding, A.K.; in *Positron-Electron Pairs in Astrophysics* (GSFC, Greenbelt, Maryland: 1983), AIP Conf. Proc. **101** (387) 1983

Davisson, C.M.; in *Alpha-, Beta- and Gamma-Ray Spectroscopy* **1** [Ed: Siegbahn, K.] North Holland publishing company, Amsterdam (1965) 37

Dean, A.J., Dipper, N.A.; MNRAS, **194** (1981) 219

Deutsch, M.; Phys. Rev., **82** (1951) 445

Dipper, N.A.; PhD Thesis, University of Southampton, UK (1980)

Dolan, J.F., Crannell, C.J., Dennis, B.R., Frost, K.J., Maurer, G.S., Orwig, L.E.; Ap. J., **217** (1977) 809

Dunphy, P.P., Forrest, D.J., Chupp, E.L., Cherry, M.L., Ryan, J.M.; Ap. J., **244** (1981) 1081

Erber, T.; Rev. Mod. Phys., **38** (1966) 626

Erdtman, G., Soyka, W.; *The Gamma Rays of the Radionuclides*, Verlag Chemie, Weinham, New York (1979)

Fabian, A.C., Nulsen, P.E.J.; MNRAS, **180** (1977) 479

Fazio, G.G.; in *Ann. Rev. of Astron. and Astrophys.* **5** [Ed: Goldberg, N.] Annular Reviews, inc, Palo Alto, California (1967) 481

Fazio, G.G., Stecker, F.W.; Nature, **226** (1970) 135

Felten, J.E., Morrison, P.; Ap. J., **146** (1966) 686

Fichtel, C.E., Hartman, R.C., Kniffen, D.A., Thompson, D.J., Bignami, G.F, Ögelman, H., Özel, M.E., Tümer, T.; Ap. J., **198** (1975) 163

Fishman, G.J., Watts, Jr, J.W.; Ap. J., **212** (1977) 211

Gardner, B.M., Forrest, D.J., Dunphy, P.P.. Chupp, E.L.; in *The Galactic Centre.* (California Institute of Technology: 1982), Riegler, G.R., Blandford, R.E. **AIP Conf. Proc.** (83) 144(1982)

Graser, U, Schonfelder, V.; Ap. J., **263** (1982) 677

Gehrels, N., Cline, T.L., Teegarden, B.J., Tueller, J., Leventhal, M., MacCallum, C.J., Hewsha, P.V., Ryge, P.; IEEE Trans. Nucl. Sci., **NS-31** (1984) 307

Gehrels, N.; NIM A, **A239** (1985) 324

Gehrels, N., Leventhal, M., MacCallum, C.J.; Ap. J. Lett., **320** (1987a) L19

Gehrels, N., Leventhal, M., MacCallum, C.J.; Ap. J., **322** (1987b) 215

Grindlay, J., Branduardi, G., Fabian, A.; Highlights Astr., **5** (1979) 741

Ginzburg, V.L.; *Elementary Processes for Cosmic Ray Astrophysics*, Gordon and Breach Publishing Company, New York (1969)

Gruber, D.E., Ling, J.C.; Ap. J., **213** (1977) 802

Hajnal, F., Klusek, C.; NIM, **122** (1974) 559

Hameury, J.M., Boclet, D., Durouchoux, P.L., Cline, T.L., Paciesas, W.S., Teegarden, B.J., Tueller, J., Haymes, R.C.; Ap. J., **270** (1983) 144

Hardee, P.E.; Ap. J., **227** (1979) 958

Harding, A.K.; Goddard Space Flight Centre Preprint (1987)

Hayakawa, S.; *Cosmic Ray Physics*, John Wiley, New York (1969)

Haymes, R.C., Walraven, G.D., Meegan, C.A., Hall, R.D., Djuth, F.T., Shelton, D.H.; Ap. J., **201** (1975) 593

Heitler, W.; *The Quantum Theory of Radiation*, Oxford University Press, Oxford (1954)

Hermsen, W.; PhD Thesis, University of Leiden, Netherlands (1980)

Higdon, J.C., Lingenfelter, R.E; Ap. J. Lett., **215** (1977) L53

Hillier, R.; *Gamma Ray Astronomy*, Oxford University Press, Oxford (1984)

Holt, S.S., Mushotzsky, R.F.; NASA Technical Memorandum, **TM-80559** (1979) 1

Hurley, K.; University of California Berkeley, Space Sciences Laboratory preprint (1987)

Imhof, W.L., Nakano, G.H., Johnson, R.G., Reagan, J.B.; J. Geophys. Res., **79** (1974) 565

Imhof, W.L., Nakano, G.H., Reagan, J.B.; J. Geophys. Res., **81** (1976) 2835

Imhof, W.L., Nakano, G.H.; Ap. J., **214** (1977) 38

Irvine, J.M; *Neutron Stars*, Oxford University Press, Oxford (1978)

Jacobson, A.S., Bishop, R.J., Culp, G.W., Jung, L., Mahoney, W.A., Willett, W.A., Willett, J.B.; NIM, **127** (1975) 115

Johnson III, W.N., Harnden, F.R.,Jr., Haymes, R.C.; Ap. J. Lett., **172** (1972) L1

Johnson III, W.N., Haymes, R.C.; Ap. J., **184** (1973) 103

Kafatos, M., Eilek, J.A.; in *Positron-Electron Pairs in Astrophysics* (GSFC, Greenbelt, Maryland: 1983), AIP Conf. Proc. **101** (354) 1983

Kanbach, G., Schlikeiser, R.; in *Positron-Electron Pairs in Astrophysics* (GSFC, Greenbelt, Maryland: 1983), AIP Conf. Proc. **101** (204) 1983

Klein, O., Nishina, Y.; Z. Physik, **52** (1929) 853

Knight, F.K.; PhD Thesis, University of California at San Diego (1981)

Knight, F.K.; Ap. J., **260** (1982) 538

Kozlovsky, B., Lingenfelter, R.E., Ramaty, R.E.; Ap. J., **316** (1987) 801

Kundt, W., Krotscheck, E.; Astron. Astrophys., **83** (1980) 1

Kurfess, J.D., Johnson, W.N.; IEEE Trans. Nucl. Sci., **22** (1975) 626

Lamb, R.C., Ling, J.C., Mahoney, W.A., Riegler, G.R., Wheaton, W.A., Jacobson, A.S.; Nature, **305** (1983) 37

Lederer, C.M., Shirley, V.S.; *Table of isotopes*, Wiley, New York (1978)

Leising, M.D., Clayton, D.D.; Ap. J., **294** (1985) 591

Leising, M.D., Clayton, D.D.; Ap. J., **323** (1987) 159

Leising, M.D., Share, G.H.; Ap. J., **328** (1988) 755

Leventhal, M., MacCallum, C.J., Watts, W.; Ap. J., **216** (1977) 491

Leventhal, M., MacCallum, C.J., Stang, P.D.; Ap. J. Lett., **225** (1978) 11

Leventhal, M., MacCallum, C.J.; Ann. N.Y. Acad. Sci., **336** (1980) 248

Leventhal, M., MacCallum, C.J., Huters, A.F., Stang, P.D.; Ap. J., **240** (1980) 338

Leventhal, M., MacCallum, C.J., Huters, A.F., Stang, P.D.; Ap. J. Lett., **260** (1982) 1

Leventhal, M., MacCallum, C.J., Huters, A.F., Stang, P.D.; Ap. J., **302** (1986) 459

Lichti, G.G., Buccheri, R., Caraveo, P. Gerardi, G., hermsen, W., kanbach, G., Masnou, J.L, Mayer-Hasselwander, H.A., Paul, J.A., Swanenberg, B.N., Wills, R.D.; COSPAR Advances in Space Exploration, **7** (1980) 49

Li, T.P., Ma, Y.Q.; Ap. J., **272** (1983) 317

Ling, J.C.; PhD Thesis, University of California, San Diego (1985d)

Ling, J.C., Mahoney, W.A., Willet, J.B., Jacobson, A.S.; Nature, **270** (1977) 36

Ling, J.C., Mahoney, W.A., Willet, J.B., Jacobson, A.S.; Ap. J., **231** (1979) 896

Lingenfelter, R.E., Ramaty, R.; Ap. J. Lett., **211** (1977) L9

Lingenfelter, R.E., Ramaty, R.; in *The Galactic Centre. (California Institute of Technology: 1982)* [Ed: Riegler, G.R., Blandford, R.E.] AIP Conf. Proc., 83 (1982) 148

MacCallum, C.J., Huters, A.F., Stang, P.D., Leventhal, M.; Ap. J., **291** (1985) 486

MacCallum, C.J., Huters, A.F., Stang, P.D., Leventhal, M.; Ap. J., **317** (1987) 877

Mahoney, W.A., Ling, J.C., Jacobson, A.S., Tapphorn, R.M.; NIM, **178** (1980) 363

Mahoney, W.A., Ling, J.C., Jacobson, A.S.; NIM, **185** (1981) 449

Mahoney, W.A., Ling, J.C., Jacobson, A.S.; Ap. J., **278** (1984) 784

Mahoney, W.A., Ling, J.C., Wheaton, Wm.A., Jacobson, A.S.; Ap. J., **286** (1984) 578

Manchanda, R.K., Bazzano, A., LaPadula, C.D. Polcaro, V.F., Ubertini, P.; Ap. J., **252** (1982) 172

Marmier, P., Sheldon, E.; *Physics of Nuclei and Particles* vol. I, Academic Press, New York (1969)

Marscher, A.P., Brecher, K., Wheaton, W.A., Ling, J.C., Mahoney, W.A., Jacobson, A.S.; Ap. J., **281** (1984) 566-69

Matteson, J.L.; in *Positron-Electron Pairs in Astrophysics* (GSFC, Greenbelt, Maryland: 1983), AIP Conf. Proc. **101** (292) 1983

Mayer-Hasselwander, H.A. et al.; Astron. Astrophys., **105** (1982) 164

McKinley, J.M., Ramaty, R.; in *Positron-Electron Pairs in Astrophysics* (GSFC, Greenbelt, Maryland: 1983), AIP Conf. Proc. **101** (428) 1983

Morini, M.; MNRAS, **202** (1983) 495

Nakano, G.H., Imhof, W.L., Johnson, R.G.; IEEE Trans. Nucl. Sci., **NS-21** (1974) 159

Owens, A.; NIM A, **A238** (1985a) 473

Owens, A.; NIM A, **A239** (1985b) 623

Owens, A.; Astrophys. Space Sci., **112** (1985c) 75

Owens, A.; PhD Thesis, University of Durham (1985d)

Owens, A., Myers, R.M., Thompson, M.G.; NIM A, **A245** (1986) 569

Paciesas, W., Baker, R., Boclet, D., Brown, S., Cline, T., Costlow, H., Durouchoux, P., Ehrmann, C., Gehrels, N., Hameury, J.M., Haymes, R., Teegarden, B., Tueller, J.; NIM, **215** (1983) 261

Paciesas, W., Cline, T., Teegarden, B., Tueller, J., Durouchoux, P., Hameury, J.M.; Ap. J. Lett., **260** (1982) L7

Paciesas, W., Baker, R., Boclet, D., Brown, S., Cline, T., Costlow, H., Durouchoux, P., Ehrmann, C., Gehrels, N., Hameury, J.M., Haymes, R., Teegarden, B., Tueller, J.; NIM, **215** (1983) 261

Phillips, G.W., Marlow, N.W.; NRL memorandum report, **3198** (1976)

Preuss, E., Kellerman, K.I., Pauliny-Toth, I.I.K., Witzel, A., Shaffer, D.B.; Astron. Astrophys., **79** (1979) 268

Ramana Murthy, P.V., Wolfendale, A.W.; *Gamma Ray Astronomy*, Cambridge University Press, Cambridge (1986)

Ramaty, R., Kozlovsky, B., Lingenfelter, R.E.; Ap. J. Suppl., **40** (1979) 487

Ramaty, R., Kozlovsky, B., Lingenfelter, R.E.; Ap. J. Lett., **283** (1984) L13

Ramaty, R., McKinley, J.M., Jones, F.C.; Ap. J., **256** (1982) 238

Riegler, G.R., Ling, J.C., Mahoney, W.A., Wheaton, W.A., Willett, J.B., Jacobson, A.S., Prince, T.A.; Ap. J. Lett., **248** (1981) L13

Riegler, G.R., Ling, J.C., Mahoney, W.A., Wheaton, W.A., Jacobson, A.S.; Ap. J., **294** (1985) L13

Rothschild, R.E., Baity, W.A., Marscher, A.P., Wheaton, W.A.; Ap. J. Lett., **243** (1981) L13

Rothschild, R.E., Mushotzsky, R.F., Baity, W.A., Gruber, A.P, Matterson, J.L., Peterson, L.E.; Ap. J., **269** (1983) 423

Ruderman, M.A., Sutherland, P.G.; Ap. J., **196** (1974) 51

Schlovsky, I.; *Cosmic Radio Waves*, Harvard University Press, Cambridge, Massachusetts (1960)

Schönfelder, V., Lichti, G., Moyano, C.; Nature, **257** (1975) 375

Schönfelder, V., Graser, U., Daugherty, J.; Ap. J., **217** (1977) 306

Schönfelder, V.; Cospar Advances in Space Exploration, Pergamon Press, **7** (1982) 371

Schönfelder, V., Graser, U., Diehl, R.; Astron. Astrophys., **110** (1982) 138

Schwinger, J.; Phys. Rev., **75** (1949) 1912

Share, G.H., Kinzer, R.L., Kurfess, J.D., Forrest, D.J., Chupp, E.L., Rieger, E.; Ap. J. Lett., **292** (1985) 61

Share, G.H., Kinzer, R.L., Kurfess, J.D., Messina, D.C., Purcell, W.R., Chupp, E.L., Forrest, D.J., Reppin, C.; Ap. J., **326** (1988) 717

Silk, J.; in *Ann. Rev. of Astron. and Astrophys.* **11** [Ed: Goldberg, N.] Annual Reviews, inc, Palo Alto, California (1979) 269

Shklovsky, I.S.; Ap. J. Lett., **159** (1970) L77

Smart, W.M.; *Text-book on Spherical Astronomy*, Cambridge University Press, Cambridge (1977)

Stecker, F.W.; *Cosmic Gamma Rays*, NASA SP-249 National Aeronautics and Space Administration, Washington, DC. (1971)

Strickman, M.S., Johnson, W.N., Kurfess, J.D.; Ap. J. Lett., **230** (1979) L15

Strickman, M.S., Kurfess, J.D., Johnson, W.N.; Ap. J. Lett., **253** (1982) L23

Sturrock, P.A.; Ap. J., **164** (1971) 529

Summers, W.M.; MSc Thesis, University of Durham (1983)

Toor, A., Seward, F.D.; Ap. J., **79** (1974) 995

Tucker, W.H.; *Radiation Processes in Astrophysics*, MIT press, Cambridge, Massachusetts (1977)

Varma, C.M.; Nature, **267** (1977) 686

Varma, C.M.; in *Positron-Electron Pairs in Astrophysics* (GSFC, Greenbelt, Maryland: 1983), AIP Conf. Proc. **101** (421) 1983

Varnell, L.S., Ling, J.C., Mahoney, W.A., Jacobson, A.S., Pehl, R.H., Goulding, F.S., Landis, D.A., Luke, P.N., Madden, N.W.; IEEE Trans. Nucl. Sci., **NS-31** (1984) 300

Wallace, R.K., Woosley, S.E.; Ap. J. Suppl., **45** (1981) 389

Walraven, G.D., Hall, R.D., Meegan, C.A., Coleman, P.L., Shelton, D.H., Haymes, R.C.; Ap. J., **202** (1975) 502

Walraven, G.D., Haymes, R.C.; Nature, **264** (1976) 42

Watanabe, H.; Astrophys. Space Sci., **111** (1985) 157

Wheaton, Wm.A., Ling, J.C., Mahoney, W.A., Jacobson, A.S.; *Proceedings of the 20th International Cosmic Ray Conference* (Moscow: 1987), OG-2.4-1

Wirth, A., Kenyon, S.J., Hunter, D.A.; Ap. J., **269** (1983) 102

Woosley, S.E., Howard, W.M.; Ap. J. Suppl., **36** (1978) 285

Woosley, S.E., Weaver, T.A.; Ap. J., **238** (1980) 1017

Woosley, S.E., Taam, R.E., Weaver, T.A.; Ap. J., **301** (1986) 601

Yau, K.K.C.; MSc Thesis, University of Durham (1984)

Yoshimori, M., Watanabe, H., Okudairi, K., Hirasima, Y., Murakami, H.; Aust. J. Phys, **32** (1979) 375